Universidade do Minho
Escola de Engenharia

Franziska Regel

A MODELLING APPROACH FOR 3D BRAID REINFORCED COMPOSITES UNDER NON-AXIAL LOADING

Julho de 2014

Universidade do Minho
Escola de Engenharia

Franziska Regel

A MODELLING APPROACH FOR 3D BRAID REINFORCED COMPOSITES UNDER NON-AXIAL LOADING

Tese de Doutoramento
Ciência e Engenharia de Polímeros e Compósitos

Trabalho efectuado sob a orientação do
Dr. Ferrie W.J. van Hattum
Dr. Gustavo A.O. Rodrigues Dias

Julho de 2014

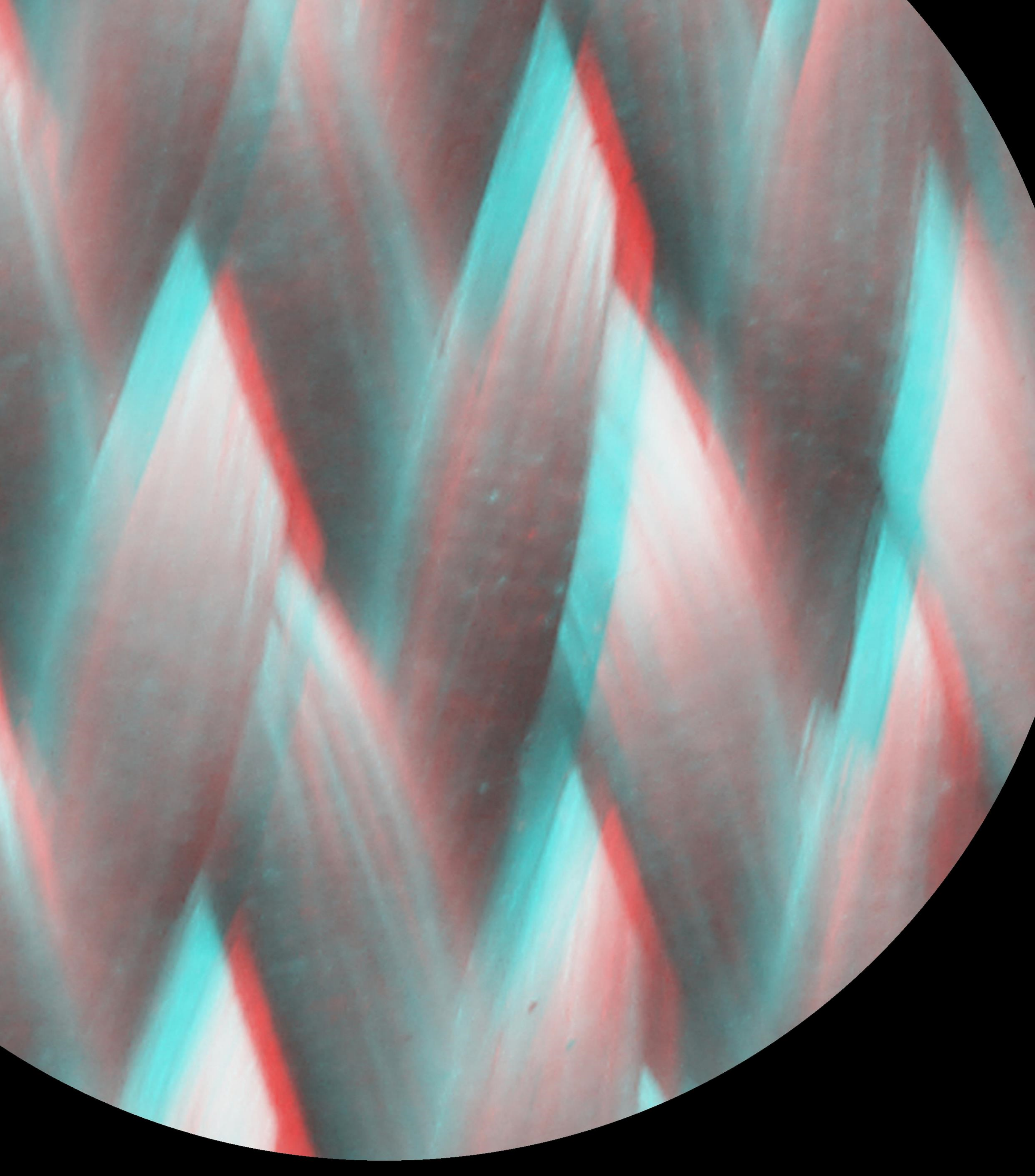

A MODELLING APPROACH FOR 3D BRAID REINFORCED COMPOSITES UNDER NON-AXIAL LOADING

FRANZISKA REGEL

A MODELLING APPROACH FOR 3D BRAID REINFORCED COMPOSITES UNDER NON-AXIAL LOADING

FRANZISKA REGEL

Universidade do Minho

A dissertation submitted to the University of Minho in partial fulfillment of the requirements for the degree of Doctor of Philosophy

July 2014

Supervised by
Dr. Ferrie W.J. van Hattum
Co-supervisor
Dr. Gustavo A.O. Rodrigues Dias

Franziska Regel: *A modelling approach for 3D braid reinforced composites under non-axial loading*, A dissertation submitted to the University of Minho in partial fulfillment of the requirements for the degree of Doctor of Philosophy, © July 2014

Abstract

Fibre reinforced composite materials are widely used in aerospace, the automotive industry or civil structures due to their high stiffness and strength to weight ratios, good fatigue strength and corrosion resistance. The mechanical performance of a composite structure particularly depends upon its type of fibre reinforcement, typically produced using textile technologies such as weaving and braiding. Compared to two-dimensional (2D) laminated composites, three-dimensional (3D) preforms allow for a better out-of-plane stiffness, strength and impact resistance. 3D braids additionally provide structural integrity and the possibility for near-net-shapes. However 3D braids as reinforcement are still hard to find in commercial use, due to the lack of braiding machines and dimensional limitations of possible preforms. Furthermore, the microstructure of 3D braid reinforced composites (3DBRC) is complicated and the prediction of their mechanical and damage behaviour challenging.

In order to support the use of 3D braids in structural composites, analytical and numerical approaches are presented in this thesis for the prediction of effective elastic properties and the analysis of the damage behaviour under lateral loading. The presented work has been related to the use of composites in guard rails, which must absorb high energies while being flexible to decelerate a colliding vehicle consistently. At first, compressive loading of traditional pultruded box beam sections has been performed to analyse their failure behaviour. In addition, profile sections were numerically modelled to identify material parameters which enhance their fracture toughness. Single- and multicellular cross-sections were analytically analysed to study the effect of geometric characteristics on their bending and buckling behaviour. Different 3DBRCs were produced and tested to reveal their failure behaviour as compared to a 2D laminate. Analytical models were established to predict elastic constants and used for parameter studies to understand the influence of processing parameters on elastic properties. A numerical modelling approach was developed based on a simplified description of the complex textile architecture. Preliminary Finite Element (FE) modelling studies were used to define the model and assess its capability for the prediction of mechanical properties. Moreover, elastic constants of the 3DBRCs are calculated and the damage behaviour simulated.

Delamination as known from 2D laminates doesn't occur in 3DBRCs owing to their yarn interlacement. Moreover, 3DBRCs present a higher fracture toughness and impact resistance compared to a 2D laminate. Although not all predicted properties agree quantitatively with experimental results, qualitatively similar trends are observed and results obtained by modelling agree well with each other.

Resumo

Os materiais compósitos reforçados com fibras são amplamente utilizados na indústria aeroespacial, na indústria automóvel e em estruturas civis, devido à sua elevada rigidez e resistência em relação ao peso, boa resistência à fadiga e à corrosão. O desempenho mecânico de uma estrutura de compósito depende particularmente das fibras de reforço usadas, que são geralmente produzidas com tecnologias de tecidos, tais como tecelagem e entrançamento. Comparados com os compósitos 2D, os tecidos 3D apresentam uma maior rigidez e resistência ao impacto. Adicionalmente, tranças em 3D fornecem maior integridade estrutural e a possibilidade de *near-net-shape*. No entanto, ainda é difícil encontrar tranças 3D como reforço na indústria devido à falta de máquinas apropriadas e limitações dimensionais das possíveis pré-formas. Por outro lado, a microestrutura dos compósitos com tranças 3D é complexa e a previsão do seu comportamento mecânico e ao dano são um desafio.

De modo a apoiar o uso de tranças 3D em estruturas de materiais compósitos, são apresentadas nesta tese abordagens analíticas e numéricas para a predição das propriedades elásticas efetivas e análise do comportamento ao efeito de carga lateral. O trabalho apresentado está relacionado com o uso de materiais compósitos nas barras de segurança das estradas, que devem ser capazes de absorver elevadas energias e ao mesmo tempo ser flexíveis para desacelerar o veículo que colide. Assim, foram realizados ensaios de compressão de seções box beam pultruded para analisar o seu comportamento de falha. Além disso, os perfis foram modelados numericamente para identificar os parâmetros do material que aumentam a sua resistência à fratura. Secções transversais simples e multicelulares foram também analisadas analiticamente para estudar o efeito das características geométricas no comportamento à flexão e encurvadura. Os diferentes 3DBRCs produzidos foram mecanicamente testados sob tração, flexão e impacto de modo a avaliar o seu comportamento de falha comparativamente aos laminados 2D. Estabeleceram-se modelos analíticos baseados num método de volume médio para prever as constantes elásticas e, adicionalmente, usados para estudar a influência dos parâmetros de processamento nas propriedades elásticas. Desenvolveu-se uma abordagem de modelação numérica com base numa descrição simplificada da arquitetura têxtil complexa e no *Binary model*. Estudos preliminares de modelação FE foram utilizados para definir o modelo e avaliar a sua capacidade de predição das propriedades mecânicas. Além disso, foram calculadas as constantes elásticas dos 3DBRCs e simulado o seu comportamento ao dano.

Os 3DBRCs, devido aos seus fios entrelaçados, não exibem a delaminação característica dos laminados 2D. Por outro lado, os 3DBRCs apresentam uma maior resistência à fractura e ao impacto em comparação com um laminado 2D. Embora nem todas as propriedades preditas analítica e numericamente estejam em concordância quantitativa com os resultados experimentais, são observadas tendências qualitativas semelhantes e os resultados obtidos por modelação estão de acordo um com o outro.

Acknowledgements

Firstly, I kindly acknowledge the financial support of the Portuguese Foundation for Science and Technology (FCT) through the PhD grant SFRH/BD/66899/2009.

I would like to express my gratitude to my supervisor Dr. Ferrie W.J. van Hattum for the chance he gave me by inviting me to Portugal, for his trust in me to build up a composite laboratory at the Pólo de Inovação em Engenharia de Polímeros (PIEP), his advice, guidance, for the exchange of ideas and his precious time for my research. I would also like to thank my co-supervisor Dr. Gustavo A.O. Rodrigues Dias for his advice and guidance.

Special thanks go to Dr. Joon-Hyung Byun and his colleagues at the Korean Institute for Materials in Changwon. I am very grateful for the provided access to a track-and-column braiding machine, their equipment, material and advice, which was crucial for the success of this work. I thank everyone of the composite group at PIEP for providing their facilities and assistance for the specimen preparation.

I would like to thank everyone who directly or indirectly supported me throughout the last years and encouraged me in the completion of this work. I would also like to express my gratitude to everyone for sharing chocolate, cake, lunch, dinner, drinks, talks, dances, all those unforgettable moments that make the last years special. In particular, I would like to thank Anna for making me laugh, spending time, sharing academic experiences, her mathematics advice and loads of personal moments. Special thanks go to Carlos for his understanding, support, and his invaluable help with Python.

Most of all, I would like to thank my mum for her love and support everywhere I go, even though ela tem saudades minhas.

Contents

List of Figures

List of Tables

Nomenclature

Acronyms

$1D$	One-Dimensional
$2D$	Two-Dimensional
$2step$	Two-step braid
$3D$	Three-Dimensional
$3DBRC$	Three-Dimensional Braid Reinforced Composite
$3DTRC$	Three-Dimensional Textile Reinforced Composite
$4stepWI$	Four-step braid WIth axial yarns
$4stepWO$	Four-step braid WithOut axial yarns
ASI	Acceleration Severity Index
BM	Binary Model
CDM	Continuum Damage Mechanics
CFE	Crush Force Efficiency
CLT	Classic Laminate Theory
CSM	Continuous Strand Mat
DOF	Degree Of Freedom
DST	Domain Superposition Technique
FE	Finite Element
GF	Glass Fibre
$GFRP$	Glass Fibre Reinforced Polymer
$KIMS$	Korea Institute for Materials Science
NCF	Non-Crimp Fabric
ROM	Rule Of Mixtures

RVE	Representative Volume Element
SEA	Specific Energy Absorption
UD	UniDirectional
UMAT	User-defined MATerial model

Coordinate systems

$1, 2, 3$	local material coordinate system with direction 1 indicating the fibre axis
X, Y, Z	global coordinate system with direction X indicating the longitudinal orientation

Greek Symbols

α	braiding angle
α'	averaged braiding angle in two-step braid
α_{av}	averaged braiding angle of all braider yarns on the machine bed
β	corner braiding angle/ orientation angle between yarn segment and projection onto XY-plane
Δx	element length in X-direction
Δy	horizontal dimension of unit volume in four-step braid
Δy	horizontal dimension of unit volume in four-step braid
Δz	vertical dimension of unit volume in four-step braid
δ	deflection
$\Delta\mathrm{Y}$	horizontal distance between axial yarns on machine bed
$\Delta\mathrm{Z}$	vertical distance between axial yarns on machine bed
$\bar{\varepsilon}$	average strain tensor
η	angle of yarn segment inclined to the X-axis
η_l	fibre length distribution factor
η_o	fibre orientation distribution factor
γ	interior braiding angle/ orientation angle of yarn projection onto XZ-plane towards the X-axis
κ	packing factor of yarn

λ	linear density of yarn
λ_m	linear mass density
ν_{ij}	Poisson's ratio
ϕ	orientation angle of yarn projection onto YZ-plane towards the Y-axis
ψ_δ	shape factor for deflection
$\psi_{\sigma_{crf}}$	shape factor for critical flange buckling stress
$\psi_{\tau_{crw}}$	shape factor for critical web buckling stress
ψ_{EI}	shape factor for bending stiffness
ψ_{kGA}	shape factor for shear stiffness
ψ_m	shape factor for mass
$\psi_{P_{crf}}$	shape factor for critical flange buckling load
$\psi_{P_{crw}}$	shape factor for critical web buckling load
ρ_f	fibre density
$\bar{\sigma}$	average stress tensor
σ_{crf}	critical local flange buckling strength
σ_{ii}	normal stress tensor (ii = 1,2,3)
τ_{crw}	critical local web buckling strength
τ_{ij}	shear stress tensor (ij = 1,2,3)
θ	surface braiding angle
θ_j	yarn orientation at jamming
ε_{kl}	strain tensor
φ	yarn inclination angle

Roman Symbols

A	boundary surface
a	axial/ side length of central axial yarn in two-step braid
A_v	area of all vertical profile members
b	braider/ width of braider yarn in two-step braid

b_f	width of flange
b_w	width of web
$\bar{C}_c$	stiffness matrix of composite
C_c	volume proportion of corner cells to the whole structrue
$\bar{C}_d$	stiffness matrix of damaged composite
C_{es}	volume proportion of exterior surface cells to the whole structrue
$\bar{C}_{ijkl}$	stiffness matrix in global coordinate system
C_i	volume proportion of interior cells to the whole structrue
C_{ijkl}	stiffness tensor in local coordinate system
C_{is}	volume proportion of interior surface cells to the whole structrue
D	flexural rigidity
d	braider yarn thickness in four-step braid
d_f	damage variable for fibre and yarn damage
d_m	damage variable for matrix and effective medium damage
d_s	damage variable for shear damage
E_{ij}	Young's modulus
E_i	initiation energy
E_p	propagation energy
F	shear rigidity
f	fibre/ flange/ yarn aspect ratio
f_{fc}	failure index for compressive fibre failure
f_{ft}	failure index for tensile fibre failure
f_{mc}	failure index for compressive matrix failure
f_{mt}	failure index for tensile matrix failure
G_c	fracture energy
G_{ij}	shear modulus
H	converging height

h	pitch length
h_c	pitch length of composite
h_j	pitch length at jamming
h_p	pitch length of preform
I	second moment of area
k	shear coefficient
K_{lt}	shear buckling coefficient
L	span
L_{pi}	total projected length of two-step braider yarns inclined to the X-, Y-, and Z-axes
L_{pxy}	total projected length of two-step braider yarns parallel to the XY-plane
L_{pxz}	total projected length of two-step braider yarns parallel to the XZ-plane
L_{pyz}	total projected length of two-step braider yarns onto YZ-plane
m	matrix/ number of columns in yarn arrangement
n	number of rows in yarn arrangement
N_a	total number of axial yarns
N_b	total number of braider yarns
$N_{Element}$	number of elements
N_{Steps}	number of steps to obtain one machine cycle
P	load
P_{crf}	critical design load for flange buckling
P_{crw}	critical design load for local web buckling
RF	reaction force
$\bar{S}_c$	compliance matrix of composite
S_l	longitudinal shear strength
S_t	transverse shear strength
T_ϵ	transformation matrix for strain tensor
T_σ	transformation matrix for stress tensor

t_a	thickness of central axial yarn in two-step braid
t_b	braider yarn thickness in two-step braid
T_c	thickness of composite
t_f	thickness of flange
T_p	thickness of preform
t_w	thickness of web
V_a	total volume of axial yarns in two-step braid
V_{bi}	volume of two-step braider yarns inclined to the X-, Y-, and Z-axes
V_{bxy}	volume of two-step braider yarns parallel to XY-plane
V_{bxz}	volume of two-step braider yarns parallel to XZ-plane
V_b	total volume of braider yarns in two-step braid
V_{fn}	fibre volume fraction of yarn group in two-step braid reinforced composite
V_f	fibre volume fraction
V_n	volume proportion of each UD yarn to the whole composite
V_t	macro-cell volume of two-step braid reinforced composite
W	section modulus
w	web/ braider yarn width in four-step braid
w_a	width of central axial yarn in two-step braid
W_c	width of composite
W_f	fibre weight fraction
W_p	width of preform
X	coordinate in X-direction
X_c	longitudinal compressive strength
X_t	longitudinal tensile strength
Y	coordinate in Y-direction
Y_c	transverse compressive strength
Y_t	transverse tensile strength
Z	coordinate in Z-direction

1. Introduction

1.1. Background and motivation

Composite materials are being widely used as structural components due to their high stiffness and strength to weight ratios, excellent corrosion resistance and thermal properties. The structural performance of a composite material is mainly dependent on its fibre reinforcement. Common composite structures are made of continuous fibre yarns or 2D fabrics. Thus, the traditional fibre architecture of a composite structure is an assembly of variously oriented layers. 2D reinforced composite materials exhibit, apart from potential weight reductions, good in-plane properties and impact energy absorption capabilities. However, their application in critical structures like aircrafts and automobiles is restricted by their inferior damage resistance under impact loads due to their limited interlaminar fracture toughness [4]. Performance and damage of composite materials, especially under impact events, has been of great interest to several researchers. A critical issue in these studies are failure mechanisms: composite materials can be damaged on the surface as well as beneath the surface, barely detectable to visual inspection [5]. Failure phenomena in fibre and matrix are well known and structural parameters have been studied to influence and improve the damage behaviour of composite materials. Major interest focused on local damages caused by the impactor, rather than the global damage due to displacement. In the last decades various methods have been developed to enhance the out-of-plane properties and delamination resistance of 2D laminates, such as toughening of the resin matrix, chemical treatments of fibre surfaces to improve their interfacial adhesion strength and manufacturing techniques to fabricate 3D textile preforms [6–9]. Grassi et al. [6] showed that Z-fibres as through-thickness reinforcement increase the delamination resistance and bridge occurring delamination cracks. Although the use of Z-fibres reduces the in-plane moduli, the through-thickness modulus could be increased.

Conventional construction materials in roadside furniture include steel, concrete, aluminium and wood. The material selection for a roadside safety element is dependent on its durability, ease of installation, maintenance, road user safety, costs as well as material behaviour, i.e. failure modes, energy absorption and stiffness. Lighting columns and sign poles must break and fall in a defined manner to avoid intrusion into vehicles, whereas guardrails must absorb high energies while being flexible to avoid hard impacts. In the light of these applications, the current research focuses on phenomena related to the damage behaviour of 3DBRCs, not on a detailed design of a novel guardrail. An important issue here is the definition of a 3D braid. Braiding processes have been developed which result in braids with 3D geometry but their fibre architecture is in fact 2D. Wulfhorst et al. [10] proposed the following summarised definition: a braid is 2D when the yarn paths in the textile architecture can be described with two coordinates and it is 3D when a third coordinate is necessary.

As guardrails are long structures with constant cross-section, pultrusion appears to be the most feasible manufacturing process to produce composites in a fast and cost-effective way. Pultrusion is a continuous process by which reinforcements, such as unidirectional (UD) yarns and 2D fabrics, are pulled through a resin bath into a heated die where the resin cures and from where consolidated profiles cut to the required length exit [9]. Pultruded profiles are typically manufactured with shapes that mimic metallic versions made of steel, aluminium and reinforced concrete. Combining the structural advantages of 3D preforms with the pultrusion process would thus allow for mechanically optimised and cost effective composite structures.

1.2. Objectives

The research work presented in this thesis was mainly inspired by the desire to use composite materials manufactured in profile shapes as roadside furniture. Lateral loading, including flexural loading and impact events, is the dominating load case in those structures. The aim of the preliminary study is to identify critical material parameters which define the crushing behaviour of a pultruded box beam and can be used to tailor its structural response. Furthermore it is aimed at investigating the capabilities of 3D braids to improve the mechanical response and energy absorption characteristics of profile shaped composites. Besides enhanced out-of plane properties attributed to 3D textile reinforcements, geometric changes allow for tailoring damage and improving fracture toughness of pultruded composites. It is aimed to investigate the capabilities of 3D braids to improve the mechanical response and energy absorption characteristics of profile shaped composites. However, the experimental characterisation of composite structures is an expensive method to evaluate the mechanical performance, whereas predictive modelling approaches allow for an inexpensive alternative [11]. Therefore, the main objectives of this research are to formulate analytical models to predict effective elastic properties and to develop a numerical model for predicting the damage behaviour of a 3DBRC under lateral loading.

1.3. Outline of the thesis

The thesis is structured in five main parts:

I Preamble

II Experimental analyses

III Modelling

IV Results and discussion

V Closure

The first part includes the current chapter (Chapter 1) and provides a literature review (Chapter 2) of the topics covered throughout the thesis. A brief introduction to the mechanical performance of pultruded profiles under lateral loading and with respect to geometric configurations is given. Various 3D fabric forming processes are reviewed with respect to their fibre architecture and delamination resistance. An overview of available analytical models for 3D textile structures is presented. Explicit explanations to each method used in this work are found in the respective Chapters 4 and 5. As the focus of this research work is on 3D braids, modelling approaches suitable for this particular type of textiles are selected, even though general models are applicable to other fibre architectures as well. All models incorporate simplified assumptions regarding geometric modelling of the textile architecture. Finally, numerical modelling strategies are presented and evaluated. While analytical models are restricted to the prediction of elastic properties and strengths, numerical approaches allow to include failure and damage modelling. Numerical modelling of 3D textiles is mainly based on FE analysis in conjunction with a homogenisation approach.

The second part concerns the experimental work (Chapter 3) developed during the research. Pultruded glass fibre reinforced polymer (GFRP) box beam sections are microscopically and mechanically analysed to evaluate their performance under lateral loading. The braiding machine and processes used to produce 3D braided preforms as well as composites are described. Analytical and numerical models highly rely on geometric yarn parameters, such as cross-sectional shapes and paths, together with geometric composite parameters, such as dimensions and overall fibre volume fractions. Experimental methods to characterise the microstructure and mechanical behaviour of 3DBRC are presented. Within the scope of this research, only the factors related to the fibre architecture of 3D braids are investigated.

The third part encompasses analytical approaches (Chapter 4) and numerical methods (Chapter 5). The global response of a pultruded profile under lateral loading depends on its bending stiffness. However premature failure may occur due to local buckling of the profile members. Both effects are determined largely, besides the material properties, by the profile geometry. Section 4.1 therefore presents closed-form expressions used in a comparative study to analyse the effect of geometric changes on the bending and buckling response of a pultruded GFRP box beam profile, with respect to mass reduction. In Section 5.1 a numerical analysis is described to predict the experimentally tested failure behaviour of pultruded box beam sections with commercially available numerical tools and simple micromechanics equations. Relationships between the braiding process and the microstructure of 3D braided preforms are presented. The thus estimated yarn and preform dimensions allow to determine the dimensions of a 3DBRC. Analytical models for the prediction of effective elastic properties are explained in Section 4.3, based on experimentally obtained parameters such as material properties, braid pattern, yarn and composite dimensions. Moreover, the numerical model (Section 5.2-5.5) developed to predict effective elastic constants, failure and damage behaviour of 3DBRC under lateral loading is formulated.

The fourth part comprises experimental, analytical and numerical results and respective discussions (Chapter 6). The analytically predicted and numerically simulated properties are compared with experimental data.

Finally, the thesis concludes (Chapter 7) with a general overview of the developed work and proposals for future research on the subjects covered.

2. Literature review

2.1. Pultruded profiles under lateral loading

Conventional pultruded fibre reinforced plastic profiles are produced with shapes that mimic metallic versions made of steel, aluminium and reinforced concrete and are used in various structural applications, such as building frames and bridge decks [12, 13]. Pultruded composites are usually made of continuous, longitudinally running rovings that provide the main load bearing component, as well as multidirectional strand mats or non-crimp fabrics to improve mechanical properties such as the transverse strength. Besides structural reinforcements, an outer mat layer or surface veil is typically used to provide smooth outer profile surfaces and acts as a corrosion barrier to prevent the protrusion of reinforcing fibres to the surface allowing corrosive media into the laminate [14] . Pultruded composites, if compared with composites made by resin transfer moulding techniques, generally show more material imperfections. A higher void content and unevenly distributed reinforcement, especially in transition regions within the cross-sections, such as the corners of box beams, increase the failure probability [13,15]. Numerous authors reported on the bending and buckling response, the progressive deformation behaviour of pultruded composites with different lay-up configurations and cross-sectional shapes as well as on energy absorption characteristics when subjected to axial, transverse and impact loads [13, 14, 16–22]. Pultruded profiles are mainly designed to carry axial loads, hence predominantly reinforced in the longitudinal direction, lacking particular out-of-plane properties. Global and local instabilities as well as global and local buckling interactions are inevitable due to their thin-walled geometry, relatively low transverse stiffness and high strength to stiffness ratio [23–25]. Hence, it is desired to design pultruded profiles with increased local buckling resistance to increase their ultimate strength [26]. For long span beams, overall Euler buckling is more likely to occur first, whereas for short span beams local buckling occurs before any other instability and may lead to large deflections, overall buckling or material degradation [15, 25, 27]. Various researchers investigated occurring buckling phenomena experimentally, analytically and numerically [12, 15, 23–31]. Gan et al. [26] presented a numerical approach to optimise the local buckling resistance of box beams. It was shown that deformations due to local buckling could be reduced by appropriately added stiffeners. Complex geometries were determined, leading to higher manufacturing costs though. Local buckling analyses of pultruded structures are generally performed by modelling flanges and webs separately, in due consideration of the flexible flange-web interaction [25]. In a beam under flexural and shear loading, the flanges are assumed to be subjected to axial compressive loads and the webs to in-plane shear loads [25,27].

A particular progressive failure mode occurring in pultruded profiles under lateral loading is tearing, the separation of webs and flanges at the corners of the cross-section precipitated by local flange buckling [31]. Tearing starts as cracking due to high stress concentrations under the loading head and propagates with increasing deflection towards the ends of the beam. Bank et al. [30,31] showed that transverse tensile stresses and in-plane shear stresses in consequence of local flange compression failure dominate the tearing failure at the web-flange junction. As tearing propagates with increasing displacement the webs are separated first from the upper flanges, get crushed by the loading head, deteriorate further which leads to tearing from the lower flange. Hence, the flanges are the remaining beam members which retain load-carrying capacities. Palmer et al. [32] numerically studied the flexural behaviour of pultruded box beams under three-point loading with focus on tearing using an explicit software package. The authors concluded that the existence and extent of tearing is decreased with increasing wall thickness and therefore could be completely excluded, resulting in single catastrophic failure instead of progressive damage propagation. As the tearing failure mode enables impact energy absorption due to progressive material separation it is considered as useful for guard-rails to restrain colliding vehicles [32]. Therefore, pultruded profiles have been considered by several researchers for use in roadside furniture [32–37]. The use of composite materials offers various advantages, including corrosion resistance, reduced maintenance, lightweight as well as crashworthiness [33]. Roadside furnitures, such as lighting columns, sign poles and guard rails, are structures which are located alongside roads and consequently can be impacted by vehicles. Especially guard rails must be designed in this way that road users and occupants of vehicles are shielded from potential risks and errant vehicles decelerated [35,36]. The errant vehicle should be redirected onto the road with the lowest possible exit angle and velocity to avoid interference with the concurrent traffic. A breach should be prevented, nor parts should become detached and potentially cause injuries to road users [36]. For this reason the main requirement on roadside furniture is a structural design with appropriate crashworthiness to ensure the safety of road users. In order to prevent a breach, the lateral velocity, the velocity perpendicular to the travelling direction, has to be reduced to zero, while absorbing and dissipating the kinetic energy generated by the vehicle mass and speed. The safety of a guardrail, its ability to decelerate a vehicle and the potential for occupants risks in a full-scale crash test can be expressed in the Acceleration Severity Index (ASI), using measured vehicle acceleration information. A maximum ASI value of 1.0 is recommended [38]. A study of the Dutch Institute for Road Safety Research showed that a collision against a more flexible guardrail yields lower ASI values than a collision against a stiffer rail [39]. Hence, the severity of an accident increases with increasing guard rail stiffness. Three major barrier systems can be distinguished, a flexible system, a semi-rigid system and a rigid system, which differ in the allowance of horizontal displacement before an errant vehicle is restrained and redirected. The most common system worldwide is a semi-rigid system which allows a horizontal displacement up to 1 m before the vehicle is restrained or redirected. The guard rail system consists of a w-shaped beam, a post and blockout made of steel [35]. Energy absorption and dissipation is accomplished through plastic flexural deformation of the guard rail system. Plastic deformation in ductile metals involve crystalline slip or molecular sliding, which are thermally activated processes [33].

Various tests on the flexural and impact behaviour of single and multi-cell cross-sections were conducted to analyse the suitability of pultruded beams. Nemes and Bodelle [40] showed in numerical simulations that open-section geometries which mimic existing steel barriers are not suitable for structures made of composite materials subjected to impact loads. Dutta et al. [33] investigated the use of composite materials using a w-beam guard rail design for direct comparison with the performance of a steel rail. The distinct lower stiffness, allowed the composite rail to be highly resilient and it bounced back after flexural tests, even when fractured. In order to improve failure characteristics and energy absorption capacities of a composite guard rail the authors suggested to review different fibre architectures and profile shapes. Tabiei et al. [37] investigated the impact behaviour of rail structures made of standard pultruded beams with open and closed cross-sections. The authors showed experimentally that beams with closed cross-sections bear higher loads than open geometries and that an increase in the number of cells and webs enhances the load bearing capacities. Smith et al. [34] numerically analysed failure characteristics and energy absorbing mechanisms of a box beam subjected to oblique impact, as in actual crash tests vehicles always impact with incident angles to the beam. Bank and Gentry [35] evaluated in a 10-year project the feasibility of pultruded profiles for guard rail systems. In an extensive experimental program various multicellular profiles made of single cell beams were analysed by means of static testing. The flexural behaviour of multicellular profiles were compared to the deformation of a conventional w-shaped guard rail made of steel. Bank and Gentry concluded that a guard rail with smooth load-displacement relationship is preferably in order to decelerate a vehicle continuously. A C-shaped guardrail prototype consisting of multiple pultruded box beams with varying sizes which demonstrated similar static behaviour as the steel rail was further analysed by full-scale pendulum impact testing and explicit FE simulations. Brown [41] reported about pendulum crash tests performed to analyse the dynamic response of the guard rail prototype. The specific C-shape was selected to enhance the guard rail's ability to retain a vehicle's bumper. The overall behaviour of the selected and patented design could replicate the dynamic response of a steel w-rail. However, the energy absorption results from tearing and splitting of the composite material and not from an elastic-plastic material behaviour.

Recently Bank [42] presented a review on fibre reinforced composites with potential for civil engineering and infrastructural applications. Most research on thin-walled structures focuses on axial crushing. Less has been reported on energy absorption capabilities under lateral loading, although this is the more relevant case for civil engineering structures. The author states that composites are rarely used due to a discomfort of designers related to the brittle, progressive material behaviour compared to the elastic-plastic behaviour of e.g. metallic materials. As the specific energy absorption of fibre reinforced composites can exceed the one of metals, composites have become widely used in the automotive and aerospace industry. Bank postulates that advantages of composite materials might have been not as appealing for civil engineering structures due to the fact that weight is generally no important concern. A further reason as noted by Bank is the missing intentional exploitation of progressive failure, such as tearing and bearing, in design procedures for profiles. In a further recent study Belingardi et al. [43] numerically analysed the crashworthiness of pultruded profiles as automotive bumper. The authors showed that a pultruded GFRP bumper beam offers comparable energy absorption to a steel beam but better progressive behaviour.

2.2. Three-dimensional braiding

Various manufacturing techniques to fabricate 3D preforms have been developed in the last decades to enhance the out-of-plane properties and delamination resistance of 2D laminates [9]. The term preform refers to the textile architecture before consolidation with a matrix material. According to the technique used to integrate reinforcements in the thickness direction, the following 3D textile reinforcements can be differentiated: woven, stitched, knitted, tufted, z-pinned and braided preforms, as shown in Figure 2.1. The selection of one of those textile processes is dependent on the product design, its mechanical performance and manufacturing criteria, such as production rate and associated costs.

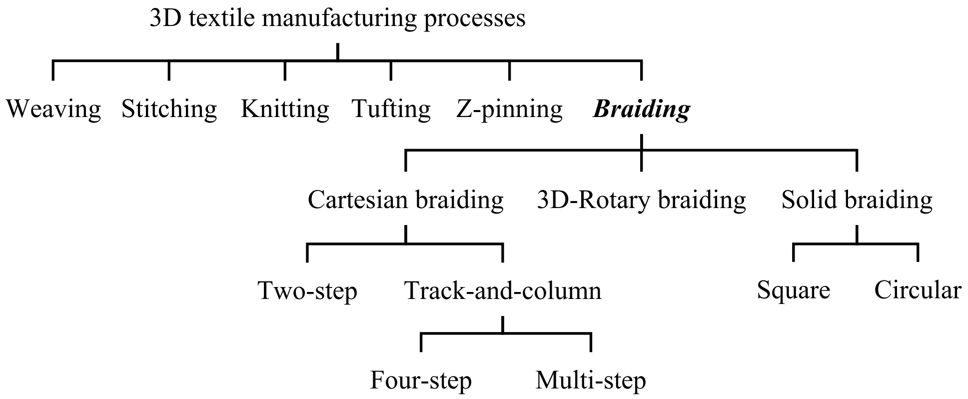

Figure 2.1.: 3D textile manufacturing processes and braiding techniques

Weaving is the method most widely used to manufacture 3D preforms because of its high productivity and the possibility to produce a wide range of through-thickness reinforcements [11]. Weft and warp yarns are not interlaced, instead a binder interconnects weft and warp layers in the through-thickness direction and ensures delamination resistance [44]. Dependent on the binder arrangement woven preforms can be distinguished between layer-to-layer angle interlock, through-thickness angle interlock and orthogonal weaves. The main disadvantage is that in-plane fibres are generally limited to 0/90° directions and preform shapes to simple and flat fabric structures with poor drapability [9]. Stitching is a highly productive and industrialised method for introducing through-thickness reinforcements into composite preforms. Complex shapes can be manufactured using robotic technology. While the interlaminar shear-strength can be increased by special double-locked stitch variations [45], the stitching process causes significant damage to the fabric, especially to the surface layers, reducing the in-plane mechanical properties of the resulting composite [46]. A knitting technique called *Multiaxial Warp Knitting* combines weaving and knitting. This manufacturing method is mostly known by the style of fabric it produces, *Non-Crimp Fabric* (NCF) [9]. Those preforms made of variously orientated layers offer high in-plane stiffness and strength due to relatively low yarn curvatures. However, the out-of-plane properties, especially the impact performance, cannot be improved by the polyester knitting thread [9, 47]. Tufting is an ancient textile manufacturing technique used for producing garments and carpets. A tufting thread is inserted through a layered fabric with a needle and left as loop on the other fabric side. The tufting thread can be inserted in diverse fabric shapes and the density of through-thickness reinforcements can be varied, meaning as local or areal reinforcement. However, similar to stitching, tufting can cause significant damage to the fabric and the loops can complicate the infusion process, such as localised air trapping [48]. Z-pinning is a further method to insert through-thickness reinforcements into a 2D fabric. UD composite rods are embedded, arranged in a square array, in a thermoplastic foam. The foam is placed on top of the fabric or prepreg and the rods are inserted, either during the autoclave process by heat and pressure or by using an ultrasonic gun to soften the matrix material and allowing to push the z-pins in. The thermoplastic foam is collapsing during this process and protruding z-pins can be trimmed. On one side this manufacturing technique improves the delamination toughness of a composite, however, a problem with z-pinning is the corresponding reduction of in-plane properties [49].

The aim of this research is to analyse the mechanical response of 3D braided composites. The first 3D textile architectures were produced in the late 1960s by braiding [9]. It is an extension of 2D braiding techniques which additionally integrates yarn intertwining in the through-thickness direction. A major limitation of traditional 2D braiding is that thick-walled preforms cannot be produced unless the mandrel is repetitively overbraided. Furthermore, the resulting multi-layered preform has no through-thickness reinforcement, similar to 2D fabric reinforced laminates [9]. A main advantage of highly interlaced yarns in the thickness direction is that delamination as known from other fabrics cannot occur. Compared to 2D fabrics, 3D braids provide structural integrity and torsional stability as well as the possibility for near-net-shape reinforcements already in the unconsolidated state [9, 50]. Braiding processes allow for manufacturing a wide range of complex open and closed shapes, from solid rods to I-beams and thick-walled structures, even with cross-sectional changes during processing [9]. 3D braided preforms exhibit a high sensitivity to cut edges. Machining a specimen to desired dimensions, thus cutting the preform into discontinuous sections was found to significantly decrease the mechanical performance of a composite, particularly the tensile strength [51, 52]. This indicates the need to produce 3D braided composite components to net-shape, removing any need for machining, in order to maintain the reinforcing effect of the complex fibre interlacement. The major drawback of 3D braided composites is their reduced in-plane properties compared to 2D laminates with equivalent fibre weight fraction. Reasons for this behaviour can be found in the fact that most braided yarns are off-axis from the loading directions and heavily curved, also called crimped [52, 53]. Additionally, the properties of 3D braided composites show sensitivity to processing parameters such as the braiding angle and the yarn size. Tensile strength and modulus increase with increasing bundle size because larger bundle sizes imply lower crimp and lower fibre angles [52]. Further drawbacks are size limitations due to available machine beds, medium productivity and long setup times [9, 47].

3D braided preforms are basically formed on two types of machines, the horngear and Cartesian machines, which differ only in their way of yarn carrier displacement [54]. The resulting manufacturing techniques include solid braiding, 3D rotary braiding and Cartesian braiding like two-step and track-and-column processes, such as four-step and multi-step braiding, see Figure 2.1. Solid braiding is based on the 2D maypole braiding technique and used to produce simple cross-sectional shapes, such as square or circular preforms, by continuous interlacing of three or more yarn groups [46, 55]. Braider yarns are moving diagonally through the cross-section and interlock inserted axial yarns [50]. Two-step braiding was first described by Popper and McConnell [56] in 1987. A two-step braided preform is made of an array of parallel longitudinally aligned stationary yarns which are interlaced by a smaller number of braider yarns. The braider yarns are placed around the axial yarn array on alternating locations. Any array, including box beams or circular profiles, can be arranged. The shape of the axial yarn array defines the final preform shape. A two-step braid is produced in two sequential steps. The braider yarns move in diagonal lines, with alternating directions through the axial array, as depicted schematically in Figure 2.2. The axial yarns are responsible for a high stiffness and strength in the longitudinal preform direction and at the same time for the relatively low Poisson's ratio [55]. Mechanical properties and preform flexibility can be obtained by varying yarn sizes and materials for axial and braider yarns. Moreover, after each step all braider yarns are simultaneously outside the axial array allowing for variations of the array shape as well as the addition of inserts [57, 58]. In the track-and-column braiding process the yarn carriers are arranged in tracks, also called rows, and columns to form the desired preform shape. Additional peripheral yarn carriers are added around the defined array in alternating locations. The braiding process is realised by alternating movements of the yarn carriers on the machine bed. A set of four carrier movement steps, as shown in Figure 2.3, is called one machine cycle and yields in a preform of one pitch length h . The 1x1 braiding pattern denotes that each carrier of the same row or column moves at each step one position either horizontally or vertically in an alternating manner. The third and the fourth step are the reverse movements of the first and second steps, respectively. At the end of one machine cycle the yarn carrier arrangement is the same as the initial configuration. The braiding process is advanced by the given pitch length and the sequence is repeated until a desired preform length or the maximal possible length, restricted by the take-up unit of the braiding machine, is obtained. Most braider yarns in a four-step braid are offset at different angles between the in-plane and through-thickness directions, no braider yarn maintains straight in a four-step braid, resulting in a less flexible preform. However, transverse properties and shear resistance are higher than in a two-step braid due to those angled braider yarns. Four-step braids offer quasi-isotropic elastic behaviour owing to their symmetric, interlaced structure. But the lack of axial reinforcements results in low stiffness and strength as well as a high Poisson's ratio in the longitudinal direction [54, 58]. Similar to the two-step or solid braiding process axial yarns can be added to improve the longitudinal stiffness and strength. Those yarns are only embedded in the four-step braid, but do not participate in the braiding process. Different profile shapes, such as I-, T- or box beams, can be realised by placing the yarn carriers at appropriate positions, including cross-sectional changes along the preform length [50, 54]. Another possibility is the design and forming of hybrid reinforcements by using two or more types of fibre material. Hybrid designs allow for tailoring preforms with combined properties, such as mechanical and electrical ones [54, 59].

Although the methods of the two-step and four-step braiding process differ, both braids are variations of a general multi-step braiding scheme [60]. Kostar and Chou [58] indicated that a two-step braid can be formed using a multi-step machine. For the fabrication of a two-step braid, the four-step braiding setup has to be modified in such a way that axial yarns are inserted, braider yarns inside the axial array removed and certain braider yarns placed at appropriate locations on the machine bed around the axial yarn array [58, 60]. Variations of the original four-step braiding process have been proposed as well, like multi-step braiding and a circular version [61]. Multi-step braiding, such as eight-step braiding, is an extension of the four-step braiding method, which allows individual displacement control of rows and columns, and any number of steps in a given machine cycle [58]. It offers the possibility of further and more integrated braid architectures for small braider yarn angles [62]. Using circular four-step braiding results in a tubular shaped preform. The carriers are arranged in rings on a circular machine bed around a mandrel. The braiding process is divided in radial beating motions and circumferential motions in a clockwise and counter-clockwise manner. 3D rotary braiding is a manufacturing process based on the traditional 2D braiding technique which allows to produce braids of almost any fibre orientation and cross-sectional geometry in near net-shape [63]. Yarn carriers can move independently and arbitrarily in a flat array of horngears, which are arranged in rows and columns, so that each yarn may be individually placed and interlaced. Each horngear is equipped with a clutch-brake mechanism to either rotate or stop. Another type of 3D braiding, which is closer to 2D braiding, is multi-layer interlock braiding. In comparison to 3D rotary braiding the carriers move on circular, concentric tracks in clockwise and counter-clockwise directions. This braiding process is capable of producing transversely

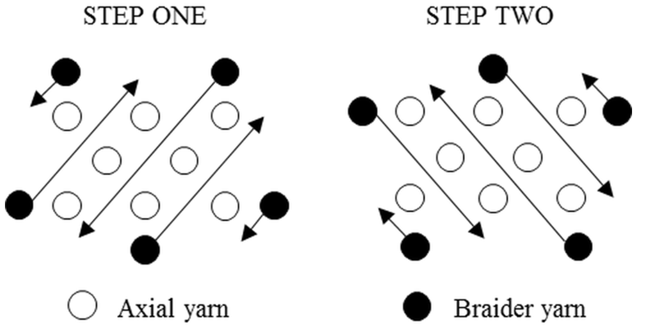

Figure 2.2.: Schematic movements in a two-step braiding process

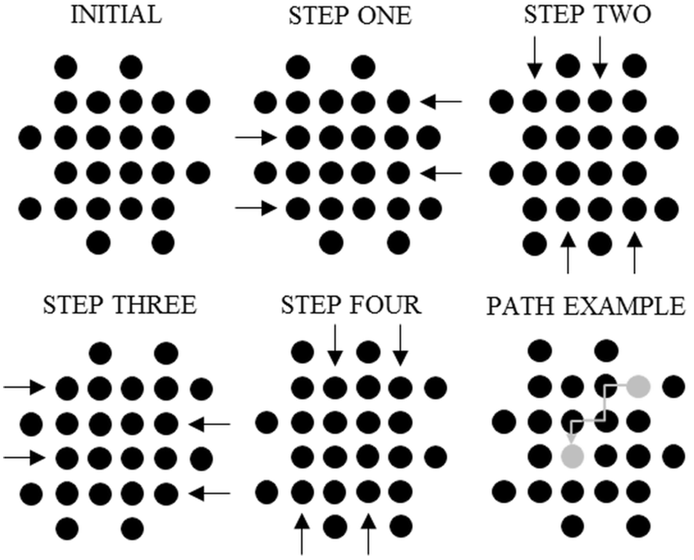

Figure 2.3.: Schematic movements in a four-step braiding process

connected 2D braided layers, by allowing yarn carriers to move in a sinusoidal manner and interlace yarns between adjacent tracks [64,65]. Yarn interlocking between adjacent layers occurs mainly in the plane and therefore does not reduce the in-plane properties [9].

2.3. Modelling

Modelling the material response of 3D textile reinforced composites (3DTRC) is complex due to intricate architectures and possible material combinations. A common method found in literature to evaluate elastic properties analytically or numerically is the orientation average method which is also referred to as volume averaging or homogenisation. The homogenisation method can be explained as a description of the global material behaviour by knowing the response of a representative volume of an inhomogeneous material. The global response of any composite results from occurring phenomena among its constituents at different length scales. Textile reinforced composites are hierarchical materials and can be classified in three levels: the macroscopic, the mesoscopic and the microscopic level [66]. The macro-level is associated with the composite as structural component. On the microscopic level a composite involves individual fibres surrounded by matrix material. Occurring failure on the micro-level affects the response of yarn and matrix on the meso-level and consequently the global response of the composite on the macro-level. Because composite constituents are separately considered, matrix, fibre and interfacial failure can be predicted. However, the microscopic level is too small for representing the behaviour of the macroscopic composite. The mesoscopic approach considers the representative volume element (RVE) distinguishable between yarn and matrix material.

2.3.1. Analytical modelling

The earliest available analytical models for textile reinforced composites were proposed by Ishikawa and Chou [67, 68], known as the mosaic, fibre undulation and bridging model. Based upon the classic laminate theory (CLT), these one-dimensional (1D) models were developed for predicting the thermo-elastic behaviour of plain weaves. In the mosaic model the woven textile composite was idealised as an assemblage of asymmetrical cross-ply laminates without considering fibre continuity and undulation. Consequently, Ishikawa and Chou developed the *fibre undulation model* to include the effects of undulation as well as fibre continuity and proposed the bridging model considering interactions between undulated regions and surrounding regions with straight yarns. The most common approach used in modelling periodic textile reinforced composites is to treat its structure as an assemblage of defined unit cell geometries. Unit cells are representative volumes which repeat throughout the entire textile by spatially translation, without rotation or reflection [69]. It is assumed that all cells are distributed homogeneously over the entire preform [60]. One of the first analytical models for studying elastic properties of 3DBRC was the so-called *diagonal brick model* proposed by Ma et al. [70]. This approach was significantly simplifying the complex textile architecture. Yarns were regarded as composite rods, diagonally oriented in a brick-shaped matrix block as shown in Figure 2.4(a). The model considered strain energies in the composite rods due to bending, extension and compression resulting from yarn interaction at interlocks. Yang et al. [71] established further the *fibre inclination model* which is an extension of the 1D fibre undulation model, analysing mechanical properties based upon the CLT. The unit cell is idealised as a parallelepiped treating the yarns of the braid as an assemblage of inclined UD laminae, see Figure 2.4(b). It is assumed that all yarns parallel to a diagonal or axial direction lie in the same layer; hence forming inclined or horizontal laminae after resin consolidation. The emphasis of this model is placed on the yarn orientation rather than the interaction among yarns. Elastic constants are calculated for the assemblage of all laminae using the stiffness matrix method of the laminate theory. Sun and Qiao [72] extended the fibre inclination model to predict the tensile strength based on yarn orientations, fibre volume fractions, stiffness averaging and the Tsai-Wu failure criterion.

Crane and Camponeschi [53] developed an analytical model based on the CLT to predict extensional stiffness in the three principal geometric directions of a 3DBRC. Treating the oriented yarns of a multi-dimensional braid as projections on various planes and assuming that all fibres in the braided composite lie in one of four possible directions, the unit cell was derived, idealised as a parallelepiped with four diagonals representing the yarn orientations. The fibre volume fraction in 3DBRC is approximately 50% or higher, therefore treating yarns as dimensionless lines crossing each other at the unit cell centre is a highly oversimplified assumption [50, 73]. A further model proposed by Kregers and Teters [74] used a stiffness averaging method to determine the deformation properties for three-dimensionally reinforced composites. The stiffness matrix of a composite made of spatially oriented structural elements is obtained by tensor transformation and volume-averaging the overall stiffness. The described modelling approaches for determining mechanical properties of 3DBRC were developed for defined unit cells without providing any relationship between processing and geometry parameters. Thus, these simple models cannot be used for optimising structural applications using braided preforms [9]. Hence, more realistic models with more accurate descriptions of the cross-sectional geometry and the paths of yarns were developed. Exemplary, the yarn paths in four-step braids are essentially helical along the longitudinal preform direction [75]. While Byun and Chou [75] assumed that the cross-section is elliptical, Li et al. [76] proposed a unit cell model with cylindrically shaped yarns. However, this model is not fully in agreement with experimental observations [73]. Byun et al. [1] developed two analytical models that consider geometric preform characteristics for predicting elastic constants of a two-step braided composite based on the laminate theory and a stiffness averaging method, the *micro-cell* and the *macro-cell model*, as depicted in Figure 2.5. The micro-cell model is designed for thin specimens, allowing the application of the 2D approximation of the CLT. In analogy to the fibre inclination method, the effective elastic properties can be determined with given geometric parameters, fibre and matrix properties as well as fibre volume fractions. However, details of the yarn arrangements at the specimen edges are not considered to simplify the calculations.

Compared to the unit cell approach, the macro-cell is the biggest repeating unit in the textile architecture which is designed for the entire cross-section of the preform and is capable of treating also thick structures. Given geometric yarn parameters as well as fibre and matrix properties, width, thickness and volume fractions volume fractions can be derived and elastic properties calculated by using tensor transformation and a stiffness averaging method. Axial and braider yarns are treated as UD composites individually orientated in a 3D coordinate system. Variations of the aforementioned braider yarn orientation along the yarn length are also considered by introducing an average orientation angle. Both fabric geometric models showed mostly good agreement between predicted and experimentally measured elastic properties, however lacking

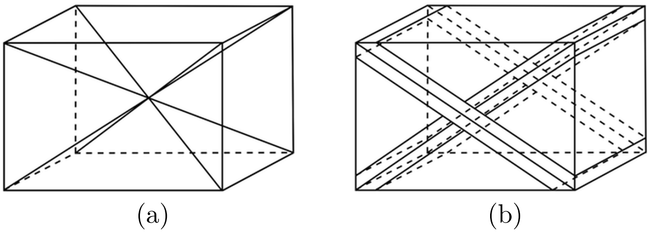

Figure 2.4.: Schematic unit cell structure of the diagonal brick model (a) and the fibre inclination model (b)

agreement for shear moduli [1]. Further models were developed which analyse the micro-structure and predict the elastic behaviour of four-step and multi-step braided composites [62, 77]. Based upon the identification of unit cells to determine braider yarn orientations and the distribution of unit cells in the macro-cell, elastic constants were calculated using coordinate transformation and stiffness averaging.

Based on topological analyses of four-step braids, Wang and Wang [78, 79] defined 3DBRC first as skin-core structures made of three types of unit cells, namely the interior, the surface and corner cell, and reported a mixed volume averaging technique to predict effective properties. However, Wang's study [78] did not consider yarn continuity on surfaces and in corners. Chen et al. [2] used these unit cell types and presented an analytical approach which established relationships between braiding parameters, the braided preform and its composite. Recently, Li et al. [80] and Shokrieh [81] presented models for predicting mechanical properties of 3D five-directional and four-directional braided composites, respectively, based on the established skin-core structure, see Figure 2.6.

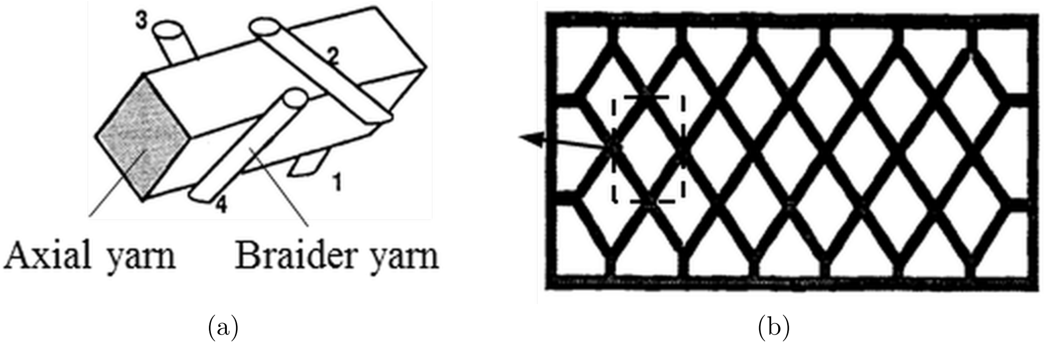

Figure 2.5.: Micro-cell and macro-cell for a two-step braid [1]

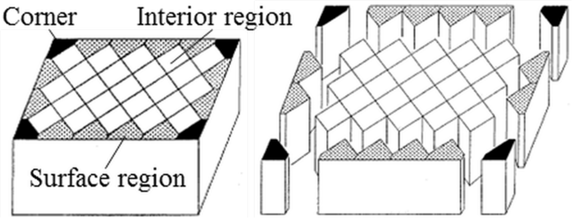

Figure 2.6.: Schematic illustration of skin-core structure in four-step braid [2]

2.3.2. Numerical modelling

Similar to analytical modelling, numerical FE methods have been developed to analyse 3DTRC. FE methods are widely used for predicting the mechanical response of textile reinforced composite structures. However, modelling complex 3DTRC is even more challenging due to their complex architecture and its accurate representation. Various numerical models have been established considering simplified geometric assumptions and approximations. The common concept of any model to predict the mechanical behaviour of 3DTRC is the identification and geometric definition of a representative volume element and the analysis of the stress-strain response using a homogenisation technique.

Lei et al. [82] developed a finite element technique in which the composite was considered as brick-shaped cells and the yarns as 3D truss structures. The matrix was assumed to act as rod members connecting the two ends of a given set of yarns in the unit cell. Chen et al. [83] proposed a finite multiphase element method to predict the effective elastic properties of 3DBRC. This numerical method is divided into two steps, a fine local mesh is first used to analyse the stress/strain of each unit cell and a coarser global mesh is used to predict the overall macroscopic behaviour. Tang and Postle [84] presented a FE approach to simulate and analyse the geometric nonlinearity of 3DBRC and their deformation behaviour considering key parameters, such as the pitch length. Sun et al. [85] and Zeng et al. [86,87] developed FE methods to analyse effective elastic moduli as well as stress fields and strength of 3DBRC using the idealised simple unit cell in which bundles are oriented in the four diagonal directions of a rectangular parallelepiped. In comparison to conventional numerical models yarns and matrix are not modelled discretely. The unit cell is modelled as an assemblage of subcells, called the yarn element, the matrix element and a mixed element. They further extended the model to predict nonlinear behaviour and failure [88]. Gu and Ding [89] presented a FE model to simulate ballistic penetration of 3DBRC. The geometric representation of the 3D braid was based on the fibre inclination model. The braid was decomposed into inclined UD laminae and the incident angle of the projectile was transformed such that the orientation of the UD yarns was adjusted to the fibre orientation in the braid. The representative architectures considered in the aforementioned models were either too simplified or not conform to the true braided microstructure.

A more accurate modelling approach, referred to as *meso-FE modelling* [66], has been increasingly used to model textile reinforced composites. This numerical technique involves the accurate geometric representation of orientations, shape as well as dimensions of yarns and matrix material based on process and structural analyses. Most of the work published about meso-FE modelling addresses 2D fabrics, such as weaves, non-crimps or braids, as well as 3D weaves [66, 90, 91]. In order to facilitate or enable the volumetric description and the discretisation of RVEs using solid elements, multi-functional software packages like WiseTex [92] or TEXGEN [93] have been developed to model various 2D textiles and 3D fabrics and predict their mechanical properties. Tolosana et al. [94] created a geometric model of a 3D rotary braid based on carrier movements, but an analysis of the braid wasn't performed. Kim et al. [95] used the TEXGEN software to model the unit cell of a multi-layer interlock braid and obtain its mechanical response. It was shown that meso-FE modelling of 3DBRC is feasible. Effective properties can be predicted and results agree with experiments. However, apart from a large number of degrees of freedom that easily reach computational capacities, the accurate representation of individual yarns and their interaction with resin and adjacent yarns is complicated or even impossible for modelling structural components made of 3D braids. The geometric model is ideally based on direct measurements of the textile architecture. However, most models use simplified assumptions, such as a fixed yarn shape with potentially changing dimensions along the path. Even the use of modelling software cannot completely exclude that yarn surfaces penetrate each other, because interpenetrations are a consequence of constant yarn shapes and a limited control of point and line contacts [66]. Nevertheless, Yu and Cui [96] developed a unit cell of a four-step braided composite to investigate stiffness and strength properties using a two-scale asymptotic analysis method. Yarn segments in the FE model were assumed to have octagonal cross-sections and were meshed with tetrahedron elements. Xu and Xu [97] as well as Li et al. [98, 99] evolved a similar 3D meso-mechanical FE model of a four-step braided composite to obtain effective elastic properties and analyse its mechanical response on the meso-scale. The geometric model was based on yarn carrier movements, considering braiding parameters as well as octagonal yarn shapes. The presented meso-FE models solely focused on an interior cell assuming that it primarily dominates stiffness and strength of the 3DBRC.

A further modelling technique is the *FE mesh superposition method.* Mohajerjasbi [100] proposed a FE approach to determine elastic and thermoelastic properties of a 3D four-step braid. The RVE was considered as skin-core structure made of interior, surface and corner cells. Yarns were represented as axial elements having solely axial stiffness and the matrix was modelled as hexagonal and pentagonal elements occupying the entire volume of the RVE. Both mesh models were superimposed to evaluate the mechanical behaviour. Cox et al. [101] and Xu et al. [102] developed a similar effective and simple modelling strategy, commonly known as the *Binary Model* (BM), to simulate the mechanical performance of 3D woven composites. The BM is subdividing the composite into two FE meshes made of 1D and 3D elements. Yarns are treated as two-node line elements which represent their axial stiffness. Cross-sectional details of the yarn are omitted. The mesh of the resin material, called effective medium, is made of eight-node solid element. The effective medium defines the specimen surfaces and represents matrix-dominated composite properties, including the transverse stiffness, shear stiffness and the Poisson's effect. There is no direct interaction between yarns, they exert only influence on each other through the effective medium. Yarns and effective medium are coupled by means of constraints. Yang et al. [103, 104] used the BM to analyse the strain distribution in a 3D braided T-stiffener during a simulated pull-off test. Predicted strains agreed well with experimental results. Yang and Cox [105] further applied the BM to investigate the effects of textile architecture in a 3D angle-interlock weave made of carbon fibre/SiC matrix on local strain variations. Recently, Yang and Cox [106] used the BM to predict the ultimate tensile strength and failure behaviour in a triaxially braided carbon/epoxy composite. Flores et al. [107] developed a model based on the BM to treat matrix nonlinearity in ceramic matrix composites reinforced by a 3D interlock weave. Haasemann [108] developed a FE code based on the BM to investigate the dynamic material behaviour of textile reinforced composites during impact. Haasemann et al. [109, 110] further applied the BM to study the tensile and flexural properties of composites with biaxial weft-knitted. More recently, Haasemann et al. [111] presented an efficient FE technique for a biaxial weft-knit which combines the BM with the extended FE method X-FEM to join advantages of both. The weft-knit is represented by line elements whereas the interfaces between pure matrix and warp or weft yarn are modelled using X-elements. Jiang et al. [112] proposed a formulation called the *Domain Superposition Technique* (DST) to analyse plain weaves. The DST is equivalent to the Binary Model. However, yarns and resin are separately modelled and independently discretised using traditional solid elements for both. The two regions are superimposed to couple them together. Properties of the matrix material are used for the elements of the resin region, whereas a modified material model, based on the difference between yarn and matrix material, is used for the yarn elements. A major advantage is the reduced model size compared to a conventional 3D FE model. Biragoni and Hallett [113, 114] further applied the DST to model 3D weaves. Recently, Tabatabaei et al. [115] used the DST to predict elastic properties of a 5H satin weave reinforced composite. However, similar to meso-FE modelling the representation of 3D braided preforms is complicated and possible yarn interpenetrations cannot be excluded.

FE methods allow further for analysing failure and damage behaviour of textile reinforced composites. Various researchers created FE models using commercial software packages, such as Ansys, ABAQUS and LS-Dyna. User-defined subroutines were developed to incorporate failure criteria and constitutive behaviour. Ivanov et al. [116] analysed the failure behaviour of 2D triaxially braided composites under tension in detail using a meso-FE model. A FE analysis was performed using Puck's criterion to predict damage initiation and a Murakami-Ohno degradation scheme employing the damage evolution law of Ladeveze for damage propagation. Li et al. [117] presented a 3D FE model to examine the failure and damage behaviour of 2D triaxially braided composites. The Hashin criteria were used as well for modelling tensile and compressive fibre failure as well as matrix failure initiation. However, progressive damage was simulated using Matzenmiller's stiffness degradation model. Additionally, a cohesive zone approach to model the fibre-matrix interface was considered. Miravete et al. [118] performed a mesomechanic FE analysis using Hashin's criteria to predict material failure in a 3DBRC. Material degradation in fibre and matrix was implemented by reducing the elastic properties to 0 by means of degradation factors between 1 and 0. Zeng et al. [87,88] established a FE method for 3DBRC to predict local stresses and strength in a simplified RVE. The failure analysis was accomplished using the Tsai-Wu polynomial criterion for fibre failure and the von Mises criterion for matrix failure. Fang et al. [119] developed a geometric FE model to analyse the failure and damage behaviour of a 3D four-directional braid subjected to uniaxial tensile loading. The RVE composed of four yarns with octagonal cross-section was chosen from the interior braided structure. Hashin failure criteria and the Murakami-Ohno damage theory were employed to model tensile, compressive and shear failure modes. Xu [120] developed a similar geometric FE model to predict the tensile strength based on a progressive damage model considering the nonlinear longitudinal shear stress-strain response of braider yarns. Debonding of the fibre-matrix interface was ignored. Jiwei and Miaolin [121,122] predicted effective properties of a 3D four-directional braid composite using an asymptotic expansion homogenisation method which was first employed by Feng and Wu [123] for 3DBRC made of piezo-ceramic fibres. Failure and damage behaviour were also studied under tensile loading. The Tsai-Wu failure criterion was applied to yarns, the von Mises criterion to matrix elements and damage was modelled with Murakami's geometric damage theory. In contrast to all aforementioned simulations they analysed besides the cell of the braid interior also the surface cell and corner cell. Failure in the interior cell is dominated by matrix cracking, while yarn breakage caused the major failure in surface and corner cells. Jiwei and Miaolin indicated that the occurring damage varies between the different kinds of unit cells. Therefore, the geometric model for a damage analysis should encompass the entire braided cross-section, rather than an interior unit cell alone.

3. Experimental analyses

3.1. Pultruded profiles under lateral loading[1]

In this study experimental analyses were performed on pultruded beams supplied by Bijl profielen B.V., The Netherlands. The studied pultruded material system consists of polyester resin reinforced with alternating layers of UD E-glass fibre (GF) rovings, continuous strand mats (CSM), e.g. a corrosion layer of GF veil, and ±45° NCF. Profile sections with the same square cross-section but two different material configurations, from here on referred to as *Configuration 1* and *Configuration 2,* were compared. Although it is generally assumed that UD rovings exit the pultrusion die at 0° orientation and oriented fabrics exit the die at their given orientations, it is known that the reinforcing material can move during the pultrusion process and that pultruded composites generally show more material imperfections, such as a higher void content. Thus pultruded materials commonly vary in orientation within the same section along the length or through the thickness [124]. Especially transition regions within the cross-sections such as the corners of box beams. Therefore, the fibre architecture is visually investigated before mechanical testing by optical microscopy.

Tabiei et al. [125] studied the effect of velocity on failure characteristics of pultruded box beam profiles by comparing the damage behaviour during quasi-static tests with failure mechanisms when subjected to falling weight impacts. According to the authors failure mechanisms in static and impact tests are identical and ultimate loads comparable [125]. Hence, a quasi-static test can be used as an indicator of the relative impact performance of pultruded box beams subjected to low velocity impacts [37]. In analogy, the crushing behaviour, occurring failure modes and energy absorption mechanisms of single-celled box beam sections are studied in simple quasi-static laboratory compression tests using flat platens at the top and bottom, as shown in studies for wet wrapped and braided composite tube sections [126–128]. Box beam sections with a width of 15 mm were cut from the selected profiles. For each material configuration six sections were randomly chosen to determine a representative mechanical behaviour under compression loading. The specimens were machined using a water-cooled bench saw and the edges were prepared by grinding to the final dimensions. Quasi-static lateral compression tests of the square profile sections were performed on a 50 kN universal testing machine from Shimadzu. The sections were loaded at a test speed of 5 mm/min until

---

[1] Section is reproduced with adaptations from "F. Regel, F.W.J. van Hattum and G.R. Dias. A numerical and experimental study of the material properties determining the crushing behaviour of pultruded GFRP profiles under lateral compression. *Journal of Composite Materials*, 47(14):1749 - 1764, 2013"

Figure 3.1.: Test set-up for lateral compression tests of pultruded box beam sections

final failure occurred. The load was applied to the specimen through flat, circular, fixed platens as shown in Figure 3.1, in such a manner that the load was uniformly distributed over the entire loading surface of the specimen. Load-displacement details were taken to determine maximum load, ultimate strength as well as energy absorption capabilities. The compression tests were additionally recorded with a Photron Fastcam APX-RS high-speed camera to provide visual insight into the progressive damage of pultruded profiles.

In order to minimise any potential errors originating from potential deviations in material specifications of the small test samples compared to data given in datasheets, lay-up details of the tested segments were further examined to supply material data for the numerical analysis. The fibre volume fractions V_f in roving and CSM layers were determined by a series of burn-out tests, following the calcination method DIN EN ISO 1172. Six specimens, for each material configuration, of about 30 mm x 15 mm x 5 mm were extracted from profile flanges and webs. In order to determine the fibre volume fraction of each reinforcement material, the layers were separated after calcination and individually weighed. Based on the obtained fibre mass of each layer the fibre volume fractions were derived using a GF density ρ_f equal to 2.6 g/cm^3.

3.2. Experimental methods for 3DBRC

3.2.1. Braiding process[2]

Although the development of 3D braids goes back to the 1960s and research was especially promoted in the 1990s, 3D braided preforms are still no commercially available reinforcement. Just a few research institutes worldwide are still in possession of own machinery and actively pursue research. In this study, a track and column type four-

---

[2] Parts of subsection are reproduced with adaptations from “F. Regel, G.R. Dias and F.W.J. van Hattum. Mechanical analysis of a two-step 3D braided composite, Proceedings of SAMPE 2013, Long Beach, CA, USA, 2013”

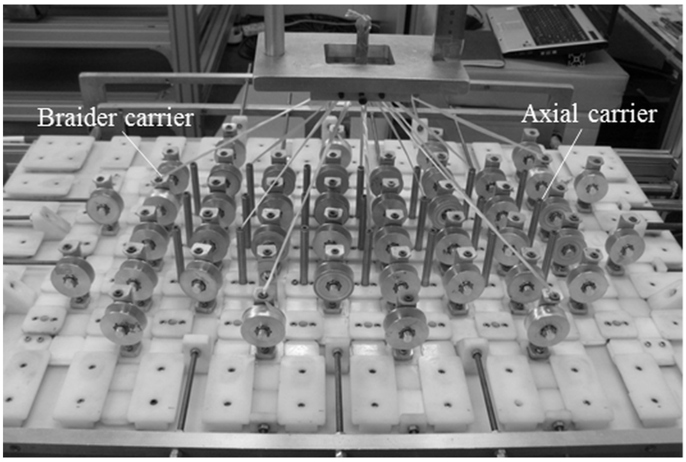

Figure 3.2.: Machine bed of used track and column machine

step braiding machine at KIMS (Korea Institute for Materials Science) [129] was used to produce four-step and two-step braided preforms. The machine basically consists of a machine bed with braider carriers and stationary guiding tubes for additional axial yarns, a take-up unit, sensors, actuators and a computer. Braider yarn carriers consist of a scroll spring and a spring stopper to supply and rewind yarns, in order to maintain a constant tension on the braider yarns. Axial yarns are directly fed from below the machine bed and the tension on them is assured with weights. The movement of columns and rows, designated as m and n, respectively, is implemented with pushing bars that are connected in parallel to move carriers with the same direction together. The sequence of the movements as well as the take-up length of the preform is controlled by a computer. Figure 3.2 shows the machine bed with braider and axial yarn carriers of the available track and column machine.

As aforementioned in Chapter 2.2, in theory, a two-step braid can be fabricated using a multi-step machine. For the fabrication of a two-step braid with a *[m x n]* configuration a *[2m, 2n]* four-step yarn array is necessary. The maximal possible size of the four-step and the two-step braid is limited by the machine bed. As depicted in Figure 3.3, the available machine bed with ten columns and six rows is sufficient to fabricate a [8,4] four-step braid and a [3x2] two-step braid.

Compared to four-step braiding, it takes several machine cycles, dependent on the number of rows, to move the braider yarn carriers diagonally trough the axial array and obtain a preform of one pitch length. Yarns, which have initially horizontal positions, need *n+1* four-step braiding machine cycles to complete one two-step braiding machine cycle. The path of yarn *1* is exemplary highlighted in Figure 3.4. In this study, three braid configurations are fabricated, a [8,4] four-step braid with and without axial yarns using a 1x1 braid pattern, as well as a [3x2] two-step braid, in the following referred to as 4stepWI, 4stepWO and 2step, respectively. The 4stepWI can be considered as a set of straight axial yarns which are intertwined by the braiders.

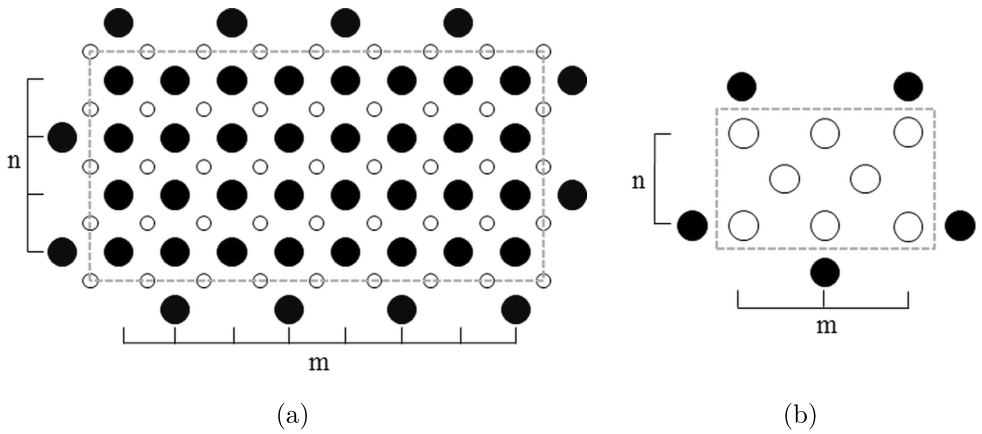

(a) (b)

Figure 3.3.: Yarn arrangements in [8,4] four-step braid (a) and [3x2] two-step braid (b)

Kostar and Chou [54] presented an adaptation of the so-called Universal Method developed by Li [76] to design 3D braids with complex shapes using Cartesian braiding. The basic idea behind this method is the division of a complex cross-section into finite rectangular elements and to braid these elements in groups. An element group is made of several row groups, which in turn are continuous series of elements along a row. Each row group which share the same left- and right-most elements regardless of its position in the cross-section belong to the same element group and may be braided during the same machine cycle. In order to determine the braiding sequence five steps can be distinguished, see Figure 3.5: (a) specifying profile dimensions, (b) dividing cross-section into equal rectangles, (c) identifying element groups, (d) determining location of peripheral yarns and (e) identifying number of machine cycles based on number of element groups which can be braided simultaneously. To facilitate the determination of peripheral yarn locations subsequent rules are followed. The yarns for columns are placed first starting at the left- and top-most element. Following the known alternating fashion the peripheral yarns are successively placed around the opposite edges. As shown in Figure 3.5(e), internal yarn elements act as peripheral yarns, which allows them to interlace flanges and webs. The peripheral yarns along the rows are subsequently placed. The total number of element groups indicated with different colours represents the number of four-step braiding machine cycles. In case of the presented box beam, two element groups imply that eight braiding steps are required, i.e. the flanges are braided first and then the webs. Although the dimensions are limited by the real machine bed, a virtual box beam is designed for numerical analyses.

3.2.2. Composite manufacturing

All braided performs were produced using GF yarns with a linear density λ of 2400 tex supplied by Owens Corning Ltd. Braid reinforced composites were produced by

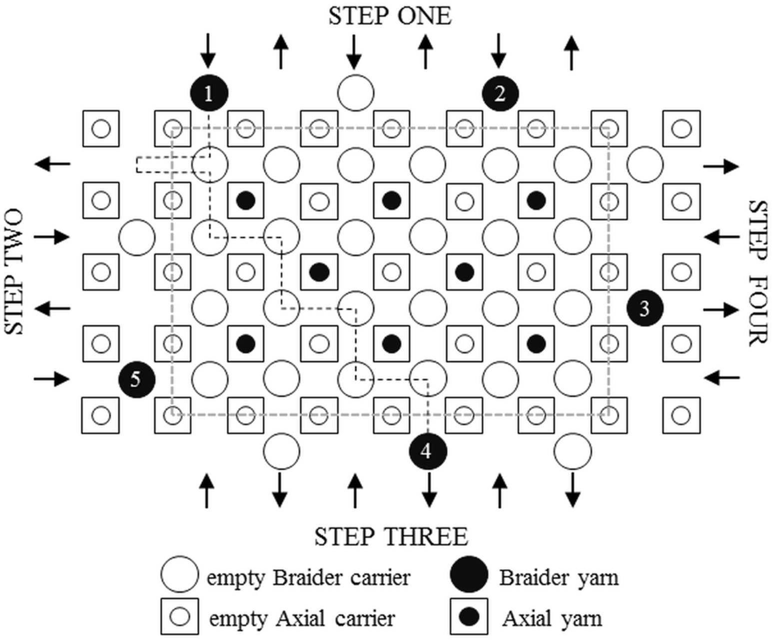

Figure 3.4.: Path of yarn *1* in a two-step braid using four-step braiding

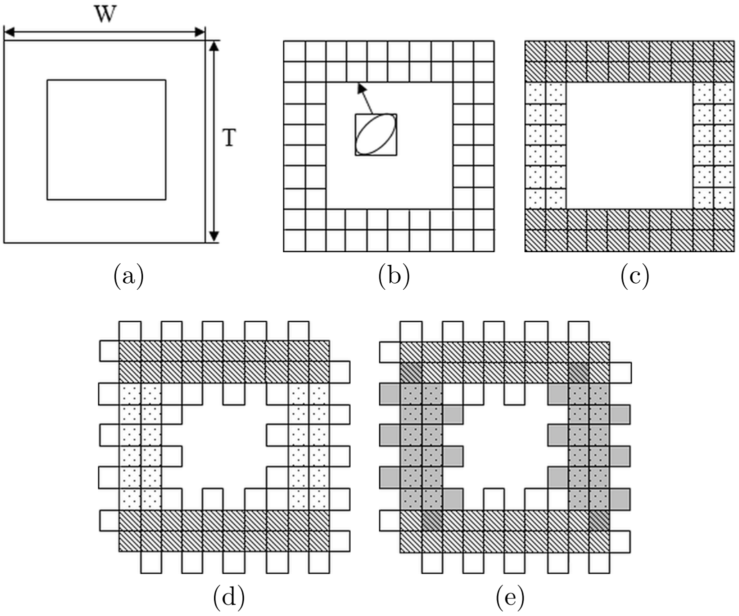

Figure 3.5.: Method to determine braiding sequence of complex profile shapes

vacuum assisted resin transfer moulding in a semi-closed aluminium mould to form flat beams, using an epoxy resin (HEXION EPIKOTE 04908). The set-up is shown in Figure 3.6. After an initial cure at room temperature for 48 h, a post cure cycle of 4 h at 70°C and 6 h at 80°C is employed to obtain the full mechanical properties. After curing, the specimens were removed from the mould and cut to their final longitudinally dimensions. Width and thickness are not altered.

For comparing the mechanical behaviour of 3DBRCs with pultruded profiles, a representative laminate was produced by vacuum infusion, using the same resin system and curing cycle as described beforehand. A press with adjustable cavity height was used to obtain a laminate thickness of 5 mm, equal to the analysed pultruded profiles. *Configuration 1* was selected as comparative study case. The lay-up of the laminate is comprised of outer layers CSM and inner layers GF UD fabrics with areal weights of 450 g/m^2 and 400 g/m^2 , respectively.

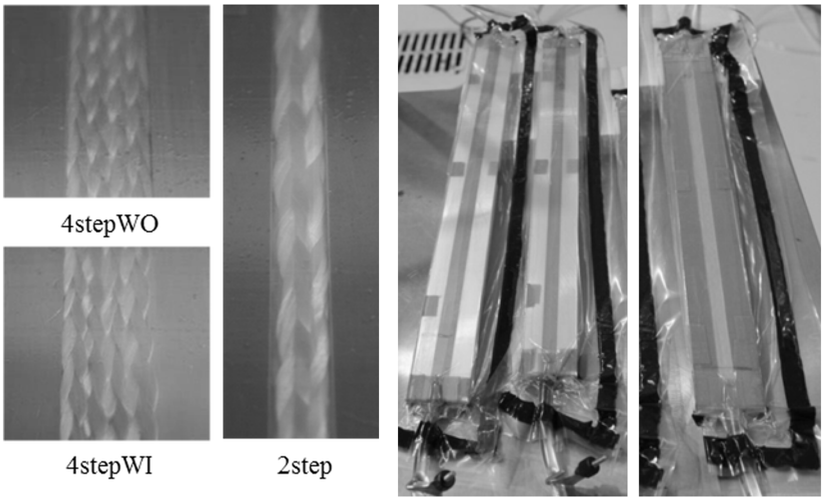

(a) (b)

Figure 3.6.: Vacuum assisted resin transfer moulding set-up in a semi-closed mould: Close-ups of preforms under vacuum (a), infusion (b)

3.2.3. Microstructural analyses

Basis for the analytical and numerical modelling approaches presented in the following chapters is a detailed analysis of the microstructure of a 3DBRC after consolidation. As textiles are hierarchically structured materials, the microstructure of a textile architecture can be divided into three levels: textile level (yarn orientations and distribution in the textile structure), yarn level (yarn geometries) and fibre level (fibre packing in the yarn) [130]. The initial cross-section of the braided structure changes first when the preform is removed from the braiding machine and again when the preform is consolidated in the mould. Physical dimensions and properties of composite and yarns were determined. Surface braiding angles, the pitch length, and yarn dimensions on the surface and in cross-sectional views can be measured with certain precision.

Moreover, calcination tests were carried out according to EN ISO 1172:1998 [131] to obtain the fibre volume fraction. The density values used for the GF were 2.6 g/cm^3 and for the epoxy resin 1.2 g/cm^3.

3.2.4. Tensile testing

Quasi-static tensile testing was performed using a displacement-controlled universal testing machine (INSTRON 4208) capable of loading 100 kN. The cross-head loading rate was held constant at 2 mm/min following the ASTM Test Method D 3039 [132]. For the laminate material a specimen width of 25 mm and length of 250 mm were used according to the standard. Dimensions of 3DBRC specimens are defined by the respective preform and infusion process, and were measured prior to testing. A change of thickness and width was avoided to ensure yarn continuity. Moreover, a length of 200 mm was selected in order to increase the number of specimens, owing to quantitative limitations of available braided preforms. Specimens were tabbed prior to testing to prevent material damage due to gripping. GF reinforced epoxy tabs with a length of 50 mm and a thickness of 2 mm were adhered to the ends of the specimens using an epoxy adhesive (3M Scotch-Weld DP 460). The measured test data were used to calculate the longitudinal modulus of elasticity as well as the ultimate tensile strength and strain.

3.2.5. Flexural testing

The flexural behaviour was obtained using the ISO 178 three point bending test [133]. The geometry of the test coupon differed from the standard. A universal testing machine (INSTRON 4505) was used together with a 50 kN load cell. Standard dimensions, a specimen width of 10 mm and a length of 100 mm, were used for the laminated material. For 3DBRCs the ratio between specimen thickness and length was likewise 20 and the ratio between span and thickness 16. Only four-step braid reinforced composites were tested as no two-step braided preform was left. The measured data were used to calculate flexural moduli as well as the flexural stress-strain behaviour.

3.2.6. Impact testing

Impact testing can be distinguished between low, medium and high velocity impact events and can be further differentiated into low and high energy impacts. Relatively low energies damage the composite partially but it remains capable of load bearing. High-energy impacts rupture or penetrate the composite completely. Low velocity and low energy impacts can be performed either on a falling-weight test machine or on a pendulum-type instrument. High energy events can be simulated with a gas gun or other ballistic launchers [20]. Studies on the impact behaviour of 3D woven fibre architectures have been performed by Chou et al. [134] and Potluri et al. [135] using a falling weight impact machine. A falling-weight tower is an inexpensive method for testing the impact behaviour of composites. A weight of known mass is dropped from a known height. The weight, which is assumed to behave as a rigid body, is instrumented with an accelerometer allowing for calculating the impact force. The impact energy can be increased by raising the mass and/or the velocity of the impactor. The velocity in the present study was limited by the height of the tower (1 m). Therefore, two different masses (10 kg and 20 kg) were selected to change the impact energy and analyse its effect on the damage behaviour. At each energy level three tests were performed. In order to perform dynamic three point bending experiments a Charpy type striker was used. The experimental setup consists of unnotched specimens, which were freely supported. A specimen length of 70 mm was chosen, based on the ISO 179 standard [136] and to fit into the specimen holder. Similar to the other experiments, specimen width and thickness of the 3DBRCs were defined by the infusion process. The laminated specimens were 10 mm wide. Force-time data was measured and used to determine the amount of energy needed to cause failure in the specimen. For the purpose of validation the experiments were recorded using high speed photography.

4. Analytical modelling

4.1. Geometry effects on pultruded profiles

Energy absorption and dissipation can be obtained by permanent deformation, friction and fracture. Deformation and fracture behaviour are limited to material properties as well as the structural stiffness defined by the structure's geometric shape. In order to analyse the influence of geometric parameters on the bending and buckling behaviour of pultruded profiles, a simple study was conducted using solely analytical methods. The study is divided in two parts. In the first part, the flexural response of single-celled profiles and multi-cellular geometries under three point bending was analysed. Moreover, the local buckling behaviour in flanges and webs of the obtained geometries was studied as it is one of the governing design criteria for pultruded structures [29]. Different profiles with equal cross-sectional areas and material properties, consequently with the same linear mass density, were compared. In the second part, the bending stiffness was retained and dimensions were derived that allow to obtain the cross-sectional area, the structural mass density as well as the local buckling behaviour of the resulting geometries.

4.1.1. Analysis of sections with same cross-sectional area

The bending response of a square pultruded box beam structure without stiffeners, referred to as $s1$, is compared to flexural properties of various quadratic and rectangular cross-sections with different stiffeners, as depicted in Figure 4.1.

- Topology $s1$: a square, hollow pultruded beam with one cell
- Topology $r1v$: a vertically oriented rectangular, hollow pultruded beam with one cell and a height to width ratio of 2
- Topology $r1h$: a horizontally oriented rectangular, hollow pultruded beam with one cell and a height to width ratio of 1/2
- Topology $s2$: a square, hollow pultruded beam with two cells
- Topology $r2v$: a vertically oriented rectangular, hollow pultruded beam with two cells and a height to width ratio of 2
- Topology $r2h$: a horizontally oriented rectangular, hollow pultruded beam with two cells and a height to width ratio of 1/2

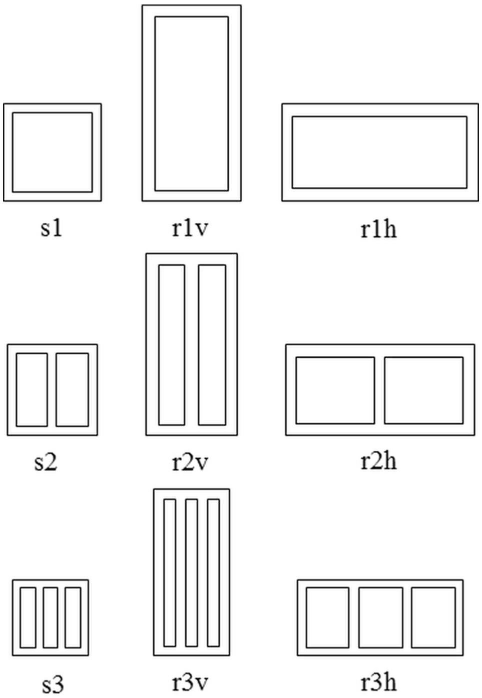

Figure 4.1.: Selected cross-sections

- Topology $s3$: a square, hollow pultruded beam with three cells
- Topology $r3v$: a vertically oriented rectangular, hollow pultruded beam with three cells and a height to width ratio of 2
- Topology $r3h$: a horizontally oriented rectangular, hollow pultruded beam with three cells and a height to width ratio of 1/2

For a direct comparison of the structural efficiency of each section, the material properties - including the laminate thickness and density - are kept constant for all sections. A change in thickness would imply a material change which is excluded from this study. Subsequently, the dimensions of all shapes (see Figure 4.2), can be derived using a constant cross-sectional area equal to the area given by box beam section $s1$, as well as the pre-defined flange and web thickness. In this way, sections with identical linear mass density are obtained. The pultruded profiles are considered as assemblies of flat plates with balanced symmetric laminates made of linearly elastic, orthotropic layers. Ply properties of *Configuration 1* determined during the preliminary study of pultruded box beam sections are exemplarily used to compute Young's and shear moduli of the laminate by means of the CLT.

The elastic behaviour of a beam subjected to lateral loading, as seen in Figure 4.2(a), can be described with the Euler-Bernoulli beam theory. However, the analytical solution to calculate the beam deflection only considers bending due to the applied load. GFRP beams with a span to depth ratio greater than 25 have negligible shear deflection in comparison to their bending deflection, whereas the deflection due to shear should

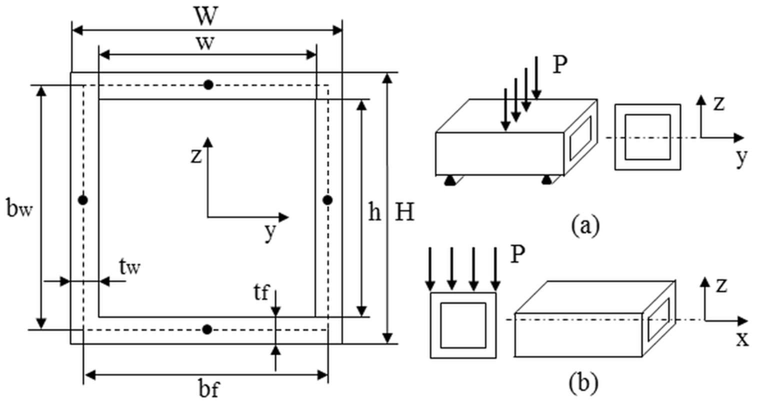

Figure 4.2.: Dimensions and modes of loading, bending (a) and buckling (b)

be determined for beams with smaller span-depth ratio [137]. According to standard EN 13706-2 [138] a pultruded profile of regular cross-section shall be loaded as a simple beam in three point flexure at a test span of 20 times the section depth to determine its effective flexural modulus. Therefore, the Timoshenko beam theory [139] considering transverse shear contributions to the deflection δ is used. The analytical solution is given as

$$\delta = \frac{PL^3}{48D} + \frac{PL}{4kF} \tag{4.1}$$

where P is the applied load, L the span, D equals E_lI the flexural rigidity consisting of the longitudinal elastic modulus E_l and the second moment of area I, F which is equal to $G_{lt}A_v$ the shear rigidity consisting of G_{lt} the in-plane shear modulus and A_v the area of all vertical profile members as well as k the shear coefficient. For beams made of homogeneous isotropic material k depends only on the geometry and the Poisson's ratio. For a solid rectangular profile the shear coefficient is about 5/6 [140]. The shear coefficients for the laminated beam elements are obtained by using Bank's variation of the Cowper method for single- and multi-cell beams [141, 142]. Hence, the bending rigidity, shear rigidity and deflection under three point bending are computed for all selected cross-sections considering a concentrated load of 1 kN and a span-depth ratio of 20. Shape factors for bending and shear stiffness as well as the deflection, ψ_{EI}, ψ_{kGA} and ψ_δ, respectively, are additionally introduced (see Equation 4.2) to compare each cross-section with the flexural behaviour of the single-cell box beam profile. Bending and shear rigidity factors bigger than 1.0 represent a stiffness increase, whereas a deflection shape factor bigger than 1.0 indicates a beam deflection reduction.

$$\psi_{EI} = \tfrac{D}{D_{s1}} \qquad \psi_{kGA} = \tfrac{kF}{kF_{s1}} \qquad \psi_\delta = \tfrac{\delta}{\delta_{s1}} \tag{4.2}$$

The main failure mode in box beam structures under flexural loading is tearing, separation of the compressed flange from the webs, triggered by local buckling. Resulting cracks and delamination extend in longitudinal direction. By means of cross-sectional changes stresses at flange-web junctions can be reduced due to improving buckling behaviour. In the following section critical local buckling stresses and loads for flanges and webs are calculated using recommended design principles from the EUROCOMP design code for structures made of polymeric composites [137]. The subscripts f and w refer hereinafter to flange and web, respectively. Local instability in the web of box beams may occur due to shear loading before the flange buckles. The flange-web interaction of a pultruded structure is no rigid connection, since the reinforcement is mainly along the beam and the corners are resin-rich. The webs of a box beam are restrained by the flanges and carry mainly shear loads, whereas longitudinal bending stresses are ignored [143]. Thus, the web can be idealised as a simply supported plate solely under in-plane shear [27]. The critical shear stress τ_{crw} for local in-plane shear buckling of a rectangular plate can be calculated according to Equation 4.29 in the EUROCOMP design code as

$$\tau_{crw} = \frac{4K_{lt}\sqrt[4]{D_l D_t^3}}{t_w b_w^2} \tag{4.3}$$

with

$$D_l = \frac{E_l t_w^3}{12\left(1 - \nu_{lt}\nu_{tl}\right)} \tag{4.4}$$

$$D_t = \frac{E_t t_w^3}{12\left(1 - \nu_{lt}\nu_{tl}\right)} \tag{4.5}$$

where t_w and b_w denote the thickness and width of the web, D_l and D_t the longitudinal and transverse plate stiffness, respectively, E_t is the transverse modulus of elasticity, ν_{lt} and ν_{tl} the major and minor Poisson's ratios as well as K_{lt} is the shear buckling coefficient and equal to 8. The critical design shear load for local web buckling P_{crw} is obtained by

$$P_{crw} = \frac{\tau_{crw} A_v}{\gamma_m} \tag{4.6}$$

where γ_m is a material strength coefficient and assumed to be 2 for ultimate strengths [137]. The critical local buckling strength of a simply supported plate under compression σ_{crf} is predicted according to Equation 4.9 in the EUROCOMP design code as follows

$$\sigma_{crf} = 2\pi^2 \frac{\sqrt{D_l D_t} + H_o}{t_f b_f^2} \tag{4.7}$$

with

$$H_o = \frac{\nu_{lt} D_t + \nu_{tl} D_l}{2} + \frac{G_{lt} t_f^3}{6} \tag{4.8}$$

where t_f and b_f denote the thickness and width of the flange. The critical design load for local flange buckling P_{crf} for a beam under three point bending can be derived by means of the critical stress and beam properties as

$$P_{crf} = \frac{8\sigma_{crf} W}{\gamma_m L} \tag{4.9}$$

where W is the section modulus of the profile. Consequently, flange and web buckling shape factors, $\psi_{\sigma_{crf}}$ and $\psi_{\tau_{crw}}$ for the stresses and ψ_P for the loads, respectively, are computed. Buckling shape factors bigger than 1.0 represent a critical stress or load increase, thus indicating a higher local buckling resistance.

$$\psi_{\sigma_{crf}} = \frac{\sigma_{crf}}{\sigma_{crf_{B_{s1}}}} \qquad \psi_{P_{crf}} = \frac{P_{crf}}{P_{crf_{B_{s1}}}} \qquad \psi_{\tau_{crw}} = \frac{\tau_{crw}}{\tau_{crw_{B_{s1}}}} \qquad \psi_{P_{crw}} = \frac{P_{crw}}{P_{crw_{B_{s1}}}} \tag{4.10}$$

4.1.2. Analysis of sections with same bending stiffness

Mass reduction is typically the main driver for structural optimisation. Thus material replacement by using composites is a common method to improve the optimisation efficiency. However, further savings in mass can be attained by geometrical optimisation. In the second part of this study, material properties as well as the flexural rigidity given by box beam section $s1$ are kept constant to derive dimensions for the selected cross-sections in an effort to gain further insight in savings through geometrical alterations. Potential savings in the linear mass density λ_m, expressed by means of a shape factor for the mass ψ_m are given by Equation 4.11. Mass factors bigger than 1.0 represent a reduction of the cross-sectional area, hence savings in the linear mass density. Similar to the first part of this study on geometry effects, the bending behaviour and buckling response of all cross-sections are analysed and compared with box beam section $s1$.

$$\psi_m = \frac{\lambda_{m_{s1}}}{\lambda_m} \tag{4.11}$$

4.2. Process-microstructure relationships in 3D braids

The following section presents analytical models dependent on process key parameters to determine the general topology of 3D braided preforms. Besides, the preform microstructure is limited by yarn jamming. Therefore, processing conditions are defined to predict feasible preform dimensions.

The arrangement of yarn carriers on the machine bed determines the cross-sectional shape of the preform and the number of yarns. The maximum possible number of braider yarns N_b in a four-step braid is determined by the braider yarn arrangement. The total number of yarns used to produce a four-step braid can be calculated using the following formula

$$N_{b-4step} = mn + m + n \tag{4.12}$$

The maximum number of additional axial yarns N_a in a four-step braid can be derived from

$$N_{a-4step} = (m-1)(n-1) \tag{4.13}$$

The arrangement of axial yarns in a two-step braid, as shown in Figure 3.3, determines the number of braider and axial yarns as

$$N_{b-2step} = m + n \tag{4.14}$$

$$N_{a-2step} = m(2n-1) - n + 1 \tag{4.15}$$

Yarn numbers of the selected braid configurations 4stepWI, 4stepWO and 2step are listed in Table 6.8. The braider yarn angle or surface braiding angle θ is the lower angle between the longitudinal direction of the braid and the braider yarns, see Figure 4.3. Besides the pitch length, it is a geometric key parameter in designing a braided preform and its mechanical properties. However it is not easy to control the angle directly. The braider yarn angle is determined by the pitch length which is controlled during processing by maintaining a constant converging height H and constant braiding angles α [129]. The braiding angle which is a machine dependent parameter before the yarns converge has to be differentiated from the braider angle. The braiding angle of braider yarns varies depending on the carrier's location on the machine bed and with respect to the preform centre, as shown in Figure 4.3. Although the angles may change during carrier movements, after each step they are fixed [129].

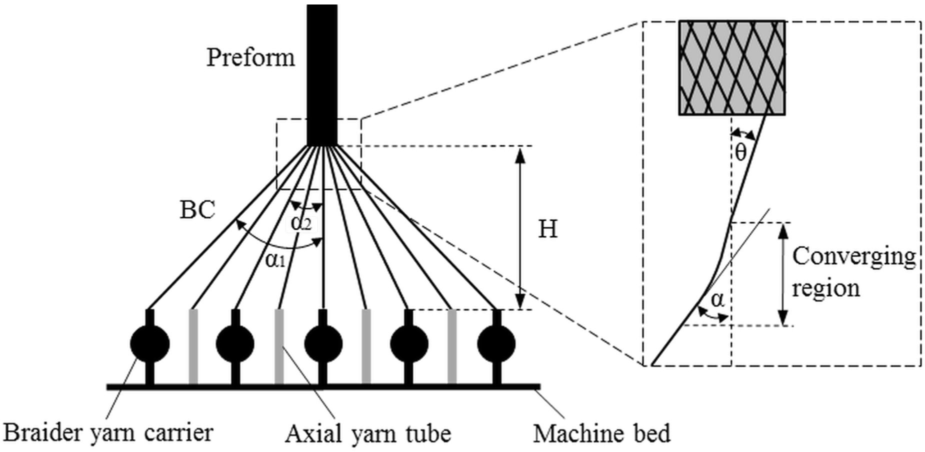

Figure 4.3.: Variation of braiding angles due to carrier location

In order to produce a consistent preform the converging height should be maintained constant during braiding. Machine parameters such as yarn distances on the machine bed determine the converging point. In case of four-step braiding, the braiding angle of each yarn at (i, j) location can be determined by means of 3D trigonometry as follows

$$\tan \alpha_{ij} = \frac{\bar{BC}}{H} = \frac{1}{H}\sqrt{\left(\frac{m-2i+3}{2}\Delta Y\right)^2 + \left(\frac{n-2j+3}{2}\Delta Z\right)^2} \tag{4.16}$$

for $(1 \leq i \leq m+1, 1 \leq j \leq n+1)$. $\bar{BC}$ is the distance between a yarn at position (i, j) and the preform centre, ΔY and ΔZ are the distances between axial yarns, respectively as shown in Figure 4.4. The distance between axial carriers on the available machine bed is 70 mm and approximate converging heights were measured during braiding. Consequently, an averaged braiding angle α_{av} can be determined as

$$\alpha_{av} = \frac{\sum \alpha_{ij}}{N_{b-4step}} = \frac{\sum \alpha_{ij}}{mn + m + n} \tag{4.17}$$

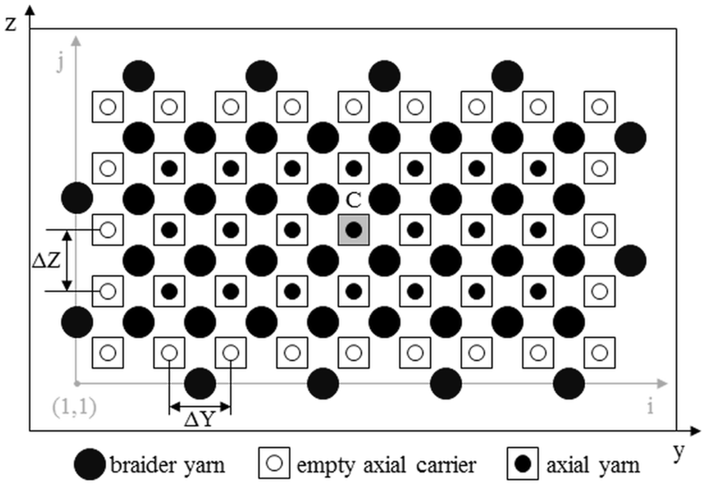

Figure 4.4.: Schematic top-view of the available machine bed and indicated yarn distances

in which $(1 \leq i \leq m+1, 1 \leq j \leq n+1)$. The surface braiding angle of the preform and the averaged braiding angle can be related as [129]

$$\theta_p = \frac{\alpha_{av}}{2} \tag{4.18}$$

As described in Section 3.2.1, the double number of columns and rows is necessary to braid a two-step braid on a four-step braiding machine. Hence, the averaged braiding angle as well as the surface braiding angle of a two-step braid can be computed by duplicating the number of columns and rows in Equation 4.16 and 4.17, respectively.

Mechanical properties of the 3DBRC depend on its constituents, the fibre architecture and the geometric pattern of yarns. The composition and number of unit cells in a braid can vary with the yarn arrangement on the machine bed, however the general topology of a 3D braided preform is only dependent on the braiding procedure and can also not be changed by cross-sectional dimensions [79]. Although the overall preform shape is defined by the braid pattern, preform parameters, such as the fibre and yarn packing factors, already vary between the on-the-machine state and the out-of-the-machine state due to yarn tension [144]. The mould used in the infusion process defines the final composite shape, can change the initial cross-section of the braided preform and its yarns as well as the key parameters of the braid geometry.

The interlocked preform architecture, composite dimensions and resulting yarn geometries define the amount and size of resin pockets in the composite. The fibre volume fraction of 3DBRC depends additionally on the packing of yarns against each other and of fibres inside a yarn during the braiding and consolidation process [57]. Multifilament yarns are used for braider and axial yarns. The filaments or fibres are assumed to have a circular cross-section and thus cannot be packed without any gap between them. Fibre yarn packing forms can be distinguished between two basic idealised patterns: open-packing, in which the fibres are arranged in a concentric pattern, and close-packing, in which the fibres are arranged in a hexagonal pattern [50]. The yarn volume fraction or packing factor κ can be computed as fibre to yarn area ratio and approaches in an open-packed yarn a value of 0.75, whereas in a close-packed yarn approximately 0.91 [57]. Fibre and yarn packing are influenced by the braiding method, yarn tension, yarn twist, the cross-sectional yarn shape, the preform geometry as well as interyarn contact [57, 144]. Byun [144] showed that the minimum and maximum yarn volume fraction in four-step braids reaches 0.5 and 0.78 for infinite m and n, respectively, whereas in two-step braids the yarn packing factor is generally in the range of 0.75 - 0.8. Axial yarns in the centre of a two-step braid have generally the highest packing factor.

Surface patterns of a four-step braid and a two-step braid as well as corresponding schematics are shown in Figure 4.5 and 4.6, respectively. The patterns are characterised by the surface braiding angle, the yarn width and the pitch length. The braid pattern repeats after one pitch length. In the free state cross-sections of yarns are assumed to be circular or elliptical. Byun, Chen et al. and Li et al. [2, 144, 145] showed that the yarn cross-section in four-step braids can be assumed as elliptic shape. In order to get a first idea and estimate yarn as well as preform dimensions of a four-step braid based on selected material parameters the following geometric relations can be used.

$$d = \sqrt{\frac{4\lambda}{\pi \rho_f \kappa f}} \tag{4.19}$$

$$w = \overline{AC} = df \tag{4.20}$$

where d is the minor ellipse axis or yarn thickness, f the aspect ratio of the yarn and w the major ellipse axis or yarn width. Using a linear yarn density λ of 2400 tex and assuming an aspect ratio of 2 as well as a packing factor of 0.7, the width $W_{p-4stepWO}$ and the thickness $T_{p-4stepWO}$ of a 4stepWO preform can be calculated as

$$W_{p-4stepWO} = m\overline{AB} = \frac{(m+1)\,w}{\cos\theta} \tag{4.21}$$

$$T_{p-4stepWO} = \frac{(n+1)\,d}{\cos\theta} \tag{4.22}$$

In consequence of additional axial yarns the surface braiding angle and thus the preform dimensions of a 4stepWI vary and can be derived from

$$W_{p-4stepWI} = \frac{mw + (m-1)\,\frac{w}{2}}{\cos\theta} \tag{4.23}$$

$$T_{p-4stepWI} = \frac{nd + n\frac{d}{2}}{\cos\theta} \tag{4.24}$$

The pitch length of four-step braids $h_{p-4step}$ can be related to yarn dimensions as

$$h_{p-4step} = 2\cos\theta\overline{AD} = \frac{2\cos\theta w}{\sin 2\theta} = \frac{w}{\sin\theta} \tag{4.25}$$

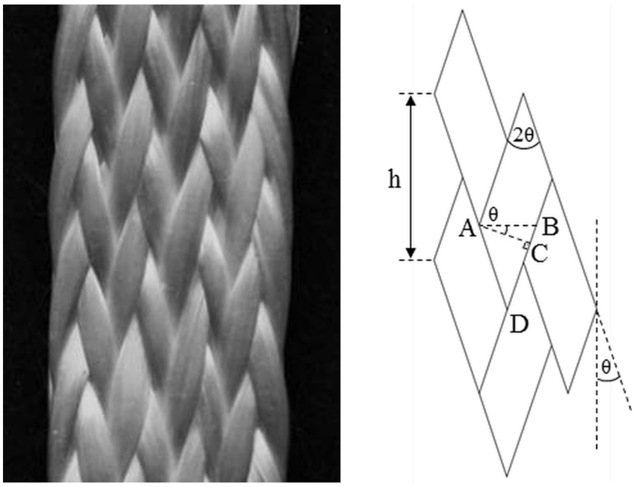

(a) (b)

Figure 4.5.: Surface pattern of a four-step braided preform (a) and an idealised schematic (b)

As seen on microscopic images (Figure 6.23) and in accordance with literature [57, 144], cross-sections of axial yarns in two-step braids can be idealised as different prismatic shapes dependent on their position in the yarn array. Central axial yarns take after consolidation diamond-like shapes, see Figure 4.6. Yarn edges along the outer composite surface edges are flat after resin infiltration and assumed to result in a pentagonal shape. The shape of braider yarns between axial yarns is assumed to be rectangular as a result of geometrical constraints by the axial yarns. Dimensions of axial (subscript a) and braider yarns (subscript b) are influenced by yarn tension or compression during consolidation and can be expressed by yarn properties according to Equations 4.26-4.31. The cross-sectional aspect ratio of braider yarns f_b is defined as the ratio of thickness to width, whereas the aspect ratio of axial yarns f_a can be defined by its inclination angle φ.

$$a = \sqrt{\frac{\lambda_a}{\rho_f \kappa_a \sin\varphi}} \tag{4.26}$$

$$f_a = \tan\frac{\varphi}{2} \tag{4.27}$$

$$w_a = 2a\cos\frac{\varphi}{2} \tag{4.28}$$

$$t_a = 2a\sin\frac{\varphi}{2} \tag{4.29}$$

$$b = \sqrt{\frac{\lambda_b}{\rho_f \kappa_b f_b}} \tag{4.30}$$

$$t_b = f_b b \tag{4.31}$$

where a is the side length, w_a the width and t_a the thickness of a central axial yarn, t_b the thickness and b the width of a braider yarn, respectively. Assuming a compact cross-section with square central yarns (inclination angle of 90°), a braider aspect ratio of 0.1 and a yarn packing factor of 0.75, the dimensions of a two-step braided preform can be estimated with

$$W_{p-2step} = \left((m-2)+1\right) w_a + 2t_b + \left(2\left(m-1\right)t_b + a\right)\cos\frac{\varphi}{2} \tag{4.32}$$

$$T_{p-2step} = \left((n-2)+1\right) t_a + 2t_b + \left(2\left(n-1\right)t_b + a\right)\sin\frac{\varphi}{2} \tag{4.33}$$

Yarns on the top surface of a two-step braid move to the bottom and yarns on the bottom surface move vice versa. From Figure 4.6 it can be seen that yarns appear on the top surface in an interval of $n+1$ axial yarns [129]. Therefore an approximate pitch length of the two-step braided preform can be obtained as

$$h_{p-2step} = \tan\left(\frac{\pi}{2} - \theta\right)\overline{AB} = \frac{\left(n+1\right)w_a + nt_b}{\tan\theta} \tag{4.34}$$

Yarn crimp is dependent on the cross-sectional area of the braid and the take-up length [146]. Yarns in corner regions of four-step braids interact less with interior yarns as a result of the braiding scheme and yarns on the edge are straighter than in the interior [146]. Due to the fact that peripheral braider carriers don't move during a step in the corresponding direction, see Figure 2.3, but they are pulled by the take-up unit at their steady position. Yarn crimp and the volume fraction increase when the cross-section of the braid is compressed. The preform microstructure and its dimensions are limited by the processing condition at which yarns jam against each other [57,75]. Yarn jamming designates the state in which the yarns contact each other and the structure is most compact [144]. The criteria for jamming signifies that certain braiding angles and preform dimensions are not possible to obtain. A jamming condition is reached at a certain pitch length which can be estimated for a two-step braid as follows [57,75,144]

$$h_{j-2step} = \frac{2t_b}{\sin\theta_p} \tag{4.35}$$

where $h_{j-2step}$ denotes the pitch length at jamming and t_b the braider width as described in Equation 4.31. A smaller pitch length is obtained with increasing braiding yarn angles. Byun and Chou [75] reported that there exist two extreme cases of yarn jamming for four-step braids. The first case is when the surface braiding angle approaches 0°, the yarn cross-section becomes flatter and all yarns are virtually UD yarns. In the other case the yarn cross-section becomes more circular, the aspect ratio approximates 1 and thus the surface braiding angle approaches 50°. Based on a geometric analysis of the yarn arrangement at jamming the authors derived Equation 4.36 for the yarn orientation at jamming θ_j [75]. Hence, the pitch length at jamming for four-step braids can be computed with Equation 4.25.

$$\cos\theta_j = 1.314\frac{m\,(m+1)\,f^2}{m^2 f^2 + (m+1)^2} \tag{4.36}$$

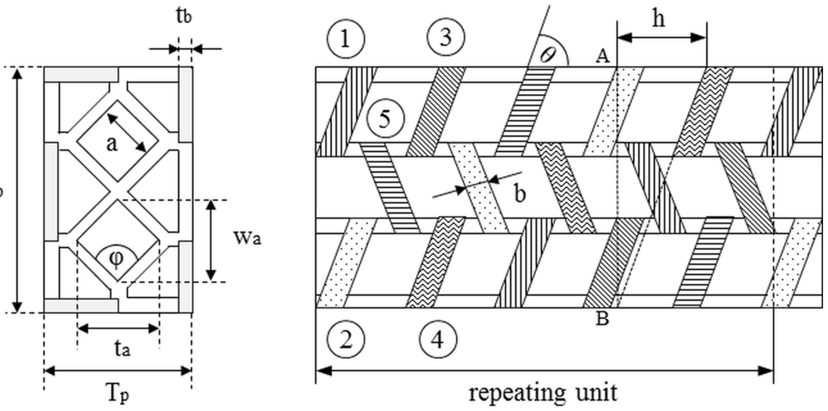

(a) (b)

Figure 4.6.: Idealised cross-section (a) and surface pattern (b) of a two-step braided preform

The software package Mathematica was used to calculate yarn and preform dimensions based on process parameters. An exemplary code for four-step braided preforms is presented in Appendix A.1.

4.3. Modelling of 3DBRC

Various analytical models have been proposed in literature, research works of Byun [1,57,75], Wang [78,79], Chen [2] and Shokrieh [81] have been very valuable to establish the presented models. However the reproduction of presented results mostly failed. For this reason, existing approaches have been reviewed and updated by own findings for the manufactured 3DBRCs. Identifying and quantifying representative volumes in the textile architecture is the basis of each analysis. Each RVE is a set of yarns, in which each yarn is considered as UD composite with spatial orientation. It is assumed that yarns are not interacting with each other. Consequently, braider yarn orientations and fibre volume fractions are analysed. Knowing yarn and matrix properties elastic constants can be predicted using a modified CLT approach. The general method used in this study to obtain mechanical properties of a 3DBRC can be summarised in the following steps:

(a) Identification and quantification of RVE

(b) Determination of local stiffness of each UD yarns along its axial direction

(c) Determination of transformation matrices of UD yarns

(d) Calculation of stiffness matrices of UD yarns in each RVE transformed to the global coordinate system

(e) Calculation of effective stiffness of each RVE

(f) Summation of RVE stiffness properties to global stiffness properties considering each volume contribution

(g) Derivation of elastic constants of braided composite.

Material properties of the constituents used in the analytical studies are shown in Table 4.1. Further input data, such as yarn and composite dimensions as well as pitch lengths, are taken from the experimental characterisations (Table 6.9 in Chapter 6).

Table 4.1.: Properties of constituents used for analytical modelling

Constituent	Young's modulus [GPa]	Shear modulus [GPa]	Poisson's ratio
GF	73	30	-
Epoxy resin	2.94	-	0.35

4.3.1. Four-step braids

Besides the concept of dividing a braid in repetitive groups of yarns which travel the same path [77], a four-step braided composite without or with axial yarn reinforcement can be considered as skin-core structure composed of interior, surface and corner cells [2, 78,145]. Cross-sections of the 4stepWO and the 4stepWI were microscopically analysed to obtain dimensions and braid properties. The input necessary for the below described modelling approach is comprised of the composite width, the composite thickness, the pitch length, the width and the thickness of a braider yarn in an interior cell as well as the surface braiding angle. Idealised yarn arrangements in a 4stepWO and a 4stepWI are presented in Figure 4.7. As seen in micrographs (Figure 6.24), the braider yarns in four-step braids take polygonal shapes (hexagonal or octagonal). For reasons of simplicity the braider yarn cross-sections are assumed to be elliptic, as shown in Figure 4.8. Axial yarns in a 4stepWI are assumed to be rhombic due to compression.
Assuming that braider yarns have equal dimensions as indicated in Figure 4.7 the width W_c and the thickness T_c of a consolidated 4stepWO and a 4stepWI are given by

$$W_{c_{4stepWO}} = (m+1)\,\Delta y \tag{4.37}$$

$$T_{c_{4stepWO}} = (n+1)\,\Delta z \tag{4.38}$$

$$W_{c_{4stepWI}} = \left(m+\frac{3}{5}\right)\Delta y \tag{4.39}$$

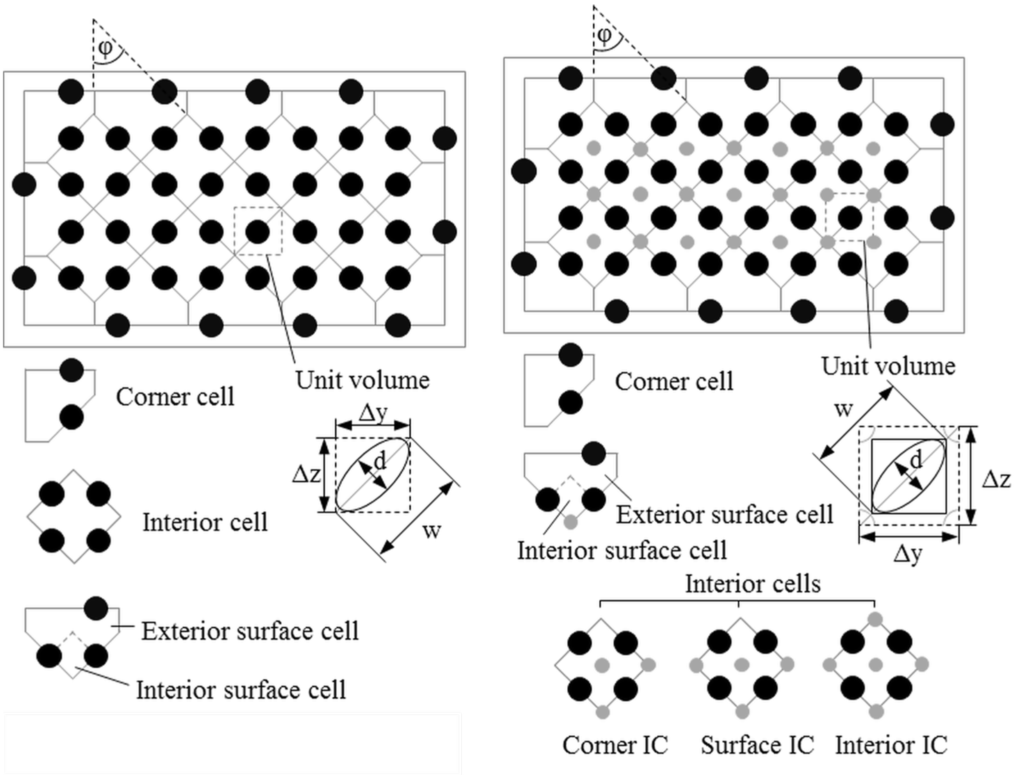

(a) (b)

Figure 4.7.: Idealised cross-sections of a 4stepWO (a) and a 4stepWI

$$T_{c_{4stepWI}} = \left(n + \frac{3}{5}\right)\Delta z \tag{4.40}$$

where Δy and Δz denote the horizontal and vertical dimensions of a unit volume, respectively, as shown in Figure 4.7.

φ is defined as the angle between the braiding yarns projected onto the cross-sectional plane and the composite thickness, also referred to as inclination angle. Analyses presented in literature [2, 80, 81, 98, 147] assume mostly a perfect condition with an angle of 45°, resulting in a transverse isotropic material behaviour. On the other hand, if the width and the thickness of a 4stepWO and a 4stepWI are given by processing, φ can be deduced with the following approximation

$$\tan\varphi_{4stepWO} = \frac{(n+1)\,W_{c_{4stepWO}}}{(m+1)\,T_{c_{4stepWO}}} \tag{4.41}$$

$$\tan\varphi_{4stepWI} = \frac{\left(n+\frac{3}{5}\right)W_{c_{4stepWI}}}{\left(m+\frac{3}{5}\right)T_{c_{4stepWI}}} \tag{4.42}$$

Various relationships of yarn angles and cell dimensions have been presented, among others by Chen et al. [2] as well as Tang and Postle [147]. Yarns with identical orient-

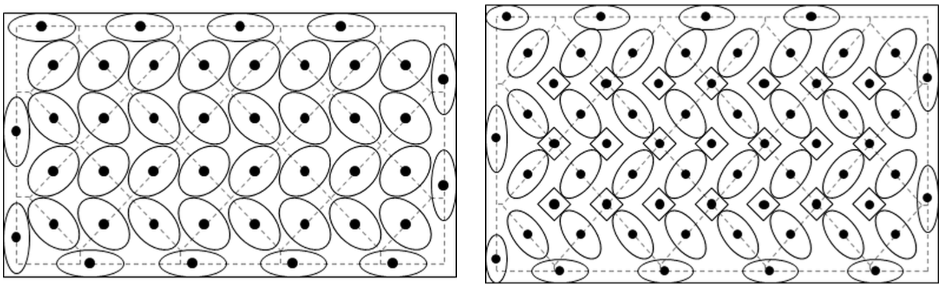

Figure 4.8.: Idealised arrangement of braider yarns with elliptic cross-section: 4stepWO (a), 4stepWI (b)

ation are summarised as one UD composite. For instance, an interior cell is a cuboid consisting of four kinds of oriented yarns with different local coordinate systems, as illustrated in Figure 4.10. The surface cell is a pentagonal prism which can be divided into two sub-cells: the interior and the exterior surface cell. Yarn orientations in the interior surface cell are similar to the interior cell, the difference is in their dimensions and fibre volume fractions. Although yarns in exterior surface cells and corner cells are curved or helical, for simplicity those yarns are assumed to be straight lines. In this study the surface braiding angle θ, which is defined as the angle between surface braiding yarn axis and the fabrication direction, is experimentally measured and used to obtain the braiding angle given by

$$\tan\alpha = \frac{12}{\pi}\tan\theta\sin\varphi \tag{4.43}$$

γ is defined as the interior braiding angle between the interior braiding yarn axis and the fabrication direction. The interior braiding angle can be deduced from the following relationship

$$\tan\gamma = \frac{1}{\sin\varphi}\tan\alpha \tag{4.44}$$

β is defined as the corner braiding angle between the corner braiding yarn axis and the fabricated direction, which can be computed as [79]

$$\tan\beta = \frac{\tan\gamma}{6} \tag{4.45}$$

Figure 4.9 illustrates the global and local coordinates for a yarn set inclined to the X-axis by the angle of η. The projection of the yarn onto the YZ-plane is oriented by the angle ϕ towards the Y-axis. The 4stepWO is made of 16 UD composites with different angles of η and ϕ, whereas the 4stepWI is composed of 18 UD composites due to axial reinforcements. Table 4.2 presents all yarn orientations in each cell.

The yarn packing factor varies between the different unit cells. The interior cell

Table 4.2.: Yarn orientations of UD composites in each cell

Type of cell	Angles (η, ϕ)	
	4stepWO	4stepWI
Interior cell	$(\gamma, \varphi), (-\gamma, \varphi), (\gamma, -\varphi), (-\gamma, -\varphi)$	$(\gamma, \varphi), (-\gamma, \varphi), (\gamma, -\varphi), (-\gamma, -\varphi), (0, 0)$
Exterior surface cell	$(\theta, 0), (-\theta, 0), (\theta, 90), (-\theta, 90)$	
Interior surface cell	$(\gamma, \varphi), (-\gamma, \varphi), (\gamma, -\varphi), (-\gamma, -\varphi)$	$(\gamma, \varphi), (-\gamma, \varphi), (\gamma, -\varphi), (-\gamma, -\varphi), (0, 0)$
Corner cell	$(\beta, 0), (-\beta, 0), (\beta, 90), (-\beta, 90)$	

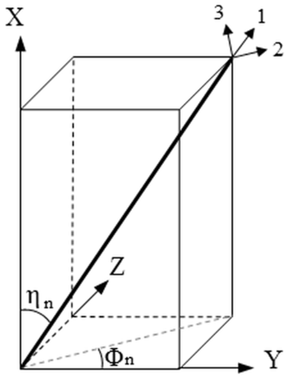

Figure 4.9.: Schematic illustration of a spatially oriented braider yarn segment in a four-step braid

occupies most of the braided volume, for this reason the packing factor of the interior braider yarn is assumed to be applicable for all regions and deviations are neglected [2]. Yarn cross-sections in the micrograph represent braider yarn cross-sections inclined by the respective braiding angle. Thus, an average braider yarn packing factor is obtained as

$$\kappa_b = \frac{\lambda}{\rho d_m \sin\gamma w_m} \tag{4.46}$$

where d_m is the minor axis and w_m the major axis measured in the elliptic yarn cross-section. The packing factor of the axial yarns in the 4stepWI is computed as

$$\kappa_a = \frac{2\lambda}{\rho w_a t_a} \tag{4.47}$$

All cells have specific yarn configurations, as shown in Figure 4.7, and geometric properties and thus have to be treated separately. A surface cell can be further divided into an interior and an exterior sub-cell. Assuming that one yarn carrier occupies one unit volume, see Figure 4.7, the volumes of each cell can be calculated in terms of unit volumes. One interior cell corresponds to 2 unit volumes, one surface cell to 1 1/2 unit volumes and 1 corner cell to 1 unit volume. Thus, the total fibre volume fraction of a four-step braided composite can be derived as

$$V_f = C_i V_{f_i} + C_{is} V_{f_{is}} + C_{es} V_{f_{es}} + C_c V_{f_c} \tag{4.48}$$

in which C_i, C_{is}, C_{es} and C_c are volume proportions of the interior, the interior surface, exterior surface and corner cells to the whole structure, respectively. The cell composition of a braid is dependent on the number of columns and rows. As an example, when both m and n are even numbers the four-step braid consists of four corner cells, whereas when m and n are both odd only two corner cells exist in the composite. The number of cells, corresponding unit volumes and volume proportions of a four-step braided composite without and with axial fibre reinforcement can be calculated as given in Table 4.3 and Table 4.4. Furthermore, the yarn configuration of an interior cell for

4stepWI is varying, see Figure 4.7(b), in dependence on the braid pattern, the number of axial yarns and their arrangement on the machine bed, similar to the cell structure in the composite. Equations given in Table 4.3 are valid for braid patterns of $m \geq 3$ and $n \geq 3$, using the maximum possible number of axial yarns.

Table 4.5.: Fibre volume fractions of unit cells in four-step braided composites

Type of cell	4stepWO	4stepWI
Interior	$\frac{\sqrt{3}\pi}{8} \sin 2\varphi \kappa_b$	-
Interior IC	-	$\frac{\sqrt{3}\pi}{64} \left(8 \sin 2\varphi \kappa_b + 2 \cos \gamma \kappa_a\right)$
Surface IC	-	$\frac{\sqrt{3}\pi}{64} \left(8 \sin 2\varphi \kappa_b + \frac{7}{4} \cos \gamma \kappa_a\right)$
Corner IC	-	$\frac{\sqrt{3}\pi}{64} \left(8 \sin 2\varphi \kappa_b + \frac{3}{2} \cos \gamma \kappa_a\right)$
Interior SC	$\frac{\sqrt{3}\pi}{8} \frac{\sin 2\varphi}{\sin(\pi - 2\varphi)} \kappa_b$	$\frac{\sqrt{3}\pi}{16} \frac{\sin 2\varphi}{\sin(\pi - 2\varphi)} \left(2\kappa_b + \cos \gamma \kappa_a\right)$
Exterior SC	$\frac{3\sqrt{3}\pi}{16} \cos \varphi \frac{\cos \gamma}{\cos \theta} \kappa_b$	$\frac{3\sqrt{3}\pi}{16} \cos \varphi \frac{\cos \gamma}{\cos \theta} \kappa_b$
Corner	$\frac{3\sqrt{3}\pi}{4} \frac{\sin 2\varphi}{(2 \cos \varphi + 1)(2 \sin \varphi + 1)} \frac{\cos \gamma}{\cos \beta} \kappa_b$	$\frac{3\sqrt{3}\pi}{4} \frac{\sin 2\varphi}{(2 \cos \varphi + 1)(2 \sin \varphi + 1)} \frac{\cos \gamma}{\cos \beta} \kappa_b$

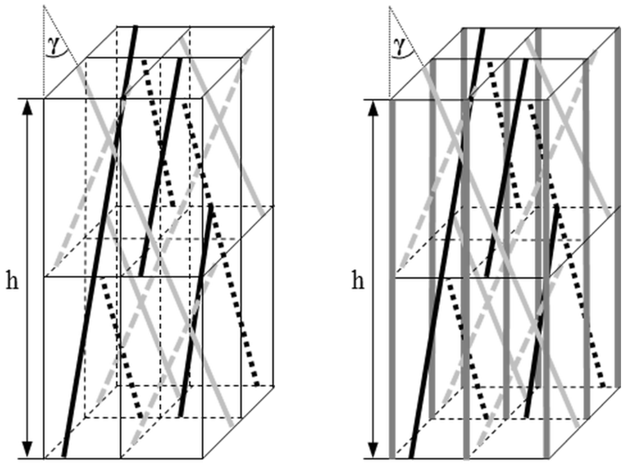

(a) (b)

Figure 4.10.: Yarn orientations in interior cells: (a) 4stepWO, (b) 4stepWI

Fibre volume fractions in the interior, surface and corner cells of a 4stepWO are in great part described by Chen et al. [2]. In case of a 4stepWI, the interior cell and the interior surface cell contain additional axial yarn volumes, as shown in Figure 4.10(b). Therefore, fibre volume fractions of both four-step braided composites are reviewed, deduced based on the assumption that the yarns take circular cross-sections and modified including a dependency on the inclination angle φ, see Table 4.5.

Table 4.3.: Number of cells and corresponding unit volumes in a four-step braid without and with axial yarns

Type of cell	Nº of cells		Nº of unit volumes	
	even m and n	odd m and/or n	even m and n	odd m and/or n
Interior (IC)	$\frac{1}{2}(mn-m-n)+1$	$\frac{1}{2}(mn-m-n+1)$	$mn-m-n+2$	$mn-m-n+1$
Interior IC	$\frac{1}{2}(mn-3m-3n)+5$	$\frac{1}{2}(mn-3m-3n+9)$	$mn-3m-3n+10$	$mn-3m-3n+9$
Surface IC	$m+n-8$	$m+n-6$	$2\,(m+n-8)$	$2\,(m+n-6)$
Corner IC	4	2	8	4
Surface (SC)	$m+n-4$	$m+n-2$	$\frac{3}{2}(m+n-4)$	$\frac{3}{2}(m+n-2)$
Interior SC	$m+n-4$	$m+n-2$	$\frac{1}{2}(m+n-4)$	$\frac{1}{2}(m+n-2)$
Exterior SC	$m+n-4$	$m+n-2$	$m+n-4$	$m+n-2$
Corner	4	2	4	2
TOTAL	$\frac{1}{2}(mn+m+n)+1$	$\frac{1}{2}(mn+m+n+1)$	$\frac{1}{2}(2mn+m+n-2)$	$\frac{1}{2}(2mn+m+n)$

Table 4.4.: Volume proportions of each cell type and of each UD composite to the whole composite in a four-step braid without and with axial yarns

Type of cell	Cell volume proportions C_n		UD volume proportions V_n	
	even m and n	odd m and/or n	4stepWO	4stepWI
Interior (IC)	$\frac{2(mn-m-n+2)}{2mn+m+n-2}$	$\frac{2(mn-m-n+1)}{2mn+m+n}$	$\frac{1}{4}C_i$	-
Interior IC	$\frac{2(mn-3m-3n+10)}{2mn+m+n-2}$	$\frac{2(mn-3m-3n+9)}{2mn+m+n}$	-	$\frac{1}{5}C_{ii}$
Surface IC	$\frac{4(m+n-8)}{2mn+m+n-2}$	$\frac{4(m+n-6)}{2mn+m+n}$	-	$\frac{1}{5}C_{si}$
Corner IC	$\frac{16}{2mn+m+n-2}$	$\frac{8}{2mn+m+n}$	-	$\frac{1}{5}C_{ci}$
Surface (SC)	$\frac{3(m+n-4)}{2mn+m+n-2}$	$\frac{3(m+n-2)}{2mn+m+n}$	-	-
Interior SC	$\frac{m+n-4}{2mn+m+n-2}$	$\frac{m+n-2}{2mn+m+n}$	$\frac{1}{4}C_{is}$	$\frac{1}{5}C_{is}$
Exterior SC	$\frac{2(m+n-4)}{2mn+m+n-2}$	$\frac{2(m+n-2)}{2mn+m+n}$	$\frac{1}{4}C_{es}$	$\frac{1}{4}C_{es}$
Corner	$\frac{8}{2mn+m+n-2}$	$\frac{4}{2mn+m+n}$	$\frac{1}{4}C_c$	$\frac{1}{4}C_c$

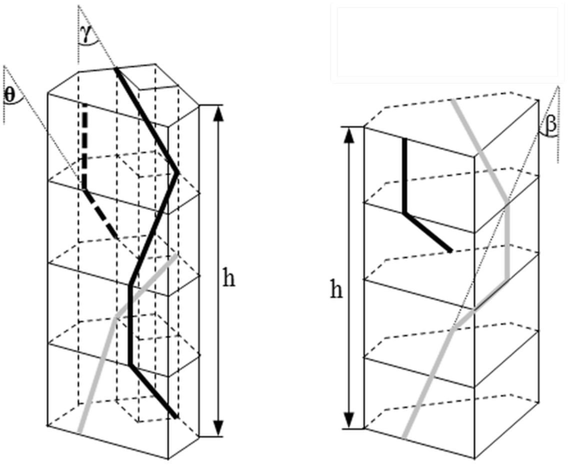

(a) (b)

Figure 4.11.: Braiding angles in a surface cell (a) and in a corner cell (b)

The basic assumption for predicting elastic constants is that each yarn group is treated as transversely isotropic composite individually orientated in the global coordinate system. Thus, mechanical properties of each UD composite are obtained with respect to its local coordinate system 1-2-3 using the *Rule of Mixtures* (ROM) and micro-mechanical equations established by Chamis [148]

$$E_{11} = V_{fn} E_{11f} + (1 - V_{fn})\, E_m \tag{4.49}$$

$$E_{22} = E_{33} = \frac{E_m}{1 - \sqrt{V_{fn}}\left(1 - \frac{E_m}{E_{22f}}\right)} \tag{4.50}$$

$$G_{12} = \frac{G_m}{1 - \sqrt{V_{fn}}\left(1 - \frac{G_m}{G_{12f}}\right)} \tag{4.51}$$

$$G_{23} = \frac{G_m}{1 - \sqrt{V_{fn}}\left(1 - \frac{G_m}{G_{23f}}\right)} \tag{4.52}$$

$$\nu_{12} = V_{fn} \nu_{12f} + (1 - V_{fn})\, \nu_m \tag{4.53}$$

$$\nu_{23} = \frac{E_{22}}{2G_{23}} - 1 \tag{4.54}$$

These semi-empirical equations are the most used and trusted formula in literature [149, 150]. In the above formulas, E_{11} signifies the longitudinal modulus, E_{22} the transverse modulus, ν_{12} the longitudinal Poisson's ratio, ν_{23} transverse Poisson's ratio, G_{12} axial shear modulus and G_{23} transverse shear modulus. The subscripts f and m indicate properties of fibre and matrix, respectively. Each yarn is assumed to have a high UD stiffness in the fibre direction (1) and to be transversally isotropic in the $(2-3)$ directions. Consequently, the stiffness matrix $[C_{ijkl}]_n$ of each UD composite at its local coordinate system is given as

$$\begin{Bmatrix} \sigma_{11} \\ \sigma_{22} \\ \sigma_{33} \\ \sigma_{23} \\ \sigma_{13} \\ \sigma_{12} \end{Bmatrix} = \begin{bmatrix} C_{11} & C_{12} & C_{12} & 0 & 0 & 0 \\ & C_{22} & C_{23} & 0 & 0 & 0 \\ & & C_{33} & 0 & 0 & 0 \\ & sym & & C_{44} & 0 & 0 \\ & & & 0 & C_{66} & 0 \\ & & & 0 & 0 & C_{66} \end{bmatrix} \begin{bmatrix} \varepsilon_{11} \\ \varepsilon_{22} \\ \varepsilon_{33} \\ \gamma_{23} \\ \gamma_{13} \\ \gamma_{12} \end{bmatrix} \tag{4.55}$$

in which $\gamma_{ij} = 2\varepsilon_{ij}$ are the engineering shear strains and

$$C_{11} = \left(1 - \nu_{23}^2\right) \frac{E_{11}}{\Delta}$$

$$C_{12} = C_{13} = C_{21} = C_{31} = \nu_{12} \left(1 + \nu_{23}\right) \frac{E_{22}}{\Delta}$$

$$C_{22} = C_{33} = \left(1 - \nu_{12}^2 \frac{E_{22}}{E_{11}}\right) \frac{E_{22}}{\Delta}$$

$$C_{23} = \left(\nu_{23} + \nu_{12}^2 \frac{E_{22}}{E_{11}}\right) \frac{E_{22}}{\Delta}$$

$$C_{44} = G_{23}$$

$$C_{55} = C_{66} = G_{12}$$

$$\Delta = 1 - \nu_{23}^2 - 2\nu_{12}^2 \frac{E_{22}}{E_{11}} \left(1 + \nu_{23}\right)$$

For the purpose of transforming the stiffness matrix of each UD composite from the local to the global coordinate system transformation matrices for the stress tensor T_σ (Equation 4.56) and for the strain tensor T_ε (Equation 4.57) are established

$$[T_\sigma] = \begin{bmatrix} l_1^2 & m_1^2 & n_1^2 & 2m_1n_1 & 2l_1n_1 & 2l_1m_1 \\ l_2^2 & m_2^2 & n_2^2 & 2m_2n_2 & 2l_2n_2 & 2l_2m_2 \\ l_3^2 & m_3^2 & n_3^2 & 2m_3n_3 & 2l_3n_3 & 2l_3m_3 \\ l_2l_3 & m_2m_3 & n_2n_3 & m_2n_3 + m_3n_2 & l_2n_3 + l_3n_2 & l_2m_3 + l_3m_2 \\ l_1l_3 & m_1m_3 & n_1n_3 & m_1n_3 + m_3n_1 & l_1n_3 + l_3n_1 & l_1m_3 + l_3m_1 \\ l_1l_2 & m_1m_2 & n_1n_2 & m_1n_2 + m_2n_1 & l_1n_2 + l_2n_1 & l_1m_2 + l_2m_1 \end{bmatrix} \tag{4.56}$$

$$[T_\varepsilon] = \begin{bmatrix} l_1^2 & m_1^2 & n_1^2 & m_1n_1 & l_1n_1 & l_1m_1 \\ l_2^2 & m_2^2 & n_2^2 & m_2n_2 & l_2n_2 & l_2m_2 \\ l_3^2 & m_3^2 & n_3^2 & m_3n_3 & l_3n_3 & l_3m_3 \\ 2l_2l_3 & 2m_2m_3 & 2n_2n_3 & m_2n_3+m_3n_2 & l_2n_3+l_3n_2 & l_2m_3+l_3m_2 \\ 2l_1l_3 & 2m_1m_3 & 2n_1n_3 & m_1n_3+m_3n_1 & l_1n_3+l_3n_1 & l_1m_3+l_3m_1 \\ 2l_1l_2 & 2m_1m_2 & 2n_1n_2 & m_1n_2+m_2n_1 & l_1n_2+l_2n_1 & l_1m_2+l_2m_1 \end{bmatrix} \tag{4.57}$$

in which l, m and n are direction cosines defined as cosines of the angles η and ϕ (Equation 4.58).

$$\begin{bmatrix} l_1 & m_1 & n_1 \\ l_2 & m_2 & n_2 \\ l_3 & m_3 & n_3 \end{bmatrix} = \begin{bmatrix} \cos\eta & \sin\eta\cos\phi & \sin\eta\cos\phi \\ 0 & \sin\phi & -\cos\phi \\ -\sin\eta & \cos\eta\cos\phi & \cos\eta\sin\phi \end{bmatrix} \tag{4.58}$$

The stiffness matrix of each UD composite $\left[\bar{C}_{ijkl}\right]_n$ in the global coordinate system X-Y-Z can be derived as

$$\left[\bar{C}_{ijkl}\right]_n = [T_\sigma]_n^{-1}\,[T_\varepsilon]_n\,[C_{ijkl}]_n \tag{4.59}$$

The effective stiffness matrix of the composite $\bar{C}_c$ is obtained by averaging the stiffness matrix based upon their volume contribution

$$\bar{C}_c = \sum V_n \left[\bar{C}_{ijkl}\right]_n \tag{4.60}$$

where V_n is the volume proportion of each UD yarn to the whole composite with $n = (ii, si, ci, is, es, c)$, as listed in Table 4.2. Finally, the stiffness matrix is inverted into the compliance matrix $\bar{S}_c = \left[\bar{C}_c\right]^{-1}$ and elastic constants of the entire four-step braided composite are calculated using the following relations

$$\begin{aligned} E_{xx} &= \tfrac{1}{\bar{S}_{11}} & E_{yy} &= \tfrac{1}{\bar{S}_{22}} & E_{zz} &= \tfrac{1}{\bar{S}_{33}} \\ G_{xy} &= \tfrac{1}{\bar{S}_{66}} & G_{xz} &= \tfrac{1}{\bar{S}_{55}} & G_{yz} &= \tfrac{1}{\bar{S}_{44}} \\ \nu_{xy} &= -\tfrac{\bar{S}_{12}}{\bar{S}_{11}} & \nu_{xz} &= -\tfrac{\bar{S}_{13}}{\bar{S}_{11}} & \nu_{yz} &= -\tfrac{\bar{S}_{23}}{\bar{S}_{22}} \end{aligned} \tag{4.61}$$

The software package Mathematica was again used to implement the outlined analytical models. The procedure to calculate elastic properties of a 4stepWO is exemplarily presented in Appendix A.2.

4.3.2. Two-step braids

The analytical approach for two-step braids is based on the macro-cell model [1]. At the end of one machine cycle the yarn carrier arrangement equals the initial configuration which implies that a braid produced after two steps equals a repetitive unit in the entire structure. Based on microscopic observations yarn dimensions and braid properties were analytically predicted as described below. The necessary input is comprised of the composite width W_c, the composite thickness T_c, the pitch length h_c, the width w_a and the thickness t_a of the axial yarn in the centre, the inclination of the central axial yarn φ as well as the braider yarn thickness t_b and width b. Thus, geometric parameters shown in Figure 4.12 can be derived by means of m and n as

$$W_c = 2t_b + 2Y_c + (m-2)\,Y_e + (m-1)\,Y_g \tag{4.62}$$

$$T_c = 2t_b + 2Z_c + (n-2)\,Z_e + (n-1)\,Z_g \tag{4.63}$$

with

$$a = \sqrt{\left(\frac{w_a}{2}\right)^2 + \left(\frac{t_a}{2}\right)^2}$$

$$\sin\varphi = \frac{w_a t_a}{2a^2}$$

$$Y_c = a\cos\frac{\varphi}{2} + t_m$$

$$t_m = \frac{a}{2}\cos\frac{\varphi}{2}$$

$$Z_c = a\sin\frac{\varphi}{2} + t_n$$

$$t_n = \frac{a}{2}\sin\frac{\varphi}{2}$$

$$Y_e = 2a\cos\frac{\varphi}{2}$$

$$Z_e = 2a\sin\frac{\varphi}{2}$$

The orientation of braider yarns is determining the effective properties of the braid. Placing the macro-cell in a Cartesian coordinate system X-Y-Z, as depicted in Figure 4.13, and projecting the yarns on the YZ- as well as XZ-plane the yarn orientations can be identified. Consequently, projected lengths of yarn segments inclined to the X-Y-Z axes L_{pi}, parallel to the XY-plane L_{pxy} and parallel to the XZ-plane L_{pxz} can be derived

$$L_{pi} = 2(m-1)(n-1)\left(a + \frac{bf_b}{\sin\varphi}\right) \tag{4.64}$$

$$L_{pxy} = 2[(n-1)t_m + 2(m-1)a\cos\frac{\varphi}{2}] \tag{4.65}$$

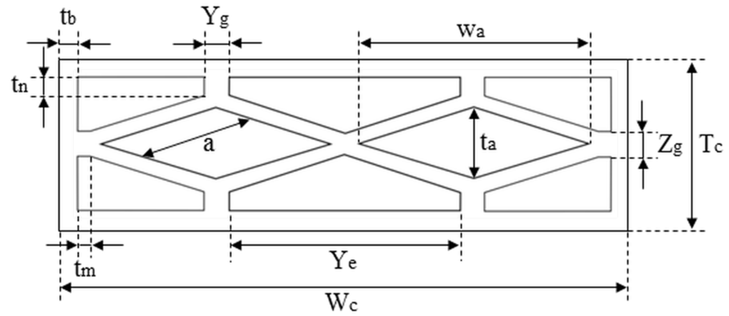

Figure 4.12.: Idealisation of cross-section in consolidated two-step braid with geometric parameters

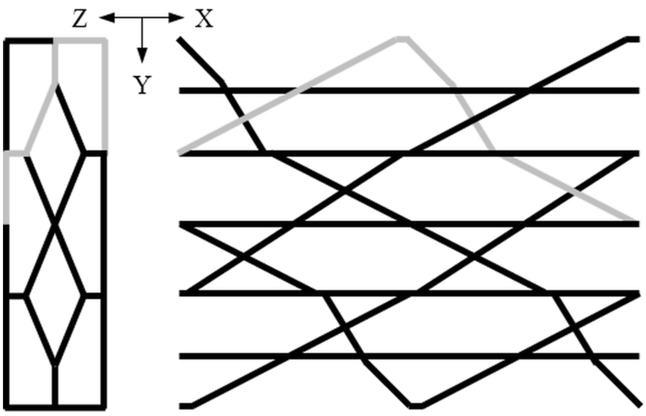

Figure 4.13.: Schematic projections of braider yarns onto the YZ-plane and the XY-plane after one machine cycle with highlighted braider 1

$$L_{pxz} = 2[2mt_n + (n-1)a\sin\frac{\varphi}{2}] \tag{4.66}$$

The path of yarn carriers at the corners of a two-step braid with rectangular cross-section is shorter than the path through the array. Because all braider yarns must exhibit the same pitch length after each step, the inclination angles of the braider yarns vary. Braider yarns at the corner have smaller inclinations angles [1]. For this reason, variations of the angle along the pitch length are considered by calculating an averaged braiding angle α'

$$\alpha' = \tan^{-1}\left(\frac{2L_{pyz}}{(2m+n+1)\,h_c}\right) \tag{4.67}$$

with $L_{pyz} = L_{pi} + L_{pxy} + L_{pxz}$, which is the projected length of the braider yarn onto the YZ-plane. Thus, the volume of the braider yarns V_b can be derived by

$$V_b = V_{bi} + V_{bxy} + V_{bxz} \tag{4.68}$$

with

$$V_{bi} = \frac{L_{pi}}{\sin\alpha'} b^2 f_b$$

$$V_{bxy} = \frac{L_{pxy}}{\sin\alpha'} b^2 f_b$$

$$V_{bxz} = \frac{L_{pxz}}{\sin\alpha'} b^2 f_b$$

As seen in Figure 4.6, axial yarns take three cross-sectional shapes. The total volume of all axial yarns V_a can be computed as follows

$$\begin{aligned} V_a &= \Big((mn-2)\, a^2 \sin\varphi + (2m-4)\, t_n Y_e + (2n-4)\, t_m Z_e \\ &\quad +4\left(t_n Y_c + (Z_c - t_n)\, t_m\right)\Big)\, h_c \end{aligned} \tag{4.69}$$

The macro-cell encompasses the entire cross-section by one pitch length. Hence, its volume V_t can be calculated as

$$V_t = W_c T_c h_c$$

The total fibre volume in a two-step braid is the sum of braider and axial volumes. Fibre volume fractions of each yarn group V_{fn} are given by

$$V_{fn} = \frac{V_n}{V_t} \tag{4.70}$$

The subscript n represents the braider and axial yarn groups with $n = (bi, bxy, bxz, a)$. The stiffness matrix $\left[\bar{C}_{ij}\right]_n$ of each yarn group in the global coordinate system X-Y-Z is obtained by transforming the stiffness matrix $\left[C_{ij}\right]_n$ in the local coordinates according to Equation 4.55 and 4.59 using the direction cosines of the angles β and γ (Equation 4.71) between the local axes and the global coordinate system of the RVE, as depicted in Figure 4.14.

$$\begin{bmatrix} l_1 & m_1 & n_1 \\ l_2 & m_2 & n_2 \\ l_3 & m_3 & n_3 \end{bmatrix} = \begin{bmatrix} \cos\beta\cos\gamma & \cos\beta\sin\gamma & \sin\beta \\ -\sin\gamma & \cos\gamma & 0 \\ \sin\beta\cos\gamma & \sin\beta\sin\gamma & -\cos\beta \end{bmatrix} \tag{4.71}$$

The X-direction coincides with the braiding axis, which forms the angle α with the braider yarn. Yarn orientations of each braider type are listed in Table 4.6. The orientations of the inclined braider yarns can be expressed in terms of α' and f_a

$$\beta = \arctan \frac{f_a \sin\alpha'}{\sqrt{1 + f_a^2 \cos^2\alpha'}} \tag{4.72}$$

$$\gamma = \arctan \frac{\tan\alpha'}{\sqrt{1 + f_a^2}} \tag{4.73}$$

The effective stiffness matrix of the macro-cell in the global coordinate system is computed using the volume averaging method as shown in Equation 4.60, where V_n for $n = (bi, bxy, bxz, a)$ are the fibre volume fractions (Equation 4.70) of each yarn group

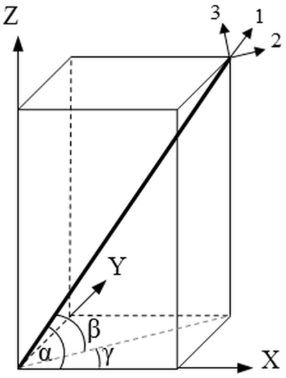

Figure 4.14.: Schematic illustration of a spatially oriented yarn segment in a two-step braid

Table 4.6.: Yarn orientations in a two-step braid

Type of braider yarn	Angles (β, γ)
Axials	$(0, 0)$
Braiders inclined to X-Y-Z axes	(β, γ)
Braiders parallel to XY-plane	$(0, \alpha')$
Braiders parallel to XZ-plane	$(\alpha', 0)$

to the whole composite. The compliance matrix is calculated using $\bar{S}_c = \left[\bar{C}_c\right]^{-1}$ and the elastic constants of the two-step braided composite are determined by Equation 4.61.

5. Numerical modelling

5.1. Pultruded profiles under lateral loading[3]

The pultruded box beam sections tested under lateral compression, as described in Section 3.1, were used to calculate their quasi-static response in nonlinear analyses using the FE software ABAQUS Standard with implicit time integration. 3D FE models were developed using the built-in damage model to study the influence of material properties on the mechanical performance. This damage model is based on criteria proposed by Hashin to predict failure onset in brittle fibre-reinforced composites [3, 151]. The implementation of the Hashin damage model demands the use of elements with plane stress formulation. For a layer-wise failure analysis and its contribution to the overall performance, a 3D geometric model with 22200 hexahedral continuum shell elements was created. An analytical rigid surface is used to model the circular loading block. The value for the vertical motion of the rigid surface is taken from the displacement data from the experimentally tested profile sections. The displacements of the bottom surface of the FE model is fixed in loading direction. A typical mesh definition for computations is shown in Figure 5.1(a). According to experimental results described in Section 6.1.1 the corners are the critical spots; hence the mesh was locally refined at the junctions between flanges and webs: the mesh density in the corners was 8x increased. A further FE model of *Configuration 1* was created to analyse the influence of pre-existing defects on the material behaviour. As the combination of a 45° corner crack and surface rupture induced always fractures up to complete failure of a junction, an elliptic eye and a surface cut were integrated in the upper left corner of the model. The elliptic defect is representing an enclosed void due to wrinkling during processing of the inner CSM layer. The dimensions of the eye in the FE model are 0.5 mm and 0.1 mm, major and minor ellipse axis respectively, see Figure 5.1(b). The triangular surface cut along the section width had a width of 0.1 mm and a depth of 0.15 mm, as shown in Figure 5.1(c).

Hashin considers four different modes of failure, distinguishing between fibre and matrix as well as tension and compression failure [151, 152], see Equations 5.1-5.4. σ_{11}, σ_{22} and τ_{12} are components of the effective stress tensor used to evaluate failure initiation criteria, X_t, X_c, Y_t, Y_c, S_l and S_t denote the longitudinal (X), transverse composite strengths (Y) under tensile (subscript t) and compressive loading (subscript

---

[3] Section is reproduced with adaptations from "F. Regel, F.W.J. van Hattum and G.R. Dias. A numerical and experimental study of the material properties determining the crushing behaviour of pultruded GFRP profiles under lateral compression. *Journal of Composite Materials*, 47(14):1749 - 1764, 2013"

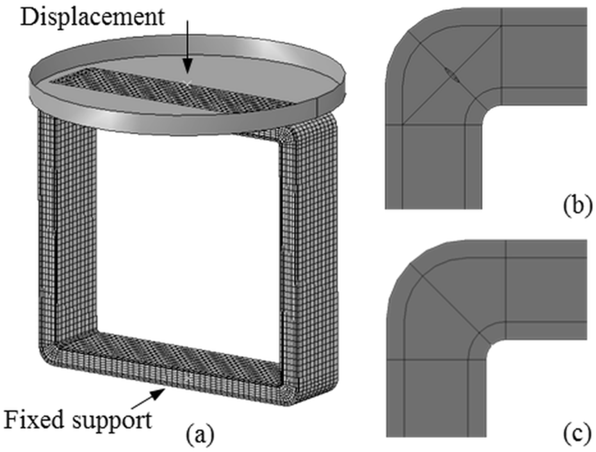

Figure 5.1.: FE mesh model of profile section (a), elliptic eye (b) and surface cut (c)

c) as well as the longitudinal and transverse shear strength (S), respectively.

Tensile fibre failure ($\sigma_{11} \geq 0$)

$$f_{ft} = \left(\frac{\sigma_{11}}{X_t}\right)^2 + \left(\frac{\tau_{12}}{S_l}\right)^2 \geq 1 \tag{5.1}$$

Compressive fibre failure ($\sigma_{11} < 0$)

$$f_{fc} = \left(\frac{\sigma_{11}}{X_c}\right)^2 \geq 1 \tag{5.2}$$

Tensile matrix failure ($\sigma_{22} \geq 0$)

$$f_{mt} = \left(\frac{\sigma_{22}}{Y_t}\right)^2 + \left(\frac{\tau_{12}}{S_l}\right)^2 \geq 1 \tag{5.3}$$

Compressive matrix failure ($\sigma_{22} < 0$)

$$f_{mc} = \left(\frac{\sigma_{22}}{2S_t}\right)^2 + \left[\left(\frac{Y_c}{2S_t}\right)^2 - 1\right]\frac{\sigma_{22}}{S_l} + \left(\frac{\tau_{12}}{S_l}\right)^2 \geq 1 \tag{5.4}$$

Kachanov [153] proposed that damage propagation can be characterised by degradation of material stiffness. The damage evolution within ABAQUS is based on the extended damage model for elastic-brittle fibre-reinforced composites, proposed by Matzenmiller et al. [154], where the reduction of stiffness matrix coefficients is controlled by damage variables that can take values between zero (undamaged state) and one (fully damaged state) [3]. When the stress state is determined and the onset of degradation is evaluated for each material point, the material response is computed from

$$\sigma_{ij} = \left[\bar{C}_{ijkl}\right]_d \varepsilon_{kl} \tag{5.5}$$

Table 5.1.: Fracture energies and viscosity coefficients [3]

Parameter	Fracture energy [Nmm^{-1}]	Viscosity [s]
Fibre failure	12.5	0.001
Matrix failure	1	0.005

where ε_{kl} is the strain tensor and $\bar{C}_d$ is the stiffness matrix, that reflects any damage and is obtained as [3]

$$\bar{C}_d = \frac{1}{D}\begin{bmatrix} (1-d_f)\,E_{11} & (1-d_f)\,(1-d_m)\,\nu_{21}E_{11} & 0 \\ (1-d_f)\,(1-d_m)\,\nu_{12}E_{22} & (1-d_m)\,E_{22} & 0 \\ 0 & 0 & (1-d_s)\,GD \end{bmatrix} \tag{5.6}$$

where $D = 1-(1-d_f)\,(1-d_m)\,\nu_{12}\nu_{21}$, d_f, d_m and d_s denote the current state of fibre, matrix and shear damage, respectively. E_{11}, E_{22} and G_{12} represent the undamaged material moduli and ν_{12}, ν_{21} the undamaged Poisson's ratios. The stiffness degradation causes stress redistributions and leads to higher stress states which in combination with degraded material constants lead to failure. The overall damage variables d_f, d_m and d_s are derived from damage variables corresponding to the four failure modes d_f^t, d_f^c, d_m^t and d_m^c as explained in [3, 151]. The increase of these damage variables, based on the approach proposed by Camanho and Davila [155] for modelling interlaminar delamination using cohesive elements, is governed by equivalent displacements that are calculated during the damage process from dissipated fracture energies G_c defined for each failure mode [3]. To improve convergence problems in the softening regime, the ABAQUS damage model offers a viscous regularization scheme, which causes the tangent stiffness matrix of the softening material to be positive definite for sufficiently small time increments [151]. Hence, the response of the damaged material is computed using regularized damage variables from

$$\frac{\partial \Delta\sigma}{\partial \Delta\varepsilon} = \bar{C}_d + \left[\left(\frac{\partial \bar{C}_d}{\partial d_m^{\nu}}\right) : \varepsilon \left(\frac{\partial d_m}{\partial f_m}\frac{\partial f_m}{\partial \varepsilon}\right) + \left(\frac{\partial \bar{C}_d}{\partial d_f^{\nu}}\right) : \varepsilon \left(\frac{\partial d_f}{\partial f_f}\frac{\partial f_f}{\partial \varepsilon}\right)\right]\frac{\Delta t}{\eta + \Delta t} \tag{5.7}$$

As the value of fracture energy and viscosity influence the damage propagation, values presented in Lapczyk's study [3] which showed good correlations between numerical and experimental results were applied, see Table 5.1.

Pultruded composites are heterogeneous material systems with nonlinear behaviour due to the fact that these profiles are mainly reinforced in axial direction to carry predominant axial loads [156]. As mentioned before, even layer thicknesses are used

Table 5.2.: Material properties of composite constituents

Material	E	G	ν	ρ	X_t	X_c
	[GPa]			[kgm^{-3}]	[MPa]	
E-glass fibre	73	30	0.22	2600	2000	600
Polyester resin	3.5	1.3	0.35	1300	50	150

for numerical modelling. Glass fibres and resin matrix are singularly considered as homogeneous, linearly elastic, isotropic materials and are assumed to have the same values in all layers. The matrix volume is defined as a collective medium that includes additives along with voids and microcracks. Knowing the material data of glass fibre reinforcement and polyester resin in Table 5.2, the material properties of unidirectional, bidirectional and multidirectional layers were derived with micromechanics equations based on the ROM, using the fibre volume fractions obtained from calcination tests and given in Table 6.1 in Chapter 6. Young's moduli were estimated using an extended rule-of-mixtures

$$E_c = \eta_l \eta_o V_f E_f + (1 - V_f)\, E_m \tag{5.8}$$

where E_c, E_f, E_m denote moduli of the composite, the fibre and the matrix, respectively, η_l denote the fibre length distribution factor and η_o the fibre orientation distribution factor. A fibre length distribution factor of 1 for continuous fibres, based on the equation of Cox [157], is used for all layers. According to the equation proposed by Krenchel [158] fibre orientation distribution factors of 1 for unidirectional layers in fibre direction, 0 for unidirectional layers perpendicular to the fibres, 0.25 for biaxial fabric with ±45° fibre orientation and 3/8 for random in-plane layers such as the CSM were applied. The in-plane shear moduli were predicted using an equation proposed by Huber [159]. Equations used for the estimation of longitudinal composite strengths under tension and compression are modified rules-of-mixtures. As the tensile failure strain, the ratio of tensile strength to longitudinal Young's modulus, for glass fibres is bigger than the tensile failure strain of polyester resin only the fibres contribute to the longitudinal tensile strength of the composite and can be calculated using [160]

$$X_t = \eta_o V_f X_f^t \tag{5.9}$$

where X_f^t denote the longitudinal tensile strength of the fibres. Similar to the equation for the tensile strength, the longitudinal compressive strength can be calculated for the case that the compressive fibre strain, the ratio of compressive strength to longitudinal Young's modulus, is less than the matrix strain by using [160]

$$X_c = \eta_o V_f X_f^c + (1 - V_f)\, E_m \frac{X_f^c}{E_{1f}} \tag{5.10}$$

where X_f^c, E_m and E_{1f} denote the compressive strength of the fibre, the Young's

Table 5.3.: Material strengths used in the FE analysis

N°	Layer	X_t	X_c	Y_t	Y_c	$S_t = S_c$
				[MPa]		
1	CSM outer	153	69			
	UD	1095	342	50	150	29
	CSM inner	144	66			
2	CSM outer	83	50			
	±45° outer	188	74			
	UD	1133	352	50	150	29
	CSM inner	138	65			
	±45° inner	221	82			

modulus of the matrix and the longitudinal Young's modulus of the fibres, respectively. The transverse composite material properties Y_t and Y_c were assumed to be equal to the equivalent property of the matrix material. Moreover, it is assumed that the shearing capacity of the composite is matrix dominated, hence longitudinal and transverse shear strengths are derived from

$$S_l = S_t = \frac{Y_m^t}{\sqrt{3}} \tag{5.11}$$

based on the von Mises shear stress criterion [160], where Y_m^t denotes the tensile strength of the matrix. The obtained and implemented material strengths are reported in Table 5.3. A further objective of this FE analysis is to identify material parameters for improving the fracture toughness of pultruded GFRP profiles. From the above it can be observed that many parameters depend on the tensile matrix strength, thus this property becomes a critical parameter for the overall fracture toughness. Out-of-plane reinforcements are one obvious way to increase the transverse strength, and thus improve fracture toughness. For this purpose, analyses to simulate the effect of out-of-plane reinforcements were conducted with single tensile matrix strength $1{*}Y_m^t$ and a tripled value $3{*}Y_m^t$ leading to tripled shear strengths, as well.

5.2. FE modelling study[4]

The micro-structure of textile reinforced composites is generally complex in nature. Therefore, various FE techniques have been proposed to simplify mechanical analyses of composite structures. Most of the models are based on the definition of RVE geometries

---

[4] Parts of section are reproduced with adaptations from "F. Regel, G.R. Dias and F.W.J. van Hattum. Numerical modelling approach for 3D braided composites under lateral loading, Proceedings of ECCM15 - 15th European Conference on Composite Materials, Venice, Italy, 2012"

and the use of a homogenisation approach. The elastic properties obtained in this way are used as material input in an multi-scale modelling approach for single finite elements in the composite structure [161]. This approach is feasible as long as the RVE is small compared to the structure.

A 3D model of a RVE can be created by two different approaches: (a) resin pockets are obtained by subtracting yarn volumes from a matrix volume, thereafter modelled yarn volumes and resin pockets are assembled, and (b) resin as well as yarn volumes are obtained by successive partitioning. The difficulties to define material orientations, poor mesh qualities as well as high computational costs are well-known drawbacks of using 3D solid elements. As aforementioned in Section 2.3.2, Cox et al. [101] developed a FE method which uses two-node line elements to represent axial properties of yarns, while transverse and shear properties are represented by the matrix using solid elements. Another superposition technique proposed by Jiang et al. [112] utilises 3D solid elements for the matrix as well as the fibre reinforcements. Even though 3D modelling of the yarns allows for a more accurate representation and analysis of the textile architecture the DST method is no ease for modelling 3D braids. The fundamental difficulty in modelling the intricate architecture of 3D braids is to build the geometry without interpenetrations at crossing yarns. For this reason a superposition technique based on the BM is proposed for the simulation of 3D braid reinforced composites. Instead of modelling the yarns and the resin pockets among the yarns explicitly and interrelated, the constituents are separately modelled. The BM facilitates modelling and additionally needs less computational effort compared to a solid element model.

Nevertheless, the textile architecture must be represented in correspondence to the real preform structure. Yarns can be locally regarded as UD composites. Effective elastic properties of a UD composite can be predicted numerically as well as analytically using various approaches, such as the generalised method of cells developed by Aboudi [162] for metal matrix composite materials, semi-empirical models by Halpin-Tsai [163] or Chamis [148] and homogenisation models by Mori-Tanaka [164].

To assess the capability of this method and verify for 3DBRCs different simplified models were first investigated. 1D element models of UD reinforced composites with different straight yarn configurations were compared with 3D solid element models. Six different case studies were considered, the first four models were used for verification of the modelling approach to calculate elastic properties. The numerical results of the single yarn models were additionally compared with results from analytical models, i.e. Mori-Tanaka for an infinite long inclusion and Halpin-Tsai, to validate the predictability of the BM. The overall aim of this study was to develop a modelling approach for 3DBRCs under lateral loads. Therefore, the last models were used to examine the superposition technique for yarn reinforced composites subjected to flexural loading.

Generally fibre architectures are designed such to be aligned with expected loads and the BM enables the prediction of the structural response. For through-thickness loads and in the case fibres are not aligned with loads properties of the matrix material are more important [165]. Xu et al. [102] indicated that the definition of elastic constants for the effective medium have to be tested and compared with experiments. For this reason the studies were extended by a comparison between a 1D model using the ROM as formulated by Cox et al. [101] and modified models using equations proposed by Chamis [148] and Halpin-Tsai [163]. All numerical calculations are executed with the FE software ABAQUS Standard.

The FE meshes of yarns and matrix material in the 1D element model were generated independently. Node coordinates and element definitions of yarns in the 1D FE models were created by means of Python codes and imported into ABAQUS. The yarns were treated as 1D truss elements (T3D2) and for comparison as 1D beam elements (B33) to represent their axial stiffness. A truss element is assumed to be straight, obey the Hooke's law, but just supports axial loads. Modelling with truss elements in ABAQUS requires only the assignment of a cross-sectional area for each yarn. The B33 beam element uses the Euler-Bernoulli beam theory and requires a specific definition of the cross-sectional geometry along the yarn length. A circular yarn cross-section was assumed and implemented. The mesh of the resin material, from now on called effective medium, was made of eight-node linear hexahedral elements (C3D8R) which were generated inside ABAQUS. Yarns and matrix were joined by means of multi-point constraints, using the embedded element function incorporated in the software. The embedded element constraint relates the nodal degrees of freedom (DOF) of both meshes. Yarn meshes are placed and embedded inside the hosting matrix mesh. This implies that the translational DOFs of an embedded node are constrained to the interpolated DOFs of the host element in which it lies.

The yarns have solely longitudinal elastic properties, which can be estimated by the ROM [101]

$$E_x^{UD} = V_{f_{UD}} E_f + \left(1 - V_{f_{UD}}\right) E_m \tag{5.12}$$

where $V_{f_{UD}}$ is the volume fraction or packing factor of the fibres within a single yarn and E_f and E_m are the Young's moduli of fibres and resin, respectively. The axial elastic modulus of each truss element in the BM is given by

$$E^{Yarn} = E_x^{UD} - E^{Medium} \tag{5.13}$$

The Young's modulus of the effective medium needs to be subtracted from the Young's modulus of the yarns to avoid double counting of the matrix dominated stiffness contribution due to the volumetric overlap. The effective medium is assumed to be homogeneous and isotropic in the elastic regime similar to epoxy resin. Its properties, such as the Young's modulus of the effective medium equals the transverse modulus of a UD composite [102, 165] and is defined by the ROM as

$$\frac{1}{E^{Medium}} = \frac{V_f}{E_{f_2}} + \frac{1 - V_f}{E_m} \tag{5.14}$$

where E_{f_2} and E_m are the transverse moduli of fibres and resin, respectively. The

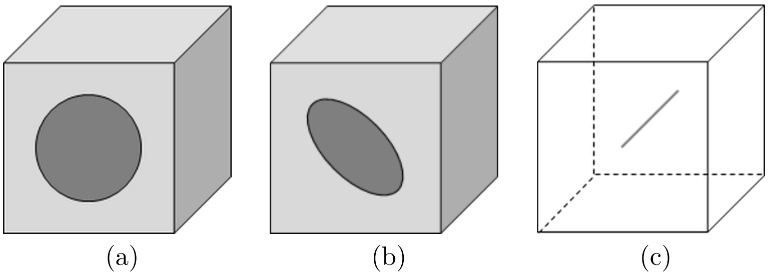
(a) (b) (c)

Figure 5.2.: UD yarn models used to verify modelling approach for prediction of elastic properties: (a) 3D circular UD yarn model, (b) 3D elliptical UD yarn model and (c) 1D truss model

Poisson's ratio and the shear modulus, are given as [101]

$$\nu^{Medium} = V_f \nu_f + (1 - V_f)\, \nu_m \tag{5.15}$$

$$\frac{1}{G^{Medium}} = \frac{V_f}{G_{f_{12}}} + \frac{1 - V_f}{G_m} \tag{5.16}$$

where ν_f and ν_m are the Poisson's ratios and $G_{f_{12}}$ as well as G_m the shear moduli of fibres and resin matrix, respectively. In the first modified 1D FE model Equations 5.14 and 5.16 for Young's modulus and shear modulus of the effective medium were replaced by Equations 4.50 and 4.51 described in Section 4.3.2, respectively. In the second modified 1D FE model based on Halpin-Tsai the transverse modulus, the in-plane and the out-of-plane shear moduli were obtained as follows

$$\frac{M}{M_m} = \frac{1 + \xi \eta V_f}{1 - \eta V_f} \tag{5.17}$$

with $\eta = (\frac{M_f}{M_m} - 1)/(\frac{M_f}{M_m} + \xi)$, where M stands for either the transverse or shear modulus of fibres and matrix. ξ is equal to 2 for the transverse and the out-of-plane shear moduli and equal to 1 for the in-plane shear modulus.

The first and the second continuum element model consisted of a single glass fibre yarn in an epoxy matrix cube. The difference between both models was the cross-sectional yarn shape, namely a cylindrical and an elliptical cross-section, as shown in Figure 5.2. The aim of this comparison was to analyse the influence of different yarn cross-sections as the truss model considers solely a general cross-sectional area but no geometric specifications. The elliptical yarn cross-section with an aspect ratio of 0.5 was inclined at an angle of 45°. The yarns in this study had a linear density of 2400 tex, a density of 2.6 g/cm^3 and a yarn packing factor of 0.75 was assumed. Five different V_f (10%, 20%, 35%, 45% and 60%) were considered to investigate the proposed modelling technique. The dimensions of the yarn were maintained while the dimensions and volume of the matrix are altered. Further material properties of the constituents used are shown in Table 4.1. The third and the fourth model were two different configurations of ten UD yarns with a V_f of 10% and 45%, respectively, as

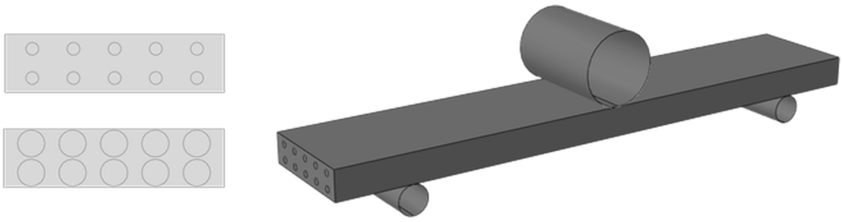
(a) (b)

Figure 5.3.: UD yarn models used to verify modelling approach for flexural loading: (a) Configuration of 10 UD yarns with 10% and 45% V_f, (b) 3D model of flexural specimen

shown in Figure 5.3. Width and thickness of the matrix cube were defined according to ISO178 [133] as 15 mm and 4 mm, respectively. The diameters of all ten yarns were equal and derived by means of the given V_f. The higher V_f in the fourth model was obtained by an increased yarn diameter. Similar to the first two case studies three different superposition models were created. Properties of yarns and effective medium in these 1D FE models were based on formulations from Cox, Chamis and Halpin-Tsai. Periodic boundary conditions were applied to all models and elastic properties were calculated as described in the upcoming Section 5.4. The fifth and the sixth model were flexural specimens with a length of 80 mm according to ISO178 [133]. The dimensions of the loading nose and supports were also given by the standard. Frictionless surface-to-surface contacts were used between the impactor, the supports and the specimen. Static analyses were used and a displacement of 5 mm was applied to all specimens. The X-axis in each described case study was aligned with the fibre direction, the Y- and Z-axis were perpendicular to the fibres and correspond to the width and thickness, respectively. The specimen movement was constrained in the Y-direction as well as the movement in the X-direction of the peripheral nodes at the specimen centre.

Yang and Cox [104,105] considered and resumed from experimental observations that all failure mechanisms in textile reinforced composites can be related to a length scale which is comparable to characteristic yarn dimensions. A coarse mesh cannot follow variations on the scale of a single yarn whereas a finer mesh causes an unnecessary rise of degrees of freedom and computational costs [103]. The authors obtained accurate predictions using meshes at the lowest level of refinement, which keeps the model simple and computational costs low. The authors [104] showed in numerical studies with different meshing orders that predictions of local strains are mesh independent and valuable for failure analyses when stresses and strains are averaged over a cuboidal volume, a so-called gauge volume, which is equal to or greater than about half the yarn width in the in-plane directions and equal to the yarn thickness in the out-of-plane direction. Accurate predictions were obtained for meshes at the lowest level of refinement, which keeps the model simple and computational costs low.

Convergence analyses were conducted using the strain energy of the whole model as solution variable. Two methods are generally available, the p- and the h-method. The p-method refers to an increase of the element order while the mesh is not changed. On the contrary the h-method, also known as mesh convergence, signifies that the mesh is stepwise refined until the solution approaches the analytical solution of the governing equations. Mesh sensitivity studies were selected to analyse the influence of different element sizes on the elastic and flexural properties. A dependence of the mesh size on the yarn diameter is selected to find a general definition for a recommended element size. The 3D FE models reinforced with single UD yarns use reasonable fine meshes. In the first and the second case study the yarn geometry and thus the number of elements were retained. Analyses of the 1D FE models with single UD yarns showed no influence of the element size on the properties. The initial element size for yarns and effective medium in the 3D and 1D FE models of the third and fourth case study was equal to twice the yarn diameter (2d). The element size was successively decreased to fractions of the diameter (d, d/2, d/4). The length of each 1D element was similarly altered. Although a general element size is assigned, the actual element lengths are dependent on the composite dimensions. The yarn diameter in the model with a V_f of 45% is about twice as big as the yarn diameter in the model with a V_f of 10%. To exemplify the differences between element sizes in both models, an element size of 2d in the 10% model equals approximately an element size of d in the 45% model. Thus, the initial element size of 2d and d, respectively, results in two elements per thickness in the 1D element models. The minimum selected element sizes of d/2 in the 10% model and d/4 in the 45% model result in nine elements per thickness.

5.3. FE model of 3DBRC[5]

The periodic structure of braids makes it sufficient to investigate the elastic properties of a representative volume. The identification and description of a RVE is crucial for mechancial analyses and yet difficult especially for 3D preforms. As described in Section 4.3 Cartesian braids can be divided in multiple cells. Hence, selecting the smallest RVE which incorporates several volumes is impossible [146]. As the structural contribution of exterior cells is generally expected to be small compared to interior cells, several authors considered in their models solely interior regions [97–99, 146]. However, Li et al. [145] showed that with respect to their volume proportions surface regions cannot be neglected for small m and n. For this reason, in contrast to a unit cell approach analyses in this study are conducted using Byun's macro-cell [1] as RVE. The volume of a macro-cell encompasses the entire preform cross-section by the pitch length obtained after a completed machine cycle. As found in literature (Section 2.3.2) for all modelling approaches, a FE analysis of a RVE is performed according to the following successfully proven method

(a) Dividing textile composite into RVE

---

[5] Parts of section are reproduced with adaptations from "F. Regel, G.R. Dias and F.W.J. van Hattum. Numerical modelling approach for 3D braided composites under lateral loading, Proceedings of ECCM15 - 15th European Conference on Composite Materials, Venice, Italy, 2012"

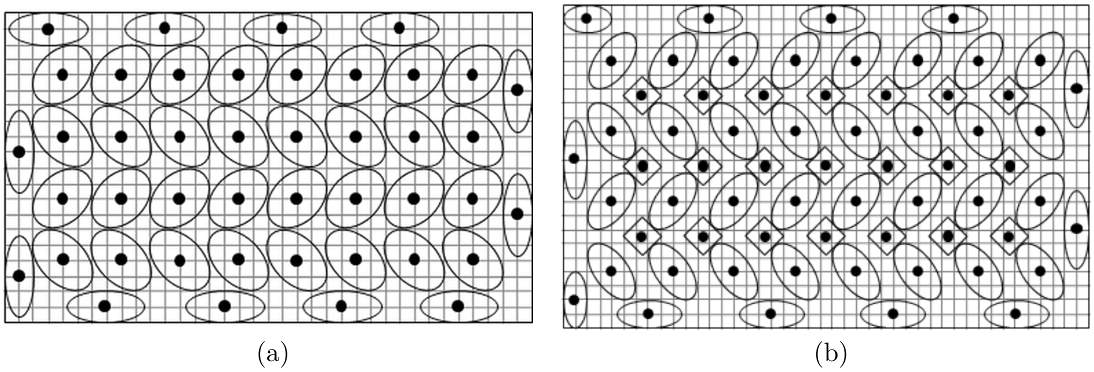
(a) (b)

Figure 5.4.: Schematic views of node arrays in four-step braid reinforced composites: 4stepWO (a), 4stepWI (b)

(b) Creating geometric model of RVE

(c) Applying loads (typically three tensile and three shear cases) in the principal directions and boundary conditions on RVE

(d) Calculating elastic properties of RVE using averaging and homogenisation techniques

With respect to the complex geometry of 3D braided reinforcements a conventional modelling procedure becomes a time-consuming task. Moreover, methods to create a 3D FE model based on processing is computationally expensive [166]. By means of the subsequently described procedure a 1D element model of the yarn architecture is obtained for the mechanical analysis of each 3DBRC. The wavy structure of each yarn is idealised by a number of linear 1D elements. The yarn centre lines are assumed to follow braiding scheme paths. The approach in this study can be summarised as

(a) Microscopic analysis of 3DBRC cross-section

(b) Calculation of yarn centroid and node positions based on geometric description

(c) Calculation of yarn path coordinates based on carrier movements

(d) Construction of 1D element model with node coordinates

Cross-sections of preform and composite vary dependent on jamming condition and mould dimensions. Therefore, yarn arrays are based on the cross-sections of consolidated preforms derived from microscopy and described in Section 4.2. The node coordinates of axial and braider yarns were generated outside ABAQUS by means of Python codes. The coordinates of braider yarn paths were calculated such that the movements of the track and column machine are related to the braid architecture using specified node arrays.

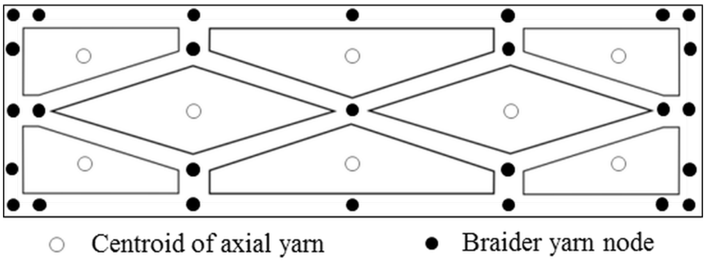

Figure 5.5.: Schematic view of node array in two-step braid reinforced composite

The node array and the position of braider yarn centroids in four-step braids are idealised based on microscopic views, see in Figure 5.4. The entire cross-section can be divided into equally sized rectangles which define the number of nodes and their position in the array. Each braider yarn is shifted similar to the row and column movements of braider carriers on the machine bed. Distances between the centroids are given in Equations 4.37 - 4.40 and hence node distances as well as Y, Z coordinates can be derived. The X coordinate is dependent on the number of steps N_{Steps} necessary to obtain one machine cycle. The number of steps varies from the number of braiding steps as it is defined by the node array. In case of a 4stepWO four steps are needed to move a braider carrier during one braiding step. Consequently, 16 steps are necessary for one machine cycle and each node coordinate in the longitudinal direction can be derived from

$$\Delta x = \frac{h}{N_{Steps}} \tag{5.18}$$

$$X^i = \Delta x \, (i - 1) \tag{5.19}$$

in the range $1 \leq i \leq (N_{steps} + 1)$. In case of a 4stepWI five steps are needed to move a braider during one step, thus 20 steps are necessary to conclude one machine cycle. The coordinates of the peripheral yarns are calculated in two steps. In the first calculation step the peripheral yarns are aligned with the other braider yarns arranged in rows and columns. In the second step the peripheral yarns are compressed and shifted to positions as indicated in Figure 5.4.

In comparison to braider yarns axial yarns have two stationary coordinates which are defined by its centroid. Thus the area and the coordinates Y, Z of each centroid can be computed. The X coordinate is dependent on the braid length, the number of elements $N_{Elements}$ and consequently the number of nodes in the longitudinal direction and can be derived from

$$\Delta x_a = \frac{h}{N_{Elements}} \tag{5.20}$$

$$X_a^i = \Delta x_a \, (i - 1) \tag{5.21}$$

where Δx_a denotes the element length, h the pitch length and i the i-th node in the range $1 \leq i \leq (N_{Elements} + 1)$.

In case of a two-step braid axial yarns are assumed to be polygons as described in Section 4.3.2. The coordinates of axial yarns are similarly derived as explained above. The area and the coordinates Y, Z of each centroid can be computed using dimensions given in Equations 4.62 and 4.63. The Y and Z coordinates of the braider yarns are defined by a specified node array and can be similarly computed using derived braid dimensions. Figure 5.5 depicts the node array and the initial position of each braider yarn. The defined node array represents the minimum number of nodes required to move a braider through the axial yarn array and to reproduce the topology of the reinforcement. A higher number could be chosen but would betray the concept of the FE model [101]. The number of nodes in the longitudinal direction is defined by the number of shifts necessary to accomplish one machine cycle as shown in Figure 2.2. For the [3x2] braid in this study eight steps are needed resulting in nine nodes. The X coordinates can be determined by means of 3D trigonometry using the Y and Z coordinates of each node as well as the averaged braiding angle α' obtained with Equation 4.67

$$\Delta x_b = \frac{\sqrt{\Delta y^2 + \Delta z^2}}{\tan \alpha'} = \frac{\sqrt{\left(Y^{i+1} - Y^i\right)^2 + \left(Z^{i+1} - Z^i\right)^2}}{\tan \alpha'} \tag{5.22}$$

$$X_b^i = \Delta x_b \, (i-1) \tag{5.23}$$

in the range $1 \leq i \leq (N_{steps} + 1)$.

Moreover, the Python code is used to generate ABAQUS input files containing element numbers with corresponding node connectivity as well as cross-sectional yarn areas. These files are then integrated into the main ABAQUS input file which defines the solid element model of the effective medium, the embedded constraints and boundary conditions. Visualisation of the yarn paths in the FE model of the 4stepWO and 4stepWI are presented in Figure 5.6 and 5.7, respectively. The size of the depicted planes are equal to the outer dimensions of the effective medium. An example of a Python code to calculate yarn coordinates and generate respective input files for a 4stepWO is presented in Appendix B.1.

As aforementioned in Section 3.2.1 a further aim of this study is to design and analyse a virtually braided box beam profile. The four-step braiding process without additional axial yarns is selected for this implementation. The pultruded box beam in Section 3.1 is 70 mm wide, 70 mm deep and has a laminate thickness of about 5 mm. In order to exclude geometric effects the same dimensions are used for the braid reinforced profile section. Based on assumed 4stepWO dimensions (a κ of 0.7, an f_b of 2 and an φ of 45°), a [55,3] braid configuration is selected to fabricate the flanges and webs of the desired profile. Consequently, the total number of yarns necessary to produce such a four-step braid can be calculated using the following formulas (Equations 5.24 and 5.25). For the case that the number of horizontal columns m_h and vertical columns m_v are even,

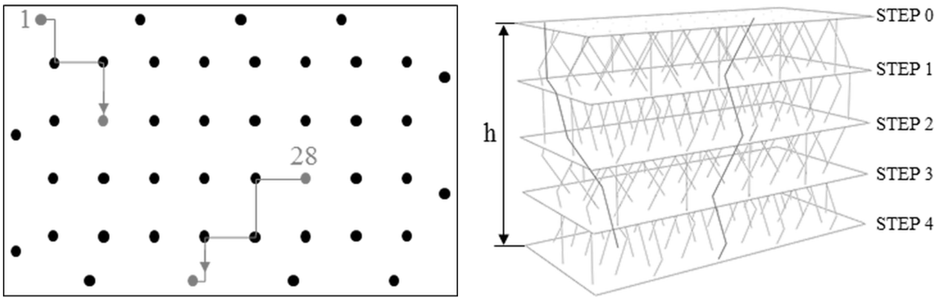

(a) (b)

Figure 5.6.: Visualisation of yarn paths in 4stepWO: highlighted exemplary top view (a) and 3D view (b) for two braiders

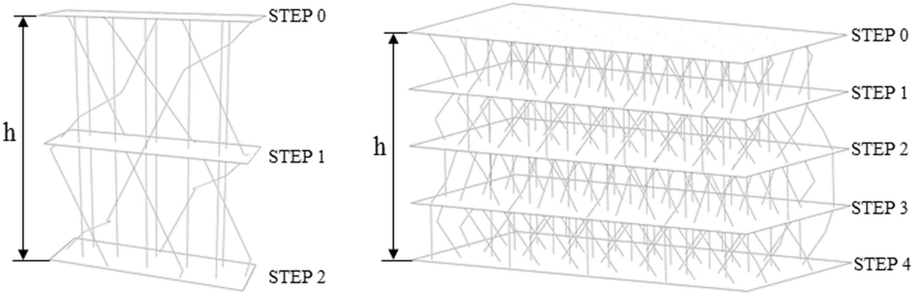

(a) (b)

Figure 5.7.: 3D visualisation of yarn paths in 2step (a) and 4stepWI (b)

the total number of yarns can be derived as

$$\begin{aligned} N_{b_{Peven}} &= m_h\,(2n_v+1) + m_v\,(2n_h+1) - 4n_hn_v + \\ &\qquad 2|\frac{(m_h-2n_h)}{2} + \frac{((m_v-2n_v)-2)}{2}| \end{aligned} \tag{5.24}$$

and if m_h or m_v is odd

$$\begin{aligned} N_{b_{Podd}} &= m_h\,(2n_v+1) + m_v\,(2n_h+1) - 4n_hn_v + \\ &\qquad 2|\frac{(m_h-2n_h)}{2} + \frac{((m_v-2n_v)-2)}{2}| + 1 \end{aligned} \tag{5.25}$$

The total number of yarns in the 3D braided box beam profile is 831. As a clear depiction of the node array for this braid is impaired by available space, Figure 5.8 shows an exemplary node array of a quadratic box beam with a [11,3] braid configuration for flanges and webs and a total number of 127 braider yarns. A visualisation of the FE model of the box beam profile with 831 yarns is presented in Figure 5.9.

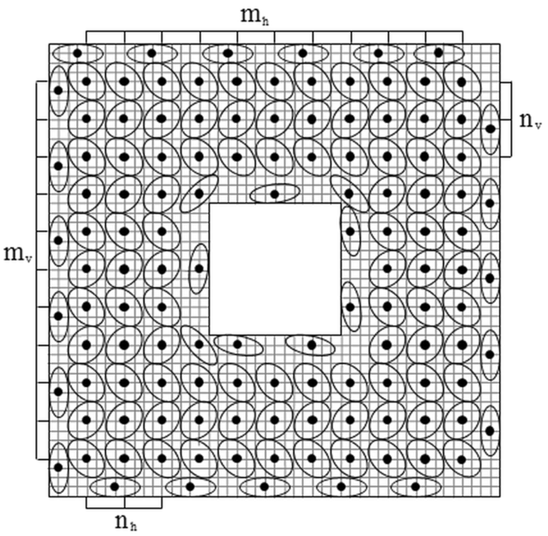

Figure 5.8.: Schematic view of node array in four-step braided box beam

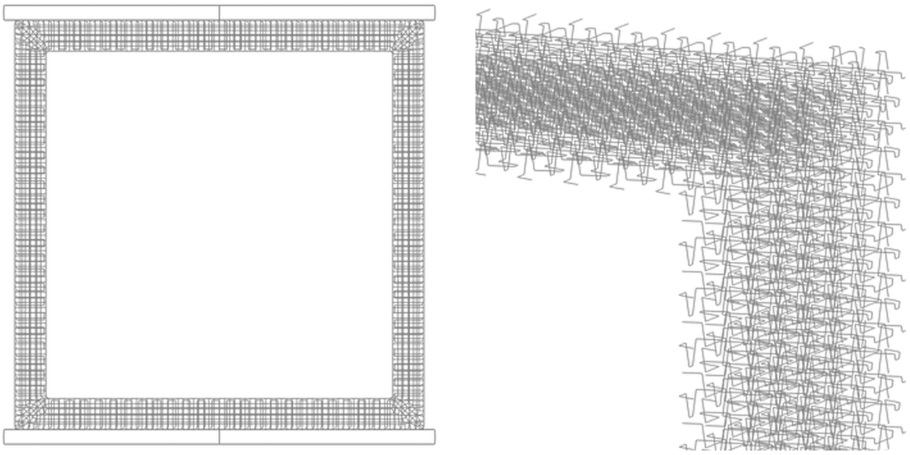
(a)
(b)

Figure 5.9.: FE model of 3D braided box beam profile (a) and magnification of yarn paths (b)

In contrary to generally ideal modelled yarn geometries, yarns possess no uniform cross-sections and are in reality not straight. As seen in micrographs and reported by [167,168] multifilament yarns exhibit non-uniform fibre distributions over the cross-section, particularly towards their edges. Koissin et al. [168] showed in a numerical study of an elliptical yarn the influence of the distribution and the importance of occurring irregularities for the damage resistance as their local mechanical properties vary. Chen [2] revealed in microscopic experiments that yarn compression induced by processing or yarn intersections lead to localised distortion. Insufficient tension during braiding causes yarn twist, consequently the fibres change their direction with the braider movement and are not parallel to the yarn axis. Yarn distortion influences the cross-section and the packing factor of the braider yarn. Yarn squeezing was considered in numerical modelling approaches by using a hexagonal or octagonal yarn cross-section [97–99,119,120]. Moreover, misalignments and crimp reduces not only the stiffness of a composite, but decreases also the composite strength [169,170]. When the composite is elongated resin in misaligned yarns deforms plastically in shear, allowing the yarn to straighten out and contributing to nonlinearity of the material [171]. Moreover, straight filaments can react simultaneously to external loads and thus contribute to the overall strength. On the contrary a waved filament structure, such as in braider yarns, induces higher loads in the yarn and consequently premature failure, which reduces the overall composite strength [170,172]. Dadkah et al. [169] introduced in their model a knockdown factor for the modulus in fibre direction, estimated from distributions of out-of-plane misalignment angles, to represent the softening of yarns due to waviness. The authors computed stiffness losses of 2-10% for axial yarns and 10-30% for braiders in a triaxial braid reinforced composite. According to Cox et al. [101] a typical knockdown factor is about 0.9. Fang et al. [173] showed that irregularities of the cross-sectional shapes due to yarn compression have a significant effect on the mechanical properties. The authors modelled a four-step braid reinforced unit cell by dividing each octagonal yarn into seven regions. Fibre paths in the braid surface and resulting yarn properties were calculated using stochastic functions. The longitudinal modulus and the strength were particularly influenced by the twisting angle, whereas the other properties were only slightly affected, thus an effect is negligible. As an example, a twisting angle of about 5° results in a modulus reduction of 10%. Further, topological constraints and applied pressure during the composite fabrication cause transversal forces leading to variations of the cross-sectional shape along the yarn length [130]. Although yarn dimensions can alter it can be assumed that the shape type does not change along the axis [92].

Nevertheless, in order to simulate the yarn geometry in this study the following basic assumptions are used

(a) Multifilament yarns are used for braiders and axial yarns. Filaments follow the same path as the corresponding yarn and are parallel to its axis, not twisted

(b) Yarns have no crimp owing to sufficiently high tension during processing

(c) Uniform yarn geometry and size along an idealised centreline of the yarn path

(d) All yarns have uniform packing factor

(e) Yarn cross-sections are elliptic or polygonal with respect to the type of braiding

5.4. Effective elastic properties

In order to analyse elastic properties of the repetitive RVE boundary conditions need to be chosen such that applied load cases and consequent deformations of the RVE are appropriately simulated. In case of periodic structures, such as the UD composite model, periodic boundary conditions were applied to the surfaces of the RVE to ensure stress continuity across its boundaries. Periodic boundary conditions make use of translatoric symmetries of the given geometry. In order to use periodic boundaries the RVE must consist of pairs of faces, as an example the bottom and top faces shown in Figure 5.10. Each pair of opposite faces must be discretised identically, meaning nodal points must have identical positions in the face. The macro-cell model of a 3DBRC is a periodic, repetitive structure with outer composite surfaces. Thus, periodic boundary conditions are solely applied to opposing faces in longitudinal direction.

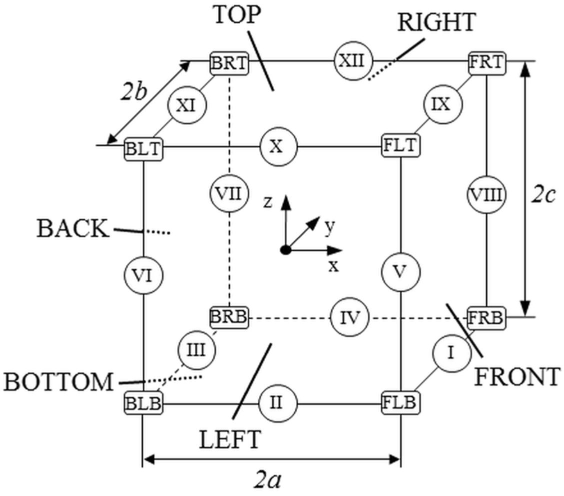

Figure 5.10.: Periodic cube with designated faces, edges and corner nodes

The RVE is assumed to be orthotropic and hence six load cases of prescribed principal strains are applied as displacements to determine six independent stiffness coefficients [91, 174]. For each load case the strain components, except for one, are kept zero as listed in Table 5.4. The appropriate boundary conditions for each load case can be expressed as

$$u_i|_{+j} - u_i|_{-j} = \varepsilon_{ij} \Delta x_j \tag{5.26}$$

where u is a displacement, i and j are coordinates in the Cartesian coordinate system, Δx_j is the distance between corresponding opposite faces and ε_{ij} the applied strain.

The notations $|_{+j}$ and $|_{-j}$ in Equation 5.26 signify the boundary face along the positive direction and along the negative direction, respectively, with

- $x = \pm a$ where $+$ denotes face FRONT and $-$ face BACK
- $y = \pm b$ where $+$ denotes face LEFT and $-$ face RIGHT
- $z = \pm c$ where $+$ denotes face TOP and $-$ face BOTTOM

The boundary conditions were implemented in the FE software ABAQUS with constraint equations between nodal displacements of opposite faces. Node pairs were identified and corresponding equations defined using a Python algorithm. Vertices and nodes along the edges of the RVE are treated separately. Edges are shared by two faces and vertices by three edges. In order to avoid redundant constraints and associated modelling problems in ABAQUS sets of independent displacement boundary conditions are defined according to Li and Wongsto [175].

Table 5.4.: Applied strain cases to compute elastic constants

	1	2	3	4	5	6
ε_{xx}	0.001	0	0	0	0	0
ε_{yy}	0	0.001	0	0	0	0
ε_{zz}	0	0	0.001	0	0	0
γ_{xy}	0	0	0	0.002	0	0
γ_{xz}	0	0	0	0	0.002	0
γ_{yz}	0	0	0	0	0	0.002

Subsequently, static FE analyses were performed to numerically solve the deformation mode for each load case. The general approach for determining the effective material properties of the RVE relates volume averaged stress and strain fields through Hooke's law

$$\bar{\varepsilon} = S\bar{\sigma} \tag{5.27}$$

where S is the compliance tensor, $\bar{\varepsilon}$ the average strain tensor and $\bar{\sigma}$ the average stress tensor. Important for this approach is that the size of the homogenisation volume is sufficient to contain all information necessary for describing the material behaviour [176]. Another more efficient method proposed by Kästner et al. [177] which is independent from element type and size utilises associated reaction forces at master nodes to apply the displacements, in this case at vertices. The effective stiffness properties can be computed by relating the average stress and reaction forces as follows

$$\bar{C}_{ijkl} = \frac{1}{\bar{\varepsilon}}\bar{\sigma}_{ij}\left(\bar{\varepsilon}_{kl}\right) = \frac{1}{A|_{+j}\bar{\varepsilon}} RF_i|_{+j}\left(\bar{\varepsilon}_{kl}\right) \tag{5.28}$$

where $\bar{\sigma}_{ij}$ $(\bar{\varepsilon}_{kl})$ is the volume average of the stresses in the RVE for the average strain vector given as input for each load case (Table 5.4), $\bar{\varepsilon}$ a scalar defining the magnitude of the non-zero strain component, RF the reaction force and A the associated surface at the respective boundary. Hence the effective engineering constants can be extracted from the compliance matrix.

5.5. Damage model

5.5.1. Failure criteria

Damage accumulation is a complex multi-scale process which is influenced by the textile architecture and the applied load case [116]. Failure mechanisms can be generally distinguished between longitudinal mechanisms including fibre and inter fibre failure, also known as matrix failure, as well as transverse mechanisms including matrix cracking and fibre-matrix interface failure. Boehm et al. [178] classified occurring damage phenomena with respect to their experimental observability in addition into two categories, namely discrete and diffuse damage mechanisms. Failure which can be quantified, such as fibre, matrix failure and delamination, fall under discrete mechanisms. Diffuse damage, such as void growth, whitening and interface failure, cannot be quantified by means of experiments and are just quantitatively measurable. As reported by Boehm et al. diffuse damage in the form of whitening occurs first as observed during experimental testing. Fang et al. [119] showed that various failure mechanisms can be found in 3DBRC, such as longitudinal rupture of yarns, transverse cracking and shear failure modes. Delamination as known from 2D composites does not exist.

Numerous failure criteria have been developed in the last decades. Hashin [179] established in 1973 failure criteria for fibre and matrix based on failure mechanisms observed in experiments. The work was extended and Hashin [152] introduced in 1980 criteria which in addition distinguish between tensile and compressive failure. The author assumed that matrix failure was caused due to the interaction of normal and shear stresses acting on a plane parallel to the fibres. Although Hashin originated the idea of a fracture plane, owing to the computational effort he did not calculate the orientation of this plane. Moreover, it was shown in various studies that Hashin's criteria do not always comply with experiments and may not predict failure initiation correctly, particularly for compressive loading [3, 180]. Therefore, the action plane concept was extended by Puck and Schürmann [181] who considered the influence of matrix compression on the matrix shear strength. Further physically based failure models and criteria have been developed using the fracture plane concept [180,182,183]. Moreover, as composite failure does not always involve a fracture plane Cuntze [184] developed invariant formulated strength criteria assuming that micro-mechanical and statistical interactions cannot be differentiated. This approach was further extended to determine failure in 2D and 3D textile reinforced composites by adding diffuse failure criteria [185]. Puck's criteria are considered as one of the best currently available theories according to the World-Wide Failure Exercise [186]. However, the drawback of those sophisticated physically based models is the numerical search for the fracture angle in each element at each time step by maximising the failure index. Although Wiegand et al. [187] developed a more efficient algorithm to determine the fracture angle using the Golden section search, it is still a computationally expensive model. The in-built damage model in ABAQUS uses the 2D Hashin damage initiation criteria. Another widely used failure criteria for laminated composite materials subjected to impact events was proposed by Chang and Chang [188]. However, those 2D criteria use only plane stresses, thus in load cases with significant out-of-plane stresses damage prediction can be insufficient. As the shear stress σ_{23} is a dominant contributor to matrix shear cracking, Hou et al. [189] suggested that σ_{23} must be integrated into a failure criterion for matrix cracking.

In the following sections the implemented failure criteria are described. The failure index f in each criterion enables the assessment of the likelihood of damage initiation. A criterion is satisfied when f is equal or greater than 1. Fibre-matrix debonding occurs only in the presence of matrix cracking and fibre failure. An explicit failure criterion for fibre-matrix debonding is not considered. This failure mode occurs only in the presence of matrix cracking and fibre failure which induced prior material degradation.

Fibre failure

The mechanics of fibre failure are complex due to phenomena such as interface debonding, yarn splitting or the load transfer through the matrix to other fibres [104]. Experimental observations showed that yarns break entirely rather than partially [171]. Hence, tensile fibre failure is an explosive failure mode, large amounts of energy are released and if the load cannot be redistributed it induces catastrophic failure [190]. The use of 1D elements is limiting the selection of possible damage initiation criteria. However, the main stress inducing tensile fibre failure is the longitudinal stress, therefore the maximum stress failure criterion was used. According to Juhasz et al. [191] the criterion is valid when fibre failure occurs before matrix failure. This is true when the composite strength in the fibre direction is dominated by the fibre strength, which applies when the failure strain of the fibre is lower than the failure strain of the matrix. Compressive stresses may be generated either due to direct compressive loading or due to bending and impact loading. Two mechanisms are responsible for fibre failure under compressive loads, microbuckling and consequent kinking [192]. Numerous researchers analysed the kinking phenomenon and established models to predict the compressive behaviour of UD composites [180, 183, 192–195]. An initial fibre misalignment due to manufacturing defects and material imperfections induces shear stresses between fibres leading to fibre rotation and consequently to increasing shear stresses. When the matrix locally fails to support misaligned fibres the formation of kink bands is triggered, which occurs for example near yarn crossings. Fleck [195] stated that the compressive strength in polymer matrix composites is generally lower, about 60 % less, than the tensile strength.

Tension ($\sigma_{11} \geq 0$)

$$f_{ft} = \left(\frac{\sigma_{11}}{X_t}\right)^2 \geq 1 \tag{5.29}$$

where σ_{11} denotes the longitudinal stress and X_t the longitudinal tensile strength of a UD yarn. The tensile strength was obtained by means of Equation 5.9 using the yarn packing factor of each yarn as well as the tensile strength of glass fibres listed in Table 5.2.

Compression ($\sigma_{11} < 0$)

$$f_{fc} = \left(\frac{\sigma_{11}}{X_c}\right)^2 \geq 1 \tag{5.30}$$

where X_c denotes the longitudinal compressive strength of a UD yarn, which was calculated according to Equation 5.10 using the compressive strength of glass fibres listed in Table 5.2.

Matrix failure

The fracture conditions for matrix failure are in comparison to fibre failure more complex. The stress-strain relationship in a polymeric matrix is not linear, thus the polymeric matrix induces nonlinear behaviour on the overall composite stiffness. Transverse matrix cracking causes stiffness degradation and causes other failure along the yarn boundaries [196]. Under compression the matrix fails by shear at an angle with the loading direction, whereas fracture under tensile loading occurs usually normal to the loading direction [190]. As aforementioned sophisticated, even though more accurate, failure models are computationally demanding. Guo et al. [197] implemented the stress based failure criteria proposed by Hashin [152] for a 3D state to simulate carbon fibre reinforced epoxy laminates under low-velocity impact. The prediction of damage and deformation agreed with observed experimental results. For this reason, Hashin's failure criteria were selected to predict failure in the effective medium.

Tension ($\sigma_{22} + \sigma_{33} > 0$)

$$f_{mt} = \frac{1}{Y_t^2}\left(\sigma_{22} + \sigma_{33}\right)^2 + \frac{1}{S_t^2}\left(\sigma_{23}^2 - \sigma_{22}\sigma_{33}\right) + \frac{1}{S_l^2}\left(\sigma_{12}^2 + \sigma_{13}^2\right) \geq 1 \tag{5.31}$$

where σ_{22} and σ_{33} are the transverse stresses, σ_{12}, σ_{13} and σ_{23} the shear stresses, Y_t the transverse tensile strength as well as S_l and S_t the longitudinal and transverse shear strengths, respectively.

Compression ($\sigma_{22} + \sigma_{33} < 0$)

$$f_{mc} \quad = \quad \frac{1}{Y_c}\left(\left(\frac{Y_c}{2S_t}\right)^2 - 1\right)\left(\sigma_{22} + \sigma_{33}\right) + \frac{\left(\sigma_{22} + \sigma_{33}\right)^2}{4S_t^2} +$$

$$\frac{(\sigma_{23}^2 - \sigma_{22}\sigma_{33})}{S_t^2} + \frac{(\sigma_{12}^2 + \sigma_{13}^2)}{S_l^2} \geq 1 \tag{5.32}$$

where Y_c denotes the transverse compressive strength of the UD yarn.

The strength values of the effective medium were obtained by means of formulations for a fibre reinforced composite described by Li et al. [117].

$$Y_t = \beta \left(1 - \sqrt{V_f}\right) \frac{E_{f2}}{E_m} \frac{E^{Medium}}{E_{f2} - \sqrt{V_f} E^{Medium}} X_m^t$$

$$Y_c = \beta \left(1 - \sqrt{V_f}\right) \frac{E_{f2}}{E_m} \frac{E^{Medium}}{E_{f2} - \sqrt{V_f} E^{Medium}} X_m^c$$

$$S_l = \beta \left(1 - \sqrt{V_f}\right) \frac{G_{f12}}{G_m} \frac{G_{12}^{Medium}}{G_{f12} - \sqrt{V_f} G_{12}^{Medium}} S_m$$

with

$$\alpha = \sqrt{\frac{\pi}{4V_f}}$$

$$\beta = \frac{1}{\alpha - 1} \left(\alpha - \frac{E_m}{E_{f2}\left(1 - \sqrt{V_f}\left(1 - \frac{Em}{E_{f2}}\right)\right)}\right)$$

where V_f, E_{f_2} and E_m are the fibre volume fraction of the composite, the transverse moduli of the fibres and resin, respectively. X_m^t, X_m^c and S_l denote the tensile strength, the compressive strength and the longitudinal shear strength of the resin, respectively. The tensile strength of the epoxy resin was assumed to be 50 MPa and the compressive strength 120 MPa. Moreover, it was assumed that the S_t is equal to S_l and equal to 60 MPa.

5.5.2. Material degradation

Elastic material behaviour is assumed until failure onset is detected. Most implementations of material degradation in FE methods are based on continuum damage mechanics (CDM) using a gradual unloading scheme. Matzenmiller et al. [154] developed a well-known CDM based model by introducing a damage variable which characterises damage induced changes in the material behaviour. Damage propagation and consequent energy dissipation are either induced by strain based evolution functions [3, 183] or by approaches using a rate at which failure criteria are exceeded [198,199]. On the contrary to the use of a progressively increasing damage variable are instantaneous degradation approaches. Once a failure initiation criterion at an integration point is satisfied damage occurred and the material stiffness will be reduced. Miravete et al. [118] proposed instantaneous approaches for the elastic properties of 2D triaxial braid reinforced composites and Xu [120] for a 3D four-step braid reinforced composite.

The ABAQUS documentation provides a user-defined subroutine UMAT, based on the damage model proposed by Linde et al. [200], to simulate the failure behaviour of glass fibre reinforced epoxy laminates. Failure initiation criteria and damage evolution in this model are expressed in terms of strains. Similar to the damage model outlined in Section 5.1 the degradation of the stiffness matrix is controlled by damage variables. Although Linde's model is designated to 2D laminates, it was first adapted to model the damage behaviour of a 4stepWO under flexural loading. Thereafter, a 3D damage model proposed by Guo et al. [197], which is based on Linde's model, was adapted for modelling damage in the effective medium and in the yarns. Global damage variables were used to combine damage due to tensile and compressive failure, as defined in Equations 5.33 and 5.34. d_f is associated to yarn failure and d_m to failure in the effective medium.

$$d_f = 1 - (1 - d_{ft})(1 - d_{fc}) \tag{5.33}$$

$$d_m = 1 - (1 - d_{mt})(1 - d_{mc}) \tag{5.34}$$

where d_{ft}, d_{fc}, d_{mt} and d_{mc} are the variables associated with tensile and compressive failure in the yarn and effective medium, respectively. The damage variables are defined such that they have the value 0 at failure onset and take the value 1 at final failure. The increase of each damage variable is controlled by exponential functions based on energies dissipated through fracture.

$$d_{mt} = 1 - \left(\frac{1}{f_{mt}}\right) e^{\left(-C_{22}\varepsilon_{22}^{mt}\varepsilon_{22}^{mt}(f_{mt}-1)\frac{L_c}{G_m}\right)} \tag{5.35}$$

$$d_{mc} = 1 - \left(\frac{1}{f_{mc}}\right) e^{\left(-C_{22}\varepsilon_{22}^{mc}\varepsilon_{22}^{mc}(f_{mc}-1)\frac{L_c}{G_m}\right)} \tag{5.36}$$

$$d_{ft} = 1 - \left(\frac{1}{f_{ft}}\right) e^{\left(-C_{11}\varepsilon_{11}^{ft}\varepsilon_{11}^{ft}(f_{ft}-1)\frac{L_c}{G_f}\right)} \tag{5.37}$$

$$d_{fc} = 1 - \left(\frac{1}{f_{fc}}\right) e^{\left(-C_{11}\varepsilon_{11}^{fc}\varepsilon_{11}^{fc}(f_{fc}-1)\frac{L_c}{G_f}\right)} \tag{5.38}$$

The energy released by a crack (energy per unit area) is dependent on the element size. Therefore, the above equations are dependent on the characteristic element length L_c. G_f and G_m are fracture energies of fibres and matrix, respectively, see Table 5.1. When failure in the effective medium is initiated the transverse properties and the shear moduli are degraded, whereas in case of the 1D elements of the yarn only the longitudinal modulus is affected. The stiffness matrix of the effective medium C_d^m is reduced as follows

$$C_d^m = (1-d_m)\begin{bmatrix} \frac{C_{11}}{(1-d_m)} & C_{12} & C_{13} & 0 & 0 & 0 \\ & C_{22} & C_{23} & 0 & 0 & 0 \\ & & C_{33} & 0 & 0 & 0 \\ & & & C_{44} & 0 & 0 \\ & & & & C_{55} & 0 \\ sym & & & & & C_{66} \end{bmatrix} \tag{5.39}$$

In order to improve convergence problems, which can occur when the matrix stiffness is reduced, a viscous regularisation scheme was applied as described in Equation 5.7 in Section 5.1. The values of the fracture energies and viscosities influence the damage propagation, therefore the values listed in Table 5.1 were also applied in this case.

5.5.3. Implementation into FE environment

The proposed 1D FE method is based on two independently generated geometries. Therefore, two independent material models are necessary. A static analysis was selected to simulate a quasi-static flexural test. The FE mesh model of a 4stepWO subjected to flexural loading is presented in Figure 5.11. A displacement of 10 mm is applied, which is sufficient to analyse and compare the damage initiation with the experimental data. A higher displacement results in numerical instabilities. Hence, the material models were implemented in ABAQUS Standard by means of a UMAT.

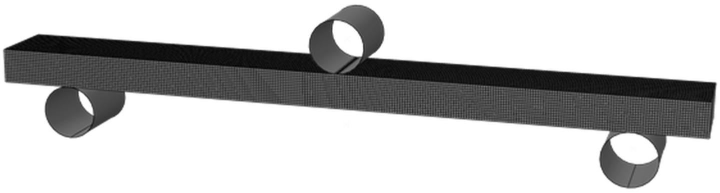

Figure 5.11.: FE mesh model of 4stepWO subjected to flexural loading

A flowchart of the subroutine is shown in Figure 5.12. Each subroutine contains a description of the respective stiffness matrix, failure initiation criteria, damage evolution and stiffness degradation. The defined stiffness matrix is used to obtain the stresses for each element at the integration points, which are used to check for failure initiation. Once a failure criterion is satisfied, damage variables are calculated and the material stiffness is degraded. The stress analysis is repeated to obtain the progressive damage propagation. If no damage occurred the predicted linear-elastic stress tensor is taken as the effective stress tensor. State variables are used to store information about the failure and damage state. The UMAT for the effective medium is exemplarily presented in Appendix B.2.

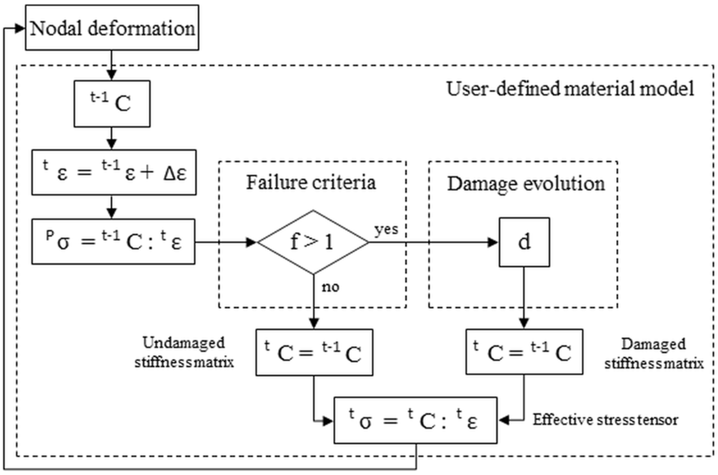

Figure 5.12.: Flowchart of UMAT for ABAQUS Standard

6. Results and discussion

The following chapter presents the results of all experimental, analytical and numerical analyses explained and conducted in this thesis. Briefly summarised, it comprises the compressive loading of pultruded box beam sections to analyse their failure behaviour (Section 3.1). In addition, those profile sections were numerically modelled in order to identify material parameters which enhance their fracture toughness (Section 5.1). Besides material properties geometric characteristics define the mechanical response. Therefore, analytical studies described in Section 4.1 were performed to analyse the effect of different cross-sections on the bending and buckling behaviour. Different 3DBRCs were mechanically tested as outlined in Section 3.2 under tensile, flexural and impact loading to reveal their failure behaviour and characterise damage mechanisms. Moreover, microscopy and calcination tests were performed to obtain details of the microstructures. Described analytical models in Section 4.2 and 4.3 were used to predict preform dimensions and elastic properties of the 3DBRC. Additional parameter studies were conducted to understand the influence of processing parameters on elastic properties. Numerical modelling of 3DBRC consists of various parts. Preliminary FE modelling studies (Section 5.2) are used to define a numerical model and assess its capability for the prediction of mechanical properties. Moreover, elastic constants of the 3DBRCs are calculated and the damage behaviour simulated.

6.1. Pultruded profiles under lateral loading

6.1.1. Experimental study

In Figure 6.1(a) and (b) pictures taken from cross-sections of the two different studied material configurations and with exemplarily bad fabric orientations are shown. As exemplified the layer thickness and geometry were found constantly changing along the profiles tested. Therefore, layer thickness were measured along the perimeter of each section and averaged. Besides these variations of layer thickness and through-thickness position of both profiles, the specimen preparation revealed visible pre-existing laminate defects in *Configuration 1* such as wrinkling of the inner layer and cracks in 45° direction in the profile corners (see Figure 6.2(a)), as well as partial damages of the inner profile surface as shown in Figure 6.2(b), whereas *Configuration 2* samples presented no visible defects. The average fibre volume fractions relative to the overall volume, within each material system, CSM and roving, were obtained for *Configuration 1* as 0.14 and 0.36, respectively. Hence, the total V_f of the pultruded composite profile section is 0.50. The V_f within each layer were calculated with respect to the

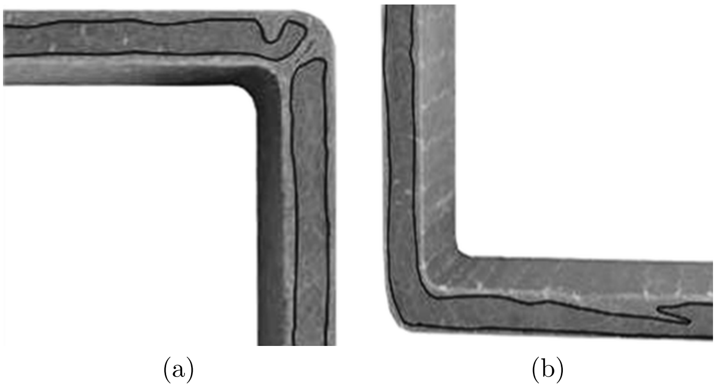
(a) (b)

Figure 6.1.: Layer deviations in *Configuration 1* (a) and *2* (b)

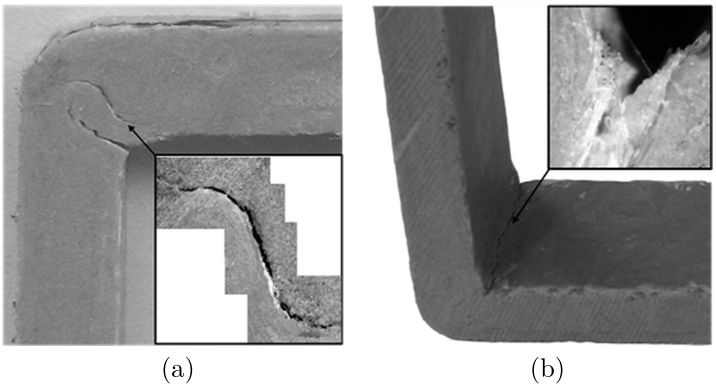
(a) (b)

Figure 6.2.: Microscopic views of pre-existing defects in *Configuration 1* (a) and (b)

average volume of each layer using relative thickness based on determined averaged layer thickness during microscopy. Thickness, calculated V_f, fibre weight fractions W_f and constituents' properties are reported in Table 6.1.

Mechanical behaviour and load responses

Load displacement curves for *Configuration 1* and *2* under compressive loading are presented in Figure 6.3 and 6.4, respectively. Averaged curves were derived and used as representative load-displacement curves of both pultruded profiles for further discussion, see Figure 6.5. The differing shapes of the load-displacement curves reveal the diverse material behaviour of the configurations. Sections of *Configuration 2*, as seen in Figure 6.4, present a distinct load peak, a continuing load bearing phase, as well as a sudden load drop indicating the final fracture. In contrast, the load-displacement curves of *Configuration 1*, as shown in Figure 6.3, are characterised by gradual material failure induced by minor fractures in the corners due to pre-existing defects. Both profiles show stiffening-softening-stiffening trends. Unlike *Configuration 2*, the load-

Table 6.1.: Lay-up details of box beam profiles

N°	Fibre	Resin	Lay-up	t [mm]	V_f [%]	W_f
1	E-glass	Polyester	Laminate	5.00	49.5	66.2
			CSM outer	0.83	20.4	33.9
			Roving	3.27	54.8	70.8
			CSM inner	0.90	19.1	32.1
2	E-glass	Polyester	Laminate	5.00	54.8	70.8
			CSM outer	0.52	11.1	20.0
			±45° NCF outer	0.37	37.5	54.5
			Roving	3.08	56.7	72.4
			CSM inner	0.49	18.5	31.2
			±45° NCF inner	0.36	44.2	61.3

displacement curve of *Configuration 1* shows after occurring drops in load more phases of increasing load bearing capacities caused by altering load distributions in the profile section. Transitions from a stiffening phase to a softening phase are marked by sudden material rupture and sound. Furthermore it is evident that *Configuration 1* allows higher vertical deformations, whereas *Configuration 2* reaches lower deformations but higher peak loads.

In order to quantitatively compare the tested profiles, following parameters were determined from the test data to assess the structural crush characteristics of each

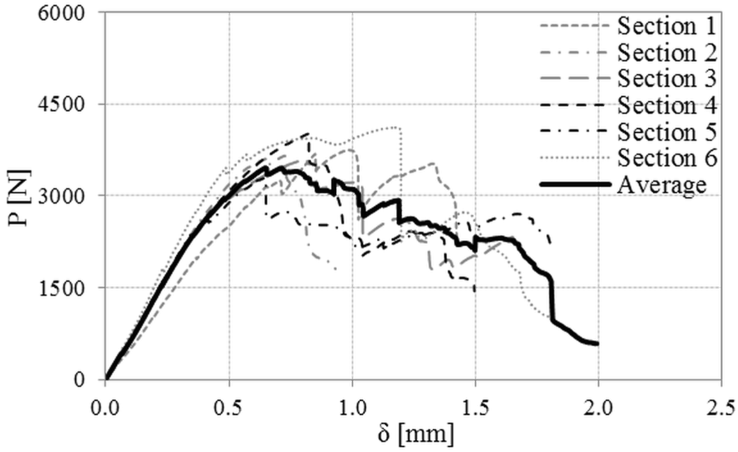

Figure 6.3.: Load vs. displacement response of *Configuration 1* sections

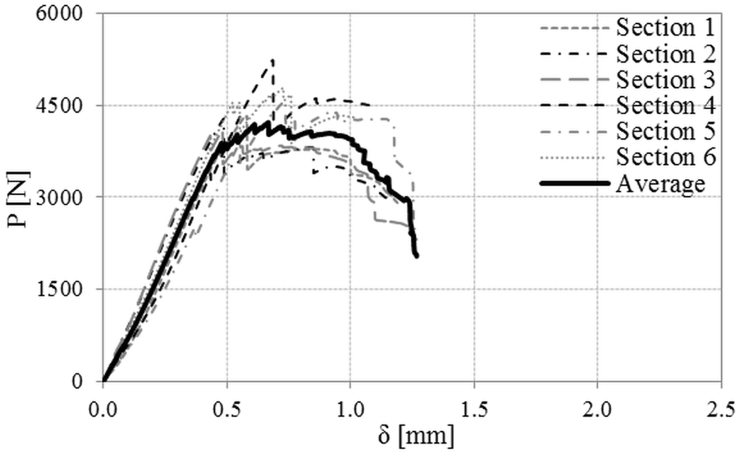

Figure 6.4.: Load vs. displacement response of *Configuration 2* sections

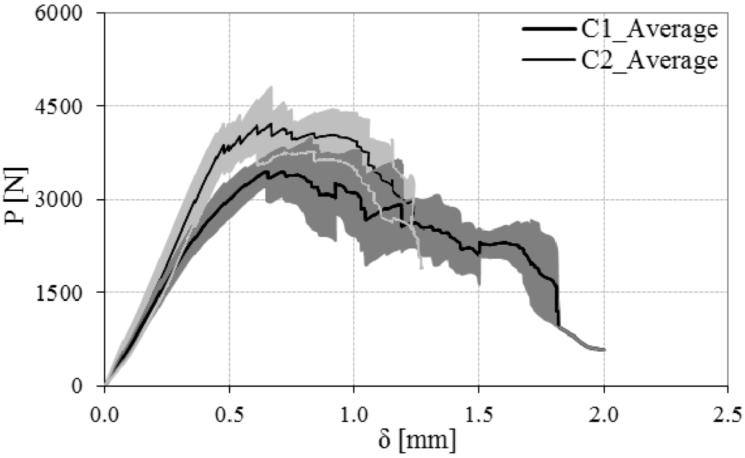

Figure 6.5.: Representative load vs. displacement responses with standard deviations of *Configuration 1* and *2*

profile.

- The *compressive strength* of the profiles was calculated as the ratio of load divided by the total cross-sectional area of the pultruded laminate.
- The total area under the load-displacement curve represents the *total absorbed energy* which is defined as the work done by the loading plate; while the *peak energy* is defined as the amount of absorbed energy until the maximum load is reached.
- The *specific energy absorption* (SEA) is defined as the ratio of the total energy absorbed by a structure to its mass.
- A further parameter to evaluate the mechanical performance of structures during crushing is the *crush force efficiency* (CFE), the ratio between mean force during crushing and the maximum force.

Results in Figure 6.6(a) show that sections of *Configuration 2* bear higher peak forces and consequently the ultimate compression strength is higher as well. In general, a stiffer material stores less energy than a more flexible material. The results reveal that sections cut from *Configuration 1* present better energy absorption capacities: peak energy and total absorbed failure energy are higher for *Configuration 1*. This can be explained by the longer lasting load bearing capacities due to a more flexible material behaviour, resulting in a higher overall toughness. Standard deviations for failure energies show that sections of *Configuration 1* present stronger varying failure behaviours than sections of *Configuration 2* caused by different pre-existing defects and related occurring failure modes. Regarding the SEA, results in Figure 6.6(b) show that *Configuration 1* presents better energy dissipation capacities due to higher total failure energies and lower V_f, which results in a lower density. Results for CFE reveal that *Configuration 2* is more efficient than *Configuration 1* due to a more consistent load bearing behaviour.

Failure modes

Progressive fracturing is generally the major contributor for energy absorption capabilities of pultruded composites during impact events, rather than plastic deformation [17, 32]. Before the maximum load is reached, energy absorbed by the laminate is dissipated due to microcracking of the matrix [201]. Due to further increased crushing loads and developed strains the density and extent of matrix cracks increases leading to interfacial fibre-matrix debonding [14, 201] due to the mismatch of fibre and matrix properties [202]. At the macro level energy dissipation during crushing results from bending, deformation of the profile section and forming of fracture lines [128]. It is well-known that progressive material degradation reduces the bending stiffness of pultruded profiles, changes the deflected shape and causes the separation of the profile

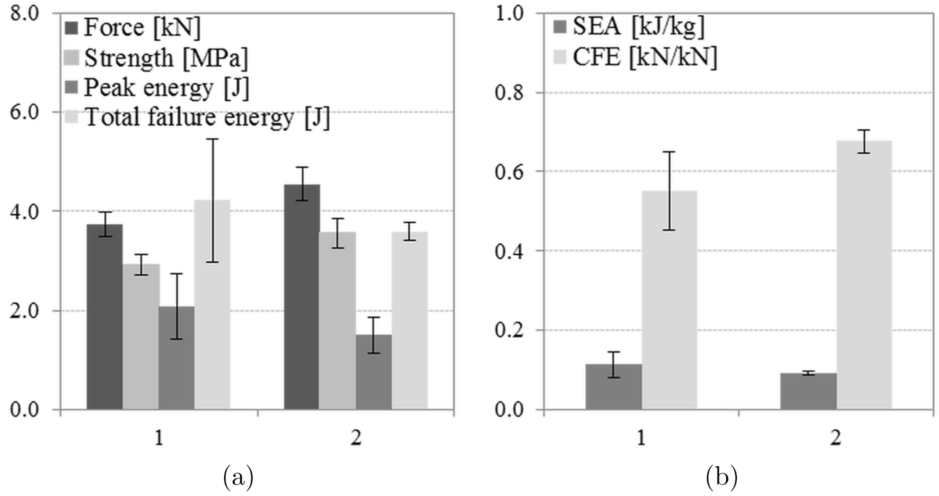

(a) (b)

Figure 6.6.: Mechanical properties (a) and crashworthiness parameters (b) of *Configuration 1* and *2* under compressive loading

junctions [32]. Hence the fibres are unsupported due to interfacial debonding, leading to delamination and fibre breakage during deformation of a pultruded profile [128]. Figure 6.7 and 6.9 show typical load and absorbed energy versus displacement curves together with photographs of failure modes showing the characteristic deformation history of a pultruded box beam section of *Configuration 1* and *2*, respectively. It can be observed that the absorbed energy during the initial crushing phase is for both laminates smaller compared to the phase after reaching the maximum load.

Occurring failure modes in *Configuration 1* sections were matrix cracking and intra-yarn failure in the roving layer (see photo B in Figure 6.8, showing a tested *Configuration 1* section after calcination), delamination between inner CSM and roving layer as well as cracking and fracturing in the profile junctions due to fibre breakage in CSM layers (see Figure 6.7 and Figure 6.8, photo C and A, respectively). As sections made of *Configuration 1* presented pre-existing defects, several relationships between defects and occurring failure can be deduced. A surface rupture along the section width induced 45° cracks in flange-web junctions. Although a pre-existing 45° corner crack promoted progressive cracking of junctions due to compression, only the combination of a 45° corner crack and a surface rupture induced fractures up to complete failure (see Figure 6.7, photo F). Chotard et al. [14, 203] observed that CSM layers provide a stopping effect on the crack growth, although the damage propagation is not totally prevented as cracks carry on causing delamination at the interfaces. This study revealed the same effect as shown in Figure 6.7, photo C, presenting an undamaged CSM layer wrinkle that stopped the crack growth of a pre-existing 45° rupture. Photo D in Figure 6.7 depicts occurring interface failure between inner CSM and roving layer in the section corner. The final failure in *Configuration 1* sections under compressive loading was the complete rupture of its corners. As outlined in Section 2.1, several authors reported on the tearing failure in junctions of pultruded profiles due to high shear-stress concentrations. Chotard et al. [203] identified the junction between flange and web as the weakest point of a box beam structure as manufacturing induced defects coupled with high stress fields lead to a high failure probability. The tested sections of *Configuration 2* showed delamination at the corners between inner layers and roving layer, see photos A and B in Figure 6.9, intra-yarn failure between rovings see photo F and B in Figure 6.9 and 6.10, respectively, delamination in the profile webs between outer layers and roving layer as well as fibre breakage in outer and inner profile layers as shown in photo C and F in Figure 6.9 or A and C in Figure 6.10 due to flange or web buckling. Moreover, it could be observed that flange buckling caused a reduction of delamination and crack growth in the corners as well as the opposed effect of lowered buckling fracture in the flanges as a result of corner delamination due to increased bending. However sections of *Configuration 2* showed no tearing failure in the junctions. The final failure in *Configuration 2* occurred due to flange or web buckling as a consequence of fibre-matrix debonding, in combination with matrix cracks and intra-yarn failure in the roving layer. The presence of ±45° fabric improved the bending performance of *Configuration 2* and reduced failure in the corners due to delamination. However, it could be observed that occurring delaminations cannot be prevented with bi-directional fabrics due to poor interlaminar through-thickness shear resistance. Delamination along the profile webs may be attributed to improper shear transfer between fabrics as a result of tensile and shear strength mismatch between adjacent layers [14, 203] as well as bending stiffness mismatch due to altering fibre orientations [202]. Moreover, webs are susceptible to local failure due to the relatively low transverse compressive strength and material stiffness.

6.1.2. Numerical study

The numerical buckling behaviour of both profiles corresponds to the observed behaviour and occurring failure during mechanical testing. As the mean experimental displacement for *Configuration 1* is bigger, higher compressive stresses occur at the bottom of the outer profile layer. As *Configuration 2* presents a stiffer material behaviour higher tensile stresses in loading direction occur in this model. Delamination in the junctions occurred during mechanical testing in both profiles between roving layer and adjacent inner layers, as shown in Figure 6.7(D) and Figure 6.9(F). *Configuration 1* shows higher shear stresses than *Configuration 2*, however the highest shear stresses occur in both profiles in the junctions. A detailed study revealed that main shear stress differences in the FE models occur also between roving layer and adjacent layers. The highest shear stresses in the numerical models could be observed in *Configuration 1* between the roving and inner CSM layer whereas in *Configuration 2* between the

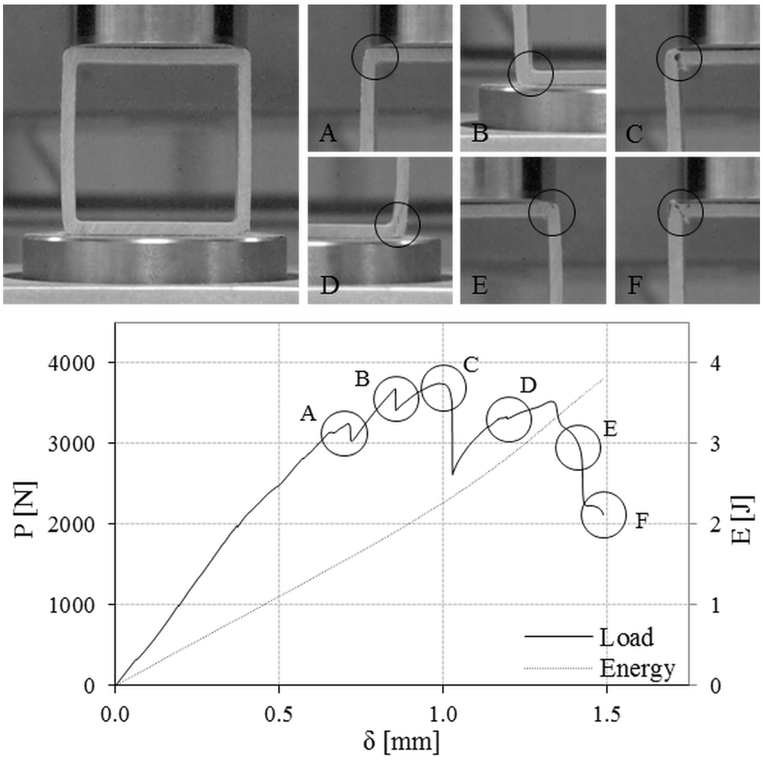

Figure 6.7.: Typical load and absorbed energy vs. displacement curves with deformation history for a *Configuration 1* section

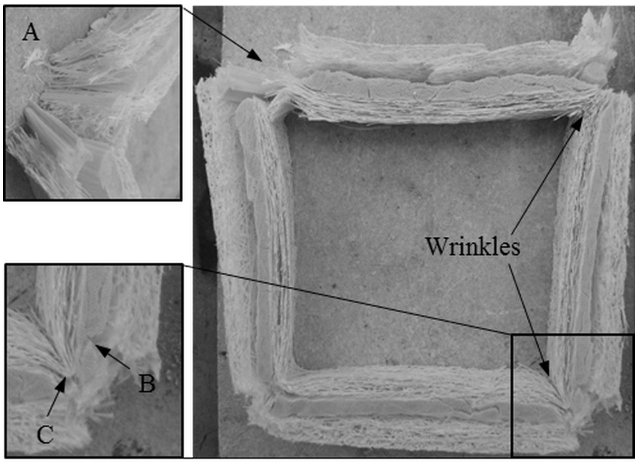

Figure 6.8.: Fracture details of a *Configuration 1* section after calcination

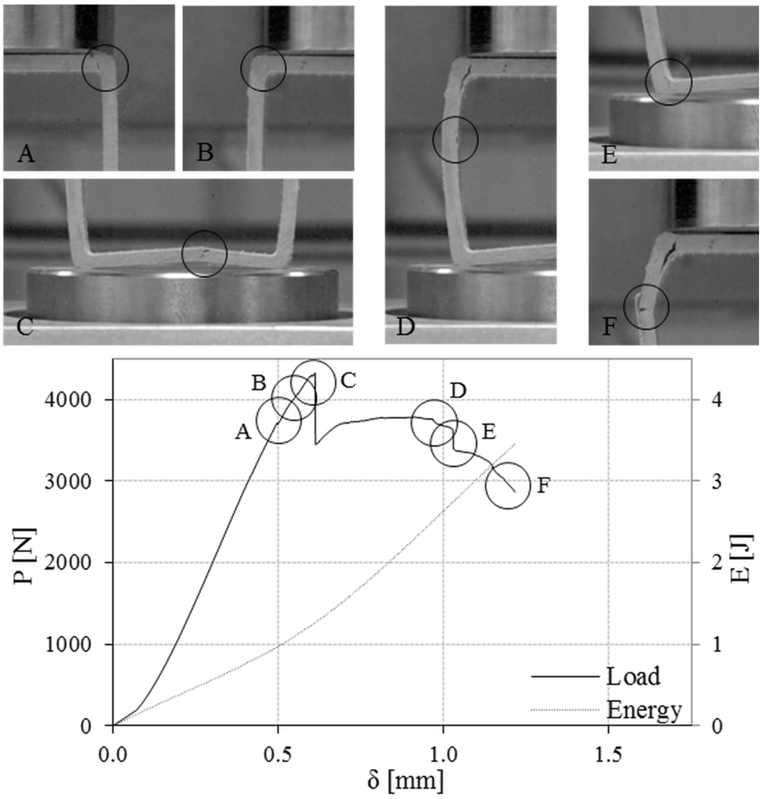

Figure 6.9.: Typical load and absorbed energy vs. displacement curves with deformation history for a *Configuration 2* section

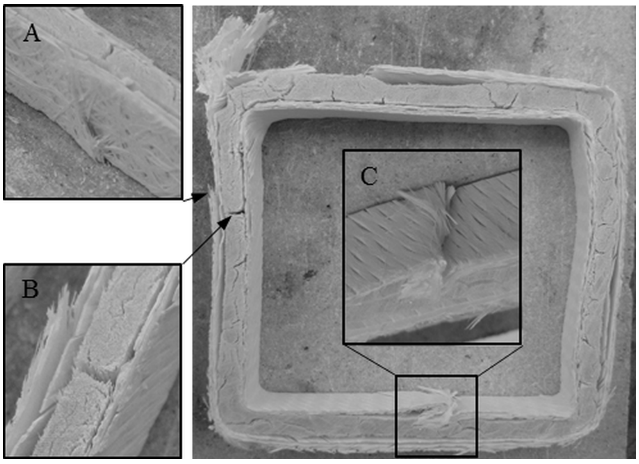

Figure 6.10.: Fracture details of a *Configuration 2* section after calcination

roving and outer ±45° NCF layer. However, fibre damage in *Configuration 2* in inner flange and outer web layers as seen in experiments, Figure 6.9(C) and (F), could not be observed in numerical analyses. A comparison of further numerical analyses of both profiles, without damage model, subjected to the mean displacement of *Configuration 1* showed that tensile and compressive stresses in loading direction are higher in *Configuration 2* than in *Configuration 1*, as a result of the stiffer material behaviour. While in-plane shear stresses in *Configuration 2* remained similar with increased displacement and much lower than in *Configuration 1*, the out-of-plane shear stresses increased significantly to the stress levels of *Configuration 1*. This comparison showed the importance of out-of-plane properties for the toughness of pultruded profiles. Hashin failure analyses revealed that matrix failure is dominating the damage propagation in the studied pultruded profiles. Tensile matrix failure occurs mainly in the inner and outer web layers of both profiles. Furthermore, it occurs in the inner flange layers close to the corners and propagates due to buckling, through the corners. As the Hashin criterion for tensile matrix failure is governed by the transverse tensile strength Y_t, it could be observed that an increased material parameter reduces failure in the inner layers and stops failure in the outer layers as well as the failure propagation in the corners. Compressive matrix failure occurs in all junctions of both profiles, mainly in the roving layer. In case of increased shear strengths, compressive matrix failure in the corners was stopped, see Figure 6.11. As the Hashin criterion for compressive matrix failure is influenced by the transverse compressive strength as well as shear strengths, the governing effect of increased shear strengths could be proved. Furthermore, analyses showed that tensile fibre failure occurs in the inner section layers located at the corners, progressing through the thickness of the junctions similar to failure modes seen in experiments. The Hashin criterion for compressive fibre failure indicates in both profiles corner damage in the outer CSM layer due to the influence of the loading plate and compression on the support.

Generally matrix cracking in tension and compression occurs due to shear stresses. Therefore, high shear stress concentrations in the corners in combination with occurring matrix failure as identified in numerical analyses lead to further damage such as fibre debonding, hence causing delamination as observed for both profiles in the experiments. As discussed before, progressive material degradation reduces the bending stiffness of pultruded profiles, causes a separation of profile junctions and changes the deflected shape. In analogy to experimental results, the final failure mode in *Configuration 1* is cracking and fracturing of the profile junctions, resulting in vertical sliding of the upper flange, see Figure 6.12(a), similar to the experimentally tested section in Figure 6.7(C) and (F), whereas *Configuration 2* presents no tearing as shown in Figure 6.12(c) and Figure 6.9. Experiments showed that a combination of 45° corner crack and surface rupture promoted progressive cracking of junctions. The FE analysis of *Configuration 1* with an elliptic hole in the roving layer and triangular surface cut at one inner corner

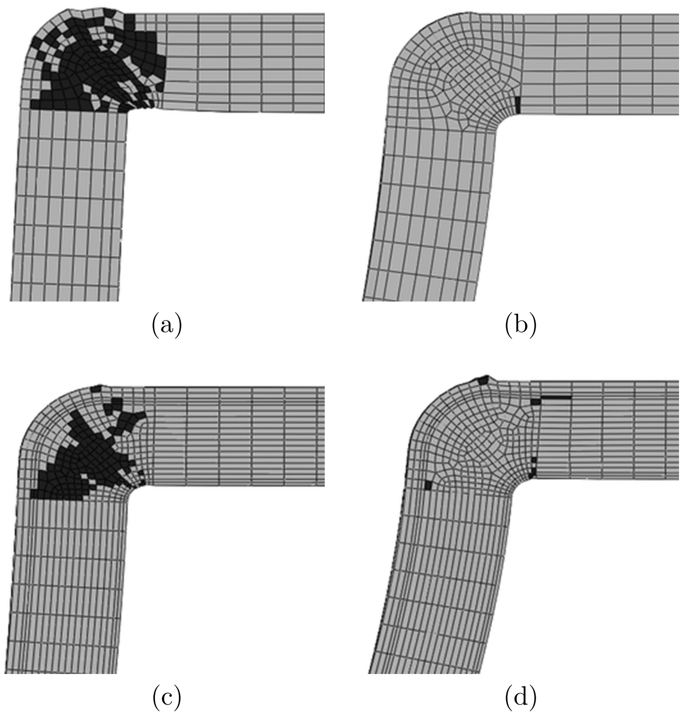

(a) (b)

(c) (d)

Figure 6.11.: Final states of compressive matrix failure in *Configuration 1* with 1*Y_t (a), with 3*Y_t (b) and in *Configuration 2* with 1*Y_t (c), with 3*Y_t (d)

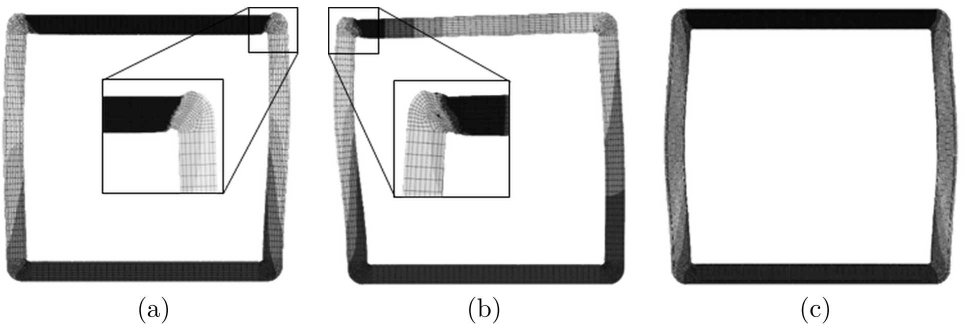

(a) (b) (c)

Figure 6.12.: Buckling modes of *Configuration 1* without defect (a), with elliptic hole and surface cut (b) and *Configuration 2* (c) under compressive loading

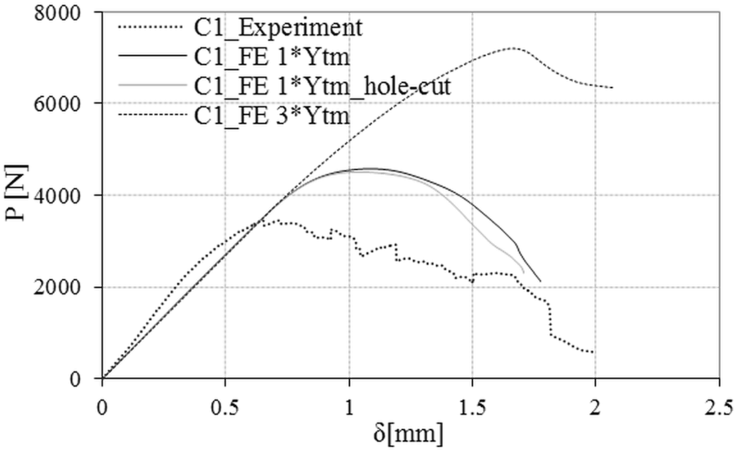

Figure 6.13.: Numerical load-displacement curves of *Configuration 1*

shows the influence of pre-existing defects on the fracture behaviour. Occurring failure is particularly located on the side with the defect, explaining sliding and stronger buckling to the defected section side, as shown in Figure 6.12(b), which was experimentally observed in Figures 6.7(C) and (F). Due to shear stresses, located around the defect, increase and main stresses decrease compared to a profile without defect, however the highest tensile stresses occur in the inner layer of the opposite upper corner. Comparing the experimental and numerical load-displacement curves of *Configuration 1*, an initial analogy in the stiffness behaviour can be observed (see Figure 6.13), however maximum force and strength are overpredicted. These differences can be largely attributed to pre-existing defects in the tested sections, as the load-displacement curve of the model with elliptic hole and surface cut presents faster damage propagation with lower forces. The comparison of experimental and numerical load-displacement curves of *Configuration 2* shows that the calculated stiffness underestimates the experimental behaviour (see Figure 6.14). However, here, the maximum crushing load and strength are well-predicted. Comparing the curves of *Configuration 1* and *2*, the longer lasting load bearing capacities of *Configuration 1* can be observed, resulting in a bigger displacement.

Matrix cracking is mainly contributing to energy dissipation under compressive loading. Further energy absorption during crushing results from the deformation of the profile and the forming of fracture lines. Conformity between experimental and numerical energy characteristics can be observed for *Configuration 1* with single Y_m^t, whereas properties of *Configuration 2* are over-estimated, see Figure 6.15, related to differing numerical loads and displacements. Therefore, an exact comparison of both profiles with increased Y_m^t is difficult as the mechanical behaviour could not be predicted correctly. However, it can be assumed that SEA with increased Y_m^t could be improved as shown in Figure 6.15. As mentioned before, numerical studies with increased transverse tensile and shear strengths showed that matrix failure and shear stresses in the

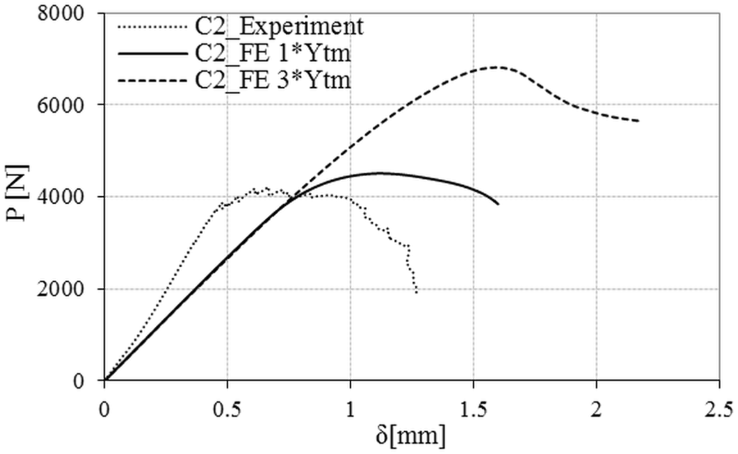

Figure 6.14.: Numerical load-displacement curves of *Configuration 2*

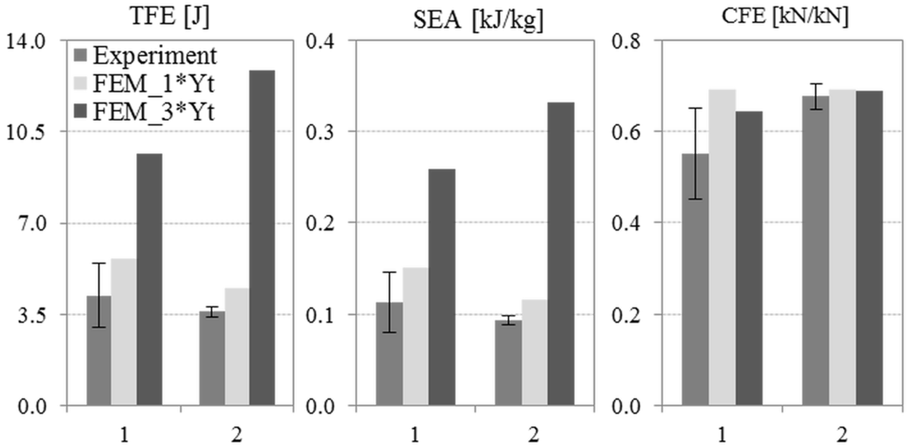

Figure 6.15.: Comparison of numerical and experimental energy absorption capacities of *Configuration 1* and *2*

flange-web junctions of pultruded profiles can be decreased. Hence, final corner fracture and flange sliding as seen in *Configuration 1* could be prevented. Moreover, due to enhanced out-of-plane and shear properties, the overall mechanical behaviour can be improved resulting in increasing maximal force and displacements, hence leading to higher energy absorption capacities. Consequently, enhanced out-of-plane material parameters, as it can be expected from using textiles with out-of-plane reinforcements, allow for tailoring shear damage and improving fracture toughness of pultruded GFRP box beam structures subjected to lateral compression loading. However, due to larger overall deformations, increased tensile stresses in the outer layer of the upper corners can be expected, which could lead to premature failure.

Table 6.2.: Ply properties

Layer	V_f	t	E_{lt}	E_t	G_{lt}	ν_{lt}
		[mm]		[GPa]		
CSM	20.4	0.83	8.36	8.36	1.61	0.32
UD	54.8	3.27	41.55	7.31	2.73	0.28
CSM	19.1	0.9	8.07	8.07	1.59	0.32

6.2. Geometry effects on pultruded profiles

6.2.1. Analysis of cross-sections with same area

The pultruded *Configuration 1* tested beforehand (Section 3.1) was selected for this analytical study as reference sample. Necessary material properties Young's and shear moduli of the laminate were obtained by means of the CLT and are given in Table 6.2. The dimensions of all geometries with same cross-sectional area are listed in Table 6.3. Stiffness, deflections as well as shape factors of the various cross-sections are listed in Table 6.4. A summary of the flexural response is presented in Figure 6.16. As can be seen from Table 6.4 and Figure 6.16, the bending stiffness has compared to the shear stiffness the bigger effect on the beam deflection. Cross-section $r1v$, the vertical profile with one cell shows solely improved bending and shear stiffness. However, the deflection is increased resulting from a bigger loading span due to its height. The addition of stiffeners is consistently improving the shear stiffness. The deflection can be improved for square and horizontally oriented cross-sections. Although a vertical orientation can benefit the bending stiffness owing to an increased span the overall flexural performance is impaired. The smallest deflections can be observed for horizontally orientated cross-sections $r1h$, $r2h$ and $r3h$ as their span is decreased. Outer dimensions, mainly the depth of a cross-section influence the deflection most as it defines the span.

The buckling response of the various cross-sections is listed in Table 6.5. In summary, Figure 6.17 presents the web buckling load versus the flange buckling load and Figure 6.18 shows the critical design loads for flange and web buckling versus the deflection of all selected cross-sections. The buckling stresses in Table 6.5 reveal that the local buckling strength of the webs is smaller than the local flange buckling strength, apart from profile $r1h$ as a consequence of its greater flange width. Nevertheless, the critical buckling loads also dependent on beam properties. As reported in literature [143], flange buckling occurs in all single cell box beams before instability in the web arises. A horizontal orientation benefits the web buckling load whereas the critical flange

Table 6.3.: Dimensions of selected cross-sections

Section		A	$t_f = \mathrm{t}_w$	W	H
		[mm^2]		[mm]	
□	$s1$	1300	5	70	70
▯	$r1v$			46.67	93.33
▭	$r1h$			93.33	46.67
◫	$s2$			58	58
▯▯	$r2v$			72.5	36.25
□□	$r2h$			41.43	82.86
▥	$s3$			50	50
▯▯▯	$r3v$			30	60
□□□	$r3h$			75	37.5

Table 6.4.: Flexural behaviour under 3-point bending for cross-sections with same area

Section		D	ψ_D	kF	ψ_{kF}	L	δ	ψ_δ
		[Nmm^2]		[Nmm^2]		[mm]		
□	$s1$	2.76 E+10	1	6.35 E+5	1	1400	2.62	1
▯	$r1v$	4.18 E+10	1.51	1.29 E+6	2.03	1867	3.6	0.73
▭	$r1h$	1.35 E+10	0.49	2.05 E+5	0.32	933	2.4	1.09
◫	$s2$	1.64 E+10	0.59	1.33 E+6	2.1	1160	2.2	1.19
▯▯	$r2v$	2.16 E+10	0.78	1.91 E+6	3.01	1450	3.13	0.84
□□	$r2h$	9.47 E+9	0.34	7.04 E+5	1.11	829	1.55	1.69
▥	$s3$	1.08 E+10	0.39	1.69 E+06	2.66	1000	2.07	1.26
▯▯▯	$r3v$	1.31 E+10	0.47	2.15 E+6	3.39	1200	2.89	0.91
□□□	$r3h$	7.03 E+9	0.25	1.08 E+6	1.69	750	1.42	1.84

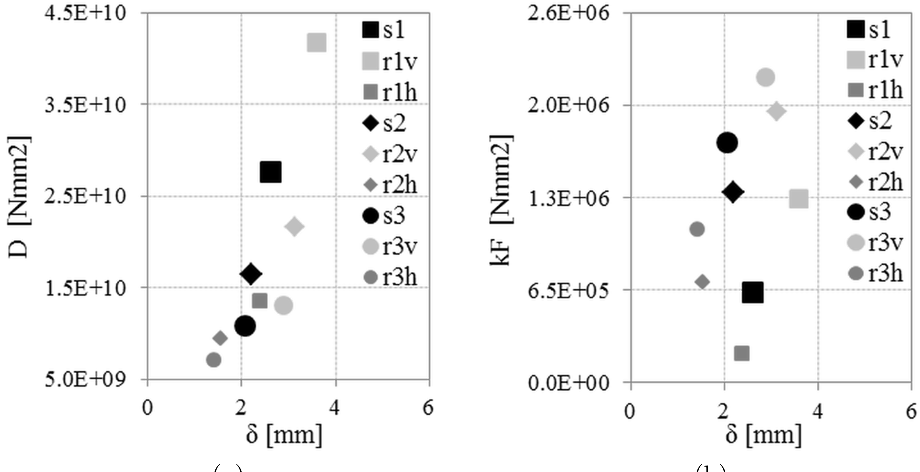

(a) (b)

Figure 6.16.: Flexural response of selected cross-sections with same area

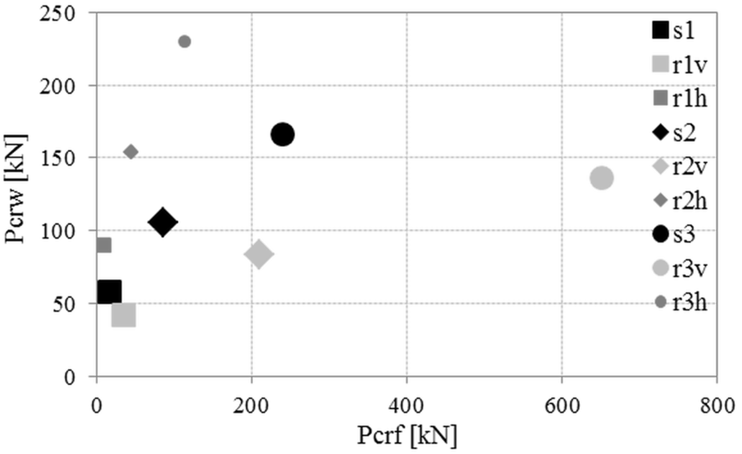

Figure 6.17.: Web buckling vs. flange buckling load for cross-sections with same area

buckling loads are impaired. The addition of stiffeners is improving both the buckling strength and critical buckling load of flanges and webs in multicellular square and horizontally oriented cross-sections. As the flange width in multicellular cross-sections decreases the flange buckling properties improve. Vertically oriented multicellular cross-sections present much better flange buckling strengths and loads owing to their shorter flange widths. Consequently, longer webs in vertical multicellular profiles fail due to instability caused by shear loads, as explained by Barbero and Raftoyiannis [27]. In summary, mainly flanges fail due to local buckling prior to occurring web instabilities. The shorter a web or a flange is, the higher is the local buckling strength of this profile member. As the critical buckling load is dependent on beam properties such as the bending stiffness and its loading span the horizontally oriented rectangular pultruded beam with three cells presents the best flexural and local buckling behaviour, as shown in Figure 6.18.

Table 6.5.: Local buckling stresses and critical design loads for cross-sections with same area

Section		σ_{crf} [MPa]	$\psi_{\sigma_{crf}}$	P_{crf} [N]	$\psi_{P_{crf}}$	τ_{crw} [MPa]	$\psi_{\tau_{crw}}$	P_{crw} [N]	$\psi_{P_{crw}}$
□	$s1$	221	1	1.66 E+4	1	177	1	5.75 E+4	1
▯	$r1v$	538	2.43	3.44 E+4	2.07	96	0.54	4.23 E+4	0.74
▭	$r1h$	120	0.54	9.85 E+3	0.59	430	2.43	8.97 E+4	1.56
◫	$s2$	1330	6.02	8.65 E+4	5.2	266	1.5	1.06 E+5	1.84
◫	$r2v$	3826	17.31	2.09 E+5	12.59	164	0.93	8.3 E+4	1.44
◫	$r2h$	616	2.79	4.53 E+4	2.73	563	3.18	1.54 E+5	2.68
▥	$s3$	4151	18.78	2.4 E+5	14.42	369	2.09	1.66 E+5	2.89
▥	$r3v$	13451	60.84	6.51 E+5	39.19	247	1.4	1.36 E+5	2.36
▥	$r3h$	1716	7.76	1.14 E+5	6.88	708	4	2.3 E+5	4

6.2.2. Analysis of cross-sections with same bending stiffness

Dimensions, stiffness, deflections as well as shape factors of all geometries with same cross-sectional bending stiffness are listed in Table 6.6. Figure 6.19 presents linear mass density savings and gains expressed in percentages. Apart from beam $r1v$ the linear mass density of each cross-section increases. As the bending stiffness is mainly influenced by the beam depth, all vertically oriented profiles present the lowest linear mass density gains in their category. On the contrary, horizontally oriented profiles gain most as shown in Figure 6.19. Similar to the first part of this study, a vertical orientation increases the deflection resulting from an enlarging span. The addition of stiffeners increases the shear stiffness, decreases the span and hence reduces the beam deflection. The smallest deflection can be observed in the horizontally oriented profile with three cells B_{r3h}.

The buckling response of cross-sections with the same bending stiffness matches the response seen in cross-sections with the same area. Apart from profile B_{r1h} the local web buckling strengths are smaller than the local flange buckling strengths. As can be seen from the critical design loads in Table 6.7 the selected cross-sections fail mainly due to local flange buckling. A horizontal orientation benefits the web buckling properties whereas the critical flange buckling properties are impaired. The addition of stiffeners improves distinctly the buckling strength and critical buckling load of flanges. While a vertically oriented single cell beam fails due to local flange buckling, in multicellular vertical profiles local web buckling occurs prior to flange instabilities due to reduced

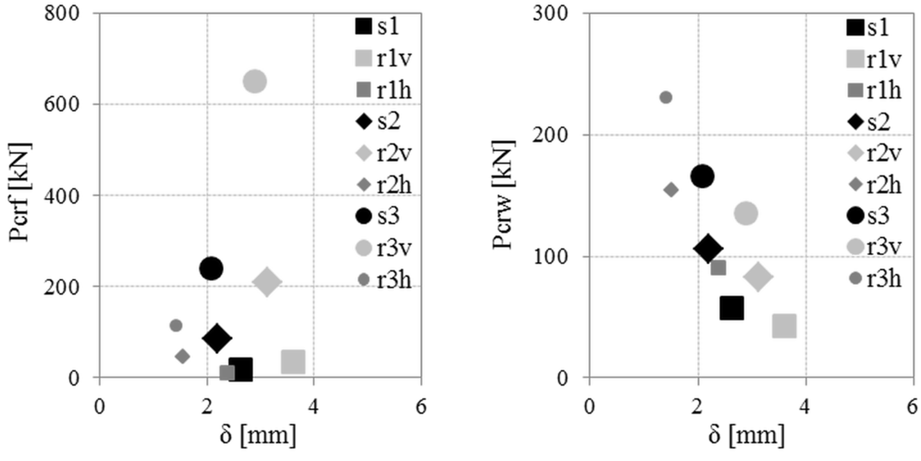

(a) (b)

Figure 6.18.: Critical flange buckling (a) and web buckling (b) design loads vs. beam deflections for cross-sections with same area

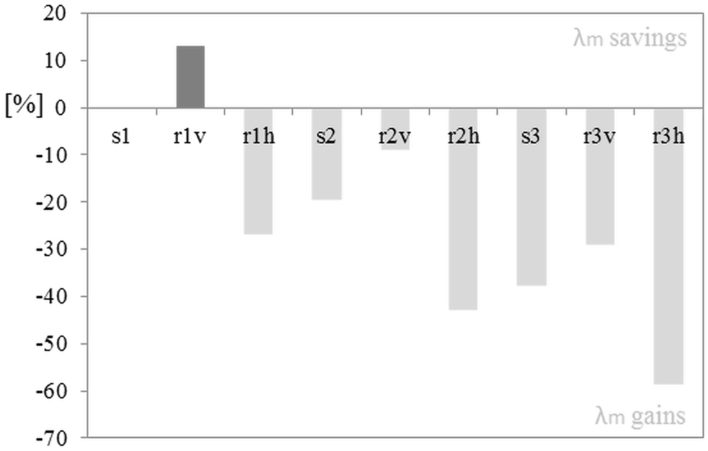

Figure 6.19.: Linear mass density savings in % for selected cross-sections

Table 6.6.: Dimensions and flexural behaviour under 3-point bending for cross-sections with same bending rigidity

Section		D	W	H $[mm]$	A	ψ_m	kF	ψ_{kF}	L	δ	ψ_δ
		[Nmm^2]	[mm]		[mm^2]		[Nmm^2]		[mm]		
□	$s1$	2.76 E+10	70	70	1300	1	6.35 E+5	1	1400	2.62	1
▯	$r1v$		41.02	82.03	1131	1.15	1.13 E+6	1.78	1641	3.69	0.71
▭	$r1h$		116.46	58.23	1647	0.79	2.65 E+5	0.42	1165	2.29	1.15
◫	$s2$		68.02	68.02	1550	0.84	1.59 E+6	2.5	1360	2.11	1.24
◫	$r2v$		39.1	78.19	1414	0.92	2.07 E+6	3.26	1564	3.07	0.85
◫	$r2h$		114.7	57.35	1857	0.7	1.02 E+6	1.61	1147	1.42	1.85
▥	$s3$		66.28	66.28	1788	0.73	2.3 E+6	3.62	1326	1.9	1.38
▥	$r3v$		37.54	75.07	1677	0.78	2.74 E+6	4.32	1501	2.69	0.97
▥	$r3h$		113.06	56.63	2061	0.63	1.72 E+6	2.7	1131	1.25	2.09

Table 6.7.: Local buckling stresses and critical design loads for cross-sections with same bending rigidity

Section		σ_{crf} [MPa]	$\psi_{\sigma_{crf}}$	P_{crf} [N]	$\psi_{P_{crf}}$	τ_{crw} [MPa]	$\psi_{\tau_{crw}}$	P_{crw} [N]	$\psi_{P_{crw}}$
□	$s1$	221	1	1.66 E+4	1	177	1	5.75 E+4	1
▯	$r1v$	720	3.26	3.94 E+4	2.37	126	0.71	4.85 E+4	0.84
▭	$r1h$	75	0.34	8.17 E+3	0.49	264	1.49	7.02 E+4	1.22
◫	$s2$	941	4.26	7.49 E+4	4.51	188	1.06	8.89 E+4	1.55
▯▯	$r2v$	3214	14.54	1.94 E+5	11.65	140	0.79	7.66 E+4	1.33
▭▭	$r2h$	310	1.4	3.48 E+4	2.09	273	1.54	1.07 E+5	1.86
▥	$s3$	2238	10.13	1.88 E+5	11.29	199	1.13	1.22 E+5	2.12
▯▯▯	$r3v$	7941	35.92	5.19 E+5	31.23	152	0.86	1.07 E+5	1.86
▭▭▭	$r3h$	720	3.26	8.3 E+4	4.99	281	1.59	1.45 E+5	2.52

flange widths.

In summary, the addition of stiffeners improves particularly the shear stiffness as well as the local buckling behaviour of flanges and webs. However, each additional stiffener results in bigger cross-sectional areas which leads to linear mass density gains. As the area of vertical members increases the shear stiffness can be enhanced which results in a smaller shear contribution to the deflection. The depth in multicellular profiles is reduced entailing a shorter span and a smaller deflection due to the applied load. Shorter webs induce higher local web buckling strengths. Together with the increasing cross-sectional area for each vertical profile member the critical shear loads are improved. As the flange width decreases in cross-sections with additional webs the local flange buckling strength can be enhanced. Moreover, a smaller profile depth results in a higher section modulus, thus leading to higher critical flange buckling loads. As can be seen from Figure 6.20, multicellular horizontally oriented and square profile geometries, especially cross-sections with three cells, present smaller deflections and higher critical buckling loads compared to the single cell box beams.

6.3. Experimental characterisation of 3DBRC

In this section a material characterisation of the 3DBRCs is presented. Experimental data for 3DBRCs are very rare as 3D braids are no commercial off-the-shelf product. A range of experimental data are available, not comprehensive and mainly the longitudinal tensile properties under quasi-static loading were examined [1,59,83,85,204,205]. The

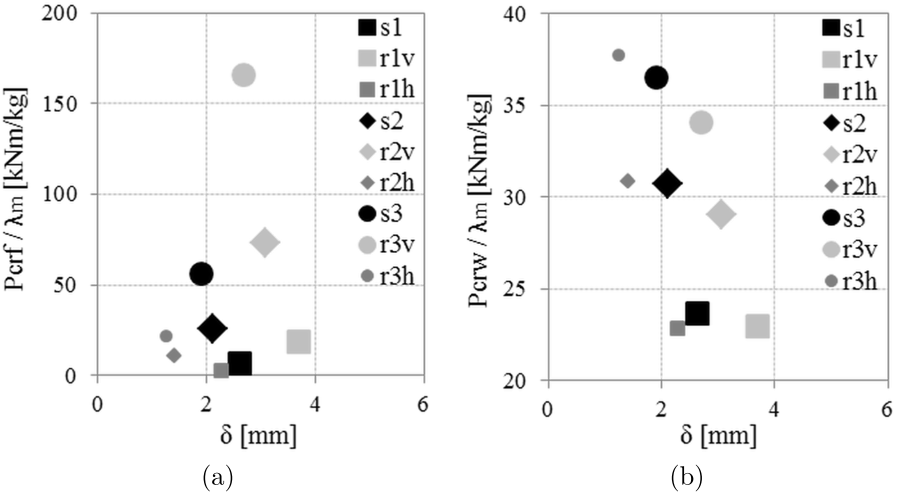

(a) (b)

Figure 6.20.: Critical flange buckling (a) and web buckling (b) design loads normalised over the linear mass density versus beam deflections for cross-sections with same bending stiffness

comparison of experimental results obtained by other authors is difficult as constituents, the braiding process or braid and composite architectures vary [50,65,89,127,206–208]. Out-of-plane properties are difficult to address experimentally, standardised methods are not available. Gerlach [209] developed a cross like shape, obtained by grinding. A U shaped steel rig is used to apply compression loads, which cause a tensile stress state in the specimen centre. Despite, the investigation of stiffness properties was still very difficult as the gauge section was very small. Stig and Hallström [210] adhesively bonded coin shaped specimens between aluminium cylinders to measure the out-of-plane strength. However, an ultimate strength could not be obtained as the specimens showed adhesion failure. Out-of plane properties are not examined in the scope of this work.

The main aim of this research was to investigate the effect of through-thickness reinforcement on failure and damage behaviour of profile shaped composites under lateral loading. Theoretically an extensive characterisation requires tests in all normal and shear directions. However, owing to constraints by limitations in size and quantity of available braided preforms as well as the lack of adequate testing equipment, the four material configurations were identically characterised with restrictions under quasi-static and dynamic loading. The purpose of the tensile experiments was a qualitative and quantitative investigation of the 3DBRCs to serve as validation data for the presented modelling approaches in Chapter 4 and Chapter 5 as well as for comparisons with a 2D laminate. Three point bending and falling weight impact tests address the delamination resistance at quasi-static and low impact rates of loading. The results serve as validation for the developed damage model in Section 5.5. The experimental programme was designed to serve following purposes:

- To provide tensile and flexural stiffness and strength properties

- To characterise local failure and damage mechanisms
- To examine the effect of 3D reinforcement on delamination behaviour
- To investigate and compare the effect of braid type and the addition of axial yarns on properties
- To generate validation data for analytical and numerical models

All experiments were performed identically at room temperature for all four material configurations. The number of specimens per material and experiment was the maximum possible. Several specimen dimensions vary from recommended dimensions according to standards to ensure yarn continuity.

6.3.1. Microstructural analyses

The braided preform has an initial cross-section during braiding due to yarn tensioning, which changes first when the preform is removed from the braiding machine. Details, such as the width W_p, the thickness T_p, the pitch length h_p and the surface braiding angle θ_p, of the loose braided preform were measured and are presented in Table 6.8.

The cross-section changes another time when the preform is consolidated in the mould. Figure 6.21 presents surface views of braided preforms and corresponding consolidated composites. In a first vacuum infusion trial polyester resin was used. The achieved infiltration was very good, however the consolidated composite showed various shrinkage cracks, see Figure 6.22. In the second trial with epoxy resin no cracks could be detected. The microstructure of the consolidated 3DBRCs was microscopically analysed to derive idealised yarn arrangements. Physical dimensions and properties of composite and yarns were determined as averages from micrographs, as shown in Figure 6.23 and 6.24. Although it is aimed to contain measuring inaccuracies which affect modelling results, those cannot be excluded. The dimensions are used as input for the modelling approaches and in turn to validate those. Surface braiding angles, the pitch length, yarn dimensions on the surface and in cross-sectional views were measured, see Table 6.9. Moreover, calcination tests were carried out to obtain fibre weight W_f and fibre volume fractions V_f of the 3DBRCs as well as the laminate. Subscripts a, b and t refer to axial yarns, braider yarns and total, respectively.

Fibre reinforcements in the out-of-plane direction are generally unfavourable for in-plane properties [55]. Additional resin pockets result in reduced fibre volume fractions and thus decreased mechanical properties. In order to be able to compare the effect of each textile architecture to a pultruded laminate it was aimed to obtain composites with equal fibre volume fractions. It can be seen from Table 6.9 that the volume fraction of the vacuum infused laminate is conform with the corresponding pultruded laminate as shown in Table 6.1. Due to differences in textile architecture and composite dimensions the fibre volume fractions of 3DBRCs vary to some extent. Owing to its architecture a smaller fibre volume fraction for the two-step braid reinforced composite is not possible.

Table 6.8.: Preform details of selected braid configurations

Braid type	Configuration	$N^{o}_{Braiders}$	N^{o}_{Axials}	W_p	T_p [mm]	h_p	θ_p [°]
2step	[3x2]	5	8	9.4	2.7	16.9	28.9
4stepWO	[8,4]	44	-	16.7	6.4	9.5	17.6
4stepWI	[8,4]	44	21	20.5	8.4	10.2	17.9

Four-step braided preforms could be more or less adjusted, width and thickness could be compressed to some degree. Whereas the two-step braid was rather fixed in shape owing to its small yarn array. A smaller fibre volume fraction could be just obtained by adding resin-rich edges without reinforcing yarns. Moreover, in consequence of its yarn array the two-step braid is compared to the four-step braids dominated by longitudinal axial yarns.

It can be seen from the micrographs that dependent on the compression of the preform the yarns take different positions and shapes. The two-step braid is very compact, all yarns are in contact with each other. Cross-sections of axial yarns can be idealised as prismatic shapes dependent on their position in the yarn array. Central axial yarns take after consolidation rhombic shapes. Yarns along the outer surface edges are flat and can be assumed as pentagonal shapes. Braider yarns between the axial yarns take rather rectangular shapes. Because of the spiral nature of braider yarns in four-step braids, cross-sections vary along the longitudinal direction. However, yarn cross-sections can be idealised as elliptic shapes. Axial yarns in the 4stepWI take similar to the two-step braid rhombic shapes. Due to the preform compression the orientation of yarn cross-sections varies between yarns in the centre and those on the edges.

6.3.2. Tensile testing

In order to assess the longitudinal in-plane tensile properties rectangular shaped specimens were cut at random positions from the parent material. Compared to UD, 2D and 3D woven composites transverse tensile testing of the braids is not possible due to their rod like design. A change of the specimen thickness and width was avoided, which ensures the continuity of yarns and results in an increased resistance. The results obtained from all tested materials are listed in Table 6.10. Stress-strain curves for each material and typical final damage are presented in Figure 6.25. Tensile test results for

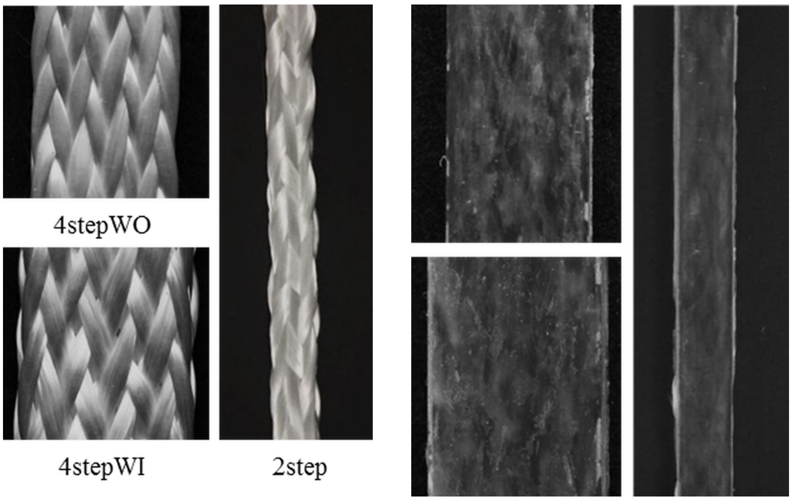

(a) (b)

Figure 6.21.: Surface view of braided preforms (a) and consolidated 3DBRCs (b)

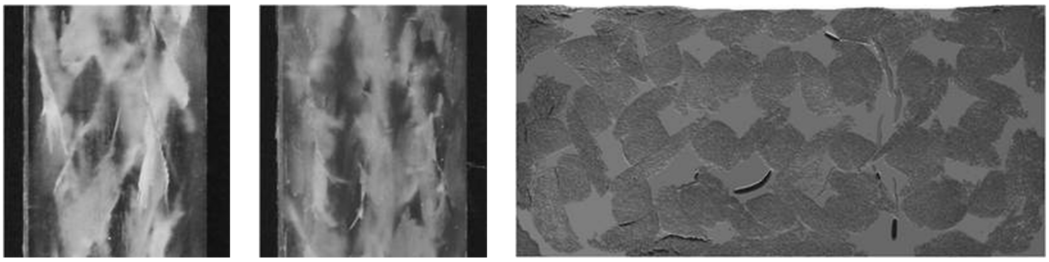

(a) (b) (c)

Figure 6.22.: Shrinkage cracks in four-step braid reinforced composites infused with polyester resin: surface view 4stepWO (a) and 4stepWI (b), cross-section of 4stepWI (c)

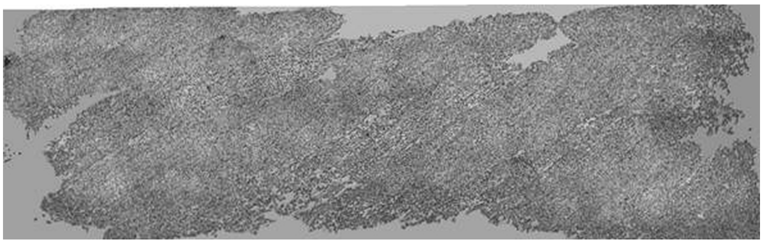

Figure 6.23.: Micrograph of a two-step braid reinforced composite cross-section

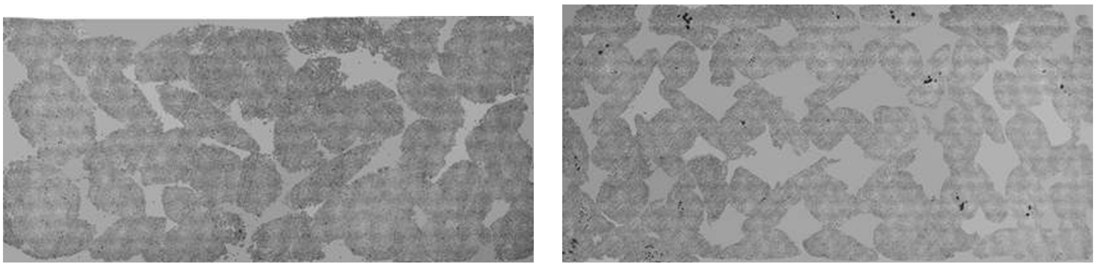

(a) (b)

Figure 6.24.: Micrographs of 4stepWO (a) and 4stepWI (b) cross-sections

Table 6.9.: Measured composite details of selected material configurations

Material	W_c	T_c	φ_c	h_c	θ_c	V_{fa}	V_{fb}	V_{ft}	d	w	w_a	t_a	b	t_b
	[mm]		[°]	[mm]	[°]	[%]			[mm]					
Laminate	-	5.0	-					47.9	-					
2step	8.6	2.5	38.0	10.51	26.8	41.2	29.6	70.8	-		2.82	0.95	2.86	0.39
4stepWO	14.0	6.4	49.4	9.16	21.2	-	44.5	44.5	0.92	2.10	-			
4stepWI	17.1	8.1	45.6	9.87	23.2	13.3	30.5	43.8	0.63	2.85	1.49	1.44	-	

the braid reinforced composites give at the minimum a qualitative evaluation of their mechanical behaviour. Numeric values have to be treated with caution, particularly for the 4stepWI specimens. The specimens broke not just close to the grip, also in the upper tabbed section.

Tensile forces and displacements cannot be compared as the geometric dimensions differ from all materials. The average elastic moduli of the four-step braids are lower and of the two-step braid higher than of the laminate. The elastic properties of the 2step are not only higher due to a longitudinal yarn orientation but also higher due to its higher fibre volume fraction. As aforementioned, tensile testing of the 4steps exhibited unfavourable test endings. Although it cannot be seen from the results, it is assumed that the axial reinforcement enhances the longitudinal modulus. The quasi-static stress strain response of the laminate follows a comparably linear trend. Whereas non-linear stress-strain behaviour can be observed for all braids, indicating progressive failure owing to their complex architecture and the different occurring failure modes. Brittle failure occurs in all materials with final fibre breakage.

Owing to the complex interlaced architecture a failure analysis of a 3DBRC is difficult. Damage states are coupled even under tensile loading [119]. Matrix micro-cracking is recognised first. Its presence mainly induces a stiffness reduction. Laminated specimens delaminate and splinter, whereas 3DBRCs show more localised damage after failure. In two-step braids and 4stepWI specimens the epoxy resin crazes at the crossings between braider and axial yarns, which is visible as whitening. It is believed that the tensile load forced the braider yarns to straighten. When the braid is stretched axially the matrix, which prevents such straightening, is shearing parallel to each yarn and fails [211]. The closer the tensile load approaches its maximum the more noisy crackling accompanies the test. The fracture plane in 4stepWI is perpendicular to the loading direction. In 4stepWO specimens are no continuous longitudinal yarns which can extend in the direction of loading. Instead yarns are transverse to the loading direction and orientations terminate on the specimen edge. Compared to the 4stwpWI the fracture plane of 4stepWO specimens is rather transverse to the loading direction. Damage initiates in yarns close to the edge and propagates as shear failure along their longitudinal orientation. A gradual stiffness reduction can be observed at higher strains, presumably due to matrix cracking. As the specimen elongates, the fibres scissor and cracking within the matrix spreads. Matrix cracking and break off is marked by crackling and progressive fibre rupture by disruptive noise at equal intervals. With increasing load the cracking sounds are cumulative until final rupture.

Corresponding to experimental findings, Fang et al. [119]and Xu [120] showed in FE simulations that matrix damage and fibre damage initiates at the interfaces between yarns and matrix. Li et al. [80] showed in scanning electron micrographs that the matrix shears and deforms plastically. With increasing tensile load matrix failure propagates in the resin pockets. Fang et al. observed in the braider yarns that transverse tensile and shear damage occurs first in stress concentration zones where yarns contact each other. As shown in micrographs of Li et al. [80] fibre bundles are pulled out and

Table 6.10.: Engineering constants obtained for longitudinal tensile testing

Material	Nº tests	Modulus [MPa]		Strength [MPa]	
		Mean	StDev	Mean	StDev
Laminate	5	10390	376.9	671.6	40.4
2step	2	18864	355.6	902.0	0.5
4stepWO	3	8101	535.2	573.1	30.3
4stepWI	3	7478	626.7	445.9	32.6

broken. Fibre failure propagates along the longitudinal yarn direction until damaged zones join neighbouring zones. Jiwei and Feng [121] as well as Xu [120] demonstrated that the occurrence of failure mechanisms in 3D braids is also influenced by the braiding angle. 3DBRCs with lower braiding angles show an almost linear mechanical behaviour. Tensile failure is mainly caused by longitudinal yarn rupture [121], as the fibre damage propagation velocity is high [120]. Increasing braiding angles induce more complex failure mechanisms, including matrix cracking and transverse shear damage. The sequence of occurring damage is shown in a non-linear mechanical behaviour. The propagation velocity is reduced, the fracture strain is increased whereas the tensile strength is reduced [121].

6.3.3. Flexural testing

Flexural properties obtained for all materials are listed in Table 6.10. Representative stress-strain curves for each material and typical final damage are presented in Figure 6.25. The tests were stopped when the loading force reached or passed 50 N in the descending loading phase. Peak and total absorbed energies were determined. The absorbed energy is proportional to the area below the load-displacement curve. To enable a comparison of the results, the energies were normalised to the section modulus S of each beam. In order to analyse the type of observed damage the specimens were cut along the centre line and visually inspected.

The flexural stress-strain curves keep linear until the peak strength is reached. Laminated specimens present a higher peak strength compared to the four-step braid reinforced composites, which can be attributed to its higher tensile strength. 4stepWO specimens are characterised by a single distinct peak, while 4stepWI specimens present successive peaks.

The observed stiffness loss is initiated in all materials at an approximately equal flexural strain, presumably owing to matrix micro-cracking. Once damage occurred in the laminate specimens, it propagated rapidly. Damage was initiated below the

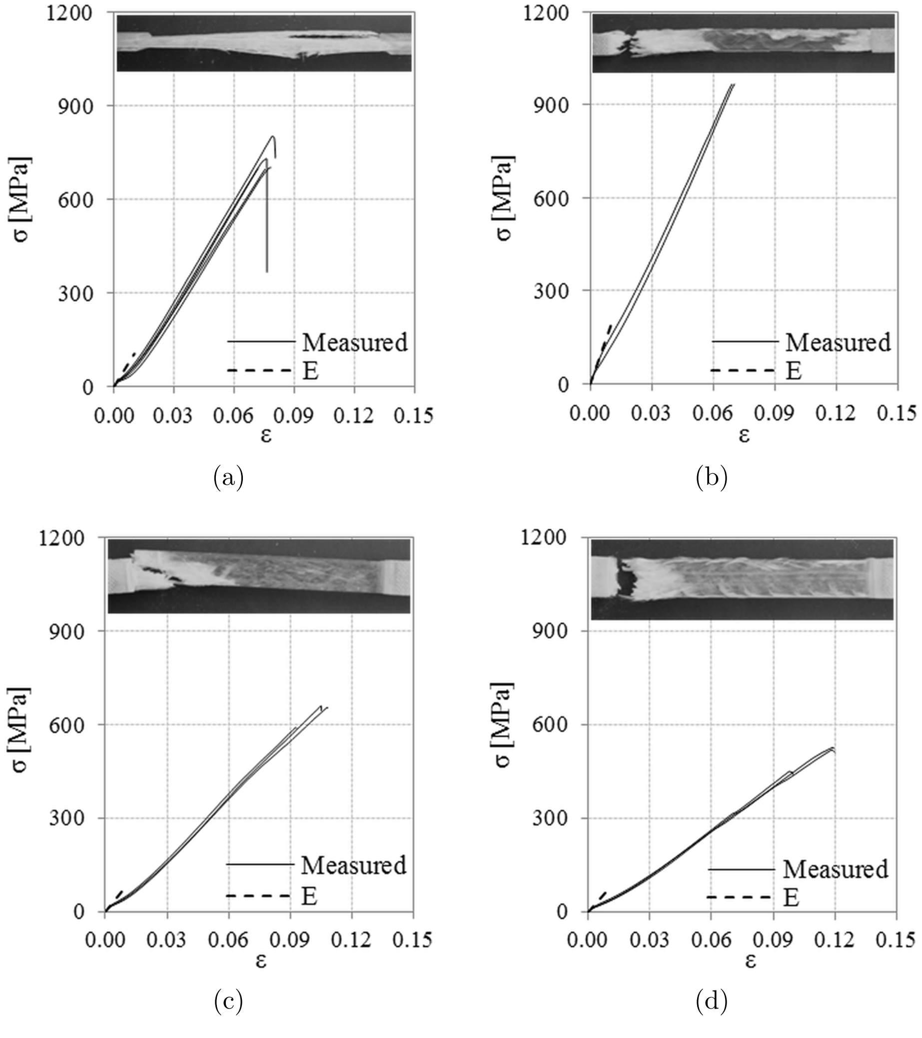

(a) (b)

(c) (d)

Figure 6.25.: True stress-true strain curves of all specimens: laminate (a), 2step (b), 4stepWO(c), 4stepWI(d)

loading nose, propagated as shear cracks accompanied by cracking sound, which led to a distinct stiffness loss. Failure extended wedge-shaped from the top to the centre of the specimen. Matrix damage also occurred on the bottom side due to high tensile bending stresses. Cracks propagated through the ply thickness and along the ply interfaces. Moreover mat and UD yarns ruptured, further load drops were observed. Fibre-matrix debonding extended into the UD layer. Inter-ply failure was the final mode observed in the laminated composite material which impaired its strength. The upper and lower mat layers are delaminated from the UD layer. Due to occurring delamination events laminate properties present a bigger scatter as shown in Figure 6.26(a) and visible from the standard deviation of the normalised total absorbed energy in Figure 6.26(d).

Damage propagated in the 3DBRCs gradually and accumulated with a slower speed compared to the laminated material. 3DBRCs lose their load bearing capacity successively, the span between the peak strength and the test stop is longer. In both materials the resin matrix is damaged below the loading nose. A wedge-shaped blurring and whitening of the matrix is visible. Due to deflection different oriented braider yarns close to the surface are broken out of the matrix and partially ruptured. On the tension side of the beams braider yarns as well as axial yarns in the 4stepWI are ruptured. Fibre fracture extended progressively further than the neutral axis into the upper beam section. The remaining load bearing capacities are enabled by yarns on the compression side of the beam. 4stepWI specimens present lower flexural peak strengths but higher flexural moduli owing to the axial yarn reinforcement. Compared to the laminated material the normalised peak energy is lower, whereas the normalised total energy is equal. Thus, it is concluded that the progressive damage behaviour due to yarn interlacement is contributing to a higher resistance to lateral loads of four-step braid reinforced composites.

6.3.4. Impact testing

Several factors, such as material and testing conditions influence the impact damage response. In the scope of this work, only the fibre architecture was investigated. All specimens were subjected to drop weight impact tests using a Charpy impactor with energy levels of 98 J and 196 J. The specimens are placed such that the loading direction coincides with the thickness direction. Three specimens per energy level are tested for the laminated material and for the 3DBRC. Absorbed energies, ductility indices as well as Charpy strengths were determined. The results obtained from all tested materials are listed in Table 6.12. Representative load-time and energy-time curves for each material and impact energy are presented in Figure 6.25. The absorbed energy is proportional to the area below the force-time curve. The initiation energy E_i equals the energy absorbed up to the peak load and the propagation energy E_p the energy absorbed after the peak load. The ductility index, which is the ratio of propagation to initiation

Table 6.11.: Engineering constants obtained for flexural testing

Material	Nº tests	Modulus [GPa]		Peak load [kN]		Strength [MPa]		E_{peak}/S [J/mm^3]		E_{total}/S	
		Mean	StDev	Mean	StDev	Mean	StDev	Mean	StDev	Mean	StDev
Laminate	5	26.20	1.27	1.25	0.08	631.36	29.12	0.10	0.01	0.19	0.02
4stepWO	3	26.39	0.60	1.94	0.17	528.92	45.04	0.06	0.01	0.18	0.01
4stepWI	3	28.58	0.97	2.89	0.28	505.97	37.97	0.06	0.01	0.20	0.01

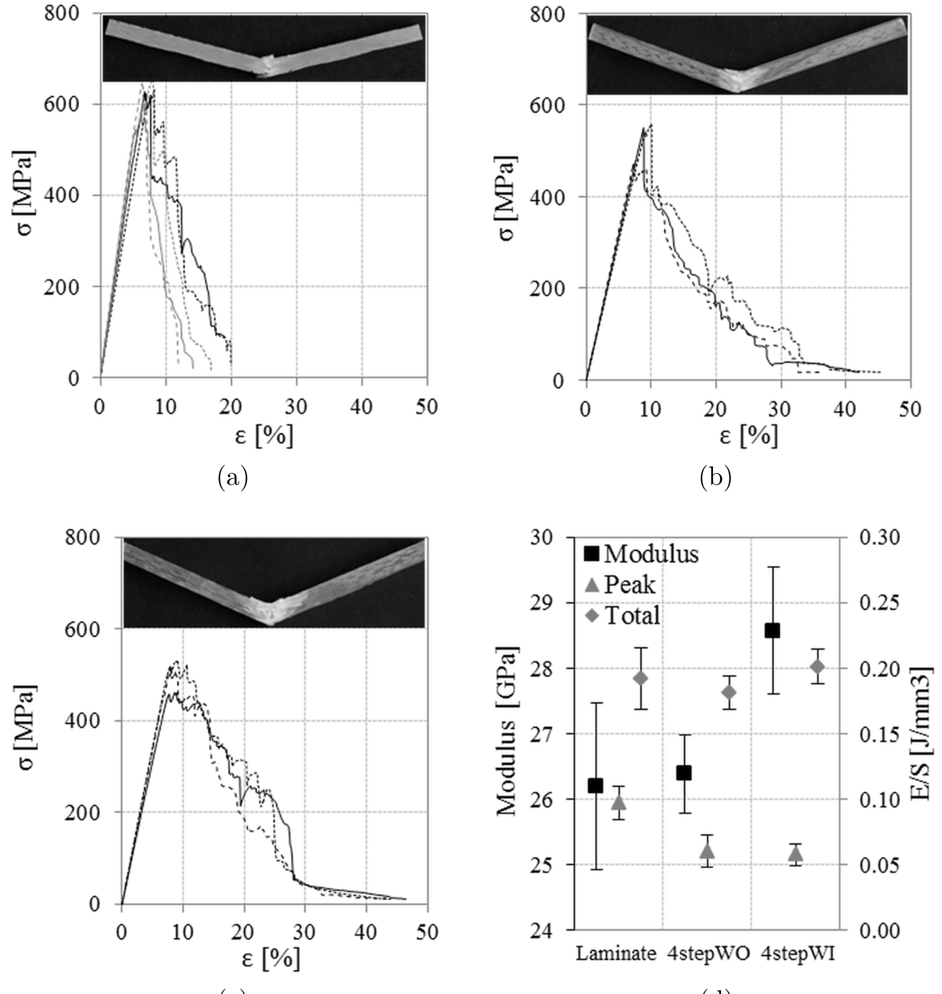

(a) (b)

(c) (d)

Figure 6.26.: Flexural stress-strain curves of all specimens: laminate (a), 4stepWO (b), 4stepWI (c), comparison of flexural moduli and normalised absorbed energies (d)

energies, provides information about the fracture behaviour. The bigger the ductility index the more ductile behaves the material. The Charpy strength is defined as the ratio of the total absorbed energy to the cross-sectional area.

The load-time curves of all specimens show slight vibration during the initial stage, which was probably due to vibration of the unclamped specimen ends. Peak loads of the four-step braid reinforced composites are higher than of the laminated specimens, resulting from their bigger cross-sections. In order to compare load bearing capabilities, absorbed energies were normalised to the section modulus of each beam. The normalised initiation and propagation energies in laminated specimens are for both impact energies approximately equal. A large initiation energy and a small propagation energy, also denoted by a small ductility index, indicates a brittle high strength material [212]. The initiation energies in 4stepWO and 4stepWI specimens are lower, whereas the propagation energies are higher. Ductility indices and Charpy strengths are for both impact energies higher than the values for the laminated specimens. Therefore it was concluded that the 3DBRCs have a higher impact resistance. It can be seen from Figure 6.27(d) absorbed energies and Charpy strengths neither increase nor decrease distinctly with increasing impact energy.

Textile reinforced composites subjected to low velocity impact dissipate the imparted energy through various failure modes rather than through deformation alone. Occurring failure mechanisms can be generally distinguished between matrix cracking, fibre-matrix interface debonding and yarn rupture. In laminated specimens the final damage mode is inter-ply failure. Damage propagated parallel to the fibre direction of the inner UD layer. In 3DBRC specimens the damage is localised to the area under the impactor and spreads in the thickness direction. Due to yarn interlacement damage can also not propagate along the axial yarns in the 4stepWI. Figure 6.28 shows damage in all representative specimens impacted at 98 J and at 196 J.

Laminate damage was initiated below the loading nose leading to transverse cracking as shown in Figure 6.28(a). Matrix damage also occurred on the bottom side due to high tensile bending stresses. Matrix cracks propagated leading to debonding on ply interfaces. Fibre failure occurred in mat and UD yarns. Yarns of mat and UD layers on the compression side remain undamaged, enabling some residual strength.

Matrix damage was first initiated on the upper surface of 4stepWO specimens below the striker. Due to deflection variously oriented braider yarns close to surface were broken out of the resin matrix and in specimens subjected to 196 J partially ruptured, as shown in Figure 6.28(c) and (d). Tensile failure occurred in the matrix on the bottom surface and yarns were partially broken out. In specimens subjected to the higher impact energy, see Figure 6.28(d), it can be observed that fracture on the compression side as well as tensile matrix damage extended further, causing fibre-matrix interface debonding as well as yarn fracture. A small amount of residual strength remained, resulting from a few yarns in the upper beam section. Similar to 4stepWO specimens, matrix damage on the compression side occurred first below the impactor. Subsequent transverse cracking could be observed. From the damaged specimens in Figure 6.28(e)

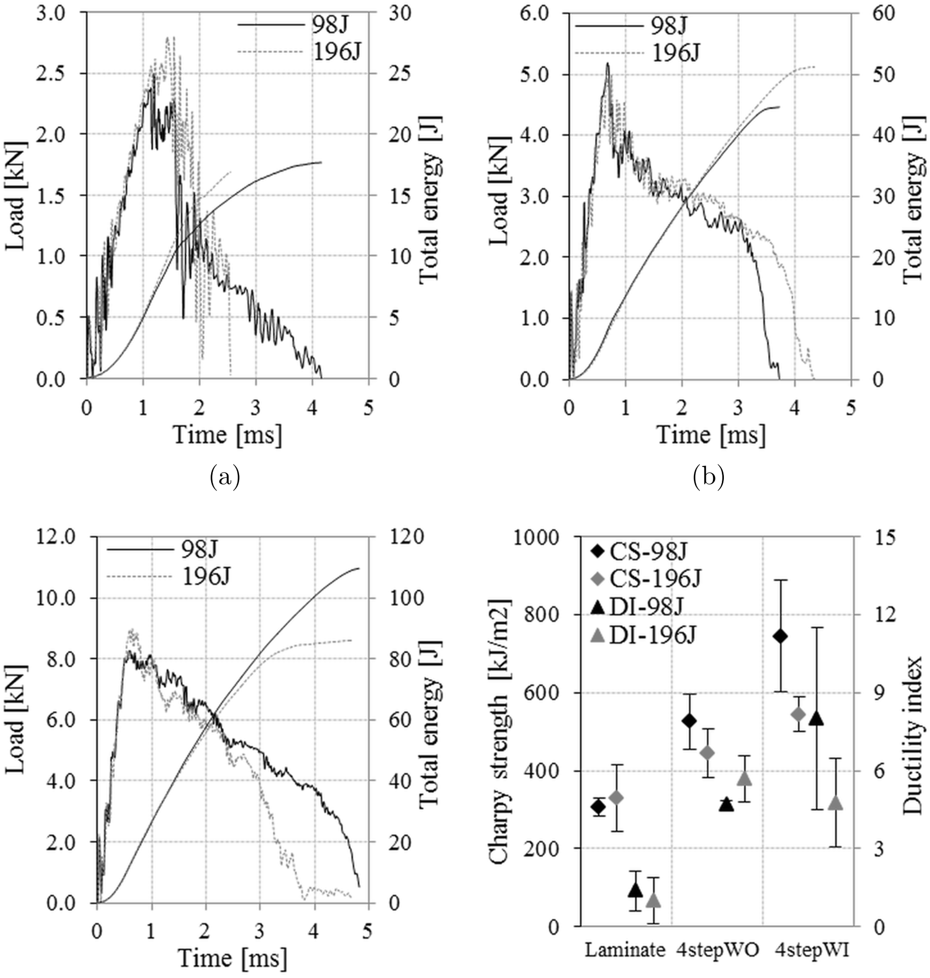

(a)

(b)

(c)

(d)

Figure 6.27.: Representative load-time and energy-time curves of all specimens: laminate (a), 4stepWO (b), 4stepWI (c), comparison of Charpy strength and ductility indices (d)

and (f) it can be seen that surface yarns are broken out and partially ruptured. On the tension side of the specimens braider yarns were similarly ruptured. Tensile failure as well as compressive failure extended through the matrix and axial yarns, causing fibre-matrix interface failure. Specimens subjected to 196 J were completely fractured through the thickness, see 6.28(f). The deflection of both 3DBRCs increased with the impact energy. All four-step braid reinforced specimens showed a wedge-shaped, almost rectangular matrix blurring through the thickness.

Table 6.12.: Loads, strengths and absorbed energies obtained for impact testing

Impact energy	Material	Nº tests	Peak load [kN]		$E_{initiation}/S$ [J/mm^3]		$E_{propagation}/S$		Ductility index		Charpy strength [kJ/m^2]	
			Mean	StDev	Mean	StDev	Mean	StDev	Mean	StDev	Mean	StDev
98 J	Laminate	3	2.40	0.22	0.18	0.07	0.21	0.06	1.38	0.77	306.74	21.61
	4stepWO	3	5.14	0.36	0.09	0.01	0.41	0.05	4.68	0.18	526.58	70.49
	4stepWI	3	8.25	0.00	0.08	0.03	0.54	0.08	8.02	3.50	743.80	142.55
196 J	Laminate	3	2.73	0.24	0.22	0.07	0.20	0.14	1.01	0.89	330.08	84.33
	4stepWO	3	4.72	0.40	0.08	0.02	0.42	0.06	5.67	0.88	444.92	63.03
	4stepWI	3	8.97	0.09	0.09	0.03	0.41	0.04	4.76	1.70	543.44	44.61

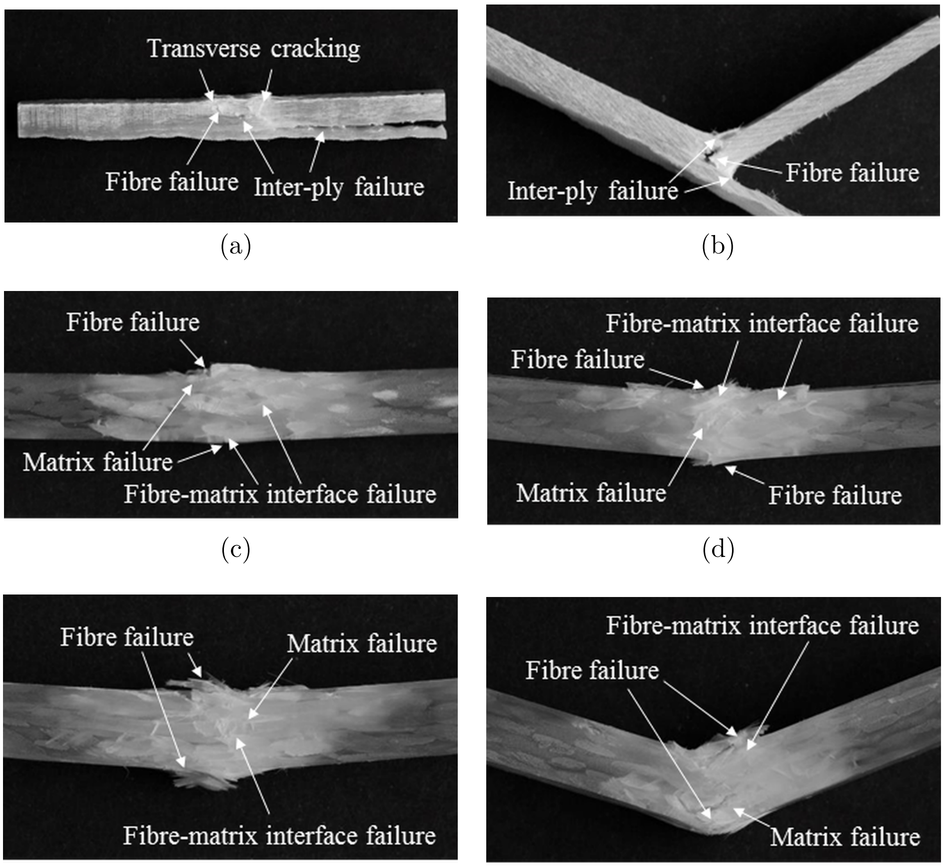

(a) (b)

(c) (d)

(e) (f)

Figure 6.28.: Damage states in representative specimens: laminate subjected to 98 J (a), laminate subjected to 196 J (b), 4stepWO - 98J (c), 4stepWO - 196J (d), 4stepWI - 98J (e), 4stepWI - 196J (f)

6.4. Analytical predictions for 3DBRCs

6.4.1. 3D braided preforms

The analytical models described in Section 4.2 were employed to have a first idea of yarn and preform dimensions. For both braid types GF yarns with a linear yarn density of 2400 tex were used. The distances between axial yarns on the machine bed are fixed to 70 mm. Converging heights were measured and are approximately 140 mm and 155 mm for the 4stepWO and the 4stepWI, respectively, as well as 170 mm for the 2step. A packing factor of 0.7 for braider yarns in four-step braids and 0.75 for axial yarns in four-step braids as well as those in the 2step were used. Moreover, a yarn aspect ratio of 2 for four-step braids, an aspect ratio of 1 for central axial yarns, which corresponds to a square cross-section, and an aspect ratio of 0.1 for braider yarns in the two-step braid were assumed. The resulting estimates of yarn and preform dimensions are presented in Table 6.13.

It can be seen from Table 6.8 and Table 6.13 that the measured and estimated dimensions are different. As aforementioned in Section 4.2, the preform shape is defined by the braid pattern whereas varying dimensions can be ascribed to differences between the on-the-machine state and the out-of-the-machine state as well as handling. The out-of the machine 2step is wider and flatter, thus it can be deduced that the surface braiding angle is increasing, and the central axial yarns are not square and rather flat as seen in the micrograph (Figure 6.23). The width of the manufactured four-step braids is smaller, whereas the thickness is increased. Moreover, it can be seen from the pitch lengths that the braids are not close to yarn jamming, thus the structure is not highly compacted. A finding which can be confirmed by microscopy (see Figure 6.24).

6.4.2. Four-step braids

Analytically obtained elastic properties for the 4stepWO and the 4stepWI, using the measured composite and yarn dimensions listed in Table 6.9, are presented in Table 6.15. As experimental results have to be treated with caution a direct comparison is difficult. Nevertheless, Table 6.15 presents percent errors between the experimentally known and the analytically calculated results. The analytical moduli are higher than the obtained experimental values, although the predicted volume fractions V_f are in good agreement. It can be seen from Table 6.15, a good agreement with the experimentally obtained inclination angle φ was found as well. Moreover, the addition of axial yarns enhances according to the predictive model the longitudinal modulus E_{xx}. The transverse moduli are also increased, whereas the shear properties are in part reduced.

As described in Section 5.3, various numerical studies were conducted to analyse the effect of yarn misalignment and distortion by implementing a modulus reduction of 10%. Therefore, elastic properties were recalculated using a knockdown factor for the longitudinal modulus of each UD yarn segment. As expected the elastic properties of

Table 6.13.: Estimated preform dimensions

Material	d	w	w_a	t_a	b	t_b	W_p	T_p	h_p	θ_p	θ_j	h_j
					$[mm]$					$[°]$		$[mm]$
2step	-		1.57	1.57	3.51	0.35	5.62	3.55	13.64	21.6	-	1.90
4stepWO	0.92	1.83	-				18.36	5.10	4.17	26.1	49.3	2.42
4stepWI			1.57	1.57	-		23.21	6.05	4.38	24.8		

Table 6.14.: Ranges of values used in parametric study for four-step braid reinforced composites

Parameter		Original value	Initial value	End value	Interval
Inclination angle	φ [°]	45	15	75	15
Surface braiding angle	θ [°]	20	5	50	15
Packing factor of braiders	κ_b	0.7	0.6	0.8	0.5

the 3DBRCs are decreased. A knockdown of 10% leads in a 4stepWO to a reduction of about 5% for the longitudinal modulus and the shear moduli as well as a decrease of 2% for the out-of-plane modulus, whereas the change of the transverse modulus is negligible (see Table 6.15). In the 4stepWI, on the other hand, is the longitudinal modulus decreased by 7%, the transverse modulus by about 5% and the out-of-plane modulus by 2%. The reduction of the in-plane and transverse shear is about 4%, whereas the influence on the out-of-plane modulus is negligible.

In order to understand the influence of processing parameters on the predicted elastic properties of 4steps parameter studies were performed. Fixed composite dimensions imply additional processing constraints. Therefore, the analytical model presented in Section 4.3.1 was rearranged using equations 4.19-4.25 for yarn and preform dimensions. Processing parameters which affect the elastic properties have been identified and varied independently while the other parameters were kept at their original values. The braiding angle α influences the yarn orientation inside the braid, therefore a varying surface braiding angle θ as well as φ entail a variation of α. As reported in Section 4.3.1 the ideal inclination angle is 45° and set as original value. A packing factor κ_b of 0.7 for the braider yarns in both braids and packing factor κ_a of 0.75 for the axials were used. The effect of κ_a in the 4stepWI on the V_f and the properties is negligible and therefore not included in the presented results. The original values of θ and of the braider aspect ratio, which equal 20° and 4, respectively, are based on data of the manufactured braids. The parameter ranges as well as the original values are given in Table 6.14. Figures 6.29(b)-(f) and Figure 6.30(b)-(f) present variations of the total V_f, Young's and shear moduli as functions of the processing parameters.

Dependent on the aspect ratio of braider and axial yarns the braid dimensions, such as width, thickness and pitch length, are varying. However, an effect on the properties cannot be observed. An increasing φ induces an increase of α in the 4stepWO as well as in the 4stepWI. A braid with φ equal to 45° exhibits a transverse isotropic material behaviour. The symmetry axis is aligned with the longitudinal braid direction. A variation of φ influences the material behaviour, so that the 4step is anisotropic. It can be seen in Figure 6.29(b) and Figure 6.30(b) that a maximum V_f is obtained for an inclination angle of 45°, thus the longitudinal modulus is the greatest as shown in Figure 6.29(c) and Figure 6.30(c). The transverse moduli E_{yy} and E_{zz} as well as in-plane shear moduli behave differently. E_{yy} and G_{xy} attain their maximum at 30° and decrease with increasing φ. On the other hand E_{zz} and G_{xz} increase until 60° and decrease after, a distinct knee can be observed in the curve (Figure 6.29(d)). The addition of axial yarns causes no effect on this behaviour. The vertex of the out-of-plane modulus G_{yz} in both four-step braiding is at 45°, see Figure 6.29(f) and Figure 6.30(f). An increasing θ causes an increasing α and thus a decreasing h. Consequently, the V_f as well as the longitudinal modulus are reduced with increasing θ, whereas the transverse moduli go down and up, and the shear moduli behave contrary. E_{yy} and E_{zz} of the 4stepWO attain a minimum at 20° and for the 4stepWI at 35°. All properties of the 4stepWI are greater than the moduli of the 4stepWO. It can be seen from Figure 6.29(e)-(f) and Figure 6.30(e)-(f) that G_{xy} and G_{xz} attain their maximum in both braids at 20°, on the other hand G_{yz} increases with increasing θ. At about 50° h is smaller than h_j the jamming condition is reached and the braid is most compact. The bigger the braider yarn packing factor κ_b, the smaller is the braided preform and the shorter is h. The V_f is increased and the greater are the elastic properties. It can be seen from Figure 6.29(b)-(f) and Figure 6.30(b)-(f) that an increasing κ_b implies a linear growth.

6.4.3. Two-step braids

Analytical results obtained for the two-step braid reinforced composite, using the measured dimensions in Table 6.9, are presented in Table 6.15. A comparison between the Young's modulus obtained during tensile testing and the analytical longitudinal modulus is presented in Figure 6.316.31(a). A good agreement with the experimental result was found.

Similar to the four-step braid reinforced composites, the elastic constants of the 2step were recalculated using a knockdown factor of 10% for the longitudinal modulus of the braider yarns. Owing to its architecture it is assumed that the axial yarns of the 2step are straight and aligned. The longitudinal shear modulus and the longitudinal modulus are particularly influenced and decreased, as shown in Table 6.15.

A 2step is mainly reinforced in the longitudinal direction, therefore the longitudinal modulus is greatest as might be expected. However, also transverse properties and shear moduli can be favourably influenced by processing parameters. In order to understand the influence of processing parameters on the elastic constants of a 2step a parameter study was performed. The analytical model presented in Section 4.3.2 was rearranged using equations 4.26-4.31 for preform parameters. Geometric and processing parameters which affect the elastic properties have been identified and varied independently while the other parameters were kept at their original values. The linear yarn densities of axial and braider yarns, which ranged between 600 tex and 4800 tex, were altered by introducing a linear density ratio $\frac{\lambda_a}{\lambda_b}$. The following combinations were analysed: 1200/2400, 2400/2400, 2400/1200, 2400/600 as well as 4800/600. Moreover,

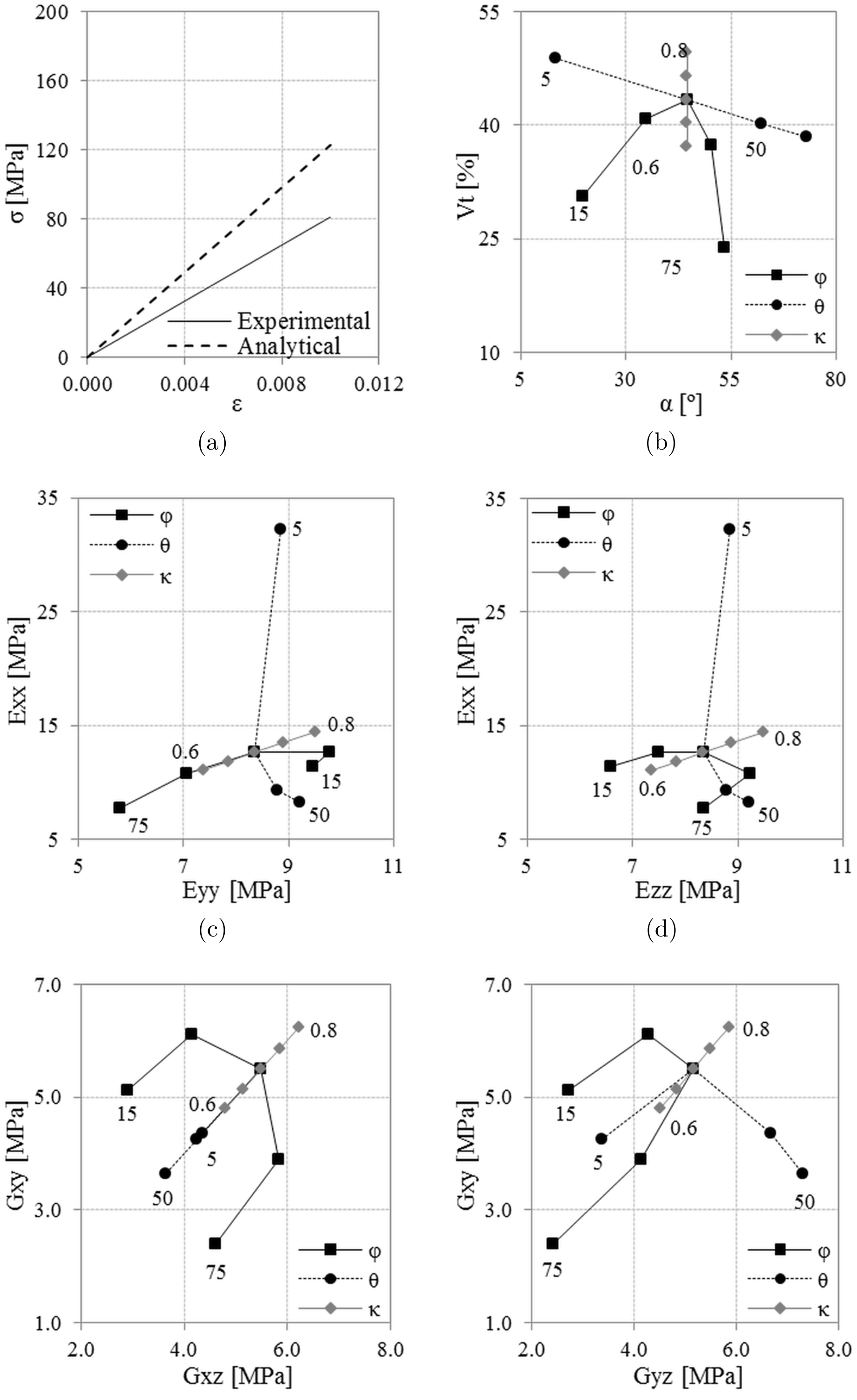

(a) (b)

(c) (d)

(e) (f)

Figure 6.29.: Analytical longitudinal modulus of 4stepWO (a) and results of parametric study (b)-(f)

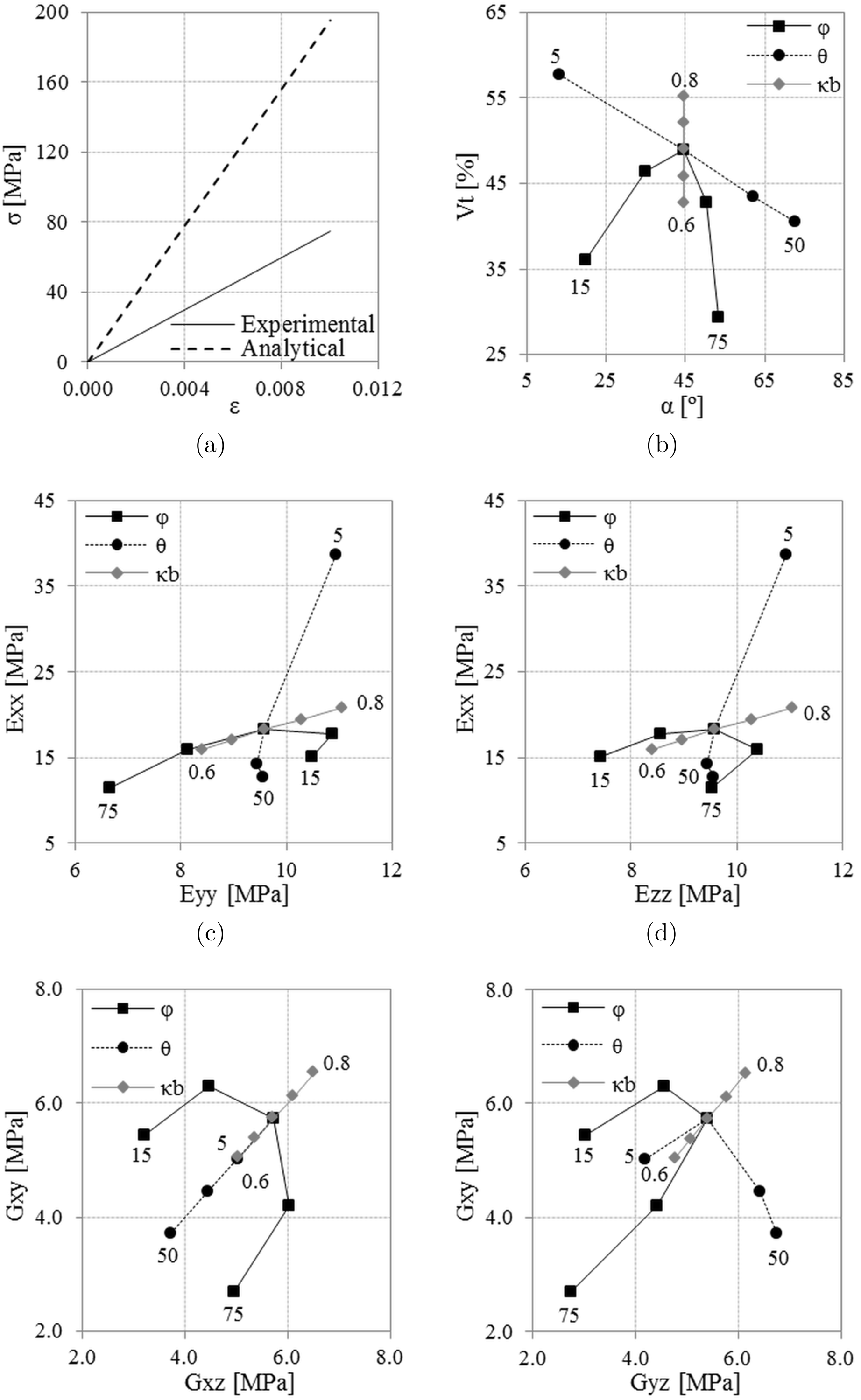

(a) (b)

(c) (d)

(e) (f)

Figure 6.30.: Analytical longitudinal modulus of 4stepWI (a) and results of parametric study (b)-(f)

Table 6.15.: Composite details and elastic constants obtained by analytical modelling

Material	α'	φ	Error	V_{ft}	Error	E_{xx}	Error	E_{yy}	Error	E_{zz}	Error	G_{xy}	Error	G_{xz}	Error	G_{yz}	Error
	[°]			[%]		[MPa]	[%]	[MPa]	[%]	[MPa]	[%]	[MPa]	[%]	[MPa]	[%]	[MPa]	[%]
2step	27.9	37.2	2.1	73.1	3.2	18506	-1.9	5170	-	5149	-	2140	-	1930	-	1910	-
						18396	-0.6	5172	0.0	5152	0.1	2104	-1.7	1925	-0.3	1910	0.0
4stepWO	-	50.6	2.3	43.9	-1.4	12261	51.4	8157	-	9219	-	5095	-	5928	-	5376	-
						11693	-4.6	8131	-0.3	9061	-1.7	4833	-5.1	5557	-6.3	5078	-5.5
4stepWI	-	48.6	1.6	45.8	4.5	19536	161.2	14794	-	10443	-	4699	-	5017	-	3462	-
						18107	-7.3	13982	-5.5	10210	-2.2	4518	-3.9	4794	-4.4	3445	-0.5

Table 6.16.: Ranges of values used in parametric study for two-step braid reinforced composites

Parameter		Original value	Initial value	End value	Interval
Linear density ratio	$\frac{\lambda_a}{\lambda_b}$	1	0.5	8	double
Aspect ratio of axials	f_a	1	0.2	1.8	0.4
Aspect ratio of braiders	f_b	0.1	0.05	0.25	0.05
Surface braiding angle	θ [°]	20	5	60	15

the aspect ratios of axial and braider yarns as well as the surface braiding angle were varied. The original values are based on data of the manufactured preform. A packing factor of 0.75 was used for axial and braider yarns. The effect of the packing factor in axial and braider yarns on the properties is marginal and therefore not included in the presented results. The parameter ranges as well as the original values are given in Table 6.16. Figures 6.31(b)-(f) present variations of the V_f, Young's and shear moduli as functions of the processing parameters.

The 2step exhibits a transverse isotropic material behaviour. The plane of isotropy is normal to the longitudinal braid direction. The linear yarn densities have the biggest effect on the elastic constants. By increasing the linear density of the axial yarns all properties can be increased and by decreasing the linear density of the braider yarns the gain can be enlarged. A $\frac{\lambda_a}{\lambda_b}$ of 0.5 implies that the linear density of the braider yarns is bigger than the linear density of the axials. Although the V_f attains the maximum value, it can be seen from Figure 6.31(e) and (f) that the properties are the lowest. The smaller the f_a, the smaller is the inclination angle, thus the flatter are the axial yarns. For this reason the braid is wider, the braiding angle α' is bigger and the h is smaller. Curves in Figure 6.31(b) and (c) present a distinct knee indicating that there is an ideal inclination angle (to be exact about 55°) to obtain a high V_f and moduli. The bigger the f_a, the smaller are the V_f of the braider yarns and the braid, which adversely affects the elastic properties. The bigger the f_b, the thicker are the braider yarns. Consequently the braid is wider, α' is smaller and h is longer. As a result, the V_f is reduced, both the V_f of the axial yarns and of the braider yarns, and hence the elastic constants are decreased. A varying θ has no effect on the V_f of the axial yarns (Figure 6.31(c)). On the other hand with increasing θ the α' increases and the h decreases, thus the V_f of the braider yarns increases (Figure 6.31(d)). The calculated α' is similar to θ but reduced as it is an average. Although the total V_f is increasing, as the longitudinal elastic modulus is mainly influenced by the axial yarns, only a slight change is visible. However, the increasing V_f of the braider yarns affects the transverse modulus as well as the shear moduli and induce an increase.

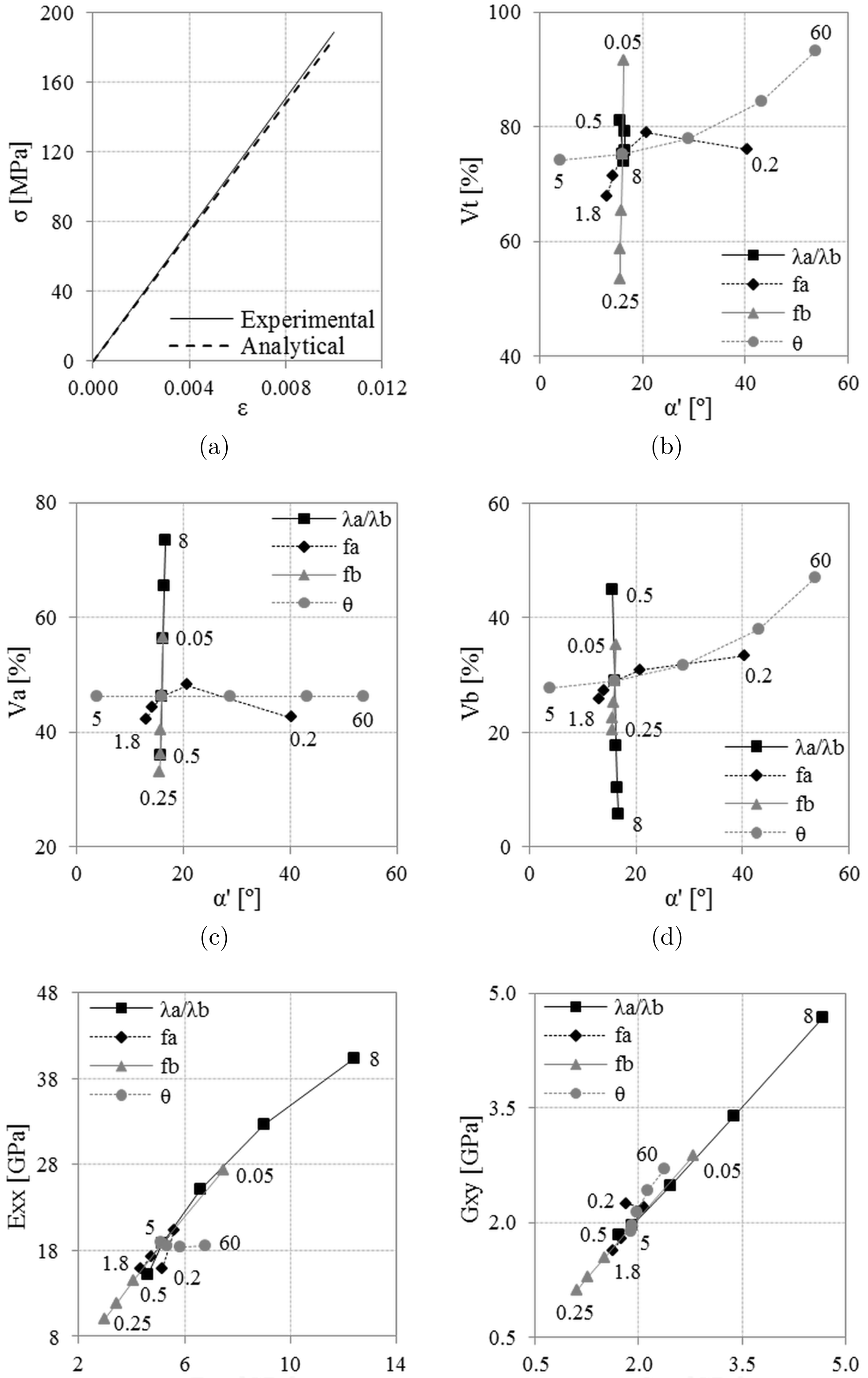

(a) (b)

(c) (d)

(e) (f)

Figure 6.31.: Analytical longitudinal modulus of 2step (a) and results of parametric study (b)-(f)

6.5. Numerical predictions for 3DBRCs

6.5.1. FE modelling study

Single yarn models

The longitudinal moduli of the 3D FE models (Figure 6.32(a)) coincide with the values of the analytical models. For low V_f the moduli obtained in the 1D FE models agree well with the analytical and 3D FE models, whereas the higher the V_f the bigger is the discrepancy. The cross-section, whether cylindrical or elliptical, has no effect on the longitudinal modulus. The results for the transverse modulus (Figure 6.32(b)) show distinct differences between analytical models, 3D as well as 1D numerical models and a particular dependence on the V_f. The Halpin-Tsai model is considered as the best for predicting the transverse modulus [150]. The results of the cylindrical 3D FE model and the Halpin-Tsai model present not only a similar trend but also numeric coincidence. The influence of the elliptical yarn cross-section and its orientation on the transverse modulus is evident, especially for higher V_f. The 1D FE model proposed by Cox [101] underestimates the transverse moduli for all V_f. Although the 1D FE models derived from Chamis and Halpin-Tsai overestimate the moduli slightly compared to the cylindrical 3D FE model, the results present a good agreement of the trend for all V_f. The in-plane shear moduli (Figure 6.32(c)) obtained by analytical and 3D numerical modelling coincide well for all V_f. The 1D FE models based on Cox undervalue the properties, whereas the models based on Chamis overestimate the in-plane shear moduli. A comparison of the in-plane shear moduli with the out-of-plane moduli (Figure 6.32(d)) reveals the transverse isotropic material behaviour of the UD composite. The analytical models as well as the 3D FE models present this material characteristic. The 1D FE models based on Cox and Chamis assumed an isotropic matrix material, whereas the model based on Halpin-Tsai considers transverse isotropy. Moreover, it can be seen that the yarn cross-section affects the out-of-plane shear properties more than the in-plane shear results. The cylindrical 3D FE model and the 1D FE model based on Cox follow a similar trend, whereas the elliptical model coincides with the analytical models. The properties obtained with the truss and beam element models coincide.

The V_f of a single yarn in a textile reinforced composite generally constitutes only a fraction of the analysed volume fractions. However, as the effective medium in the 1D modelling approach represents the transverse and shear properties of the whole fibre reinforcement V_f up to 60% are possible. The analysis of different UD composites shows that moduli obtained with 3D FE models present a good agreement with analytical methods. 1D FE models undervalue the longitudinal modulus for high V_f, whereas transverse and shear properties coincide well dependent on the material formulation. Particularly, the definition of shear properties has to account for the transverse isotropy of a UD composite. The cross-sectional yarn shape in 3DBRCs varies continuously along the yarn length. The comparison of cylindrical and elliptical yarn showed that transverse properties and out-of-plane properties are especially influenced by the yarn shape.

Models with ten yarns

Figure 6.33(a) and6.33(b) present the results of all 1D FE models with truss elements. As already observed in the single yarn models the 1D element models present no mesh sensitivity. In all models the same values for all elastic constants are obtained although the number of elements between the coarsest and the finest mesh differs enormously. The coarsest mesh of the effective medium consisted of 308 elements and the finest mesh of 115184 elements. At low V_f the elastic constants based on Chamis are the highest and in the model based on Cox the lowest (Figure 6.33(a)). At high V_f the longitudinal as well as the transverse moduli based on Halpin-Tsai are the highest (Figure 6.33(b)). While the in-plane shear properties based on Chamis and Halpin-Tsai are similar, results based on Cox are clearly underestimating the real properties.

From all three 1D element models are results based on formulations by Halpin-Tsai closest to the elastic constants of the 3D element models for low as well as high V_f, except for the out-of-plane shear modulus. In this particular case results obtained with Cox's formulation (Equation 5.16) agree well with the 3D FE results. Figure 6.34(a) and 6.34(b) present a comparison of elastic properties obtained with 3D FE models and their corresponding 1D FE model based on Halpin-Tsai. It can be seen that the longitudinal moduli in the 3D element models are particularly influenced by the element size. The smaller the element, the higher is E_{xx}. The influence of the element size is most notably in the model with a V_f of 45% as the yarn diameters are big compared to the resin gaps in the thickness direction. The finer the meshes in the 3D FE models the closer are the longitudinal and transverse moduli to the constants obtained in the 1D FE model. The 1D truss element models based on Halpin-Tsai were further compared with 1D beam element models, as shown in Figure 6.35. The 1D beam element models with a V_f of 45% present no mesh dependency and the elastic constants coincide with the 1D truss element models. However, the longitudinal and transverse moduli in the 1D beam element models with a V_f of 10% present a minor mesh dependency. The elastic constants decrease slightly from the model with the coarsest mesh to the models with smaller element sizes.

Moreover, it can be seen that the 3D FE model with a V_f of 10% presents a transverse isotropic material behaviour, whereas the model with 45% is orthotropic due to geometric conditions of the specimen. The influence of the yarns in the thickness direction (Z-axis) is increased, which is reflected in the elastic properties. E_{zz} is bigger than E_{yy} and G_{xz} bigger than G_{xy}, as shown in Figure 6.34(b). As the yarns and their

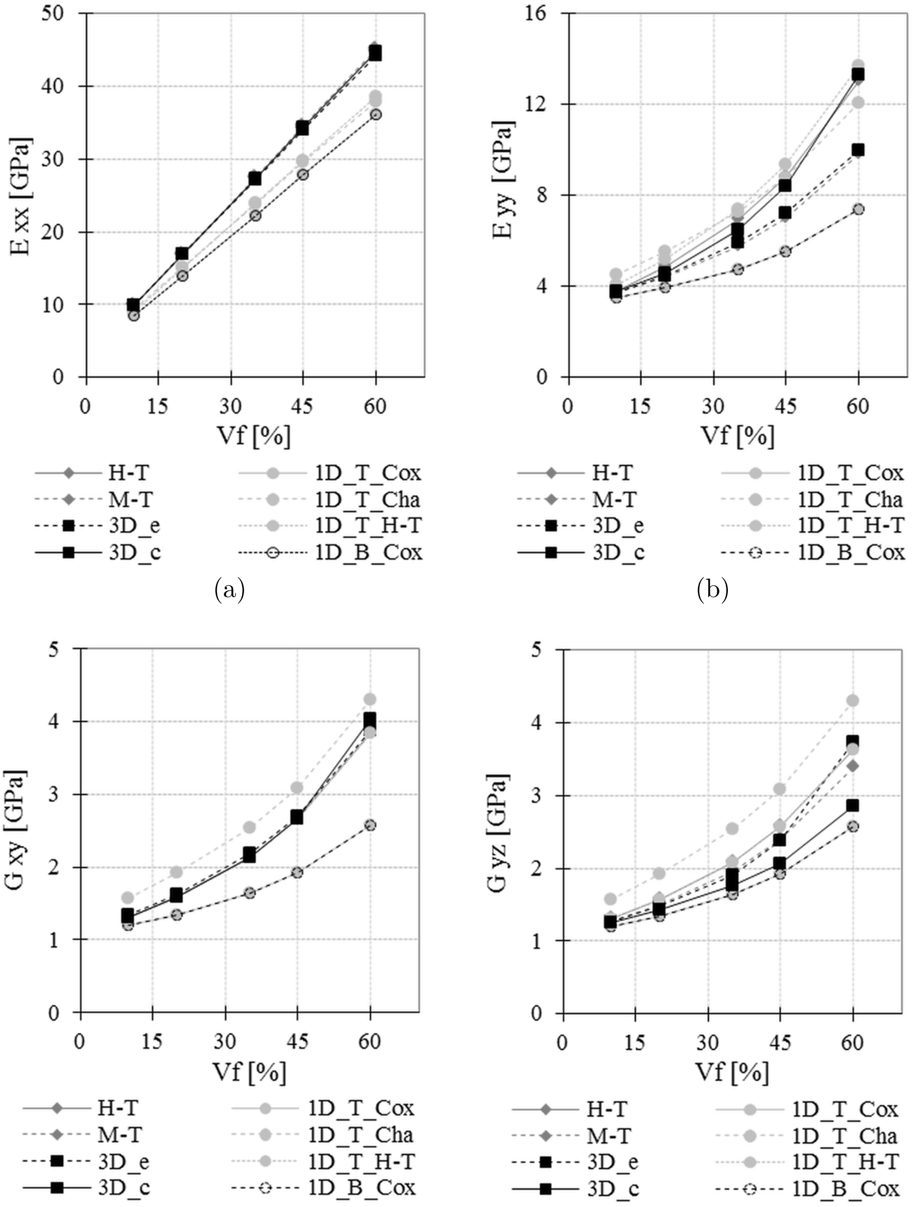

(a) (b) (c) (d)

Figure 6.32.: Elastic properties obtained for single UD yarn models

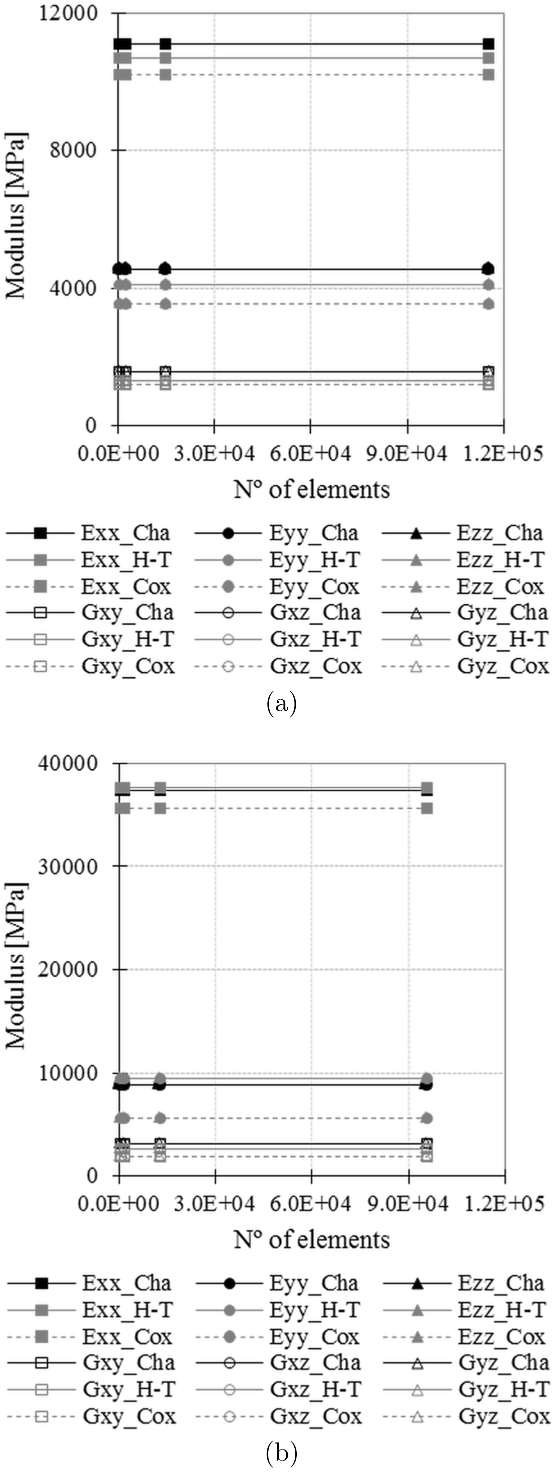

Figure 6.33.: Elastic properties obtained for different 1D FE models reinforced with 10 UD yarns: V_f = 10% (a) and V_f = 45% (b)

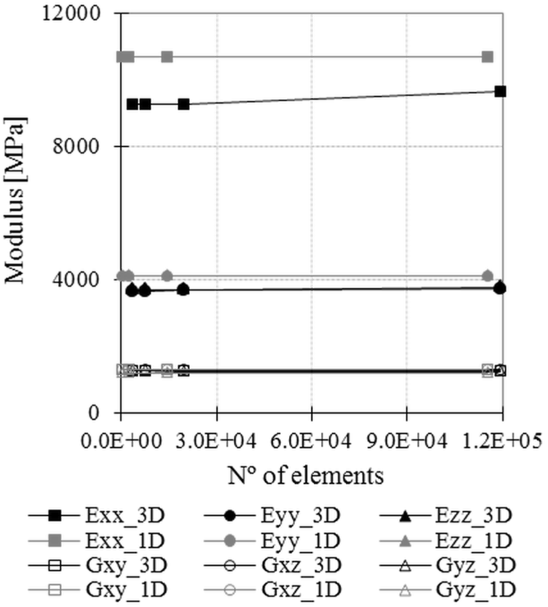

(a)

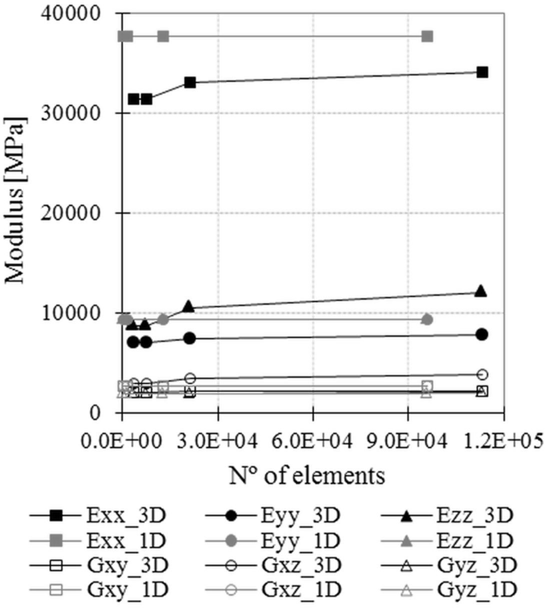

(b)

Figure 6.34.: Elastic properties obtained for 3D FE models reinforced with 10 UD yarns and 1D FE models based on Halpin-Tsai: $V_f = 10\%$ (a) and $V_f = 45\%$ (b)

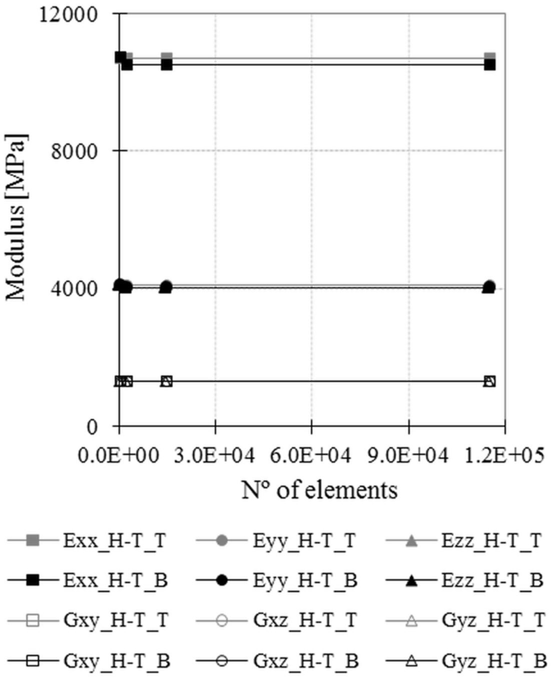

(a)

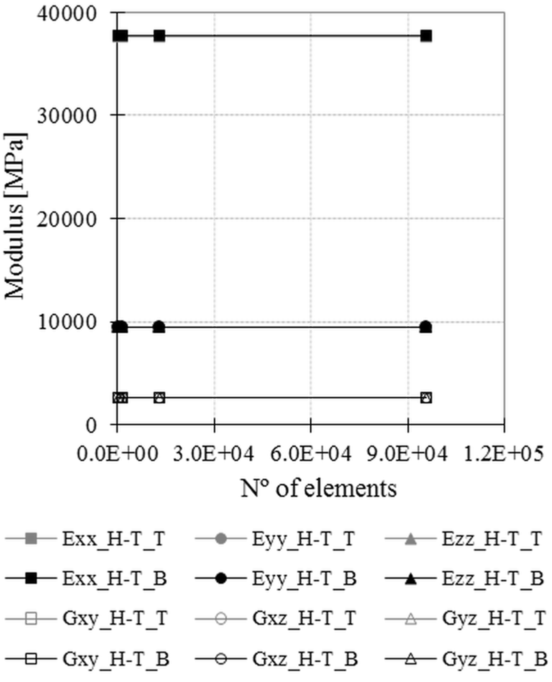

(b)

Figure 6.35.: Comparison of elastic properties obtained for 1D FE models based on Halpin-Tsai with truss and beam elements: V_f = 10% (a) and V_f = 45% (b)

geometry have no influence on the transverse and shear properties of the 1D element models a similar effect cannot be observed. Those properties are solely dependent on the material definition of the effective medium. As already concluded from the single yarn models, the effective medium should be rather transverse isotropic than isotropic.

As an overall result from the presented modelling study, it is concluded that Halpin-Tsai's formulations together with Cox's definition of the out-of-plane modulus are best to model the effective medium in the following numerical analyses.

Models under flexure

Stress patterns as well as maximum and minimum stress locations of the 1D FE models resemble the 3D FE models. However, numeric values of stresses and strains vary as besides the geometric differences material definitions of the model constituents differentiate.

Figure 6.36(a) and (b) present the total strain energies for different mesh sizes. As it can be seen for the 3D FE models the graphs approach a finite solution with an increasing number of elements. On the other hand, the graphs for the 1D FE models present a distinct kink rather than a convergence of the solution. Figure 6.36(c) and (d) show load-displacement curves for the 3D and 1D FE models with a V_f of 10% and 45%, respectively. The element size influences the results of the 3D FE models slightly compared to the results of the 1D FE models. Deviations are for the models with a V_f of 45% much more pronounced, especially for the 1D FE models (Figure 6.36(d)). The reaction forces in the 3D FE models increase with decreasing element size. On the contrary, similar to the graphs of the total strain energies no consistent behaviour can be observed for the 1D FE models. The load-displacement curves for the models with the lowest number of elements, 1D-10-2d and 1D-45-d, coincide most with the results of the 3D FE models. Moreover, it can be seen that the results of 1D FE models with smaller element sizes present non-linear behaviour.

In a further test the element size of the effective medium was maintained while the number of elements per yarn was altered. Two elements along the whole specimen length are obviously not enough to represent the flexural behaviour of the yarns, as shown in Figure 6.36(e) and (f). As the joining node between both elements coincides with the loading centre the reinforcing effect of the yarns on the flexural behaviour is undervalued. It can be further seen that the load-displacement curves of the 10% models coincide for equally long yarn and matrix elements as well as for yarn elements with a halved length. A decrease of the element length for yarns in the 45% model leads to a decreased flexural response, see Figure 6.36(f).

Next the flexural behaviour of models with equal element length for matrix and yarns (Figure 6.36(c) and (d)) is compared with models consisting of effective medium elements with a length that is twice as big as the yarn element length (Figure 6.36(e) and (f)). The reaction forces in the 10% model as well as in the 45% model with varying element lengths are higher. Moreover, it can be seen that the load-displacement curves in the model with equal element lengths show a non-linear behaviour. It can be inferred that a smaller yarn element length compared to the element length of the effective medium influences the flexural behaviour favourably and results in higher reaction forces.

In summary, it can be stated that the 1D modelling approach presents for lateral load cases clear drawbacks in case the yarns have big dimensions and their associated shares of the overall V_f are high. Moreover, it can be seen that the element size, particularly the element length, of the effective medium should be bigger than the element length of the yarn.

6.5.2. 3DBRCs

Effective elastic properties

Element lengths of the effective medium are selected according to yarn dimensions and evaluated. The cross-section of the 4stepWO is dominated by the interior cell, see Figure 4.7. As aforementioned it is aimed to find a general relation between mesh size and yarn dimensions. For this reason, the width and the thickness of the interior braider yarn are selected and varied to analyse a wider range of mesh sizes. The element lengths of the 4stepWO models vary between 2w, w, d and d/2, which are equal to 3.48 mm, 1.74 mm, 0.92 mm and 0.46 mm. The element length of the yarns is defined by the node array and the movements of the braider carriers. The minimum element length of the braider yarns is about 0.57 mm and the maximum element length is about 0.69 mm. The interior cells of the 4stepWI consist additionally of axial yarns which take a rhombic cross-section. Width and thickness of axial yarns are approximately equal. In the 4stepWI models the chosen element sizes are 2w, w, ta and d which correspond to 5.18 mm, 2.59 mm, 1.44 mm and 0.63 mm, respectively. The minimum and the maximum element lengths of braiders are about 0.49 mm and 0.63 mm. The element length of the axial yarns is equal to the element length of the effective medium. Analyses, which are not presented here, showed that smaller element lengths have no effect on the properties of the 3DBRC. Selected numeric values and percent errors between the analytically known and the numerically calculated results are listed in Table 6.17.

As shown in Table 6.17 the initial models result in overestimated overall V_f. The model of the 3D braid architecture is created using uniform packing factors and uniform yarn geometries along idealised centrelines of the yarn path. However, cross-sectional areas change along the path and κ varies dependent on the location in the braid. Hence, the experimentally obtained V_f are used to calculate reduced cross-sectional areas and create adjusted models. A decrease of about 38% (37.5% for the 4stepWO and 38.9% for the 4stepWI) is needed to adjust the V_f of the braider yarns in four-step braids. The cross-sectional area of the axial yarns in the 4stepWI was decreased by 18.5%. As can be seen from the results and percent errors, the longitudinal moduli as well as the

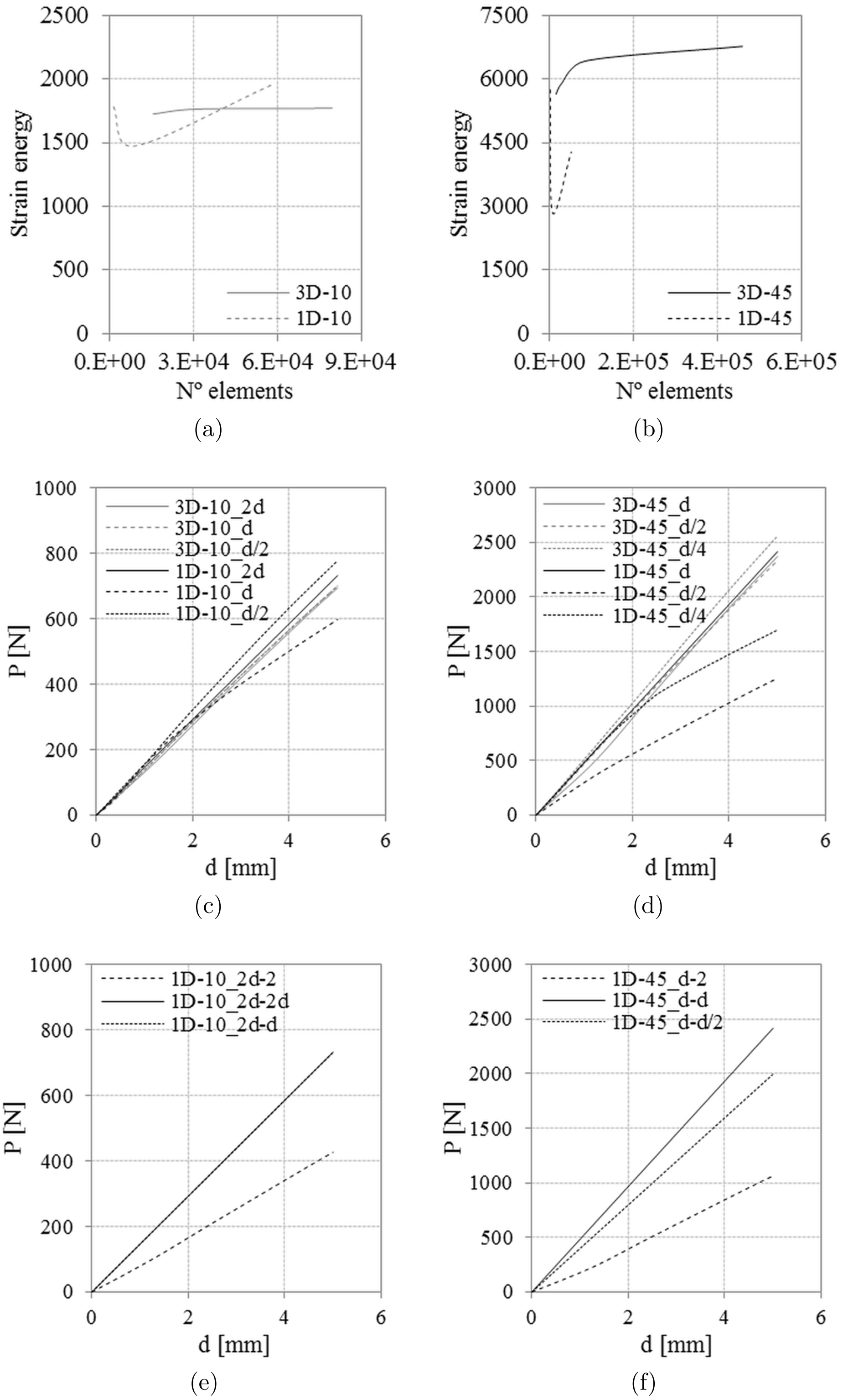

(a) (b)

(c) (d)

(e) (f)

Figure 6.36.: Flexural behaviour obtained for 3D and 1D FE models reinforced with 10 UD yarns: mesh convergence for $V_f = 10\%$ (a) and $V_f = 45\%$ (b), load-displacement curves with equal and varying element lengths for $V_f = 10\%$ (c) and (d) as well as for $V_f = 45\%$ (d) and (f), respectively

in-plane shear moduli are mainly affected by the cross-sectional change.

Figure 6.37(a) and 6.38(a) present the results of mesh convergence analyses for the 4stepWO and the 4stepWI with reduced cross-sections, respectively. It can be seen that the longitudinal moduli are particularly influenced by the element size. While E_{xx} of the 4stepWO is steadily decreasing, E_{xx} of the 4stepWI presents a distinct drop. The in-plane shear properties show similar behaviour due to the influence of E_{xx}. Figure 6.37(b) and 6.38(b) present experimental, analytical and numerical results of the 4stepWO and the 4stepWI. Compared to the experimental result the longitudinal moduli of both 4step braids are both analytically and numerically overestimated. However, analytical and numerical values are in very good agreement. Transverse and shear properties don't coincide but agree well in their trend, apart from the transverse modulus in the Y-axis of the 4stepWI. According to the analytical results the 4stepWI is an orthotropic material whereas the 4stepWO possesses similar transverse properties. As the material model for the effective medium defines a transverse isotropic behaviour for the 3DBRC, which can be observed in the obtained numerical results, the orthotropic characteristics of the 4stepWI cannot be reproduced. Deviations in the numeric values (Table 6.17) result from contributions of yarn segments oriented in the Y- and Z-axis.

In regard to a recommended element size for the prediction of elastic properties it can be inferred from the presented results that a general rule for Cartesian braids is not derivable. In case of a 4stepWO the best element length of the effective medium is smaller than the minimum yarn element length and in case of a 4stepWI the best element size is bigger than the maximum yarn element length.

The 2step has a very high V_f of about 71% and as seen in the micrograph (Figure 6.23) the cross-section is very compact and possesses only a few small resin pockets. Moreover, the 2step is mainly reinforced in the longitudinal direction and rather similar to a UD reinforced as seen from elastic properties obtained by analytical properties (see Table 6.15). One of the conclusions from the preliminary modelling studies was the inaccuracy or more specifically the overprediction of elastic properties for composites with high V_f, particularly of the transverse properties. The 1D FE model of the 2step was equally created with Halpin-Tsai's formulations. The first model resulted in a total V_f of 81%. Thus, the cross-sectional areas of the braiders and the axial yarns were reduced by about 12% and 14%, respectively, to obtain the experimental V_f presented in Table 6.9. Figure 6.39 presents the elastic properties obtained for various models with and without reduced cross-sections. Similar to the 4step braids the longitudinal modulus is overestimated which can be attributed to the use of idealised straight fibres without reductions due to twist. Moreover, it can be seen from the results that the transverse properties are highly overrated. Consequently, a further model was created assigning solely unreinforced matrix properties to the effective medium. As shown in Figure 6.39 all elastic properties are reduced, especially the transverse moduli. Besides the longitudinal modulus, the transverse properties as well as the shear properties are in good agreement with the analytical results.

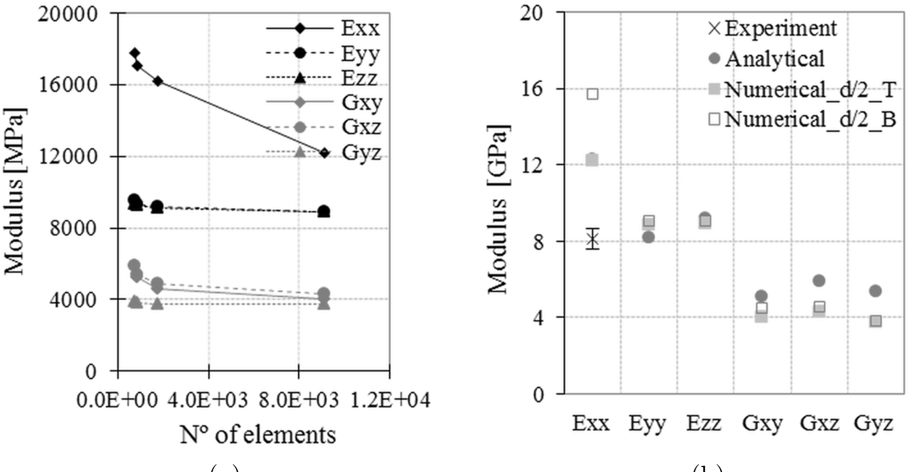

Figure 6.37.: Elastic constants obtained by numerical modelling for 4stepWO: mesh convergence (a), comparison with experimental and analytical results (b)

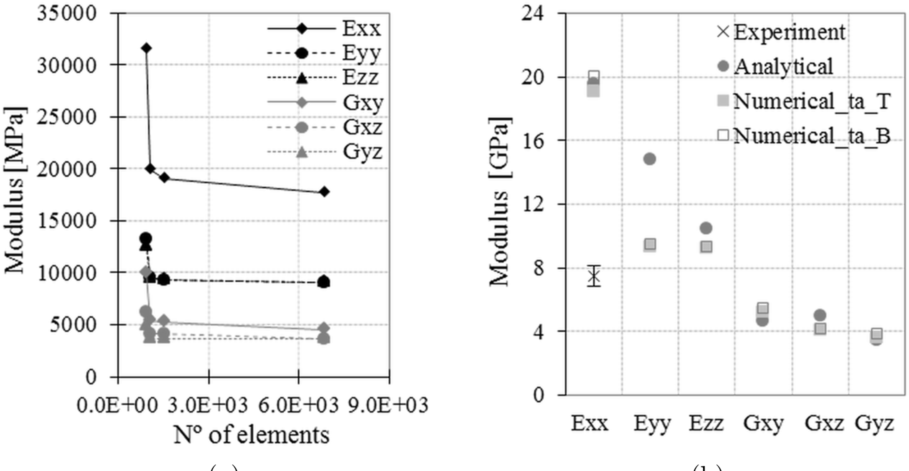

Figure 6.38.: Elastic constants obtained by numerical modelling for 4stepWI: mesh convergence (a), comparison with experimental and analytical results (b)

In further studies the 1D truss elements were replaced by 1D beam elements assuming a circular cross-section. Compared to the truss element model of the 4step braids all elastic properties of beam element models are slightly increased, as shown Table 6.17. Results for the 4stepWO, the 4stepWI and the 2step show that E_{xx} is particularly influenced by the use of beam elements, see Figure 6.37. E_{xx} of the 4stepWO is highly overestimated compared to the analytical result, whereas the discrepancy in 3DBRCs with axial reinforcement is relatively small.

Table 6.17.: Elastic constants obtained by numerical modelling for 3DBRCs

3DBRC	Model [a]	V_f	Error	E_{xx}	Error	E_{yy}	Error	E_{zz}	Error	G_{xy}	Error	G_{xz}	Error	G_{yz}	Error
			[%]	[MPa]	[%]	[MPa]	[%]	[MPa]	[%]	[MPa]	[%]	[MPa]	[%]	[MPa]	[%]
4stepWO	Analytical	43.9	-	12261	-	8157	-	9219	-	5095	-	5928	-	5376	-
	d/2	71.2	62.4	12777	4.2	8893	9.0	8932	-3.1	4135	-18.8	4358	-26.5	3744	-30.3
	d/2_rA_T	44.5	1.4	12191	-0.6	8879	8.8	8911	-3.3	4013	-21.2	4285	-27.7	3744	-30.4
	d/2_rA_B			15713	28.2	9025	10.6	9049	-3.3	4496	-11.8	4562	-23.1	3831	-28.7
4stepWI	Analytical	45.8	-	19536	-	14794	-	10443	-	4699	-	5017	-	3462	-
	ta	66.3	44.8	22004	12.6	9564	-35.4	9421	-9.8	5793	23.3	4417	-11.9	3617	4.5
	ta_rA_T	43.8	-4.3	19080	-2.3	9355	-36.8	9256	-11.4	5231	11.3	4079	-18.7	3613	4.4
	ta_rA_B			20020	2.5	9488	-35.9	9354	-10.4	5495	16.9	4200	-16.3	3846	11.1
2step	Analytical	73.1	-	18506	-	5171	-	5149	-	2142	-	1928	-	1910	-
	wa	81.1	11.0	38416	107.6	19262	272.5	20013	288.7	4478	109.0	5514	186.0	3586	87.7
	wa_rA_HT	70.7	-3.2	35955	94.3	19114	269.6	19779	284.1	4257	98.7	5484	184.4	3564	86.6
	wa_rA_m_T			26501	43.2	4257	-17.7	4939	-4.1	2194	2.4	1324	-31.3	1264	-33.8
	wa_rA_m_B			27411	48.1	4443	-14.1	5090	-1.1	2358	10.1	1423	-26.2	1428	-25.3

---

[a] rA - reduced cross-sectional area, T - 1D truss element (T3D2), B - 1D beam element (B33), m - matrix

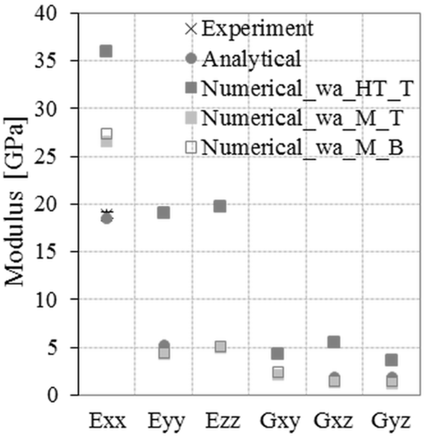

Figure 6.39.: Elastic constants obtained by numerical modelling and compared to experimental and analytical results for 2step

Damage modelling

As the 1D truss element model of the 4stepWO agrees best with analytical results, the model is further used to simulate the mechanical behaviour under flexural loading. Figure 6.40 presents load-displacement curves obtained by means of the described damage models in Section 5.5. Three simulations were conducted for the 2D damage model and for the 3D damage model. The damage models for the effective medium and for the yarns were separately and in combination implemented to analyse the effect of each damage variable on the overall behaviour. It can be seen that the numerically obtained mechanical behaviour of the 4stepWO under flexural loading does not completely correspond to the observed behaviour during mechanical testing: the bending stiffness is highly underestimated. Moreover, it can be seen that the influence of yarn damage is more pronounced, particularly in the 3D damage model using maximum stress criteria (Figure5.5(a)). The load vs. displacement curve of the 2D damage model coincide mostly with the curve obtained from the model without implemented damage model. On the other hand damage in the effective medium still didn't occur. The load vs. displacement curves of the model with a 2D and a 3D damage model coincide with the results of the model without implemented damage model. Figure 5.5(b) presents the results of the simulations with combined damage models. It can be seen that the calculations aborted although no distinct damage can be observed.

Stress patterns as well as maximum and minimum stress locations agree with experimentally observed material behaviour. Tensile failure occurs in the yarns and in the effective medium on the bottom side of the specimen. However, only yarn damage was predicted as shown in Figure 6.41(a). On the other hand, compressive failure is indicated in the effective medium and in the yarns below the loading nose, which corresponds to the experimentally observed damage modes. Similar to occurring tensile damage only compressive yarn damage was predicted, see Figure 6.41(b). However, the obtained stress and strain values, which are dependent on the element size, impair

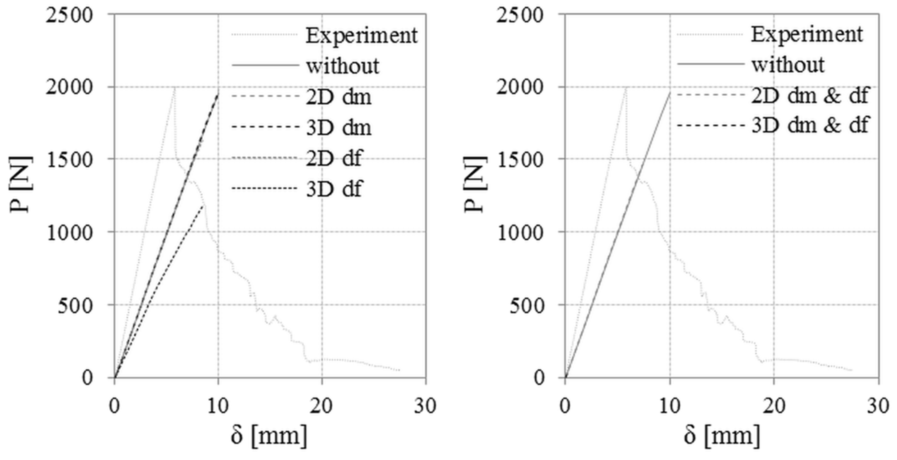

(a) (b)

Figure 6.40.: Flexural behaviour of the 4stepWO obtained by damage modelling: separated damage variables (a) and combined damage variables (b)

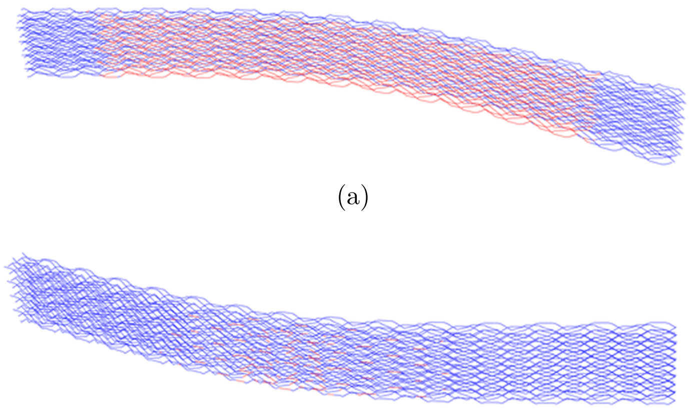

(a)

(b)

Figure 6.41.: Yarn damage predicted with the 3D damage model: tensile damage (a), compressive damage (b)

additionally the predictions. Moreover, due to computational difficulties a progressive damage behaviour wasn't obtained. From literature it is known that the selected progressive damage models are successfully used to model 2D composite materials subjected to low-velocity impact. The arising difficulties and numerical instabilities are likely to occur due to the proposed FE modelling approach, in which on the contrary to general 2D laminate simulations two different mesh geometries are joined. Although analysed in-depth, it was concluded that a solution for the occurring numerical problems is beyond the scope of this work and remains for future studies.

3D braided box beam section

A direct comparison between a pultruded section and the 3D braid reinforced box beam section described in Section 5.3 is difficult due to different mesh definitions. Moreover, due to a missing progressive damage model, neither load vs. displacement curves can be obtained nor conclusions about energy absorption concluded. However, it can be said that the maximum shear stresses do not occur only in the junctions between web and flanges but are rather spread along the webs instead.

7. Conclusions

The development of 3D braids goes back to the 1960s and research was particularly promoted in the 1990s. However 3D braided preforms as reinforcement in composite materials are still hard to find for commercial use. Reasons for this are the lack of braiding machines, dimensional limitations of currently possible preforms as well as easy modelling strategies for the textile architecture in 3D braid reinforced composite structures. The research work presented in this thesis aimed at characterising experimentally and modelling analytically as well as numerically the mechanical behaviour of 3D braid reinforced composites. The aim of this chapter is to discuss findings of the presented studies, to highlight significant conclusions and to give recommendations for future work.

7.1. Pultruded profiles under lateral loading

A preliminary study was presented as starting point, in which the mechanical behaviour of pultruded box beam profiles under lateral compressive loading is experimentally and numerically analysed. Pultruded profiles, which can be found in roadside furniture, are mainly reinforced in the longitudinal direction, particular reinforcements for out-of-plane properties are missing, thus 3DBRCs can potentially offer great benefits. It was shown that the junction between flange and web is the weakest point of a box beam profile. High shear stress fields in combination with manufacturing induced defects lead to a high failure probability. Transverse matrix failure propagates to fibre debonding, hence causing delamination, fibre rupture and finally the separation of the junction, the so-called tearing failure. 2D textile reinforcements as used generally in pultruded profiles present relatively low transverse compressive strength and material stiffness and cannot prevent occurring damage due to poor interlaminar shear strength. However, numerical studies have shown that enhanced out-of-plane properties, such as transverse tensile and shear strengths, decrease occurring stresses in the junctions, enhance the overall mechanical behaviour and further the fracture toughness box beam structures subjected to lateral compression loading. Moreover, the studies showed that the ideal material to obtain an overall better toughness is flexible allowing bigger deformations, thus longer lasting load bearing capacities with a consistent failure progression. Among various methods that have been developed to enhance out-of-plane properties and the delamination resistance of fibre reinforced composites are manufacturing techniques to fabricate 3D textile preforms.

As the mechanical response of a composite structure is additionally influenced by its geometry analytical studies were performed to analyse the bending and buckling behaviour of different single cell and multicellular beam cross-sections. The addition of stiffeners is improving the shear stiffness of a beam, the buckling strength as well as the critical buckling load, distinctly of flanges in multicellular square and horizontally oriented cross-sections. However, the addition of stiffeners results in bigger cross-sectional areas, which leads to linear mass density gains.

7.2. 3DBRCs

7.2.1. Experimental analyses

Experimental data for 3DBRCs are very rare as 3D braids are no commercial off-the-shelf product. The comparison of experimental results obtained by other authors is difficult as constituents, the braiding process or braid and composite architectures vary. The main aim of this research was to investigate the effect of through-thickness reinforcement on the failure behaviour and energy absorption of profile shaped composites under lateral loading. Three different types of 3D Cartesian braids were produced using a track and column type four-step braiding machine. Besides, it was shown that this machine type can be also applied for the production of two-step braided preforms using a varied braider carrier configuration and additional machine cycles. 3DBRCs were manufactured by vacuum assisted resin transfer moulding in a semi-closed mould to form flat beam structures. Tensile experiments were performed to serve as validation data for the presented analytical and numerical modelling approaches. Three point bending and falling weight impact tests, which address the delamination resistance at quasi-static and low impact rates of loading, were used to determine failure mechanisms and examine the effect of the 3D reinforcement on the damage propagation in comparison to a 2D laminate.

The braided preform has an initial cross-section during braiding due to yarn tensioning, which changes first when the preform is removed from the braiding machine. The cross-section changes another time when the preform is consolidated in the mould. Two vacuum infusion trials were conducted using polyester and epoxy resin. Although the infiltration with polyester resin was very good the consolidated composite showed various shrinkage cracks, which didn't occur in composites with epoxy resin.

In order to be able to compare the effect of each textile architecture to a pultruded laminate it was aimed to obtain composites with equal fibre volume fractions. Specimen dimensions for the 3DBRCs were kept unmachined to ensure yarn continuity and therefore vary from recommended dimensions according to standards.

Quasi-static testing

The quasi-static tensile stress strain response of the laminate follows a comparably linear trend, whereas nonlinear stress-strain behaviour can be observed for all braids, indicating progressive failure owing to their complex architecture and different failure modes. Brittle failure occurs in all materials with final fibre breakage. Laminated specimens delaminate and splinter, whereas 3DBRCs show more localised damage after failure. In braid reinforced specimens braider yarns are transverse to the loading direction. The epoxy resin starts to craze at the yarn crossings, which is visible as whitening. As the specimen elongates, the fibres scissor and cracking within the matrix spreads. Matrix cracking and break off is marked by crackling and progressive fibre rupture, which is identifiable by disruptive noise at equal intervals. With increasing load the cracking sounds are cumulative until final rupture occurs. The progressive damage behaviour of 3DBRCs indicated by the occurring failure modes is beneficial for composite structures compared to a sudden damage generally occurring in 2D laminates.

The flexural stress-strain curves in 3DBRCs as well as in the 2D laminate behave linearly until the peak strength is reached. Stiffness loss is initiated in all materials at an approximately equal flexural strain, presumably owing to matrix micro-cracking. Once damage occurred, it propagated rapidly. Inter-ply failure is the final mode observed in the laminated composite material which impaired its flexural strength. Due to occurring delamination events laminate properties present a bigger scatter. On the contrary, damage propagates in the 3DBRCs gradually and accumulates with a slower speed compared to the laminated material. 3DBRCs lose their load bearing capacity successively. In both 3DBRCs the resin matrix is damaged below the loading nose and matrix whitening is visible. Due to deflection different oriented braider yarns close to the surface are broken out of the matrix and partially ruptured. On the tension side of the beams braider yarns as well as axial yarns in a four-step braid with axials are ruptured. Fibre fracture extended progressively further than the neutral axis into the upper beam section. The remaining load bearing capacities are enabled by yarns on the compression side of the beam. Four-step braids with axial yarns present lower flexural peak strengths but higher flexural moduli owing to the axial reinforcement. Compared to the laminated material the normalised peak energy of four-step braid reinforced composites is lower, whereas the normalised total energy is equal. Thus, it is concluded that the progressive damage behaviour due to yarn interlacement is contributing to a higher resistance of 3DBRCs to lateral loads.

Impact testing

Impact damage is in all tested materials (laminate, 4stepWO, 4stepWI) initiated below the loading nose and propagates in the thickness direction due to transverse matrix cracking. On the bottom side of the beams matrix damage also occurs due to high tensile bending stresses. In laminated composites the propagation of matrix cracks leads to debonding on ply interfaces, which is also the main final damage mode. Moreover, damage in the laminated composites propagates parallel to the fibre direction of the inner UD layer and additional fibre failure occurs. Yarns on the compression side remain undamaged, enabling a residual strength. In 3DBRC specimens matrix damage is clearly visible as whitening. Due to deflection variously oriented braider yarns close

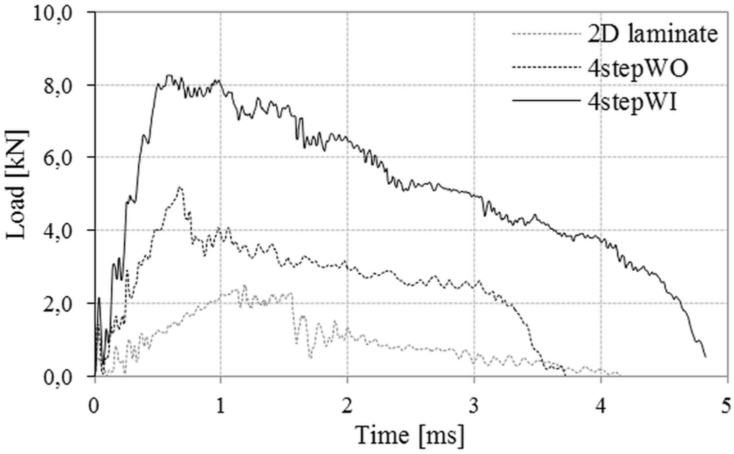

Figure 7.1.: Comparison of representative load-time curves of all specimens subjected to an impact energy of 98 J

to the surface are breaking out and partially rupture. Although fibre-matrix interface failure can be observed, damage cannot propagate as in laminates, also not along axial yarns in the four-step braid with axial yarns, due to yarn interlacement. Delamination as known from 2D laminates doesn't exist in 3DBRC. The through-thickness reinforcement is impeding the propagation, causes diversion and thus a longer lasting, continuous fracture process, as shown in Figure 7.1. With respect to energy absorption capacities it can be seen, that the initiation energies in four-step braid reinforced composites are lower than for the laminate, whereas the propagation energies are higher. Moreover, the ductility indices and Charpy strengths are for both impact energies higher than the values for the laminated specimens. In general a large initiation energy and a small propagation energy, also denoted by a small ductility index, indicates a brittle high strength material. Considering the observed failure behaviour and the numeric results, it can be concluded that 3DBRCs have a higher impact resistance compared to a 2D laminate.

7.2.2. Analytical modelling

Analytical models for three different types of 3D Cartesian braids are presented. Equations based on yarn characteristics, the braid configuration and machine parameters are used to predict preform properties and to estimate dimensions of the mould and the consolidated composite. Moreover, for each braid type analytical models are presented to calculate the elastic properties of the consolidated 3DBRC. Necessary input of yarn and composite parameters are taken from microscopic analyses. Predicted volume fractions and inclination angles of all 3DBRCs are in good agreement with the experimental values. The Young's modulus of the two-step braid reinforced composite is also in good agreement with the tensile test result, however the results for the four-step braid reinforced composites differ. The analytical moduli are higher than the experimental values. On the one hand it can be assumed that the analytical model overestimates true properties, on the other hand the experiments exhibited problems, which might affect the properties negatively. Thus, it is assumed that the elastic properties of the four-step braid reinforced composites lie in between. Furthermore, according to the predictive model the longitudinal modulus is enhanced by the addition of axial yarns.

Composite shape and dimensions imply geometric constraints which influence the elastic properties. Therefore, additional parametric analytical studies were performed in order to understand the effect of processing parameters on the properties of the selected 3DBRCs. The inclination angle in four-step braid reinforced composites influences the overall material behaviour. It defines whether the 3DBRC is transverse isotropic or anisotropic and influences the volume fraction, which in turn influences the elastic properties. The surface braiding angle which is related to the braiding angle significantly influences the elastic properties of four-step braid reinforced composites. Small surface braiding angles result in four-step braids with high volume fractions and high longitudinal moduli. The out-of-plane shear modulus increases with increasing surface braiding angle. Transverse and shear moduli vary with increasing surface braiding angles, the values go up and down. The bigger the yarn packing factor of the braiders, the smaller is the braided preform, the higher are the volume fraction and the greater are the elastic properties. The linear yarn densities have the biggest effect on the elastic constants in two-step braid reinforced composites. By increasing the linear density of the axial yarns all properties can be increased and by decreasing the linear density of the braider yarns the gain can be enlarged. The bigger the aspect ratio of the braider yarns, the thicker are the braiders, the smaller is the volume fraction and the lower are the elastic constants. An ideal inclination angle of 55° for the axial yarns was observed, which results in a high volume fraction and high moduli. Smaller and bigger aspect ratios adversely affect the elastic properties. As the available braid configuration is small a distinct influence of the surface braiding angle on the longitudinal modulus cannot be observed. On the other hand, transverse and shear moduli are increasing with increasing surface braiding angle.

7.2.3. Numerical modelling

FE tools are nowadays essential in the design process of composite structures. 3D FE models are computationally expensive, allow for predicting homogenised properties but are not applicable for modelling large structures. A good and yet simple numerical modelling technique as well as a simplified description of the complex textile architecture is indispensable to broaden the use of 3D braids, especially for the simulation of large 3DBRC structures. Numerical descriptions of the textile geometry were created using Python codes based on the braiding process and phenomenological knowledge obtained by microscopy. Initially various simplified FE modelling studies were conducted to assess the capability of the proposed 1D FE method and to compare it with 3D solid element models. Elastic properties of single UD yarn models were analytically and numerically calculated. The longitudinal moduli of the 3D FE models coincide with the values of the analytical models. For low volume fractions the moduli obtained in the 1D FE models agree well with the analytical and 3D FE models, whereas the higher the volume fraction the bigger is the discrepancy. The results for transverse properties in 1D FE models show also distinct differences and a particular dependence on the volume fraction. Moreover, the definition of shear properties has to account for the transverse isotropy of a UD composite. The properties obtained with the truss and beam element models coincide. The results of the cylindrical 3D FE model and the 1D FE model with the Halpin-Tsai definition presented not only a similar trend but also numeric coincidence. However, an influence of the cross-sectional shape and its orientation could be observed for the transverse modulus, especially for higher volume fractions. In a similar manner, the elastic properties of models with ten yarns were predicted. A distinct mesh sensitivity or differences in results between 1D truss and 1D beam elements couldn't be observed. From all 1D FE models are results based on formulations by Halpin-Tsai closest to the elastic constants of the 3D element models for low as well as high volume fractions, except for the out-of-plane shear modulus. In this particular case results obtained with Cox's formulation agree best with the 3D FE results. Thus, it is concluded that Halpin-Tsai's formulations together with Cox's definition of the out-of-plane modulus are best to model the effective medium.

Based on this conclusion elastic properties of all 3DBRCs were calculated. Compared to the FE models reinforced with one and ten UD yarns, results for the 3DBRCs are clearly mesh dependent. The longitudinal moduli were particularly influenced by the element size. The initial geometric models of the 3D braided architectures result in overestimated volume fractions as a uniform packing factor and uniform yarn geometries along idealised yarn centrelines, determined as averages from micrographs, were used. In order to adjust the volume fraction to experimentally obtained values cross-sectional areas of braider yarns in four-step braids were reduced by about 38%. The cross-sectional area of the axials in the four-step braid reinforced composite with axial yarns was decreased by 18.5%. The longitudinal moduli as well as the in-plane shear moduli were mainly affected by the cross-sectional change. Compared to the obtained experimental results the longitudinal moduli of both four-step braids were numerically overestimated. However, analytical and numerical values are in very good agreement. Although transverse and shear properties don't coincide their trend agrees well with analytical results. With regard to a recommended element size for the prediction of elastic properties it can be inferred from the presented results that a general rule for Cartesian braids is not derivable. In case of a in the four-step braid reinforced composite without axial yarns the best element length of the effective medium is smaller than the minimum yarn element length and in case of a in the four-step braid reinforced composite with axial yarns the best element size is bigger than the maximum yarn element length. The cross-section of the two-step braid reinforced composite is very compact, with only a few small resin pockets and its volume fraction is very high. The initial volume fraction was equally overestimated. Hence, the cross-sectional areas of the braiders and the axial yarns were reduced by about 12% and 14%, respectively, to obtain the experimental volume fraction. One of the conclusions from the preliminary modelling studies was the inaccuracy or more specifically the overprediction of elastic properties for composites with high volume fractions, particularly of the transverse properties. Moreover, the two-step braid reinforced composite is mainly reinforced in the longitudinal direction and rather similar to a UD reinforced. The elastic constants obtained with a 1D FE model of the 2step using Halpin-Tsai's formulations were overrated, particularly the transverse properties. Therefore, a further model was created assigning solely unreinforced matrix properties to the effective medium. All elastic properties were reduced, especially the transverse moduli. Apart from the longitudinal modulus, the transverse properties as well as the shear properties are in good agreement with the analytical results.

In further studies the 1D truss elements were replaced by 1D beam elements assuming a circular cross-section. Compared to the truss element model of the 4step braids all elastic properties of beam element models are slightly increased. Results for the in the four-step braid reinforced composite without and with axial yarns as well as the two-step braid reinforced composite show that longitudinal modulus is particularly influenced by the use of beam elements. Compared to the analytical result the longitudinal modulus of the in the four-step braid reinforced composite without axial yarns is highly overestimated, whereas the discrepancy in 3DBRCs with axial reinforcement is relatively small.

The ABAQUS manual provides a UMAT to simulate the failure behaviour of 2D laminates using the concept of progressively increasing damage variables. This 2D damage model as well as a 3D damage model found in literature were adapted to model the damage behaviour of a 4stepWO under flexural loading. The damage evolution in both model is expressed in terms of strains. Although, stress patterns as well as maximum and minimum stress locations agree with experimentally observed material behaviour. However, the obtained stress and strain values, which are dependent on the element size, impair the predictions. Moreover, due to computational difficulties a progressive damage behaviour wasn't obtained. From literature it is known that the selected progressive damage models are successfully used to model 2D composite materials subjected to low-velocity impact. The arising difficulties and numerical instabilities are likely to occur due to the proposed 1D FE modelling approach. In this approach, unlike general 2D laminate simulations, two different mesh geometries are joined. Although analysed in-depth, it was concluded that a solution for the occurring numerical problems is beyond the scope of this work and remains for future studies.

7.3. Overall conclusions

Summarising the aforementioned remarks, the following conclusions can be drawn:

Experimental analyses

- Numerical studies revealed that a flexible material with enhanced out-of-plane properties enhances the overall mechanical behaviour and fracture toughness of box beam structures subjected to lateral loading.
- Addition of stiffeners in box beam profiles improves the shear stiffness and buckling strength of a beam, but can lead to mass gains.
- Two-step braids can be produced using a track and column type four-step braiding machine, a varied braider carrier configuration and additional machine cycles.
- Compared to 2D laminates which fail by delamination and splintering under tensile loading 3DBRCs present a non-linear stress-strain behaviour indicating progressive failure, including matrix cracking visible as whitening, successive fibre-matrix debonding up to final fibre rupture.
- 3DBRCs present a progressive damage behaviour under lateral loading. Damage propagates under flexural loading gradually and accumulates with a slower speed compared to a 2D laminate.
- Delamination as known from 2D laminates doesn't exist in a 3DBRC as the through-thickness reinforcement is impeding the propagation and causes diversion. 3DBRCs present a longer lasting fracture process and higher impact resistance compared to a 2D laminate.
- The tested 3DBRCs and the 2D laminate have similar volume fractions. However, due to processing issues the compression of 3DBRCs is limited, which results in bigger cross-sectional dimensions, thus in higher section moduli and automatically in improved mechanical behaviour under lateral loading compared to the 2D laminate.

Modelling

- Analytically obtained volume fractions and inclination angles of all 3DBRCs are in good agreement with experimental values.
- The smaller the surface braiding angle and hence the braiding angle in four-step braids, the higher are the volume fraction and the longitudinal modulus. However, the out-of-plane shear modulus increases with increasing surface braiding angle.
- The bigger the yarn packing factor in four-step braid reinforced composites, the higher are the volume fraction and the greater are the elastic properties.
- An increasing linear density of axial yarns in two-step braid reinforced composites increases all properties. The gain can be additionally enlarged by decreasing the linear density of braider yarns.

- The smaller the aspect ratio of braider yarns in a two-step braid reinforced composite, the higher is the volume fraction and the better are the elastic constants.
- Analytical results obtained for the two-step braid reinforced composite agree well with experimentally obtained properties.
- FE modelling studies showed that 1D FE models with property definitions for the effective medium based on Halpin-Tsai and Cox's equation for the out-of-plane modulus agree best with 3D FE modelling results. However, the higher the volume fraction the lower the numeric agreement.
- Uniform packing factor and yarn geometries along idealised yarn centrelines result in overestimated volume fractions and properties. A reduction of the cross-sectional area of about 38% for braiders in four-step braid reinforced composites allows for adjusting the volume fraction and hence the elastic constants.
- Elastic constants of a two-step braid reinforced composite with Halpin-Tsai's formulation are overrated owing to the high volume fraction. However, the results of a 1D FE model using solely unreinforced matrix properties for the effective medium are in good agreement with the analytical results.
- Analytically and numerically obtained properties of the four-step braid reinforced composites don't agree quantitatively with the experimental results, however the results obtained by modelling show good agreements. Thus it is concluded that the simple numerical modelling approach is applicable to predict elastic properties of 3DBRCs. Therefore, the proposed methodology is the main contribution of this thesis to the field of FE simulation of composite materials.
- Attempts were made to implement the studied material behaviour of the 3DBRC into a progressive damage model within ABAQUS combining proposed and successfully working models with the 1D FE modelling approach. However, due to computational difficulties a progressive damage model wasn't obtained.

7.4. Recommendations for future work

Upon reaching the current development multiple research topics have inevitably revealed their importance. Therefore, recommendations for future work are listed below.

Experimental analyses

- Production of various 3DBRC configurations for studies on the effect of processing parameters on the mechanical behaviour
- More elaborated experimental analyses to reveal testing errors and obtain sound validation data for modelling approaches

- Development of experimental approach to quantify the increase in out-of-plane strength and understand the benefits of yarn interlacement for damage tolerance
- Studies towards optimised fibre architectures and incorporation of additional functionality for composite structures used as roadside furniture

Modelling

- Studies on the effect of microscopic parameters, such as yarn geometry, dimensions and packing factor, on the predicted mechanical behaviour and the mesh dependency of modelling approach
- Implementation of 1D beam elements in FE models of 3DBRCs and analyses under flexural and impact loading
- Development of damage model which allows for better numerical simulations of the experimentally observed progressive damage behaviour and of 3D braid reinforced profiles
- Implementation of explicit FE modelling method to analyse the impact behaviour of 3DBRCs

7.5. Publications

The research presented in this thesis has resulted in a number of contributions in the field of modelling 3D braid reinforced composites, which have been published as oral communications and peer-reviewed publications as listed in reverse chronological order below.

- F. Regel, G.R. Dias and F.W.J. van Hattum. Microstructure-performance relationships of four-step 3D braided composites, ICCS17 - 17th International Conference on Composite Structures, Porto, Portugal, 2013
- F. Regel, G.R. Dias and F.W.J. van Hattum. Mechanical analysis of a two-step 3D braided composite, Proceedings of SAMPE 2013, Long Beach, CA, USA, 2013
- F. Regel, F.W.J. van Hattum and G.R. Dias. A numerical and experimental study of the material properties determining the crushing behaviour of pultruded GFRP profiles under lateral compression. *Journal of Composite Materials*, 47(14):1749 - 1764, 2013
- F. Regel, G.R. Dias and F.W.J. van Hattum. Numerical modelling approach for 3D braided composites under lateral loading, Proceedings of ECCM15 - 15th European Conference on Composite Materials, Venice, Italy, 2012
- F. Regel, G.R. Dias and F.W.J. van Hattum. Improved lateral crushing behaviour of GFRP box-beam structures, IV Annual Meeting I3N, Quiaios, Portugal, 2012

- F. Regel, G.R. Dias and F.W.J. van Hattum. Improved crushing behaviour of GFRP box-beam structures under lateral loading, ICCS16 - 16th International Conference on Composite Structures, Porto, Portugal, 2011

Bibliography

[1] J-H. Byun, T.J. Whitney, G-W. Du, and T-W. Chou. Analytical characterization of two-step braided composites. *Journal of Composite Materials*, 25:1599 – 1618, 1991.

[2] L. Chen, X.M. Tao, and C.L. Choy. On the microstructure of three-dimensional braided composites. *Composites Science and Technology*, 59:391 – 404, 1999.

[3] I. Lapczyk and J.A. Hurtado. Progressive damage modeling in fiber-reinforced materials. *Composites Part A: applied science and manufacturing*, 38:2333 – 2341, 2007.

[4] A.P. Mouritz, M.K. Bannister, P.J. Falzon, and K.H. Leong. Review of applications for advanced three-dimensional fibre textile composites. *Composites Part A: Applied Science and Manufacturing*, 30:1445 – 1461, 1999.

[5] S.J. Kim and K.H. JI. Material and low velocity impact characterization of textile composites plates. Proceedings of the 17th Annual Technical Conference of American Society for Composites, West Lafayette IN, USA, 2002.

[6] M. Grassi, X. Zhang, and M. Meo. Prediction of stiffness and stresses in z-fibre reinforced composite laminates. *Composites Part A: Applied Science and Manufacturing*, 33:1653 – 1664, 2002.

[7] R. Park and J. Jang. A study of the impact properties of composites consisting of surface-modified glass fibres in vinyl ester resin. *Composite Science and Technology*, 58:979 – 985, 1998.

[8] S-J. Park, M-K. Seo, T-J. Ma, and D-R. Lee. Effect of chemical treatment of Kevlar fibers on mechanical interfacial properties of composites. *Journal of colloid and interface science*, 252:249 – 255, 2002.

[9] L. Tong, A.P. Mouritz, and M.K. Bannister. *3D Fibre Reinforced Polymer Composites.* Elsevier, 2002.

[10] B. Wulfhorst, T. Gries, and D. Veit. *Textile technology.* Hanser Gardner Publications, 2006.

[11] M. Ansar, W. Xinwei, and Z. Chouwie. Modeling strategies of 3D woven composites: A review. *Composite Structures*, 93:1947 – 1963, 2011.

[12] G.J. Turvey and Y. Zhang. A computational and experimental analysis of the buckling, postbuckling and initial failure of pultruded GRP columns. *Computer and Structures*, 84:1527 – 1537, 2006.

[13] C. Dispenza, A.A. Pisano, and P. Fuschi. Numerical simulations of the mechanical characteristics of glass fibre reinforced C-profiles. *Composites Science and Technology*, 66(15):2980 – 2989, 2006.

[14] T.J. Chotard and M.L. Benzeggagh. On the mechanical behaviour of pultruded sections submitted to low-velocity impact. *Composites Science and Technology*, 58:839 – 854, 1998.

[15] J. Tomblin and E. Barbero. Local buckling experiments on FRP columns. *Thin-Walled Structures*, 18:97 – 116, 1994.

[16] J.F. Davalos, H.A. Salim, P. Qiao, and R. Lopez-Anido. Analysis and design of pultruded FRP shapes under bending. *Composites Part B*, 27:295 – 305, 1996.

[17] S. Palanivelu, W. Van Paepegem, J. Degrieck, J. Van Ackeren, D. Kakogiannis, D. Van Hemelrijck, J. Wastiels, and J. Vantomme. Experimental study on the axial crushing behaviour of pultruded composite tubes. *Polymer Testing*, 29:224 – 234, 2010.

[18] Y. Bai, T. Vallée, and T. Keller. Delamination of pultruded glass fiber-reinforced polymer composites subjected to axial compression. *Composite Structures*, 91:66 – 73, 2009.

[19] M. Wisheart and M.O.W. Richardson. Low velocity response of simple geometry pultruded glass/polyester composite. *Journal of Materials Science*, 34:395 – 406, 1999.

[20] Z.Y. Zhang and M.O.W. Richardson. Low velocity impact induced damage evaluation and its effect on the residual flexural properties of pultruded GRP composites. *Composite Structures*, 81:195 – 201, 2007.

[21] S. Charoenphan, L.C. Bank, and M.E. Plesha. Progressive tearign failure in pultruded composite material tubes. *Composite Structures*, 63:45 – 52, 2004.

[22] F. Regel, F.W.J. Van Hattum, and G.R. Dias. A numerical and experimental study of the material properties determining the crushing behaviour of pultruded GFRP profiles under lateral compression. *Journal of Composite Materials*, 47:1749 – 1764, 2013.

[23] G.J. Turvey. Effects of load position on the lateral buckling response of pultruded GRP cantilevers - comparisons between theory and experiment. *Composite Structures*, 35:33 – 47, 1996.

[24] J.F. Davalos and P. Qiao. Analytical and experimental study of lateral and distortional buckling of FRP wide-flange beams. *Journal of Composites for Construction*, 1(4):150 – 159, 1997.

[25] P. Qiao, J.F. Davalos, and J. Wang. Local buckling of composite FRP shapes by discrete plate analysis. *Journal of Structural Engineering*, 127:245 – 255, 2001.

[26] L-H. Gan, L. Ye, and Y-W. Mai. Optimum design of cross-sectional profiles of pultruded box beams with high ultimate strength. *Composite Structures*, 45:279 – 288, 1999.

[27] E.J. Barbero and I.G. Raftoyiannis. Local buckling of FRP beams and columns. *Journal of Materials in Civil Engineering*, 5:339 – 355, 1993.

[28] J.F. Davalos, P. Qiao, and H.A. Salim. Flexural-torsional buckling of pultruded fiber reinforced plastic composite I-beams: experimental and analytical evaluations. *Composite Structures*, 38(1 – 4):241 – 250, 1997.

[29] L.C. Bank, J. Yin, and M. Nadipelli. Local buckling of pultruded beams - nonlinearity, anisotropy and inhomogeneity. *Construction and Building Materials*, 9:325 – 331, 1995.

[30] L.C. Bank, T.R. Gentry, and M. Nadipelli. Local buckling of pultruded FRP beams - Analysis and design. *Journal of Reinforced Plastics and Composites*, 15:283 – 294, 1996.

[31] L.C. Bank and J. Yin. Failure of web-flange junctions in postbuckled pultruded I-beams. *Journal of Composites for Construction*, 3:177 – 184, 1999.

[32] D.W. Palmer, L.C. Bank, and T.R. Gentry. Progressive tearing failure of pultruded composite box beams: Experiment and simulation. *Composite Science and Technology*, 58:1353 – 1359, 1998.

[33] R.K. Dutta. Investigations of plastic composite materials for highway safety structures. Technical Report CRREL REPORT 98-7, U.S. Army Cold Regions Research and Engineering Laboratory, 1998.

[34] J.R. Smith, L.C. Bank, and M.E. Plesha. Preliminary study of the behaviour of composite material box beams subjected to impact. Proceedings of the 6th International LS-DYNA conference, Detroit MI, USA, 2000.

[35] L.C. Bank and T.R. Gentry. Development of a pultruded composite material highway guardrail. *Composites Part A*, 32:1329 – 1338, 2001.

[36] A. Hoebergen and P. Sheard. A pultruded composite guid rail - Phase 1. Technical Report 5049/'93, TNO Plastics and Rubber Research Institute, 1993.

[37] A. Tabiei, A. Svenson, M. Hargrave, and L. Bank. Impact performance of pultruded beams for highway safety applications. *Composite Structures*, 42:231 – 237, 1998.

[38] D. Gabauer and H.C. Gabler. Evaluation of Threshold Values of Acceleration Severity Index by Using Event Data Recorder Technology. *Transportation Research Record: Journal of the Transportation Research Board*, 1904:37 – 45, 2006.

[39] C.C. Schoon. Aanrijdingen met in stijfheid verschillende typen geleiderailconstructies. Technical Report R-85-63 SWOV, Stichting Wetenschappelijk Onderzoek Verkeersveiligheid, 1985.

[40] J.A. Nemes and G. Bodelle. Simulation of vehicle impact on steel and composite highway guardrail structures. Proceedings of the Symposium on Crashworthiness and Occupant Protection in Transportation Systems, pages 179 – 190, San Francisco CA, USA, 1995.

[41] C.M. Brown. Pendulum Testing of an FRP Composite Guardrail: FOIL Test Numbers 96PO19 Through 96PO23, 97POO1, and 97POO2. Technical Report FHWA-RD-98-017, Federal Highway Administration, 1998.

[42] L.C. Bank. Progressive failure and ductility of FRP composites for construction: review. *Journal of Composites for Construction*, 17:406 – 419, 2013.

[43] G. Belingardi, A.T. Beyene, and E.G. Koricho. Geometrical optimization of bumper beam profile made of pultruded composite by numerical simulation. *Composite Structures*, 102:217 – 225, 2013.

[44] R. Gerlach, C.R. Siviour, J. Wiegand, and N. Petrinic. In-plane and through-thickness properties, failure modes, damage and delamination in 3D woven carbon fibre composites subjected to impact loading. *Composites Science and Technology*, 72:397 – 411, 2012.

[45] W. Hufenbach, N. Petrinic, A. Hornig, A. Langkamp, M. Gude, and J. Wiegand. Delamination behaviour of 3D-textile reinforced composites - Experimental and numerical approaches. *e-Journal of Nondestructive Testing*, 11, 2006.

[46] R. Kamiya, B.A. Cheeseman, P. Popper, and T-W. Chou. Some recent advances in the fabrication and design of three-dimensional textile preforms: a review. *Composites Science and Technology*, 60(1):33 – 47, 2000.

[47] H.B. Dexter. Development of Textile Reinforced Composites for Aircraft Structures. Proceedings of the 4th International Symposium for Textile Composites, Kyoto, Japan, 1998.

[48] G. Dell'Anno, D.D. Cartiié, I.K. Partridge, and A. Rezai. Exploring mechanical property balance in tufted carbon fabric/epoxy composites. *Composites Part A: Applied Science and Manufacturing*, 38(11):2366 – 2373, 2007.

[49] A.P. Mouritz. Design dilemma for z-pinned composite structures. Proceedings of the 27th Congress of International Council of the Aeronautical Sciences, Nice, France, 2010.

[50] G-W. Du and F. K. Ko. Unit Cell Geometry of 3-D Braided Structures. *Journal of Reinforced Plastics and Composites*, 12:752 – 768, 1993.

[51] A.K. Pickett and M. Fouinneteau. Material characterisation and calibration of a meso-mechanical damage model for braid reinforced composites. *Composites Part A: Applied Science and Manufacturing*, 37:368 – 377, 2006.

[52] A.B. Macander, R.M. Crane, and E.T. Camponeschi. Fabrication and mechanical properties of multidimensionally (X-D) braided composite materials. Proceedings

of the 7th Conference on Composite materials: Testing and Design, ASTM STP-893, pages 422 – 443, Philadelphia PA, USA, 1986.

[53] R.M. Crane and Jr. Camponeschi, E.T. Experimental and analytical characterization of multidimensionally braided graphite/epoxy composites. *Experimental Mechanics*, 26(3):259 – 266, 1986.

[54] T.D. Kostar and T-W. Chou. A methodology for Cartesian braiding of three-dimensional shapes and special structures. *Journal of Materials Science*, 37:2811 – 2824, 2002.

[55] T-W. Chou. *Microstructural design of fiber composites.* Cambridge University Press, 1992.

[56] P. Popper and R. McConnell. A new 3D braid for integrated parts manufacture and improved delamination resistance - the 2-step process. Proceedings of the 32nd International SAMPE Symposium, pages 92 – 103, Anaheim CA, USA, 1987.

[57] G-W. Du, T-W. Chou, and P. Popper. Analysis of three-dimensional textile preforms for multidirectional reinforcement of composites. *Journal of Materials Science*, 26:3438 – 3448, 1991.

[58] T.D. Kostar and T-W. Chou. Process simulation and fabrication of advanced multi-step three-dimensional braided preforms. *Journal of Composite Materials*, 29:2159 – 2167, 1994.

[59] T.D. Kostar, T-W. Chou, and P. Popper. Characterization and comparative study of three-dimensional braided hybrid composites. *Journal of Materials Science*, 35:2175 – 2183, 2000.

[60] J-H. Byun and T-W. Chou. Chapter 1.23 - Mechanics of Textile Composites. In Editors in Chief: A. Kelly and C. Zweben, editors, *Comprehensive Composite Materials*, pages 719 – 761. Pergamon, Oxford, United Kingdom, 2000.

[61] K. Jung, S.J. Kim, T.J. Kang, K. Chung, and J.R. Youn. Optimum modeling of 3-D circular braided composites. Proceedings of the 14th International Conference on Composite Materials - ICCM-14, San Diego CA, USA, 2004.

[62] J-H. Byun. Mechanical model of 3-dimensional multi-step braided composites. Proceedings of the 11th International Conference on Composite Materials - ICCM-11, pages V–356 – V–365, Gold Coast, Australia, 1997.

[63] M. Schneider, A.K. Pickett, and B. Wulfhorst. A new rotary braiding machine and CAE procedures to produce efficient 3D-braided textiles for composites. Proceedings of the 45th International SAMPE Symposium, Long Beach CA, USA, 2000.

[64] D. Bigaud, L. Dréano, and P. Hamelin. Models of interactions between process, microstructure and mechanical properties of composite materials - a study of the

interlock layer-to-layer braiding technique. *Composite Structures*, 67:99 – 114, 2005.

[65] G. Némoz, L. Dréano, and D. Bigaud. 3D braided preforms for shaped composite material. Proceedings of the European Conference on Spacecraft Structures, Materials and Mechanical Testing 2005, ESA SP-581, Noordwijk, The Netherlands, 2005.

[66] S.V. Lomov, D.S. Ivanov, I. Verpoest, M. Zako, T. Kurashiki, H. Nakai, and S. Hirosawa. Meso-FE modelling of textile composites: Road map, data flow and algorithms. *Composites Science and Technology*, 67:1870 – 1891, 2007.

[67] T. Ishikawa and T-W. Chou. Elastic behaviour of woven hybrid composites. *Composite Materials*, 16:2 – 19, 1982.

[68] T. Ishikawa and T-W. Chou. Stiffness and strength behaviour of woven fabric. *Journal of Material Science*, 17:3211 – 3220, 1982.

[69] B.N. Cox and G. Flanagan. Handbook of Analytical Methods for Textile Composites. Technical Report NASA Contractor Report 4750, March 1997.

[70] C-L. Ma, J-M. Yang, and T-W. Chou. Elastic stiffness of three-dimensional braided textile structural composites. Proceedings of the 7th Conference on Composite materials: Testing and Design, ASTM STP-893, pages 404 – 421, Philadelphia PA, USA, 1986.

[71] J-M. Yang, C-L. Ma, and T-W. Chou. Fibre inclination model of three-dimensional textile structural composites. *Journal of Composite Materials*, 20(5):472 – 483, 1986.

[72] H-Y. Sun and X. Qiao. Prediction of the mechanical properties of three-dimensionally braided composites. *Composites Science and Technology*, 57:623 – 629, 1997.

[73] C. Zuorong, Z. Dechao, M. Lu, and L. Ye. A homogenisation scheme and its application to evaluation of elastic properties of three-dimensional braided composites. *Composites Part B: Engineering*, 32(1):67 – 86, 2001.

[74] A.F. Kregers and G.A. Teters. Structural model of deformation of anisotropic three-dimensionally reinforced composites. *Mechanics of Composite Materials*, 18:10 – 17, 1982.

[75] J-H. Byun and T-W. Chou. Process-microstructure relationships of 2-step and 4-step braided composites. *Composites Science and Technology*, 56:235 – 251, 1996.

[76] W. Li. *On the structural mechanics of 3D braided preforms for composites.* PhD thesis, North Carolina State University, March 1990.

[77] T.D. Kostar, J-H. Byun, and T-W. Chou. Design-fabrication-performance relationship of advanced textile structural composites. In G.C. Sih, A. Carpinteri, and

G. Surace, editors, *Advanced Technology for Design and Fabrication of Composite Materials and Structures*, pages 63 – 76. Kluwer Academic Publishers, Dordrecht, The Netherlands, 1995.

[78] Y-Q. Wang and A.S.D. Wang. On the topological yarn structure of 3-D rectangular and tubular braided preforms. *Composites Science and Technology*, 51(4):575 – 586, 1994.

[79] Y-Q. Wang and A.S.D. Wang. Microstructure/property relationships in three-dimensionally braided fiber composites. *Composites Science and Technology*, 53:213 – 222, 1995.

[80] D-s. Li, Z-x. Lu, L. Chen, and J-l. Li. Microstructure and mechanical properties of three-dimensional five-directional braided composites. *International Journal of Solids and Structures*, 46:3422 – 3432, 2009.

[81] M.M. Shokrieh and M.S. Mazloomi. A new analytical model for calulation of stiffness of three-dimensional four-directional braided composites. *Composite Structures*, 94:1005 – 1015, 2012.

[82] C. Lei, Y-J. Cai, and F. Ko. Finite element analysis of 3-D braided composites. *Advances in Engineering Software*, 14:187 – 194, 1992.

[83] L. Chen, X.M. Tao, and C.L. Choy. Mechanical analysis of 3-D braided composites by the finite multiphase element method. *Composites Science and Technology*, 59:2383 – 2391, 1999.

[84] Z.X. Tang and R. Postle. Mechanics of three-dimensional braided structures for composite materials - part III: nonlinear finite element deformation analysis. *Computer Structures*, 55:307 – 317, 2002.

[85] H. Sun, S. Di, N. Zhang, N. Pan, and C. Wu. Micromechanics of braided composites via multivariable FEM. *Computers and Structures*, 81:2021 – 2027, 2003.

[86] T. Zeng, L-z. Wu, and L-c. Guo. Mechanical analysis of 3D braided composites: a finite element model. *Composites Structures*, 64:399 – 404, 2004.

[87] T. Zeng, L-z. Wu, and L-c. Guo. A finite element model for failure analysis of 3D braided composites. *Materials Science and Engineering*, A366:144 – 151, 2004.

[88] T. Zeng, D-n. Fang, L. Ma, and L-c. Guo. Predicting the nonlinear response and failure of 3D braided composites. *Materials Letters*, 58:3237 – 3241, 2004.

[89] B. Gu and X. Ding. A refined quasi-microstructure model for Finite Element analysis of three-dimensional braided composites under ballistic penetration. *Journal of Composite Materials*, 39:685 – 710, 2005.

[90] M. Sherburn. *Geometric and mechanical modelling of textiles.* PhD thesis, University of Nottingham, July 2007.

[91] F. Stig and S. Hallström. A modelling framework for composites containing 3D reinforcement. *Composite Structures*, 94:2895 – 2901, 2012.

[92] I. Verpoest and S.V. Lomov. Virtual textile composites software WiseTex: Integration with micro-mechanical, permeability and structural analysis. *Composites Science and Technology*, 65(15 – 16):2563 – 2574, 2005.

[93] M. Sherburn, A.C. Long, I.A. Jones, and C. Rudd. TexGen: Geometric modelling schema for textile composites. Proceedings of 8th International Conference on Textile Composites, Nottingham, UK, 2006.

[94] N. Tolosana, S.V. Lomov, and A. Miravete. Development of a geometrical model for a 3D braiding unit cell based on braiding machine emulation. Proceedings of the Symposium 'Finite element modelling of textiles and textile composites', St Petersburg, Russia, 2007.

[95] K.J. Kim, W-R. Yu, and J.S. Lee. Multi-scale modelling of 3D multi-layered braided composite tubes. *International Journal of Material Forming*, 1(1):33 – 47, 2008.

[96] X.G. Yu and J.Z. Cui. The prediction on mechanical properties of 4-step braided composites via two-scale method. *Composites Science and Technology*, 67:471 – 480, 2007.

[97] K. Xu and X-W. Xu. Meso-mechanical analysis of 3D braided composites based on a Finite Element model. *Journal of Engineering and Applied Sciences 2*, 10:1553 – 1562, 2007.

[98] D-s. Li, J-l. Li, L. Chen, Z-x. Lu, and D-n. Fang. Finite element analysis of mechanical properties of 3D four-directional rectangular braided composites - Part 1: Microgeometry and 3D finite element model. *Applied Composite Materials*, 17:373 – 387, 2010.

[99] D-s. Li, J-l. Li, L. Chen, Z-x. Lu, and D-n. Fang. Finite element analysis of mechanical properties of 3D four-directional rectangular braided composites - Part 2: Validation of the 3D finite element model. *Applied Composite Materials*, 17:389 – 404, 2010.

[100] S. Mohajerjasbi. Modeling and Analysis of 4-Step 3-D Cartesian Braided Composites. Proceedings of the MSC World Users' Conference, Los Angeles CA, USA, 1993.

[101] B.N. Cox, W.C. Carter, and N.A. Fleck. A Binary Model of textile composites - I. Formulation. *Acta Metallurgica et Materialia*, 42:3463 – 3479, 1994.

[102] J. Xu, B.N. Cox, M.A. McGlockton, and W.C. Carter. A Binary Model of textile composites - II. The elastic regime. *Acta Metallurgica et Materialia*, 43:3511 – 3524, 1995.

[103] Q.D. Yang, K.L. Rugg, B.N. Cox, and M.C. Shaw. Failure in the junction region of T-stiffeners: 3D-braided vs. 2D tape laminate stiffeners. *International Journal of Solids and Structures*, 40:1653 – 1668, 2003.

[104] Q. Yang and B. Cox. Spatially averaged local strains in textile composites via the Binary Model formulation. *Journal of Engineering Materials and Technology*, 125:418 – 425, 2003.

[105] Q. Yang and B. Cox. Evaluation of Macroscopic and Local Strains in a Three-Dimensional Woven C/SiC Composite. *Journal of the American Ceramic Societyy*, 88:719 – 725, 2005.

[106] Q.D. Yang and B. Cox. Predictive failure in textile composites using the Binary Model with gauge-averaging. *Engineering Fracture Mechanics*, 77:3174 – 3189, 2010.

[107] S. Flores, A.G. Evans, F.W. Zok, M. Genet, B. Cox, D. Marshall, O. Sudre, and Q. Yang. Treating matrix nonlinearity in the binary model formulation for 3D ceramic composite structures. *Composites Part A*, 41:222 – 229, 2010.

[108] G. Haasemann. An Application of the Binary Model to Dynamic Finite Element Analysis. *Proceedings in Applied Mathematics and Mechanics*, 3(1):176–177, 2003.

[109] G. Haasemann, V. Ulbricht, and J. Brummund. Modelling the mechanical properties of biaxial weft-knitted fabric reinforced composites. *Proceedings in Applied Mathematics and Mechanics*, 4(1):193–194, 2004.

[110] G. Haasemann and V. Ulbricht. Flexural properties of fiber-reinforced composites. *Proceedings in Applied Mathematics and Mechanics*, 5(1):233–234, 2005.

[111] G. Haasemann, M. Kästner, S. Prüger, and V. Ulbricht. Simulation and modeling the mechanical behavior of textile reinforced composites by combining the Binary Model and X-FEM. *Proceedings in Applied Mathematics and Mechanics*, 8:10563–10564, 2008.

[112] W-G. Jiang, S.R. Hallett, and M.R. Wisnom. Damage prediction for 3D woven composite structural features. In Editors in Chief: P.P. Camanho, C.G. Dávila, S.T. Pinho, and J.J.C. Remmers, editors, *Mechanical Response of Composites*, pages 281 – 291. Springer Netherlands, Dordrecht, The Netherlands, 2008.

[113] P.G. Biragoni and S.R. Hallett. Finite element modelling of 3D woven composites for stiffness prediction. Proceedings of the 17th International Conference on Composite Materials - ICCM-17, Edinburgh, UK, 2009.

[114] S.R. Hallett and P. Biragoni. Damage prediction for 3D woven composite structural features. In Editors in Chief: C. Binetruy and F. Boussu, editors, *Texcomp 10 - Recent Advances in Textile Composites*, pages 36 – 43. DEStech Publications, Inc., Lancaster PA, USA, 2010.

[115] S.A. Tabatabaei, S.V. Lomov, and I. Verpoest. Assessment of embedded element technique in meso-FE modelling of fibre reinforced composites. *Composite Structures*, 107:436 – 446, 2014.

[116] D.S. Ivanov, F. Baudry, B. Van Den Broucke, S.V. Lomov, H. Xie, and I. Ver-

poest. Failure analysis of triaxial braided composite. *Composites Science and Technology*, 69:1372 – 1380, 2009.

[117] X. Li, W.K. Binienda, and R.K. Goldberg. Finite Element method for failure study of two-dimensional triaxially braided composite. Technical Report NASA/TM—2010-216372, NASA Scientific and Technical Information, July 2010.

[118] A. Miravete, J.M. Bielsa, A. Chiminelli, J. Cuartero, S. Serrano, N. Tolosana, and R. Guzman de Villoria. 3D mesomechanical analysis of three-axial braided composite materials. *Composites Science and Technology*, 66:2954 – 2964, 2006.

[119] G-d. Fang, J. Liang, and B-l. Wang. Progressive damage and nonlinear analysis of 3D four-directional braided composites under unidirectional tension. *Composite Structures*, 89:126 – 133, 2009.

[120] K. Xu. A numerical study on the progressive failure of 3D four-directional braided composites. *Advances in Materials Science and Engineering*, vol. 2013, 2013.

[121] J-w. Dong and M-l. Feng. Asymptotic expansion homegenization for simulating progressive damage of 3D braided composites. *Composite Structures*, 92:873 – 882, 2010.

[122] J-w. Dong and M-l. Feng. Damage simulation for 3D braided composites by homogenization method. *Chinese Journal of Aeronautics*, 23:677 – 685, 2010.

[123] M-L. Feng and C-C. Wu. A study of three-dimensional four-step braided piezoceramic composites by the homogenization method. *Composites Science and Technology*, 61:1889 – 1898, 2001.

[124] B.S. Ye, A.L. Svenson, and L.C. Bank. Mass and volume fraction properties of pultruded glass fibre-reinforced composites. *Composites*, 26:725 – 731, 1995.

[125] A. Tabiei, A. Svenson, and M. Hargrave. Impact behavior of pultruded composite box-beams. *Composite Structures*, 36:155 – 160, 1996.

[126] N.K. Gupta and H. Abbas. Lateral collapse of composite cylindrical tubes between flat platens. *International Journal of Impact Engineering*, 24:329 – 346, 2000.

[127] O. Calme, D. Bigaud, and P. Hamelin. 3D braided composite rings under lateral compression. *Composites Science and Technology*, 65:95 – 106, 2005.

[128] E-S. Mahdi and H.E. Kadi. Crushing behavior of laterally compressed composite elliptical tubes: Experiments and predictions using artificial neural networks. *Composite Structures*, 83:399 – 412, 2008.

[129] J-H. Byun. The process model of three-dimensional rectangular braiding for textile preforms. Proceedings of the American Society for Composites 11th Technical Conference, pages 1016 – 1025, Atlanta GA, USA, 1996.

[130] S.V. Lomov, G. Huysmans, Y. Luo, R.S. Parnas, A. Prodromou, I. Verpoest, and F.R. Phelan. Textile composites: modelling strategies. *Composites Part A: applied science and manufacturing*, 32:1379 – 1394, 2001.

[131] European Standard EN ISO1172:1998. Textile-glass-reinforced plastics - Prepregs, moulding compounds and laminates - Determination of the textile-glass and mineral-filler content - Calcination methods. CEN, 1998.

[132] ASTM Standard D3039/D3039M-5a. Standard test method for tensile properties of polymer matrix composite materials. ASTM International, 1995.

[133] International Standard ISO 178. Plastics - Determination of flexural properties of rigid plastics. ISO, 1975.

[134] S. Chou, H-E. Chen, and M-S. Song. A study on impact properties of 3-D composites by falling weight test method. *Journal of the Chinese Institute of Engineers*, 19:25 – 34, 1996.

[135] P. Potluri, P. Hogg, M. Arshad, D. Jetavat, and P. Jamshidi. Influence of Fibre Architecture on Impact Damage Tolerance in 3D Woven Composites. *Applied Composite Materials*, 19:799 – 812, 2001.

[136] International Standard ISO 179. Plastics - Determination of Charpy impact strength of rigid plastics. ISO, 1975.

[137] J.L. Clarke, editor. *Structural Design of Polymer Composites - EUROCOMP Design Code and Handbook.* E & FN SPon, London, UK, 2005.

[138] European Standard EN13706-2:2001. Reinforced plastics composites - Specifications for pultruded profiles - Part 2: Methods of test and general requirements. CEN, 2001.

[139] S.P. Timoshenko. On the correction for shear of the differential equation for transverse vibrations of prismatic bars. *Philosophical Magazine Series 6*, 41(245):744 – 746, 1921.

[140] M.D. Hayes and J.J. Lesko. The effect of non-classical behaviors on the measurement of the Timoshenko shear stiffness. In R. Seracino, editor, *FRP Composites in Civil Engineering - CICE 2004*, pages 873 – 880. Taylor & Francis, Adelaide, Australia, 2004.

[141] L.C. Bank. Shear coefficients for thin-walled composite beams. *Composite Structures*, 8:47 – 61, 1987.

[142] L.C. Bank and T.P. Melehan. Shear coefficients for multicelled thin-walled composite beams. *Composite Structures*, 11:259 – 276, 1989.

[143] L.C. Bank, editor. *Composites for Construction - Structural Design with FRP Materials.* Wiley & Sons, Hoboken NJ, USA, 2006.

[144] J.-H. Byun. *Process-microstructure-performance relationships of three-dimensional textiles composites.* PhD thesis, University of Delaware, December 1991.

[145] D-s. Li, L. Chen, and J-l. Li. Microstructure and unit-cell geometry of four-step three-dimensional rectangular braided composites. *Journal of Reinforced Plastics and Composites*, 29:3353 – 3363, 2010.

[146] R. Pandey and H.T. Hahn. Visualization of representative volume elements for three-dimensional four-step braided composites. *Composite Science and Technology*, 56:161 – 170, 1995.

[147] Z.X. Tang and R. Postle. Mechanics of three-dimensional braided structures for composite materials - part I: fabric structure and fibre volume fraction. *Computer Structures*, 49:451 – 459, 2000.

[148] C.C. Chamis. Mechanics of Composite Materials : Past , Present , and Future. Technical Report NASA Technical Memorandum 100793, 1984.

[149] P.D. Soden, A.S. Kaddour, and M.J. Hinton. Recommendations for designers and researchers resulting from the world-wide failure exercise. *Composite Structures*, 64:589 – 604, 2004.

[150] R. Younes, A. Hallal, F. Fardoun, and F.H. Chehade. 17 - Comparative Review Study on Elastic Properties Modeling for Unidirectional Composite Materials. In N. Hu, editor, *Composites and Their Properties*, pages 391 – 408. InTech, 2012.

[151] Abaqus Inc. *User's Manual.* Providence RI, USA, ABAQUS 6.11 edition, 2011.

[152] Z. Hashin. Failure criteria for unidirectional fibre composites. *Journal of Applied Mechanics*, 47:329 – 334, 1980.

[153] L.M. Kachanov. On the time to failure under creep conditions. *Izv. Akad. Nauk SSR, Otd. Tekhn. Nauk*, 8:26 – 31, 1958.

[154] A. Matzenmiller, J. Lubliner, and R.L. Taylor. A constitutive model for anisotropic damage in fiber-composites. *Mechanics of Materials*, 20:125 – 152, 1995.

[155] P.P. Camanho and C.G. Davila. Failure criteria for FRP laminates in plane stress. Technical Report NASA/TM-2003-212663, 2003.

[156] R. Haj-Ali and H. Kilic. Nonlinear behaviour of pultruded FRP composites. *Composites Part B: engineering*, 33:173–191, 2002.

[157] H.L. Cox. The elasticity and strength of paper and other fibrous materials. *British Journal of Applied Physics*, 3(3).

[158] H. Krenchel. *Fibre Reinforcement: Theoretical and Practical Investigations of the Elasticity and Strength of Fibre-reinforced Materials.* Akademisk Forlag, 1964.

[159] M.T. Huber. The theory of crosswise reinforced ferroconcrete slabs and its application to various important constructional problems involving rectangular slabs. *Der Bauingenieur*, 4:354 – 360 and 392 – 395, 1923.

[160] R. Jones. *Mechanics of composite materials.* Mc Graw Hill, 1975.

[161] X. Jia, Z. Xia, and B. Gu. Numerical analyses of 3D orthogonal woven composite under three-point bending from multi-scale microstructure approach. *Computational Materials Science*, 79:468 – 477, 2013.

[162] J. Aboudi. Closed form constitutive equations for metal matrix composites. *International Journal of Engineering Science*, 25(9):1229 – 1240, 1987.

[163] J.C. Halpin and J.L. Kardos. The Halpin-Tsai equations: a review. *Polymer Engineering and Science*, 16:344 – 352, 1976.

[164] G. P. Tandon and G. J. Weng. The effect of aspect ratio of inclusions on the elastic properties of unidirectionally aligned composites. *Polymer Composites*, 5(4):327 – 333, 1984.

[165] B.N. Cox, R.M. McMeeking, and M.A. McGlockton. The Binary Model - A computational approach to textile composites. Proceedings of the 12th International Conference on Composite Materials - ICCM-12, Paris, France, 1999.

[166] A.K. Pickett, J. Sirtautas, and A. Erber. Braiding simulation and prediction of mechanical properties. *Applied Composite Materials*, 16:345 – 364, 2009.

[167] B. Van Den Broucke, K. Drechsler, V. Hanisch, D. Hartung, D.S. Ivanov, V.E. Koissin, S.V. Lomov, and P. Middendorf. Multilevel modelling of mechnaical properties of textile composites: ITOOL Project. Proceedings of the 28th SAMPE Europe International Conference - SEICO '07, pages 175 – 180, Paris, France, 2007.

[168] V. Koissin, D.S. Ivanov, S.V. Lomov, and I. Verpoest. Fibre distribution inside yarns of textile composite: gemetrical and FE modelling. Proceedings of the 8th International Conference on Textile Composites, TEXCOMP 8, Nottingham, UK, 2006.

[169] M.S. Dadkah, J.G. Flintoff, T. Kniveton, and B.N. Cox. Simple models for triaxially braided composites. *Composites*, 26:561 – 577, 1995.

[170] F. Stig. *3D-woven reinforcement in composites.* PhD thesis, KTH School of Engineering Sciences, 2012.

[171] B.N. Cox, M.S. Dadkhah, and W.L. Morris. On the tensile failure of 3D woven composites. *Composites Part A: Applied Science and Manufacturing*, 27:447 – 458, 1996.

[172] H. Gu and Z. Zhong. Tensile behaviour of 3D woven composites by using different fabric structures. *Materials and Design*, 23:671 – 674, 2002.

[173] G-d. Fang, J. Liang, Y. Wang, and B-l. Wang. The effect of yarn distortion on the mechanical properties of 3D four-directional braided composites. *Composites: Part A*, 40:343 – 350, 2009.

[174] X.F. Wang, X.W. Wang, G.M. Zhou, and C.W. Zhou. Multi-scale analyses of 3D woven composite based on periodicity boundary conditions. *Journal of Composite Materials*, 41:1773 – 1788, 2007.

[175] S. Li and A. Wongsto. Unit cells for micromechanical analyses of particle-reinforced composites. *Mechanics of Materials*, 36:543 – 572, 2004.

[176] H.J. Böhm. A short introduction to basic aspects of continuum micromechanics. Technical Report ILSB Report 206, Institute of Lightweight Design and Structural Biomechanics, 2013.

[177] M. Kästner, G. Haasemann, J. Brummund, and V. Ulbricht. 13 - Computation of Effective Stiffness Properties for Textile-Reinforced Composites Using X-FEM. In *Mechanical Response of Composites*, pages 261–279. Springer Netherlands, Dordrecht, The Netherlands, 2008.

[178] R. Böhm, M. Gude, and W. Hufenbach. A phenomenologically based damage model for textile composites with crimped reinforcement. *Composites Science and Technology*, 70:81 – 87, 2010.

[179] Z. Hashin and A. Rotem. A fatigue failure criterion for fiber-reinforced materials. *Journal of Composite Materials*, 7:448 – 464, 1973.

[180] C.G. Dávila, P.P. Camanho, and C.A. Rose. Failure criteria for FRP laminates. *Journal of Composite Materials*, 39(4):323 – 345, 2005.

[181] A. Puck and H. Schürmann. Failure analysis of FRP laminates by means of physically based phenomenological models. *Composites Science and Technology*, 58:1045 – 1067, 1998.

[182] G. Catalanotti, P.P. Camanho, and A.T. Marques. Three-dimensional failure criteria for fiber-reinforced laminates. *Composite Structures*, 95:63 – 79, 2013.

[183] S.T. Pinho, L. Iannucci, and P. Robinson. Physically-based failure models and criteria for laminated fibre-reinforced composites with emphasis on fibre kinking: Part I: Development. *Composites: Part A*, 37:63 – 73, 2006.

[184] R.G. Cuntze and A. Freund. The predictive capability of failure mode concept-based strength criteria for multidirectional laminates. *Composites Science and Technology*, 64:343 – 377, 2004.

[185] R. Böhm, M. Gude, and W. Hufenbach. A phenomenologically based damage model for 2D and 3D-textile composites with non-crimp reinforcement. *Materials and Design*, 32:2532 – 2544, 2011.

[186] M.J. Hinton, A.S. Kaddour, and P.D. Soden. A comparison of the predictive capabilities of current failure theories for composite laminates, judged against experimental evidence. *Composites Science and Technology*, 62:1725 – 1797, 2002.

[187] J. Wiegand, N. Petrinic, and B. Elliott. An algorithm for determination of the fracture angle for the three-dimensional Puck matrix failure criterion for UD composites. *Composites Science and Technology*, 68:2511 – 2517, 2008.

[188] F.-K. Chang and K.-Y. Chang. A progressive damage model for laminated composites containing stress concentrations. *Journal of Composite Materials*, 21:834 – 855, 1987.

[189] J.P. Hou, N. Petrinic, C. Ruiz, and S.R. Hallett. Prediction of impact damage in composite plates. *Composites Science and Technology*, 60:273 – 281, 2000.

[190] S.T. Pinho, C.G. Dávila, P.P. Camanho, L. Iannucci, and P. Robinson. Failure models and criteria for FRP under in-plane or three-dimensional stress states including shear non-linearity. Technical Report NASA/TM-2005-213530, NASA Scientific and Technical Information, February 2005.

[191] J. Juhasz, R. Rolfes, and K. Rohwer. A new strength model for application of a physically based failure criterion to orthogonal 3D fiber reinforced plastics. *Composites Science and Technology*, 61:1821 – 1832, 2001.

[192] N.K. Naik and R.S. Kumar. Compressive strength of unidirectional composites: evaluation and comparison of prediction models. *Composite Structures*, 46:299 – 308, 1999.

[193] A.S. Argon. Fracture of Composites. volume 1, pages 79 – 114. Academic Press, New York NY, USA, 1972.

[194] B. Budiansky and N.A. Fleck. Compressive kinking of fiber composites: A topical review. *Applied Mechanics Reviews*, 47:246 – 250, 1994.

[195] N.A. Fleck. Compressive failure of fiber composites. *Advances in Applied Mechanics*, 33:43 – 117, 1997.

[196] M.J. Hinton, A.S. Kaddour, and P.D. Soden. 3.9 - Prediction of failure envelopes and stress/strain behaviour of composite laminates. In C.T. Sun and J. Tao, editors, *Failure Criteria in Fibre Reinforced Polymer Composites: The World-Wide Failure Exercise*, pages 316 – 333. Elsevier, Oxford, UK, 2004.

[197] W. Guo, P. Xue, and J. Yang. Nonlinear progressive damage model for composite laminates used for low-velocity impact. *Applied Mathematics and Mechanics*, 34:1145 – 1154, 2013.

[198] J. Wiegand and N. Petrinic. A threedimensional damage model for UD composites. Proceedings of the 17th International Conference on Composite Materials - ICCM-17, Edinburgh, UK, 2009.

[199] W. Hufenbach, N. Petrinic, R. Böhm, J. Wiegand, A. Langkamp, F. Marques Ibraim, and B.C.F. Elliot. Multidisciplinary damage analysis of textile reinforced composites for impact and crash applications. Proceedings of the Conference on Damage in Composite Materials - CDCM2006, Stuttgart, Germany, 2006.

[200] P. Linde, J. Pleitner, H. de Boer, and C. Carmone. Modelling and Simulation of Fibre Metal Laminates. Proceedings of the ABAQUS Users' Conference, pages 421 – 439, Boston MA, USA, 2004.

[201] L.P. Durand, editor. *Composite Materials Research Progress.* Nova Science Publishers, New York NY, USA, 2008.

[202] M.O.W. Richardson and M.J. Wisheart. Review of low-velocity impact properties of composite materials. *Composites Part A*, 27:1123 – 1131, 1996.

[203] T.J. Chotard, J. Pasquiet, and M.L. Benzeggagh. Impact response and residual performance of GRP pultruded shapes under static and fatigue loading. *Composites Science and Technology*, 60:895 – 912, 2000.

[204] Q. Guo, G. Zhang, and J. Li. Process parameters design of a three-dimensional and five-directional braided composite joint based on finite element analysis. *Materials and Design*, 46:291 – 300, 2013.

[205] Z.X. Tang and R. Postle. Mechanics of three-dimensional braided structures for composite materials - part II: prediction of the elastic moduli. *Computer Structures*, 51:451 – 457, 2001.

[206] B. Sun and B. Gu. High strain rate behaviour of 4-step 3D braided composites under compressive failure. *Journal of Materials Science*, 42:2463 – 2470, 2007.

[207] J. Ren, Y.K. Kim, and J. Rice. Comparing the fracture toughness of 3-D braided preform composites with z-fiber-reinforced laminar composites. *Textile Research Journal*, 81:335 – 343, 2011.

[208] G.D. Fang, J. Liang, and J.C. Han. Experimental and numerical study of mechanical properties of three dimensional four-directional braided composites. Proceedings of the 18th International Conference on Composite Materials - ICCM-18, Jeju Island, South Korea, 2011.

[209] R. Gerlach. *Characterisation of the strain rate dependent behaviour of 3D composite using a hierarchical approach.* PhD thesis, University of Oxford, 2010.

[210] F. Stig and S. Hallström. Assessment of the mechanical properties of a new 3D woven fibre composite material. *Composites Science and Technology*, 69:1686 – 1692, 2009.

[211] Fleck N.A. Harte, A-M. On the mechanics of braided composites in tension. *European Journal of Mechanics - A/Solids*, 19:259 – 275, 2000.

[212] Instrumented impact testing of plastics and composite materials. ASTM Special Technical Publication 936, Philadelphia PA, USA, 1995.

A. Analytical modelling

A.1. Process-microstructure relationships in 4step braids

```
(*MATHEMATICA CODE TO CALCULATE PROCESS-MICROSTRUCTURE RELATIONSHIPS IN 4STEP BRAIDS*)
(*DISTANCES BETWEEN AXIAL YARN CENTRES ON MACHINE BED*)
deltay=70; (*Horizontal distance in mm*)
deltaz=70; (*Vertical distance in mm*)
(*GENERAL YARN PROPERTIES*)
Tex=2400; (*Linear density axial yarn*)
rhof=2.6; (*Fibre density axial yarn*)
(*BRAID PATTERN*)
m=8; (*Columns*)
n= 4; (*Rows*)
(*HEIGHT OF CONVERGING POINT*)
hcpwo=140;
hcpwi=155;
(*ASSUMED YARN PROPERTIES*)
ypfwo=0.7; (*Yarn packing factor*)
fbwo=2; (*Aspect ratio of braider yarn*)
ypfwi=0.7; (*Yarn packing factor*)
fbwi=2; (*Aspect ratio of braider yarn*)
pfa=0.75; (*Packing factor axial yarn*)
phi=90Degree; (*Inclination angle of axial yarn*)
(*NUMBER OF BRAIDER (AXIAL) YARNS*)
Print["Nb = ",Nb=m*n+m+n];
Print["Na = ",Na=(m-1)*(n-1)];
Nb = 44
Na = 21
(*ANGLES OF BRAIDERS AT POSITION (i,j)*)
Angles[hcp_]:=Module[{},aaij=0;Do[termij=N[ArcTan[(1/hcp)*Sqrt[((m-2*i+3)/2*deltay)^2+
((n-2*j+3)/2*deltaz)^2]]];aaij=aaij+termij,{i,1,m+1},{j,1,n+1}]];
Angles[hcpwo]; aaijwo=aaij;
Angles[hcpwi]; aaijwi=aaij;
(*AVERAGE BRAIDING ANGLE*)
Alpha[aaij_]:= Module[{},alphaa=(aaij/Nb)*180/Pi];
Print["\[Alpha]av_wo = ",Alpha[aaijwo]; avwo=alphaa];
Print["\[Alpha]av_wi = ",Alpha[aaijwi]; avwi=alphaa];
\[Alpha]av_wo = 52.1266
\[Alpha]av_wi = 49.5006
(*SURFACE BRAIDING ANGLE*)
Theta[alphaa_]:= Module[{},theta=N[(alphaa/2)]];
Print["\[Theta]_wo = ",Theta[avwo]; thetawo=theta];
Print["\[Theta]_wi = ",Theta[avwi]; thetawi=theta];
\[Theta]_wo = 26.0633
\[Theta]_wi = 24.7503
(*YARN & PREFORM DIMENSIONS 4STEPWO*)
Print["d_wo = ",dwo=Sqrt[4*(Tex/1000)/(Pi*ypfwo*rhof*fbwo)] ];(*Thickness of braider yarn in mm*)
Print["w_wo = ", wwo=dwo*fbwo](*Width of braider yarn in mm*)
Print["Wp_wo = ", Wpwo=(m+1)*wwo/Cos[thetawo*Pi/180]];(*Preform width in mm*)
Print["Tp_wo = ", Tpwo=(n+1)*dwo/Cos[thetawo*Pi/180]]; (*Preform thickness in mm*)
d_wo = 0.916242
w_wo = 1.83248
Wp_wo = 18.3593
Tp_wo = 5.09981
(*YARN & PREFORM DIMENSIONS 4STEPWI*)
Print["d_wi = ",dwi=Sqrt[4*(Tex/1000)/(Pi*ypfwi*rhof*fbwi)] ];(*Thickness of braider yarn in mm*)
Print["w_wi = ", wwi=dwi*fbwi];(*Width of braider yarn in mm*)
Print["Wp_wi = ", Wpwi=(m*wwi+(m-1)*wwi/2)/Cos[thetawi*Pi/180]];(*Preform width in mm*)
Print["Tp_wi = ", Tpwi=(n*dwi+n*dwi/2)/Cos[thetawi*Pi/180]]; (*Preform thickness in mm*)
Print["a = ",a=Sqrt[(Tex/1000)/(rhof*pfa*Sin[phi])]]; (*Side length of axial yarn in mm*)
Print["wa = ",wa=2*a*Cos[phi/2] ]; (*Horizontal width of axial yarn in mm*)
Print["ta = ",ta=2*a*Sin[phi/2] ]; (*Vertical width of axial yarn in mm*)
d_wi = 0.916242
w_wi = 1.83248
Wp_wi = 23.2052
Tp_wi = 6.05352
a = 1.1094
```

```
wa = 1.56893
ta = 1.56893
(*PITCH LENGTH in mm*)
Pitch[w_, theta_]:= Module[{},pitch=2*w*Cos [theta*Pi/180]/Sin [2*theta*Pi/180]];
Print["h_wo = ",Pitch[wwo,thetawo]; pitchwo=pitch];
Print["h_wi = ",Pitch[wwi,thetawi]; pitchwi=pitch];
h_wo = 4.17076
h_wi = 4.37697
(*YARN JAMMING CONDITION*)
fj=1; (*Aspect ratio of circular yarn cross-section*)
(*Yarn orientation at jamming in degree*)
Print["\[Theta]j_wo = ", thetajwo=ArcCos[1.314*((m*(m+1)*fj^2)/(m^2*fj^2+(m+1)^2))]*180/Pi];
Print["\[Theta]j_wi = ", thetajwi=ArcCos[1.314*((m*(m+1)*fj^2)/(m^2*fj^2+(m+1)^2))]*180/Pi];
\[Theta]j_wo = 49.272
\[Theta]j_wi = 49.272
(*Pitch length for yarn jamming in mm*)
Print["hj_wo = ", hjwo=wwo/Sin[thetajwo*Pi/180]];
Print["hj_wi = ", hjwi=wwi/Sin[thetajwi*Pi/180]];
hj_wo = 2.41811
hj_wi = 2.41811
```

A.2. Elastic properties of 4stepWO

```
(*MATHEMATICA CODE TO CALCULATE ELASTIC PROPERTIES OF 4STEPWO BRAID*)
(*BRAID PATTERN*)
n= 4; (*Rows*)
m=8; (*Columns*)
(*MATERIAL DATA*)
df=15 ; (*Diameter of fibre in\[Mu]m*)
rhof=2.6; (*Density of fibre in g/cm3*)
Tex=2400; (*Linear yarn density in tex*)
E11f=73000; (*Longitudinal modulus of fibre in MPa*)
E22f=E11f; (*Transverse modulus of fibre in MPa*)
G12f=30000; (*Longitudinal shear modulus of fibre in MPa*)
G23f=G12f; (*Transverse shear modulus of fibre in MPa*)
Em=2940; (*Young's modulus of resin in MPa*)
num=0.35; (*Poisson's ratio of resin*)
(*DATA FROM MICROSCOPIC ANALYSES OF CROSS-SECTION*)
Wcwo=14; (*Composite width in mm*)
Tcwo=6.4; (*Composite thickness in mm*)
wewo=2.1; (*Average yarn width from microscopy in mm*)
dewo=0.92; (*Average yarn thickness from microscopy in mm*)
thetawo=21.2Degree; (*Surface braiding angle in degree*)
hwo=9.16; (*Pitch length in mm*)
Gm=Em/(2*(1+num)) ; (*Shear modulus of resin in MPa*)
nu12f= E11f/(2*G12f)-1; (*Poisson's ratio of fibre*)
(*DIMENSIONS OF CIRCULAR YARN*)
Af=Pi/4*(df*0.001)^2; (*Area circular fibre*)
Nf=Tex/(1000*rhof*Pi/4*df^2*0.000001); (*Number of fibres in yarn*)
(*ANGLE BETWEEN HORIZONTAL PROJECTION AND COMPOSITE THICKNESS*)
Print["dywo = ",dywo=N[Wcwo/(m+1)]];
Print["dzwo = ",dzwo=N[Tcwo/(n+1)]];
Print["Phiwo = ",phiwo=N[(ArcTan[dywo/dzwo])]*180/Pi];
dywo = 1.55556
dzwo = 1.28
Phiwo = 50.5505
(*BRAIDING ANGLE*)
Abraiding[theta_,phi_]:= Module[{},alpha=N[ArcTan[12/Pi *Tan[theta]*Sin[phi*Pi/180]]*180/Pi]];
Print["Alphawo = ",Abraiding[thetawo,phiwo]; alphawo=alpha];
Alphawo = 48.8436
(*BRAIDING ANGLES IN INTERIOR AND CORNER CELLS*)
(*gamma - interior*)
Ainterior[alpha_,phi_]:=Module[{},gamma=N[ArcTan[Tan[alpha*Pi/180]/Sin[phi*Pi/180]]*180/Pi]];
Print["Gammawo = ",Ainterior[alphawo,phiwo]; gammawo=gamma];
Gammawo = 55.9823
(*beta - corner*)
Acorner[gamma_]:= Module[{},beta=N[ArcTan[Tan[gamma*Pi/180]/6]*180/Pi]];
Print["Betawo = ",Acorner[gammawo]; betawo=beta];
Betawo = 13.8705
(*DIMENSIONS OF BRAIDER YARNS*)
Print["wwo = ", wwo=Sin[gammawo*Pi/180]*wewo];
Print["dwo = ", dwo=dewo];
Area[wyarn_,dyarn_]:= Module[{},Ay=Pi/4*wyarn*dyarn]; (*Area of braider yarn in mm2*)
Print["Aywo = ",Area[wwo,dwo]; Aywo=Ay];
packfactor[Ay_]:= Module[{},pfy=Af*Nf/Ay]; (*Packing factor of braider yarns*)
Print["pfwo = ",packfactor[Aywo]; pfwo=pfy]; (*Aspect ratio of braider yarn*)
Print["fb = ", fb=wwo/dwo];
wwo = 1.74062
```

```
dwo = 0.92
Aywo = 1.25771
pfwo = 0.733935
fb = 1.89197
(*VOLUME PROPORTIONS OF CELLS TO COMPOSITE*)
Print["Vpi=",Vpi=N[If[Mod[m,2]==0&&Mod[n,2]==0,2*(m*n-m-n+2)/(2*m*n+m+n-2),
2*(m*n-m-n+1)/(2*m*n+m+n)]]]; (*Interior cell*)
Print["Vpis=",Vpis=N[If[Mod[m,2]==0&&Mod[n,2]==0,(m+n-4)/(2*m*n+m+n-2),
(m+n-2)/(2*m*n+m+n)]]]; (*Interior surface cell*)
Print["Vpes=",Vpes=N[If[Mod[m,2]==0&&Mod[n,2]==0,2*(m+n-4)/(2*m*n+m+n-2),
2*(m+n-2)/(2*m*n+m+n)]]]; (*Exterior surface cell*)
Print["Vpc=",Vpc=N[If[Mod[m,2]==0&&Mod[n,2]==0,8/(2*m*n+m+n-2),4/
(2*m*n+m+n)]]]; (*Corner cell*)
Vpi = 0.594595
Vpis = 0.108108
Vpes = 0.216216
Vpc = 0.108108
(*FIBRE VOLUME FRACTIONS OF CELLS*)
Print["Vfiwo=",Vfiwo=Sqrt[3]*Pi/8*Sin[2*phiwo*Pi/180]*pfwo]; (*Interior cell*)
Print["Vfiswo=",Vfiswo=Sqrt[3]*Pi*Sin[2*phiwo*Pi/180]/(8*Sin[Pi-2*phiwo*Pi/180])*pfwo]; (*Interior surface cell*)
Print["Vfeswo=",Vfeswo=(3*Sqrt[3]*Pi*Cos[phiwo*Pi/180]*Cos[gammawo*Pi/180])/
(16*Cos[thetawo])*pfwo]; (*Exterior surface cell*)
Print["Vfcwo=",Vfcwo=3*Sqrt[3]*Pi*Sin[2*phiwo*Pi/180]/(4*(2*Cos[phiwo*Pi/180]+1)*
(2*Sin[phiwo*Pi/180]+1))*(Cos[gammawo*Pi/180]/Cos[betawo*Pi/180])*pfwo]; (*Corner cell*)
Vfiwo = 0.489863
Vfiswo = 0.499204
Vfeswo = 0.285502
Vfcwo = 0.293144
(*FIBRE VOLUME FRACTION OF COMPOSITE*)
Print["Vfwo = ",Vfwo=Vpi*Vfiwo+Vpis*Vfiswo+Vpes*Vfeswo+Vpc*Vfcwo];
Vfwo = 0.43866
(*MATRIX VOLUME FRACTIONS OF CELLS*)
Vmiwo=1-Vfiwo;
Vmiswo=1-Vfiswo;
Vmeswo=1-Vfeswo;
Vmcwo=1-Vfcwo;
(*ELASTIC CONSTANTS - UD*)
LongitudinalM[Vf_,Vm_]:= Module[{},E11n=Vf*E11f+Vm*Em];
LongitudinalM[Vfiwo,Vmiwo]; E11iwo=E11n;
LongitudinalM[Vfiswo,Vmiswo]; E11iswo=E11n;
LongitudinalM[Vfeswo,Vmeswo];E11eswo=E11n;
LongitudinalM[Vfcwo,Vmcwo];E11cwo=E11n;
TransverseM[Vf_,Vm_]:= Module[{},E22n=Em/(1-Sqrt[Vf]*(1-Em/E22f))];
TransverseM[Vfiwo,Vmiwo];E22iwo=E22n;
TransverseM[Vfiswo,Vmiswo];E22iswo=E22n;
TransverseM[Vfeswo,Vmeswo];E22eswo=E22n;
TransverseM[Vfcwo,Vmcwo];E22cwo=E22n;
LongitudinalS[Vf_,Vm_]:= Module[{},G12n=Gm/(1-Sqrt[Vf]*(1-Gm/G12f))];
LongitudinalS[Vfiwo,Vmiwo];G12iwo=G12n;
LongitudinalS[Vfiswo,Vmiswo];G12iswo=G12n;
LongitudinalS[Vfeswo,Vmeswo];G12eswo=G12n;
LongitudinalS[Vfcwo,Vmcwo];G12cwo=G12n;
LongitudinalP[Vf_,Vm_]:= Module[{},nu12n=Vf*nu12f+Vm*num];
LongitudinalP[Vfiwo,Vmiwo];nu12iwo=nu12n;
LongitudinalP[Vfiswo,Vmiswo];nu12iswo=nu12n;
LongitudinalP[Vfeswo,Vmeswo];nu12eswo=nu12n;
LongitudinalP[Vfcwo,Vmcwo];nu12cwo=nu12n;
TransverseS[Vf_,Vm_,E11_,E22_,nu12_]:= Module[{},G23n=Gm/(1-Sqrt[Vf]*(1-Gm/G23f))];
TransverseS[Vfiwo,Vmiwo,E11iwo,E22iwo,nu12iwo];G23iwo=G23n;
TransverseS[Vfiswo,Vmiswo,E11iswo,E22iswo,nu12iswo];G23iswo=G23n;
TransverseS[Vfeswo,Vmeswo,E11eswo,E22eswo,nu12eswo];G23eswo=G23n;
TransverseS[Vfcwo,Vmcwo,E11cwo,E22cwo,nu12cwo];G23cwo=G23n;
TransverseP[E22_,G23_]:= Module[{},nu23n=E22/(2*G23)-1];
TransverseP[E22iwo,G23iwo];nu23iwo=nu23n;
TransverseP[E22iswo,G23iswo];nu23iswo=nu23n;
TransverseP[E22eswo,G23eswo];nu23eswo=nu23n;
TransverseP[E22cwo,G23cwo];nu23cwo=nu23n;
(*STIFFNESS MATRICES OF UDs*)
StiffnessTensor[E11_,E22_,G12_,G23_,v12_,v23_]:=Module[{},Cij={{(1-v23^2)*E11/
(1-v23^2-2*v12^2*E22/E11*(1+v23)),v12*(1+v23)*E22/(1-v23^2-2*v12^2*E22/E11*
(1+v23)),v12*(1+v23)*E22/(1-v23^2-2*v12^2*E22/E11*(1+v23)),0,0,0},
{v12*(1+v23)*E22/(1-v23^2-2*v12^2*E22/E11*(1+v23)),(1-v12^2*E22/E11)*E22/
(1-v23^2-2*v12^2*E22/E11*(1+v23)),(v23+v12^2*E22/E11)*E22/
(1-v23^2-2*v12^2*E22/E11*(1+v23)),0,0,0},{v12*(1+v23)*E22/(1-v23^2-2*v12^2*E22/
E11*(1+v23)),(v23+v12^2*E22/E11)*E22/(1-v23^2-2*v12^2*E22/E11*(1+v23)),
(1-v12^2*E22/E11)*E22/(1-v23^2-2*v12^2*E22/E11*(1+v23)),0,0,0},{0, 0, 0,G23, 0, 0},
{0, 0, 0, 0, G12, 0}, {0, 0, 0, 0, 0, G12}};Cij];
StiffnessTensor[E11iwo, E22iwo, G12iwo,G23iwo, nu12iwo, nu23iwo]; Cijiwo=Cij;
StiffnessTensor[E11iswo, E22iswo, G12iswo,G23iswo, nu12iswo, nu23iswo]; Cijiswo=Cij;
StiffnessTensor[E11eswo, E22eswo, G12eswo,G23eswo, nu12eswo, nu23eswo]; Cijeswo=Cij;
```

```
StiffnessTensor[E11cwo, E22cwo, G12cwo,G23cwo, nu12cwo, nu23cwo]; Cijcwo=Cij;
(*TRANSFORMATION MATRIX Te*)
TransformationTensor[l1__, l2__, l3__, m1__, m2__, m3__,n1__, n2__, n3__] := Module[{},
Tepsilon= {{l1^2, m1^2, n1^2, m1*n1, l1*n1, l1*m1},{l2^2, m2^2, n2^2,m2*n2, l2*n2, l2*m2},
{l3^2, m3^2, n3^2,m3*n3, l3*n3, l3*m3}, {2*l2*l3,2*m2*m3,2*n2*n3,m2*n3+m3*n2,l2*n3+
n2*l3,l2*m3+m2*l3},{2*l1*l3,2*m1*m3,2*n1*n3,m1*n3+n1*m3,l1*n3+n1*l3,l1*m3+m1*l3},
{2*l1*l2,2*m1*m2,2*n1*n2,m1*n2+n1*m2,l1*n2+n1*l2,l1*m2+m1*l2}};Tepsilon];
(*Interior cells - 4 types of fibre orientations*)
TransformationTensor[Cos[gammawo*Pi/180],0,-Sin[gammawo*Pi/180],Sin[gammawo*Pi/180]*
Cos[phiwo*Pi/180],Sin[phiwo*Pi/180],Cos[gammawo*Pi/180]*Cos[phiwo*Pi/180],Sin[gammawo*
Pi/180]*Sin[phiwo*Pi/180],-Cos[phiwo*Pi/180],Cos[gammawo*Pi/180]*Sin[phiwo*Pi/180]];
Tepsiloni1wo=Tepsilon;
TransformationTensor[Cos[gammawo*Pi/180],0,-Sin[gammawo*Pi/180],Sin[gammawo*Pi/180]*
Cos[-phiwo*Pi/180],Sin[-phiwo*Pi/180],Cos[gammawo*Pi/180]*Cos[-phiwo*Pi/180],Sin[gammawo*
Pi/180]*Sin[-phiwo*Pi/180],-Cos[-phiwo*Pi/180],Cos[gammawo*Pi/180]*Sin[-phiwo*Pi/180]];
Tepsiloni2wo=Tepsilon;
TransformationTensor[Cos[-gammawo*Pi/180],0,-Sin[-gammawo*Pi/180],Sin[-gammawo*Pi/180]*
Cos[phiwo*Pi/180],Sin[phiwo*Pi/180],Cos[-gammawo*Pi/180]*Cos[phiwo*Pi/180],Sin[-gammawo*
Pi/180]*Sin[phiwo*Pi/180],-Cos[phiwo*Pi/180],Cos[-gammawo*Pi/180]*Sin[phiwo*Pi/180]];
Tepsiloni3wo=Tepsilon;
TransformationTensor[Cos[-gammawo*Pi/180],0,-Sin[-gammawo*Pi/180],Sin[-gammawo*Pi/180]*
Cos[-phiwo*Pi/180],Sin[-phiwo*Pi/180],Cos[-gammawo*Pi/180]*Cos[-phiwo*Pi/180],
Sin[-gammawo*Pi/180]*Sin[-phiwo*Pi/180],-Cos[-phiwo*Pi/180],Cos[-gammawo*Pi/180]*
Sin[-phiwo*Pi/180]];Tepsiloni4wo=Tepsilon;
(*Interior surface cells - 4 types of fibre orientations*)
TransformationTensor[Cos[gammawo*Pi/180],0,-Sin[gammawo*Pi/180],Sin[gammawo*Pi/180]*
Cos[phiwo*Pi/180],Sin[phiwo*Pi/180],Cos[gammawo*Pi/180]*Cos[phiwo*Pi/180],Sin[gammawo*
Pi/180]*Sin[phiwo*Pi/180],-Cos[phiwo*Pi/180],Cos[gammawo*Pi/180]*Sin[phiwo*Pi/180]];
Tepsilonis1wo=Tepsilon;
TransformationTensor[Cos[gammawo*Pi/180],0,-Sin[gammawo*Pi/180],Sin[gammawo*Pi/180]*
Cos[-phiwo*Pi/180],Sin[-phiwo*Pi/180],Cos[gammawo*Pi/180]*Cos[-phiwo*Pi/180],Sin[gammawo*
Pi/180]*Sin[-phiwo*Pi/180],-Cos[-phiwo*Pi/180],Cos[gammawo*Pi/180]*Sin[-phiwo*Pi/180]];
Tepsilonis2wo=Tepsilon;
TransformationTensor[Cos[-gammawo*Pi/180],0,-Sin[-gammawo*Pi/180],Sin[-gammawo*Pi/180]*
Cos[phiwo*Pi/180],Sin[phiwo*Pi/180],Cos[-gammawo*Pi/180]*Cos[phiwo*Pi/180],Sin[-gammawo*
Pi/180]*Sin[phiwo*Pi/180],-Cos[phiwo*Pi/180],Cos[-gammawo*Pi/180]*Sin[phiwo*Pi/180]];
Tepsilonis3wo=Tepsilon;
TransformationTensor[Cos[-gammawo*Pi/180],0,-Sin[-gammawo*Pi/180],Sin[-gammawo*Pi/180]*
Cos[-phiwo*Pi/180],Sin[-phiwo*Pi/180],Cos[-gammawo*Pi/180]*Cos[-phiwo*Pi/180],Sin[-gammawo*
Pi/180]*Sin[-phiwo*Pi/180],-Cos[-phiwo*Pi/180],Cos[-gammawo*Pi/180]*Sin[-phiwo*Pi/180]];
Tepsilonis4wo=Tepsilon;
(*Exterior surface cells - 4 types of fibre orientations*)
TransformationTensor[Cos[thetawo],0,-Sin[thetawo],Sin[thetawo]*Cos[0 Degree],Sin[0 Degree],
Cos[thetawo]*Cos[0 Degree],Sin[thetawo]*Sin[0 Degree],-Cos[0 Degree],Cos[thetawo]*
Sin[0 Degree]];Tepsilones1wo=Tepsilon;
TransformationTensor[Cos[thetawo],0,-Sin[thetawo],Sin[thetawo]*Cos[90 Degree],Sin[90 Degree],
Cos[thetawo]*Cos[90 Degree],Sin[thetawo]*Sin[90 Degree],-Cos[90 Degree],Cos[thetawo]*
Sin[90 Degree]];Tepsilones2wo=Tepsilon;
TransformationTensor[Cos[-thetawo],0,-Sin[-thetawo],Sin[-thetawo]*Cos[0 Degree],Sin[0 Degree],
Cos[-thetawo]*Cos[0 Degree],Sin[-thetawo]*Sin[0 Degree],-Cos[0 Degree],Cos[-thetawo]*
Sin[0 Degree]];Tepsilones3wo=Tepsilon;
TransformationTensor[Cos[-thetawo],0,-Sin[-thetawo],Sin[-thetawo]*Cos[90 Degree],
Sin[90 Degree],Cos[-thetawo]*Cos[90 Degree],Sin[-thetawo]*Sin[90 Degree],
-Cos[90 Degree],Cos[-thetawo]*Sin[90 Degree]];Tepsilones4wo=Tepsilon;
(*Corner cells - 4 types of fibre orientations*)
TransformationTensor[Cos[betawo*Pi/180],0,-Sin[betawo*Pi/180],Sin[betawo*Pi/180]*
Cos[0 Degree],Sin[0 Degree],Cos[betawo*Pi/180]*Cos[0 Degree],Sin[betawo*Pi/180]*
Sin[0 Degree],-Cos[0 Degree],Cos[betawo*Pi/180]*Sin[0 Degree]];Tepsilonc1wo=Tepsilon;
TransformationTensor[Cos[betawo*Pi/180],0,-Sin[betawo*Pi/180],Sin[betawo*Pi/180]*
Cos[90 Degree],Sin[90 Degree],Cos[betawo*Pi/180]*Cos[90 Degree],Sin[betawo*Pi/180]*
Sin[90 Degree],-Cos[90 Degree],Cos[betawo*Pi/180]*Sin[90 Degree]];Tepsilonc2wo=Tepsilon;
TransformationTensor[Cos[-betawo*Pi/180],0,-Sin[-betawo*Pi/180],Sin[-betawo*Pi/180]*
Cos[0 Degree],Sin[0 Degree],Cos[-betawo*Pi/180]*Cos[0 Degree],Sin[-betawo*Pi/180]*
Sin[0 Degree],-Cos[0 Degree],Cos[-betawo*Pi/180]*Sin[0 Degree]];Tepsilonc3wo=Tepsilon;
TransformationTensor[Cos[-betawo*Pi/180],0,-Sin[-betawo*Pi/180],Sin[-betawo*Pi/180]*
Cos[90 Degree],Sin[90 Degree],Cos[-betawo*Pi/180]*Cos[90 Degree],Sin[-betawo*Pi/180]*
Sin[90 Degree],-Cos[90 Degree],Cos[-betawo*Pi/180]*Sin[90 Degree]];Tepsilonc4wo=Tepsilon;
(*TRANSFORMATION MATRIX Ts*)
TransformationTensor[l1__, l2__, l3__, m1__, m2__, m3__,n1__, n2__, n3__] := Module[{},
Tsigma= {{l1^2, m1^2, n1^2, 2*m1*n1,2* l1*n1,2* l1*m1},{l2^2, m2^2, n2^2,2*m2*n2,
2*l2*n2,2* l2*m2},{l3^2, m3^2, n3^2,2*m3*n3,2* l3*n3,2* l3*m3}, {l2*l3,m2*m3,n2*n3,
m2*n3+m3*n2,l2*n3+n2*l3,l2*m3+m2*l3},{l1*l3,m1*m3,n1*n3,m1*n3+n1*m3,l1*n3+n1*l3,
l1*m3+m1*l3},{l1*l2,m1*m2,n1*n2,m1*n2+n1*m2,l1*n2+n1*l2,l1*m2+m1*l2}};Tsigma];
(*Interior cells - 4 types of fibre orientations*)
TransformationTensor[Cos[gammawo*Pi/180],0,-Sin[gammawo*Pi/180],Sin[gammawo*Pi/180]*
Cos[phiwo*Pi/180],Sin[phiwo*Pi/180],Cos[gammawo*Pi/180]*Cos[phiwo*Pi/180],Sin[gammawo*
Pi/180]*Sin[phiwo*Pi/180],-Cos[phiwo*Pi/180],Cos[gammawo*Pi/180]*Sin[phiwo*Pi/180]];
Tsigmai1wo=Tsigma; TransformationTensor[Cos[gammawo*Pi/180],0,-Sin[gammawo*Pi/180],
Sin[gammawo*Pi/180]*Cos[-phiwo*Pi/180],Sin[-phiwo*Pi/180],Cos[gammawo*Pi/180]*
Cos[-phiwo*Pi/180],Sin[gammawo*Pi/180]*Sin[-phiwo*Pi/180],-Cos[-phiwo*Pi/180],
```

```
Cos[gammawo*Pi/180]*Sin[-phiwo*Pi/180]];Tsigmai2wo=Tsigma;
TransformationTensor[Cos[-gammawo*Pi/180],0,-Sin[-gammawo*Pi/180],Sin[-gammawo*
Pi/180]*Cos[phiwo*Pi/180],Sin[phiwo*Pi/180],Cos[-gammawo*Pi/180]*Cos[phiwo*Pi/180],
Sin[-gammawo*Pi/180]*Sin[phiwo*Pi/180],-Cos[phiwo*Pi/180],Cos[-gammawo*Pi/180]*
Sin[phiwo*Pi/180]];Tsigmai3wo=Tsigma; TransformationTensor[Cos[-gammawo*Pi/180],0,
-Sin[-gammawo*Pi/180],Sin[-gammawo*Pi/180]*Cos[-phiwo*Pi/180],Sin[-phiwo*Pi/180],
Cos[-gammawo*Pi/180]*Cos[-phiwo*Pi/180],Sin[-gammawo*Pi/180]*Sin[-phiwo*Pi/180],
-Cos[-phiwo*Pi/180],Cos[-gammawo*Pi/180]*Sin[-phiwo*Pi/180]];Tsigmai4wo=Tsigma;
(*Interior surface cells - 4 types of fibre orientations*)
TransformationTensor[Cos[gammawo*Pi/180],0,-Sin[gammawo*Pi/180],Sin[gammawo*
Pi/180]*Cos[phiwo*Pi/180],Sin[phiwo*Pi/180],Cos[gammawo*Pi/180]*Cos[phiwo*Pi/180],
Sin[gammawo*Pi/180]*Sin[phiwo*Pi/180],-Cos[phiwo*Pi/180],Cos[gammawo*Pi/180]*
Sin[phiwo*Pi/180]];Tsigmais1wo=Tsigma;
TransformationTensor[Cos[gammawo*Pi/180],0,-Sin[gammawo*Pi/180],Sin[gammawo*
Pi/180]*Cos[-phiwo*Pi/180],Sin[-phiwo*Pi/180],Cos[gammawo*Pi/180]*Cos[-phiwo*
Pi/180],Sin[gammawo*Pi/180]*Sin[-phiwo*Pi/180],-Cos[-phiwo*Pi/180],Cos[gammawo*
Pi/180]*Sin[-phiwo*Pi/180]];Tsigmais2wo=Tsigma;
TransformationTensor[Cos[-gammawo*Pi/180],0,-Sin[-gammawo*Pi/180],Sin[-gammawo*
Pi/180]*Cos[phiwo*Pi/180],Sin[phiwo*Pi/180],Cos[-gammawo*Pi/180]*Cos[phiwo*Pi/180],
Sin[-gammawo*Pi/180]*Sin[phiwo*Pi/180],-Cos[phiwo*Pi/180],Cos[-gammawo*Pi/180]*
Sin[phiwo*Pi/180]];Tsigmais3wo=Tsigma;
TransformationTensor[Cos[-gammawo*Pi/180],0,-Sin[-gammawo*Pi/180],Sin[-gammawo*
Pi/180]*Cos[-phiwo*Pi/180],Sin[-phiwo*Pi/180],Cos[-gammawo*Pi/180]*Cos[-phiwo*
Pi/180],Sin[-gammawo*Pi/180]*Sin[-phiwo*Pi/180],-Cos[-phiwo*Pi/180],Cos[-gammawo*
Pi/180]*Sin[-phiwo*Pi/180]];Tsigmais4wo=Tsigma;
(*Exterior surface cells - 4 types of fibre orientations*)
TransformationTensor[Cos[thetawo],0,-Sin[thetawo],Sin[thetawo]*Cos[0 Degree],Sin[0 Degree],
Cos[thetawo]*Cos[0 Degree],Sin[thetawo]*Sin[0 Degree],-Cos[0 Degree],Cos[thetawo]*
Sin[0 Degree]];Tsigmaes1wo=Tsigma;
TransformationTensor[Cos[thetawo],0,-Sin[thetawo],Sin[thetawo]*Cos[90 Degree],Sin[90 Degree],
Cos[thetawo]*Cos[90 Degree],Sin[thetawo]*Sin[90 Degree],-Cos[90 Degree],Cos[thetawo]*
Sin[90 Degree]];Tsigmaes2wo=Tsigma;
TransformationTensor[Cos[-thetawo],0,-Sin[-thetawo],Sin[-thetawo]*Cos[0 Degree],Sin[0 Degree],
Cos[-thetawo]*Cos[0 Degree],Sin[-thetawo]*Sin[0 Degree],-Cos[0 Degree],Cos[-thetawo]*
Sin[0 Degree]];Tsigmaes3wo=Tsigma;
TransformationTensor[Cos[-thetawo],0,-Sin[-thetawo],Sin[-thetawo]*Cos[90 Degree],Sin[90 Degree],
Cos[-thetawo]*Cos[90 Degree],Sin[-thetawo]*Sin[90 Degree],-Cos[90 Degree],Cos[-thetawo]*
Sin[90 Degree]];Tsigmaes4wo=Tsigma;
(*Corner cells - 4 types of fibre orientations*)
TransformationTensor[Cos[betawo*Pi/180],0,-Sin[betawo*Pi/180],Sin[betawo*Pi/180]*
Cos[0 Degree],Sin[0 Degree],Cos[betawo*Pi/180]*Cos[0 Degree],Sin[betawo*Pi/180]*
Sin[0 Degree],-Cos[0 Degree],Cos[betawo*Pi/180]*Sin[0 Degree]];Tsigmac1wo=Tsigma;
TransformationTensor[Cos[betawo*Pi/180],0,-Sin[betawo*Pi/180],Sin[betawo*Pi/180]*
Cos[90 Degree],Sin[90 Degree],Cos[betawo*Pi/180]*Cos[90 Degree],Sin[betawo*Pi/180]*
Sin[90 Degree],-Cos[90 Degree],Cos[betawo*Pi/180]*Sin[90 Degree]];Tsigmac2wo=Tsigma;
TransformationTensor[Cos[-betawo*Pi/180],0,-Sin[-betawo*Pi/180],Sin[-betawo*Pi/180]*
Cos[0 Degree],Sin[0 Degree],Cos[-betawo*Pi/180]*Cos[0 Degree],Sin[-betawo*Pi/180]*
Sin[0 Degree],-Cos[0 Degree],Cos[-betawo*Pi/180]*Sin[0 Degree]];Tsigmac3wo=Tsigma;
TransformationTensor[Cos[-betawo*Pi/180],0,-Sin[-betawo*Pi/180],Sin[-betawo*Pi/180]*
Cos[90 Degree],Sin[90 Degree],Cos[-betawo*Pi/180]*Cos[90 Degree],Sin[-betawo*Pi/180]*
Sin[90 Degree],-Cos[90 Degree],Cos[-betawo*Pi/180]*Sin[90 Degree]];Tsigmac4wo=Tsigma;
(*TRANSFORMED STIFFNESS MATRICES*)
(*Interior cell*)
Cijti1wo=Inverse[Tsigmai1wo].Cijiwo.Tepsiloni1wo;
Cijti2wo=Inverse[Tsigmai2wo].Cijiwo.Tepsiloni2wo;
Cijti3wo=Inverse[Tsigmai3wo].Cijiwo.Tepsiloni3wo;
Cijti4wo=Inverse[Tsigmai4wo].Cijiwo.Tepsiloni4wo;
(*Interior surface cell*)
Cijtis1wo=Inverse[Tsigmais1wo].Cijiswo.Tepsilonis1wo;
Cijtis2wo=Inverse[Tsigmais2wo].Cijiswo.Tepsilonis2wo;
Cijtis3wo=Inverse[Tsigmais3wo].Cijiswo.Tepsilonis3wo;
Cijtis4wo=Inverse[Tsigmais4wo].Cijiswo.Tepsilonis4wo;
(*Exterior surface cell*)
Cijtes1wo=Inverse[Tsigmaes1wo].Cijeswo.Tepsilones1wo;
Cijtes2wo=Inverse[Tsigmaes2wo].Cijeswo.Tepsilones2wo;
Cijtes3wo=Inverse[Tsigmaes3wo].Cijeswo.Tepsilones3wo;
Cijtes4wo=Inverse[Tsigmaes4wo].Cijeswo.Tepsilones4wo;
(*Corner cell*)
Cijtc1wo=Inverse[Tsigmac1wo].Cijcwo.Tepsilonc1wo;
Cijtc2wo=Inverse[Tsigmac2wo].Cijcwo.Tepsilonc2wo;
Cijtc3wo=Inverse[Tsigmac3wo].Cijcwo.Tepsilonc3wo;
Cijtc4wo=Inverse[Tsigmac4wo].Cijcwo.Tepsilonc4wo;
(*VOLUME PROPORTIONS OF EACH YARN*)
Vpiwo=Vpi/4;
Vpiswo=Vpis/4;
Vpeswo=Vpes/4;
Vpcwo=Vpc/4;
(*EFFECTIVE STIFFNESS MATRIX OF EACH CELL*)
Ceffiwo = Vpiwo*(Cijti1wo+Cijti2wo+Cijti3wo+Cijti4wo);(*Interior cell*)
Ceffiswo= Vpiswo*(Cijtis1wo+Cijtis2wo+Cijtis3wo+Cijtis4wo);(*Interior surface cell*)
```

```
Ceffeswo= Vpeswo*(Cijtes1wo+Cijtes2wo+Cijtes3wo+Cijtes4wo);(*Exterior surface cell*)
Ceffcwo= Vpcwo*(Cijtc1wo+Cijtc2wo+Cijtc3wo+Cijtc4wo);(*Corner cell*)
(*TOTAL STIFFNESS MATRIX OF BRAIDED COMPOSITE*)
Ceffbwo=Ceffiwo+Ceffiswo+Ceffeswo+Ceffcwo;
(*TOTAL COMPLIANCE MATRIX OF BRAIDED COMPOSITE*)
Seffbwo=Inverse[Ceffbwo];
(*ELASTIC CONSTANTS*)
Print["Exwo = ",Exwo=1/Seffbwo[[1,1]]];
Print["Eywo = ",Eywo=1/Seffbwo[[2,2]]];
Print["Ezwo = ",Ezwo=1/Seffbwo[[3,3]]];
Print["Gxywo = ",Gxywo=1/Seffbwo[[6,6]]];
Print["Gxzwo = ",Gxzwo=1/Seffbwo[[5,5]]];
Print["Gyzwo = ",Gyzwo=1/Seffbwo[[4,4]]];
Print["nuxywo = ",nuxywo=-Seffbwo[[1,2]]/Seffbwo[[1,1]]];
Print["nuxzwo = ",nuxzwo=-Seffbwo[[1,3]]/Seffbwo[[1,1]]];
Print["nuyzwo = ",nuyzwo=-Seffbwo[[2,3]]/Seffbwo[[2,2]]];
Exwo = 12261.3
Eywo = 8157.47
Ezwo = 9219.09
Gxywo = 5094.97
Gxzwo = 5928.
Gyzwo = 5375.74
nuxywo = 0.320976
nuxzwo = 0.355686
nuyzwo = 0.344287
```

B. Numerical modelling

B.1. Python code 4stepWO

```
#PYTHON CODE TO CREATE INP-FILES WITH NODE COORDINATES OF BRAIDER YARNS IN 4STEPWO BRAID
import os, glob, csv, math
#INPUT
input = open(’data-4stepWO.txt’, ’r’).readlines()
wc = float(input[0])
tc = float(input[1])
dy = float(input[2])
dz = float(input[3])
Ab = float(input[4])
h = float(input[5])
#CHANGE NUMSTEPS
# 4 steps needed to change the node position in 1 step
# 1 pitch length = 4 machine steps -> 16 python matrix steps in total
NUM_STEPS = 16
def AreaOutput(filename):
    """Function to write braider area to inp-file."""
    ay = Ab
    areab = open(filename, ’w’)
    areab.write("%f\n" % ay)
    areab.close()
#INITIAL CONDITION
#Matrix for node array of cross-section according to machine arrangement and movements
matrix=[
    [None,None,None,None,   0,None, ... ,None,   3,None,None,None,None,None,None,None,None],
    [None,None,None,None,None,None, ... ,None,None,None,None,None,None,None,None,None,None],
    [None,None,None,None,None,None, ... ,None,None,None,None,None,None,None,None,None,None],
    [None,None,None,None,None,None, ... ,None,None,None,None,None,None,None,None,None,None],
    [None,None,None,None,   4,None, ... ,None,  10,None,None,None,  11,None,None,None,  12],
    [None,None,None,None,None,None, ... ,None,None,None,None,None,None,None,None,None,None],
    [None,None,None,None,None,None, ... ,None,None,None,None,None,None,None,None,None,None],
    [None,None,None,None,None,None, ... ,None,None,None,None,None,None,None,None,None,None],
    [  21,None,None,None,  13,None, ... ,None,  19,None,None,None,  20,None,None,None,None],
    [None,None,None,None,None,None, ... ,None,None,None,None,None,None,None,None,None,None],
    [None,None,None,None,None,None, ... ,None,None,None,None,None,None,None,None,None,None],
    [None,None,None,None,None,None, ... ,None,None,None,None,None,None,None,None,None,None],
    [None,None,None,None,  22,None, ... ,None,  28,None,None,None,  29,None,None,None,  30],
    [None,None,None,None,None,None, ... ,None,None,None,None,None,None,None,None,None,None],
    [None,None,None,None,None,None, ... ,None,None,None,None,None,None,None,None,None,None],
    [None,None,None,None,None,None, ... ,None,None,None,None,None,None,None,None,None,None],
    [  39,None,None,None,  31,None, ... ,None,  37,None,None,None,  38,None,None,None,None],
    [None,None,None,None,None,None, ... ,None,None,None,None,None,None,None,None,None,None],
    [None,None,None,None,None,None, ... ,None,None,None,None,None,None,None,None,None,None],
    [None,None,None,None,None,None, ... ,None,None,None,None,None,None,None,None,None,None],
    [None,None,None,None,None,None, ... ,None,None,None,None,None,  43,None,None,None,None],]
#BRAIDER MOVEMENTS FOR EACH STEP
#Row movements: 0 paused, +1 to the right, -1 to the left
#Column movements: 0 paused, +1 down, -1 up
steps=(# 1st machine step
    #Step1 - inner rows move left or right
    {’rows’: (0,0,0,0,-1,0,0,0,+1,0,0,0,-1,0,0,0,+1,0,0,0,0),
    ’cols’: (0,0,0,0,0,0,0,0,0,0,0,0,0,0,0,0,0,0,0,0,0,0,0,0,0,0,0,0,0,0,0,0,0,0,0,0,0)},
    #Step 2 - inner rows move left or right
    {’rows’: (0,0,0,0,-1,0,0,0,+1,0,0,0,-1,0,0,0,+1,0,0,0,0),
    ’cols’: (0,0,0,0,0,0,0,0,0,0,0,0,0,0,0,0,0,0,0,0,0,0,0,0,0,0,0,0,0,0,0,0,0,0,0,0,0)},
    #Step 3 - inner rows move left or right
    {’rows’: (0,0,0,0,-1,0,0,0,+1,0,0,0,-1,0,0,0,+1,0,0,0,0),
    ’cols’: (0,0,0,0,0,0,0,0,0,0,0,0,0,0,0,0,0,0,0,0,0,0,0,0,0,0,0,0,0,0,0,0,0,0,0,0,0)},
    #Step 4 - inner rows move left or right
    {’rows’: (0,0,0,0,-1,0,0,0,+1,0,0,0,-1,0,0,0,+1,0,0,0,0),
    ’cols’: (0,0,0,0,0,0,0,0,0,0,0,0,0,0,0,0,0,0,0,0,0,0,0,0,0,0,0,0,0,0,0,0,0,0,0,0,0)},
    # 2nd machine step
    #Step 5 - columns move up or down
    {’rows’: (0,0,0,0,0,0,0,0,0,0,0,0,0,0,0,0,0,0,0,0,0),
    ’cols’: (0,0,0,0,+1,0,0,0,-1,0,0,0,+1,0,0,0,-1,0,0,0,+1,0,0,0,-1,0,0,0,+1,0,0,0,-1,0,0,0,0)},
```

```
    #Step 6 - columns move up or down
    {’rows’: (0,0,0,0,0,0,0,0,0,0,0,0,0,0,0,0,0,0,0,0,0),
    ’cols’: (0,0,0,0,+1,0,0,0,-1,0,0,0,+1,0,0,0,-1,0,0,0,+1,0,0,0,-1,0,0,0,+1,0,0,0,-1,0,0,0,0,0)},
    #Step 7 - columns move up or down
    {’rows’: (0,0,0,0,0,0,0,0,0,0,0,0,0,0,0,0,0,0,0,0,0),
    ’cols’: (0,0,0,0,+1,0,0,0,-1,0,0,0,+1,0,0,0,-1,0,0,0,+1,0,0,0,-1,0,0,0,+1,0,0,0,-1,0,0,0,0,0)},
    #Step 8 - columns move up or down
    {’rows’: (0,0,0,0,0,0,0,0,0,0,0,0,0,0,0,0,0,0,0,0,0),
    ’cols’: (0,0,0,0,+1,0,0,0,-1,0,0,0,+1,0,0,0,-1,0,0,0,+1,0,0,0,-1,0,0,0,+1,0,0,0,-1,0,0,0,0,0)},
    # 3rd machine step
    #Step 9 - inner rows move left or right
    {’rows’: (0,0,0,0,+1,0,0,0,-1,0,0,0,+1,0,0,0,-1,0,0,0,0),
    ’cols’: (0,0,0,0,0,0,0,0,0,0,0,0,0,0,0,0,0,0,0,0,0,0,0,0,0,0,0,0,0,0,0,0,0,0,0,0,0,0)},
    #Step 10 - inner rows move left or right
    {’rows’: (0,0,0,0,+1,0,0,0,-1,0,0,0,+1,0,0,0,-1,0,0,0,0),
    ’cols’: (0,0,0,0,0,0,0,0,0,0,0,0,0,0,0,0,0,0,0,0,0,0,0,0,0,0,0,0,0,0,0,0,0,0,0,0,0,0)},
    #Step 11 - inner rows move left or right
    {’rows’: (0,0,0,0,+1,0,0,0,-1,0,0,0,+1,0,0,0,-1,0,0,0,0),
    ’cols’: (0,0,0,0,0,0,0,0,0,0,0,0,0,0,0,0,0,0,0,0,0,0,0,0,0,0,0,0,0,0,0,0,0,0,0,0,0,0)},
    #Step 12 - inner rows move left or right
    {’rows’: (0,0,0,0,+1,0,0,0,-1,0,0,0,+1,0,0,0,-1,0,0,0,0),
    ’cols’: (0,0,0,0,0,0,0,0,0,0,0,0,0,0,0,0,0,0,0,0,0,0,0,0,0,0,0,0,0,0,0,0,0,0,0,0,0,0)},
    # 4th machine step
    #Step 13 - columns move up or down
    {’rows’: (0,0,0,0,0,0,0,0,0,0,0,0,0,0,0,0,0,0,0,0,0),
    ’cols’: (0,0,0,0,-1,0,0,0,+1,0,0,0,-1,0,0,0,+1,0,0,0,-1,0,0,0,+1,0,0,0,-1,0,0,0,+1,0,0,0,0,0)},
    #Step 14 - columns move up or down
    {’rows’: (0,0,0,0,0,0,0,0,0,0,0,0,0,0,0,0,0,0,0,0,0),
    ’cols’: (0,0,0,0,-1,0,0,0,+1,0,0,0,-1,0,0,0,+1,0,0,0,-1,0,0,0,+1,0,0,0,-1,0,0,0,+1,0,0,0,0,0)},
    #Step 15 - columns move up or down
    {’rows’: (0,0,0,0,0,0,0,0,0,0,0,0,0,0,0,0,0,0,0,0,0),
    ’cols’: (0,0,0,0,-1,0,0,0,+1,0,0,0,-1,0,0,0,+1,0,0,0,-1,0,0,0,+1,0,0,0,-1,0,0,0,+1,0,0,0,0,0)},
    #Step 16 - columns move up or down
    {’rows’: (0,0,0,0,0,0,0,0,0,0,0,0,0,0,0,0,0,0,0,0,0),
    ’cols’: (0,0,0,0,-1,0,0,0,+1,0,0,0,-1,0,0,0,+1,0,0,0,-1,0,0,0,+1,0,0,0,-1,0,0,0,+1,0,0,0,0,0)},)
u = dy/4 #equal horizontal spacing in array
v = dz/4 #equal vertical spacing in array
x0 = 0
coords=dict()
def getCoords():
    """Function to calculate X-coordinates of nodes."""
    for i in range(len(matrix)):
        for j in range(len(matrix[i])):
            if matrix[i][j] == None:
                continue
            if not matrix[i][j] in coords:
                coords[matrix[i][j]] = list()
                x = x0
            else:
                dx = h/NUM_STEPS
                x = coords[matrix[i][j]][-1][2] + dx
            coords[matrix[i][j]].append([j,i,x])
def doStep(currentStep):
    """Function to trace braider movements."""
    global matrix
    newMat = [ [None for j in range(len(matrix[0]))] for i in range(len(matrix)) ]
    for i in range(len(matrix)):
        for j in range(len(matrix[i])):
            new_i = i+steps[currentStep][’cols’][j]
            new_j = j+steps[currentStep][’rows’][i]
            if matrix[i][j] == None or new_i < 0 or new_j < 0:
                continue newMat[new_i][new_j]=matrix[i][j]
        matrix = newMat
        getCoords()
#CALL FUNCTIONS & WRITE OUTPUT FILES
def main():
    getCoords()
    currentStep = 0
    while currentStep < NUM_STEPS:
        doStep(currentStep%len(steps))
        currentStep+=1
    """Calculate Y- and Z-coordinates based on braider movements and create inp-file."""
    for n in coords.iterkeys():
        of = open(’nodesb%d.inp’ %(n+1), ’w’)
        for i in range(len(coords[n])):
            """Compress coordinates of peripheral braider yarns."""
            if coords[n][i][1] == 0: #correct for first row
                coords[n][i][0] -= 1
                coords[n][i][1] += 1
            elif coords[n][i][0] == 0: #correct for first column
```

```
          coords[n][i][0] += 1
          coords[n][i][1] += 1
        elif coords[n][i][1] == (len(matrix)-1): #correct for last row
          coords[n][i][0] -= 1
          coords[n][i][1] -= 1
        elif coords[n][i][0] == (len(matrix[0])-1): #correct for last column
          coords[n][i][0] -= 1
          coords[n][i][1] += 1
        of.write("%d,%f,%f,%f\n" % (i+1,coords[n][i][2], coords[n][i][0]*u, coords[n][i][1]*v))
      of.close()
    """Create inp-file with element list."""
    el=open(’elementsb.inp’,’wb’)
    csvWriter=csv.writer(el,delimiter=’,’,quoting=csv.QUOTE_MINIMAL)
    csvWriter.writerows(zip(range(1,len(steps)+1),range(1,len(steps)+1), range(2,len(steps)+2)))
    el.close()
    """Create inp-file with braider area."""
    AreaOutput(’areab.inp’)
if __name__ == ’__main__’:
    main()
```

B.2. UMAT

```
# USER-DEFINED MATERIAL MODEL TO IMPLEMENT DAMAGE MODEL OF EFFECTIVE MEDIUM IN ABAQUS
    SUBROUTINE MATRIX(STRESS,STATEV,DDSDDE,SSE,SPD,SCD,
    1   RPL,DDSDDT,DRPLDE,DRPLDT,
    2   STRAN,DSTRAN,TIME,DTIME,TEMP,DTEMP,PREDEF,DPRED,CMNAME,
    3   NDI,NSHR,NTENS,NSTATV,PROPS,NPROPS,COORDS,DROT,PNEWDT,
    4   CELENT,DFGRD0,DFGRD1,NOEL,NPT,LAYER,KSPT,KSTEP,KINC)
    INCLUDE ’ABA_PARAM.INC’
    CHARACTER*80 CMNAME
    DIMENSION STRESS(NTENS),STATEV(NSTATV),
    1   DDSDDE(NTENS,NTENS),
    2   DDSDDT(NTENS),DRPLDE(NTENS),
    3   STRAN(NTENS),DSTRAN(NTENS),TIME(2),PREDEF(1),DPRED(1),
    4   PROPS(NPROPS),COORDS(3),DROT(3,3),DFGRD0(3,3),DFGRD1(3,3)
    DIMENSION STRANT(6), CFULL(6,6),CDFULL(6,6)
    DIMENSION DDMDE(6), DCDDM(6,6)
    DIMENSION DTMFDE(6), DCMFDE(6), DDMTDE(6), DDMCDE(6)
    DIMENSION ATEMP1(6), ATEMP2(6)
    DIMENSION OLD_STRESS(6)
    PARAMETER (ZERO = 0.D0,ONE = 1.D0,TWO = 2.D0, HALF = 0.5D0)
    PARAMETER (THREE = 3.D0,FOUR = 4.D0)
C   GET THE MATERIAL PROPERTIES
    TENL = PROPS(1) !YOUNG’S MODULUS IN DIRECTION 1 (L)
    TENT = PROPS(2) !YOUNG’S MODULUS IN DIRECTION 2 (T)
    TENZ = PROPS(3) !YOUNG’S MODULUS IN DIRECTION 3 (Z)
    XNULT = PROPS(4) !POISON’S RATIO POI_12
    XNULZ = PROPS(5) !POISON’S RATIO POI_13
    XNUTZ = PROPS(6) !POISON’S RATIO POI_23
    SHRLT = PROPS(7) !SHEAR MODULUS IN 12 PLANE
    SHRLZ = PROPS(8) !SHEAR MODULUS IN 13 PLANE
    SHRTZ = PROPS(9) !SHEAR MODULUS IN 23 PLANE
    XNUTL = XNULT / TENL * TENT !POI_21
    XNUZL = XNULZ / TENL * TENZ !POI_31
    XNUZT = XNUTZ / TENT * TENZ !POI_32
C   GET THE FAILURE PROPERTIES
    YT = PROPS(10) !TENSILE TRANSVERSE STRENGTH
    YC = PROPS(11) !COMPRESSIVE TRANSVERSE STRENGTH
    SL = PROPS(12) !LONGITUDINAL SHEAR STRENGTH
    ST = SL !TRANSVERSE SHEAR STRENGTH
    GFMAT = PROPS(13) !FRACTURE ENERGY IN MATRIX
    ETA = PROPS(14) !VISCOSITY FOR REGULARIZATION
C   CALCULATE THE STRAIN AT THE END OF THE INCREMENT
    DO I = 1, NTENS
      STRANT(I) = STRAN(I) + DSTRAN(I)
    END DO
C   SAVE THE OLD STRESS TO OLD_STRESS
    DO I = 1, NTENS
      OLD_STRESS(I) = STRESS(I)
    END DO
C   FILL THE 6X6 FULL STIFFNESS MATRIX
    DO I = 1, 6
      DO J = 1, 6
        CFULL(I,J)=ZERO
      END DO
    END DO
    DELTA = ONE - XNULT * XNUTL - XNUTZ * XNUZT - XNULZ * XNUZL
    1   - TWO * XNULT * XNUTZ * XNUZL
```

```
    CFULL(1,1) = TENL * (ONE - XNUTZ * XNUZT) / DELTA
    CFULL(1,2) = TENL * (XNUTL + XNUZL * XNUTZ) / DELTA
    CFULL(1,3) = TENL * (XNUZL + XNUTL * XNUTZ) / DELTA
    CFULL(2,1) = TENT * (XNULT + XNULZ * XNUZT) / DELTA
    CFULL(2,2) = TENT * (ONE - XNULZ * XNUZL) / DELTA
    CFULL(2,3) = TENT * (XNUZT + XNUZL * XNULT) / DELTA
    CFULL(3,1) = TENZ * (XNULZ + XNULT * XNUTZ) / DELTA
    CFULL(3,2) = TENZ * (XNUTZ + XNULZ * XNUTL) / DELTA
    CFULL(3,3) = TENZ * (ONE - XNULT * XNUTL) / DELTA
    CFULL(4,4) = SHRLT
    CFULL(5,5) = SHRLZ
    CFULL(6,6) = SHRTZ
C   CALCULATE THE STRESS STATE
    DO I = 1, NTENS
      STRESS(I)=ZERO
      DO J = 1, NTENS
        STRESS(I) = OLD_STRESS(I) + CFULL(I,J) * STRANT(J)
      END DO
    END DO
C   SAVE THE OLD STATE VARIABLES
    TMFOLD = STATEV(1)
    CMFOLD = STATEV(2)
    DMVOLD = STATEV(3)
    DMTOLD = STATEV(4)
    DMCOLD = STATEV(5)
C   CHECK THE FAILURE INITIATION
C   Tensile matrix failure
    IF ((STRESS(2)+STRESS(3)) .GE. ZERO) THEN
      TERMT1 = ((STRESS(2) + STRESS(3)) / YT)**TWO
      TERMT2 = (STRESS(6)**TWO - STRESS(2)*STRESS(3)) / ST**TWO
      TERMT3 = (STRESS(4)**TWO + STRESS(5)**TWO) / SL**TWO
    END IF
    TERMT = TERMT1 + TERMT2 + TERMT3
    IF (TERMT .GT. ZERO) THEN
      TMF = SQRT(TERMT)
    ELSE
      TMF = ZERO
    END IF
C   Compressive matrix failure
    IF ((STRESS(2)+STRESS(3)) .LT. ZERO) THEN
      TERMC1 = ((YC/(TWO*ST))**TWO - ONE)
      TERMC2 = (STRESS(2) + STRESS(3)) / YC
      TERMC3 = (STRESS(2) + STRESS(3))**TWO / (FOUR * ST**TWO)
      TERMC4 = ((STRESS(6))**TWO - STRESS(2)*STRESS(3)) / ST**TWO
      TERMC5 = (STRESS(4)**TWO + STRESS(5)**TWO) / SL**TWO
    END IF
    TERMC = TERMC1*TERMC2 + TERMC3 + TERMC4 + TERMC5
    IF (TERMC .GT. ZERO) THEN
      CMF = SQRT(TERMC)
    ELSE
      CMF = ZERO
    END IF
C   CALCULATE THE FAILURE STRAIN BY FAILURE STRESS
    EPITT = YT / CFULL(2,2) !TENSILE FAILURE STRAIN 2 DIRECTION
    EPICT = YC / CFULL(2,2) !COMPRESSIVE FAILURE STRAIN 2 DIRECTION
    EPISLT = SL / SHRLT !FAILURE SHEAR STRAIN
C   DAMAGE EVOLUTION - DAMAGE VARIABLE TENSILE FAILURE
    DMT = ZERO
    DDMDTMF = ZERO
    DO I = 1, 6
      DTMFDE(I) = ZERO
      DDMTDE(I) = ZERO
    END DO
    IF (TMF .GT. ONE) THEN
      TERM1 = CFULL(2,2) * EPITT**2 * CELENT / GFMAT
      TERM2 = (ONE - TMF) * TERM1
      DMT = ONE - EXP(TERM2) / TMF
      DDMDTMF = (ONE / TMF + TERM1) * (ONE - DMT)
      IF (DMT .GT. DMTOLD) THEN
        DTMFDE(2) = HALF / TMF * (TWO * STRANT(2) + EPICT - EPITT)
    1     / EPICT / EPITT
        DTMFDE(3) = HALF / TMF * (TWO * STRANT(3) + EPICT - EPITT)
    1     / EPICT / EPITT
        DTMFDE(4) = ONE / TMF * STRANT(4) / EPISLT**TWO
        DTMFDE(5) = ONE / TMF * STRANT(5) / EPISLT**TWO
        DTMFDE(6) = ONE / TMF * STRANT(6) / EPISLT**TWO
        DO I = 1, 6
          DDMTDE(I) = DTMFDE(I) * DDMDTMF
        END DO
      END IF
```

```
    END IF
    DMT = MAX (DMT, DMTOLD)
C   DAMAGE EVOLUTION - DAMAGE VARIABLE COMPRESSIVE FAILURE
    DMC = ZERO
    DDMDCMF = ZERO
    DO I = 1, 6
      DCMFDE(I) = ZERO
      DDMCDE(I) = ZERO
    END DO
    IF (CMF .GT. ONE) THEN
      TERM1 = CFULL(2,2) * EPITT**2 * CELENT / GFMAT
      TERM2 = (ONE - CMF) * TERM1
      DMC = ONE - EXP(TERM2) / CMF
      DDMDCMF = (ONE / CMF + TERM1) * (ONE - DMC)
      IF (DMC .GT. DMCOLD) THEN
        DCMFDE(2) = HALF / CMF * (TWO * STRANT(2) + EPICT - EPITT)
    1     / EPICT / EPITT
        DCMFDE(3) = HALF / CMF * (TWO * STRANT(3) + EPICT - EPITT)
    1     / EPICT / EPITT
        DCMFDE(4) = ONE / CMF * STRANT(4) / EPISLT**TWO
        DCMFDE(5) = ONE / CMF * STRANT(5) / EPISLT**TWO
        DCMFDE(6) = ONE / CMF * STRANT(6) / EPISLT**TWO
        DO I = 1, 6
          DDMCDE(I) = DCMFDE(I) * DDMDCMF
        END DO
      END IF
    END IF
    DMC = MAX (DMC, DMCOLD)
C   GLOBAL DAMAGE VARIABLE
    DM = ONE - (ONE-DMT)*(ONE-DMC)
C   VISCOUS REGULARISATION OF DAMAGE VARIABLE
    DMV = ETA / (ETA + DTIME) * DMVOLD + DTIME / (ETA + DTIME) * DM
C   CALCULATE THE STIFFNESS MATRIX DEPENDENT ON THE DAMAGE VARIABLE
    DO I = 1, 6
      DO J = 1, 6
        CDFULL(I,J) = CFULL(I,J)
      END DO
    END DO
    IF (DMV .NE. ZERO) THEN
      CDFULL(1,1) = CFULL(1,1)
      CDFULL(1,2) = (ONE - DMV) * CFULL(1,2)
      CDFULL(1,3) = (ONE - DMV) * CFULL(1,3)
      CDFULL(2,1) = (ONE - DMV) * CFULL(2,1)
      CDFULL(2,2) = (ONE - DMV) * CFULL(2,2)
      CDFULL(2,3) = (ONE - DMV) * CFULL(2,3)
      CDFULL(3,1) = (ONE - DMV) * CFULL(3,1)
      CDFULL(3,2) = (ONE - DMV) * CFULL(3,2)
      CDFULL(3,3) = (ONE - DMV) * CFULL(3,3)
      CDFULL(4,4) = (ONE - DMV) * CFULL(4,4)
      CDFULL(5,5) = (ONE - DMV) * CFULL(5,5)
      CDFULL(6,6) = (ONE - DMV) * CFULL(6,6)
    END IF
C   UPDATE THE STRESS
    DO I = 1, NTENS
      STRESS(I) = ZERO
      DO J = 1, NTENS
        STRESS(I) = STRESS(I) + CDFULL(I,J) * STRANT(J)
      END DO
    END DO
C   CALCULATE THE DERIVATIVE MATRIX DC/DDM OF THE DAMAGED MATRIX
    DO I = 1, 6
      DO J = 1, 6
        DCDDM(I,J) = ZERO
      END DO
    END DO
    DCDDM(1,2) = -CFULL(1,2)
    DCDDM(1,3) = -CFULL(1,3)
    DCDDM(2,1) = -CFULL(2,1)
    DCDDM(2,2) = -CFULL(2,2)
    DCDDM(2,3) = -CFULL(2,3)
    DCDDM(3,1) = -CFULL(3,1)
    DCDDM(3,2) = -CFULL(3,2)
    DCDDM(3,3) = -CFULL(3,3)
    DCDDM(4,4) = -CFULL(4,4)
    DCDDM(5,5) = -CFULL(5,5)
    DCDDM(6,6) = -CFULL(6,6)
C   UPDATE THE JACOBIAN
    DO I = 1, NTENS
      ATEMP1(I) = ZERO
      DO J = 1, NTENS
```

```
        ATEMP1(I) = ATEMP1(I) + DCDDM(I,J) * STRANT(J)
      END DO
    END DO
    DO I = 1, NTENS
      DO J = 1, NTENS
        DDSDDE(I,J) = CDFULL(I,J) + (ATEMP1(I) * DDMTDE(J)
    1      + ATEMP1(I) * DDMCDE(J)) * DTIME / (DTIME + ETA)
      END DO
    END DO
C   UPDATE THE STATE VARIABLES
    STATEV(1) = TMF
    STATEV(2) = CMF
    STATEV(3) = DMV
    STATEV(4) = DMT
    STATEV(5) = DMC
C   COMPUTE THE SPECIFIC ELASTIC STRAIN ENERGY
    DO I = 1, NDI
      SSE = SSE + HALF * (STRESS(I) + OLD_STRESS(I)) * DSTRAN(I)
    END DO
    DO I = NDI+1, NTENS
      SSE = SSE + (STRESS(I) + OLD_STRESS(I)) * DSTRAN(I)
    END DO
    RETURN

    END
```